High resolution SOFIN CCD échelle spectroscopy

Ilya V. Ilyin

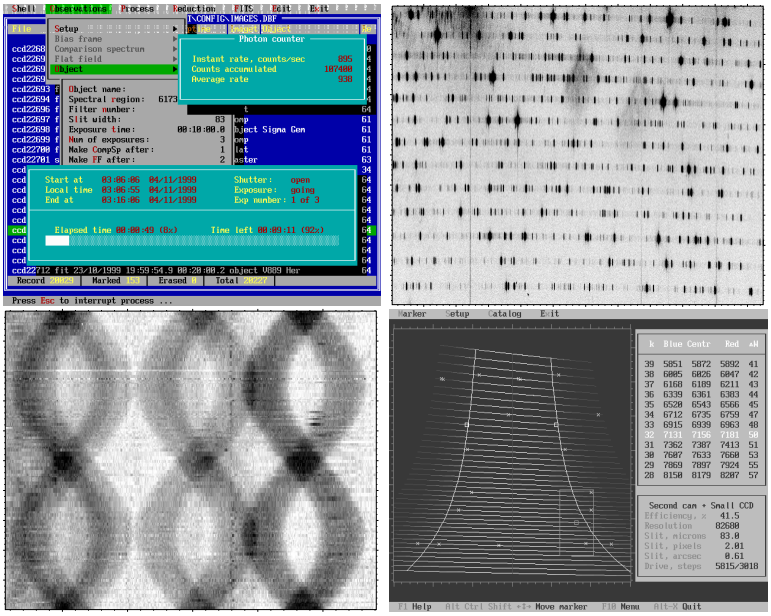

Oulu 2000

Astronomy Division
Department of Physical Sciences
University of Oulu
Finland

High resolution SOFIN CCD échelle spectroscopy

Ilya V. Ilyin

ACADEMIC DISSERTATION
To be presented, with the permission of the Faculty of Science of the University of Oulu, for public criticism in the Auditorium GO101 on September 1st, 2000, at 12 o'clock noon.

The figures on the front page are:

The console screen of the observation menu of 4A at the top left. A ThAr comparison SOFIN échelle spectrum image in the 5030 & 4924 spectral region at the top right. The selection of the spectral settings with the focal plane map of the SOFIN spectrograph at the bottom right. The phased image of spectral lines around 6430Å of the detached RS CVn binary ER Vul.

ISBN 951-42-5724-3
Oulu 2000
University Press

Preface

This work concerns observations with the SOFIN spectrograph and the data reduction of échelle spectra. The work began in 1991 when the spectrograph was for the first time installed at the Nordic Optical Telescope. In that period, the author was involved in developing the control software for the spectrograph and the CCDs, so that now the observations are almost completely remotely controlled by computer. Later, the development of the data reduction package has started which was motivated by the absence of other suitable software packages at that time, and, also, by the specific requirements to the data reduction of the SOFIN spectra. The aim of the thesis is the development of observing techniques and of optimal reduction methods, and their implementation. The use of these methods in the observation and reduction has resulted in a large number of high-quality and, in some respect, unique, échelle spectra within different astrophysical programmes and in many scientific papers. A selection from these has formed the astrophysical results of the thesis. Thus, the thesis merges three different aspects of scientific work: the instrument, the data reduction including error analysis, and the application to various astrophysical targets.

The thesis work has the following structure.

Chapter 1 gives the description of the spectrograph and scientific objectives of the observing programmes. Then, the estimation and measurement of the efficiency of the spectrograph follows. In the next sections, the model of the spectrograph is described, which is incorporated in a software tool used during observations for the proper settings of the instrument. In the last section, the stability issues of the spectrograph are discussed based upon a number of tests.

In Chapter 2, the measurements of the spectrograph instrumental profile is given which is followed by the discussion of several important issues concerning the resolving power of the instrument.

Chapter 3 concerns the CCDs. This part was specially developed to solve the initial problems and improve the performance of the SOFIN Astromed-CCD cameras. The following aspects are illustrated: the noise sources, the flat-fielding problem, and the measurable characteristics of the CCD performance. The measurement

and integration of the CCD intensity transfer function is given. In the following sections, the method of the CCD optimization is highlighted.

In Chapter 4, an overview of the data reduction package is given. The limitations on the volume of this thesis do not allow to give the whole description of all the specific algorithms developed for the data reduction. As an example, the cross-correlation method and its accuracy are discussed because it is essential for the accurate radial velocity measurements of the stellar spectra, which is demonstrated in the first papers of the thesis.

Deconvolution of stellar spectra and recovery of broadening functions are an important issue in modern methods of data analysis. A number of astrophysical aspects, the model, and the implementation of the algorithm are given in Chapter 5. The method used is based on the truncated generalized least-squares and operates with the principal components of the solution. The limitations of the method are discussed motivating the regularized principal solution extension. An example of the deconvolution of the SOFIN solar spectrum is given and discussed in brief.

The most recent, not yet published aspect of the author's work is given in Chapter 6 and concerns the mercury line profile variability of the binary star α And. The description of the analysis is given and some results are discussed.

In the Appendix, a user's guide for the reduction of SOFIN échelle spectra is given, which illustrates various aspects of the process and effects which are taken into account to achieve the maximal photometric and position quality of the spectra.

The second part of the thesis consists of selected papers based on SOFIN observations where the author's work was essential. In the preface to the second part, a short description of the author's contributions is given which is followed by the list of all papers where the author was involved.

A part of the author's dissertation work which is not included into the present thesis because of its size concerns the numerical methods of data analysis. In a separate manuscript, the following topics are described: propagation of random errors; the generalized least-squares: the linear, non-linear, and constrained cases; test of the linear hypothesis; the orthogonal polynomial series and their transformations to power series and Chebyshev forms; the smoothing splines; and the solution to the Keplerian orbit problem and the binary system parameters. These ready-to-program algorithms were derived by the author on the basis of a number of treatises on numerical analysis and implemented into the data reduction package. The most important aspect of these derivations is the proper error analysis of the parameters and the model, which plays a key role in the reduction process of the spectra where the intensities and their errors are transformed at each stage (including at some stages the wavelength errors). The description of the deconvolution of stellar spectra (Chapter 5) is a part of this handbook and uses the same style and notations.

Acknowledgements

This work was carried out as a part of the scientific project "Late type stars and interstellar matter: activity, magnetism, and turbulence" led by Prof. I.Tuominen and funded by the Academy of Finland. The work has begun in the Observatory of the University of Helsinki in 1991, and was then continued at the University of Oulu in 1996.

I express my gratitude, firstly, to Prof. I.Tuominen for giving me the possibility to join his project and for his long term support in many aspects of various kinds.

I thank very much the pre-referees of my dissertation for their careful reading, their kind suggestions for the further improvement of the text, and for the evaluation of the work in their statements. The manuscript was examined by Dr. Jaan Pelt, Tartu Observatory, Estonia, and Prof. Gösta Gahm, Stockholm Observatory, Sweden.

I want to thank Prof. Craig Mackay (Institute of Astronomy, Cambridge, England) for his stimulating discussions concerning the CCDs; the engineers at ORM, La Palma, Chris MacCovach (ING), Thomas Erm and Graham Cox (NOT), for their kind assistance to me with the CCD work, and Dr. Slavek Rucinski (Toronto, Canada) for the discussions which have stimulated my work on deconvolution of spectra.

Many thanks to my collaborators and co-workers Svetlana Berdyugina, Peter Petrov, and Nikolai Piskunov. My special thanks to Rudolf Duemmler for his close participation in many parts of my work in terms of critical assessments, detailed discussions, and for his essential help to improve the style of the manuscript.

At last, I sincerely thank my family Svetlana, Ellen, and Julia (and our dog Timon) for their invaluable support, patience and understanding.

Contents

Chapter 1

The échelle spectrograph SOFIN

1.1 Introduction

The high resolution échelle spectrograph SOFIN was designed and manufactured at the Crimean Astrophysical Observatory in collaboration with the Observatory of Helsinki University and installed at the Cassegrain focus of the 2.56 m Nordic Optical Telescope, La Palma, Canary Islands. The observations with the instrument started in June 1991 (Tuominen 1992). The spectrograph is a unique instrument in its class and is one of the few very high resolution spectrographs in the northern hemisphere. The spectrograph was designed to allow stellar spectroscopy with three different spectral resolutions $R = \lambda/\Delta\lambda = 30\,000$, $80\,000$, and $170\,000$, depending on the brightness of the star and the scientific goals. The resolution is altered by changing one of the three different optical cameras whilst all other optical elements of the spectrograph remain unchanged. The spectrograph is equipped with a cross-dispersion prism to separate spectral orders so that many different wavelengths are recorded in a single CCD exposure. The higher the spectral resolution the smaller the part of the spectral range which can be covered by the CCD. The change of the spectral setting is done by turning the échelle grating and the cross-dispersion prism.

The spectrograph is completely remotely controlled from the host computer, except for a few minor functions. Such a design provides a high operational efficiency during the observations. The spectrograph control software is currently running under MS-DOS and is a menu-driven program with a range of services to assist the observations (Ilyin 1996). It includes a database of observations where the data records are stored, which can be retrieved and displayed later, a quick-look facility

for an express analysis of the data obtained, the databases of observed objects and spectral regions to hold all information specific for the particular observation and the setup of the spectrograph. The data reduction facility is the second large part of the software developed for the spectrograph. The key points of the data reduction package are the simplicity and the high efficiency which in conjunction with the user-friendly interface provides an easy way to operate with the enormous amount and complex nature of the data.

1.2 Scientific applications

The long focus optical camera provides the highest spectral resolving power $R = 180\,000$ and is used to resolve the fine structures of spectral lines and for accurate measurements of their positions. For instance, the interstellar Na I D 5890 Å is formed on the line of sight to some background stellar object and reflects the motions of interstellar clouds. The higher the resolution, the more components can be resolved, i.e. the smaller velocity differences between different clouds can be detected. Another astrophysical aspect is to use the high resolution camera to measure the isotopic shift and hyperfine structure of the spectral lines of chemically peculiar Ap stars and of cool stars (e.g. Wahlgren et al. 1999). In the case of the Ap stars, the isotopic ratio gives an estimate of the diffusion rate of the isotopes from the enriched regions of their origin to the upper atmosphere. The very important Li I 6707 Å line is a key element for studying the history of the universe, nucleosynthethis, stellar interiors, and stellar evolution. These measurements require the accurate observation of the position and intensity of fully resolved spectral lines with the subsequent accurate analysis and comparison with a synthetic spectrum. The high resolution camera allows to increase the accuracy of radial velocity measurements, since the error of the spectral line position determination decreases as the resolution grows. This also gives the possibility to investigate the instability and variations of the radial velocities of F, G, and K-type stars, which in the past were supposed to be very stable and were used as radial velocity standards. For some stars, these variations, seen as tiny Doppler shifts of the spectral line positions, are thought to be due to a low mass companion, like a brown dwarf or a large Jupiter-like planet, perturbing the position of the main star along the line of sight, although the variations may be caused as well by non-radial pulsations of a single star. To decide which explanation is correct for a particular star, accurate observations at the highest resolution are needed, allowing to study the line profile shapes in detail.

The second optical camera provides half of the resolving power of the previous one and corresponds to about 80 000 near the échelle blaze angle. Reducing the resolution two times doubles the amount of light per resolution element, as well as allows for a doubling of the entrance slit width which reduces the light losses, and, therefore, fainter objects can be observed. The second optical camera is widely

used for Doppler imaging of late type stars. These exhibit small bumps in a spectral line which drifts over the profile as the star rotates. The solution of the inverse problem, using models of stellar atmospheres, yields the geometrical distribution of the spots and a temperature map of the stellar surface (e.g. Bergyugina 1998). The medium resolution optical camera is used for the direct measurements of the stellar magnetic field with the Stokesmeter installed in front of the spectrograph entrance slit. The Stokesmeter divides the stellar light into two beams with opposite circular polarization. In the presence of a stellar magnetic field the spectral lines in these two beams are shifted with respect to each other and the stronger the field, the larger the offset. Measurements of the Zeeman splitting of a number of spectral lines gives the effective magnetic field of the star as a function of its rotational phase. Solving the inverse problem, using models of stellar atmospheres and taking into account the effect of Zeeman splitting, gives the distribution of the magnetic field strength over the stellar surface. Another aspect of the second camera applications is the observations of the non-radial pulsations of Ap stars on the short time scale of their variability with simultaneous recording of many spectral features in one exposure. Lines of certain chemical elements exhibit small variations of their radial velocities which can be attributed to the surface inhomogeneities. On the other hand, the amplitude of the oscillations derived from broad band photometry strongly decays from the blue to the red which is attributed to the wavelength dependence of limb-darkening and the steepness of the temperature gradient with respect to the optical thickness.

The low resolution camera provides a spectral resolution around 30 000 which is typical for most other stellar spectrographs. Since there is virtually no light loss on the wide entrance slit and the spectral resolution is low, the camera is used for observations of objects as faint as 15^{m} with a 2.5 m telescope. The camera allows to record in one exposure half of the whole optical spectrum ranging from the blue spectral orders at 3500 Å to the red at 11000 Å. Such curious objects as T Tauri and FU Orionis stars (e.g. Petrov et al. 1999), chromospherically active late type binary systems, red dwarfs, and cataclysmic variables are observable with the camera with most of the hydrogen lines, ultraviolet Ca II H & K, the infrared Ca II triplet seen in the same échelle image which offers the possibility to analyze spectral lines originating in different layers of the star and the surrounding environment.

1.3 Design of the spectrograph

The optical design of the SOFIN spectrograph is similar to that of the échelle spectrograph for the CTIO 4m Blanco Telescope. The complete spectrograph design is described in four papers: the optics (Pronik 1995), the mechanics (Lagutin 1995), the electronics (Bukach & Zlotnikov 1995), and the software (Ilyin 1995, including results of the first observations).

The spectrograph is mounted on the Cassegrain rotating adapter of the alt-azimuth

Nordic Optical Telescope (NOT). The diameters of the main and secondary mirror of the telescope are 2560 and 510 mm. The effective focal length is 28160 mm, which makes the scale in the focal plane $137\,\mu\mathrm{m}/1''$.

The schematics of the optics is given in Fig. 1.1 and the layout of the main components are shown in Figs. 1.2 and 1.3. All components of the spectrograph are assembled in a rigid welded construction which has the dimension of $1800 \times 800 \times 800\,\mathrm{mm}^3$; the total weight without the CCD dewars is 240 kg. The components of the spectrograph are described in the following.

The entrance slit (1) in Fig. 1.3 is situated at the distance 210 mm below the attachment flange. The mirrored slit plane is tilted with respect to the optical axis by $13.^{\circ}5$ in order to be viewed by the intensified TV guiding camera. The slit width is remotely controlled and depends on the spectral resolution being used, whilst the width of the decker can be changed manually and defines the height of spectral orders and the interorder spacing.

The filter and shutter unit (2) in Fig. 1.3 is mounted below the entrance slit in one assembly unit. A hollow cylinder with two radial slots attached to the axis of a stepping motor constitutes the shutter. The turret with the filter wheel attached to a stepping motor contains eight holdings for filters which have 16 mm in diameter and 6 mm in thickness (the effective focal length of the collimator depends on the filter thickness). The filters reduce the amount of scattered light diffused on the spectrograph optical frames and surfaces, and are selected according to the spectral region being used. The bandpasses are given in the following table together with their numbers and positions on the turret. Some of the filters are composed of two pieces to keep the thickness constant: a metal ring spacer between the pieces eliminates possible optical interference on their surfaces.

0	0	Closed		
1	7	Open		
2	6	3000 - 25000	Neutral	double
3	5	8500 - 25000	Infrared	double
4	4	7000 - 25000	Red	single
5	3	6000 - 25000	Orange	single
6	2	3500 - 6000	Blue	double
7	1	3500 - 7500	Transparent	double

The beam switcher (3) in Fig. 1.3 is used to render the light from the two calibration sources to the slit. It consists of a pentaprism attached to the stepping motor axis via a rotating arm. In the position shown with the solid line, the slit is unobscured for the light from the telescope, the position shown with the dashed line gives the light from the flat field lamp.

The calibration sources include a tungsten flat field lamp (5) in Fig. 1.3, and a ThAr hollow cathode spectral lamp (6) manufactured by S. & J. Juniper & Co., UK. The pupils of the lamps are collimated at $f/11$.

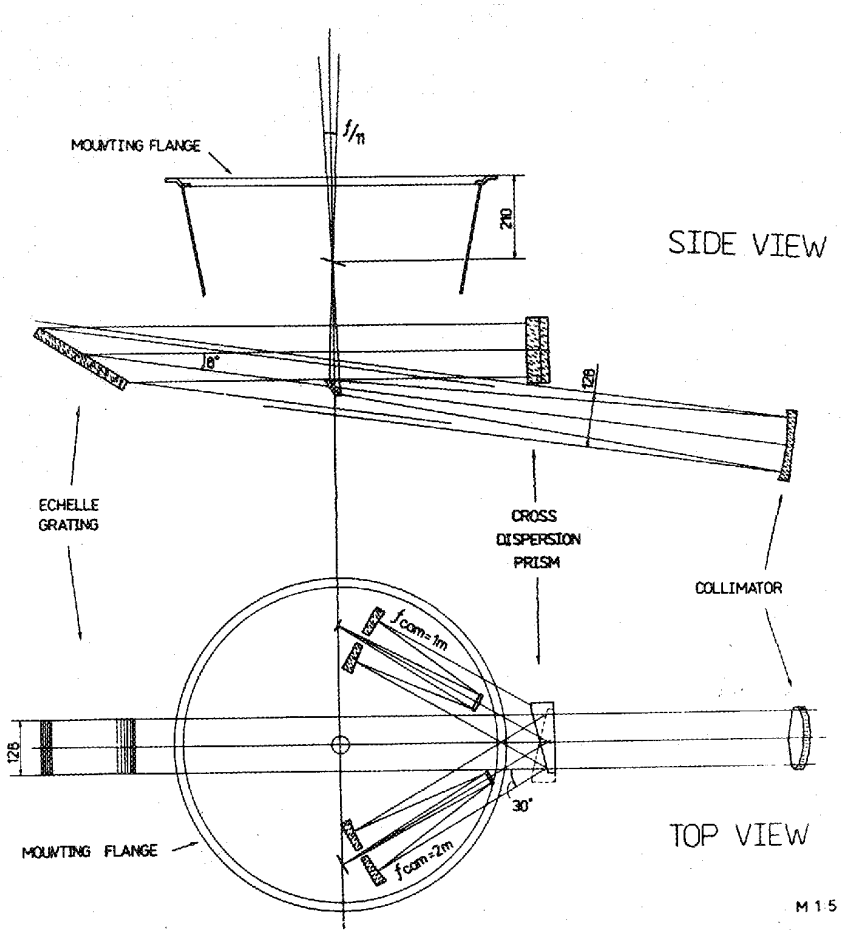

Figure 1.1: The optical layout of the SOFIN spectrograph. The converging $f/11$ beam focussed onto the slit is redirected by the flat mirror to the collimator. The collimated beam illuminates the échelle grating which renders the light dispersed in wavelength to the cross-dispersion prism to separate the spectral orders in the direction perpendicular to the dispersion. The two flipped positions of the cross-dispersion prism are shown by the solid and dashed lines. Depending on the position, the beam is directed to one of the optical cameras mounted in the spectrograph. The échelle image is formed on the CCD attached to the optical camera.

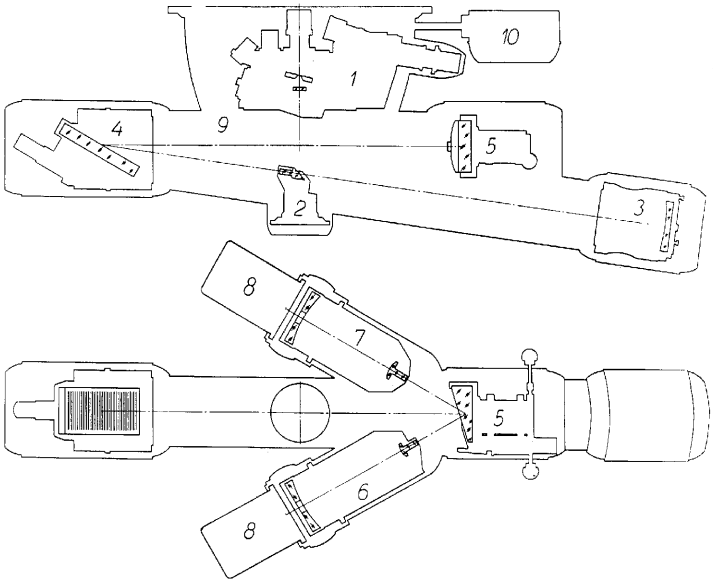

Figure 1.2: The mechanical layout of the SOFIN spectrograph: the upper unit (1) is shown in details in Fig. 1.3, flat mirror (2) with the adjustment mechanism, collimator (3), échelle grating (4), cross-dispersion prism (5) with the handle to flip the prism, two optical cameras (6 and 7) installed, CCD cameras (8), assembly frame (9), and power supply with the stepping motor amplifiers (10).

The intensified CCD TV guiding camera (4) in Fig. 1.3 is used for setting, focussing, and guiding the stellar image on the slit. The field of view on the TV screen is $70''$. With the maximum intensification a star as faint as $16^{\rm m}$ can be seen. For bright objects a gray filter with an attenuation of 100 is put in front of the TV camera. The shutter, gray filter, and open diaphragm are installed on a remotely controlled linear shaft.

The analyzer of circular polarization (Stokesmeter) (8) in Fig. 1.3 is mounted on a platform above the slit and can be positioned onto the optical axis when used for spectropolarimetry. The design of the Stokesmeter is described by Plachinda & Tarasova (1999) and is similar to that of Donati & Semel (1990). It consists of an achromatic (4000–6800 Å) turnable quarter-wave plate, a beam splitter, made of a plate of Iceland spar, and a fixed achromatic quarter-wave plate on exit which converts the linearly polarized light into circularly polarized light to avoid linear polarized light attenuation on the échelle grating. The angle of the turnable quarter-wave plate on the entrance is controlled by a stepping motor; four exposures with the plate subsequently turned by $22\overset{\circ}{.}5$ allows to measure all four Stokes

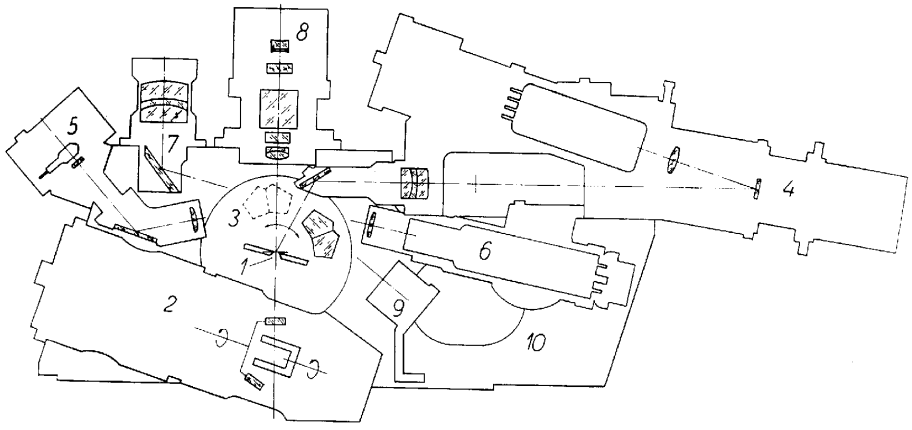

Figure 1.3: The mechanical layout of the upper unit: slit (1), filter turret and the shutter (2), pentaprism rotator (3), intensified guiding TV camera (4), flat field lamp (5), comparison spectrum ThAr lamp (6), an auxiliary viewing pupil (7), Zeeman analyzer (8), stray light absorber (9), and the assembly unit (10).

parameters. The image separation is 3″ on the slit.

The diagonal flat mirror (2) in Fig. 1.2 is located 300 mm below the entrance slit and turns the optical axis by 98°. The projected diameter is 32 mm.

The parabolic collimator mirror (3) in Fig. 1.2 has a diameter of 128 mm and a focal length of 1396 mm. The effective focal length of the collimator coupled with the filters is 1400 mm. The mirror has been aligned once during assembly and any temperature changes of its focal length are compensated by the focussing of the optical cameras.

The photon counter (not shown but located between 2 and 3 in Fig. 1.2) is used to estimate the amount of light passed through the slit of the spectrograph and consists of a small prism installed in the collimated beam and a photomultiplier. The photon count rate and accumulated sum during the object exposure are displayed in real-time in order to suggest the exposure time in case of observing in modest weather conditions.

The R2 échelle (4) in Fig. 1.2 (Milton Roy Co., USA), has a grooved area of $128 \times 256\,\mathrm{mm}^2$ and is ruled with $79\,\mathrm{grooves\,mm}^{-1}$. The blaze angle is 63.°435 (arctan 2). The incident and diffracted beams are separated by a fixed angle of 8° and the angles are coplanar with the échelle normal. The échelle tilt mechanism changes the angle of incidence by turning the frame around ball-edged pivots within

$\pm 3^\circ$ by driving the tangent arm attached to the axis of the remotely controlled stepping motor. The motor step size is about one pixel on the CCD for the long camera. The working spectral orders are 20–65 (11 300 – 3500 Å).

The double-pass cross-dispersion prism (5) in Fig. 1.2 is made of BK7 glass and mounted 800 mm apart from the échelle. The prism apex angle is $17^\circ.0212$ which makes the interorder spacing 75% of the order height at 5650 Å in the central 40th order. The positioning mechanism of the prism is similar to that of the échelle and allows to change the spectral setting in the cross-dispersion direction. The motor step size is about one pixel on the CCD for the long camera. The prism assembly is mounted on a mechanism which allows to turn the prism around the optical axis to redirect the refracted beam to one of the two optical cameras installed simultaneously in the spectrograph.

Three optical cameras provide three different spectral resolutions; two of them (6 and 7 in Fig. 1.2) can be installed in the optical ports at the same time and the resolution is altered by flipping the cross-dispersion prism. The short and long cameras are interchangeable, the medium camera is mounted permanently.

1. The long optical camera is a Cassegrain mirror system with an effective focal length of 2079 mm and provides a resolving power ranging from 150 000 to 185 000 which depends on the échelle deflection angle. The entrance slit width projected on two CCD pixels is 38 μm ($0''.28$ on the sky) at the blaze angle. The light loss on the slit with a seeing of $1''$ is 75%. The length of the spectral orders is about 20 Å around 5500 Å which corresponds to a pixel size of about 1000 m s^{-1} in radial velocities. About 15 adjacent spectral orders can be covered in one CCD image. The vignetting in the image centre is about 7% and almost homogeneous along the image.

2. The medium optical camera is a Ritchey-Chrétien mirror system with an effective focal length of 1000 mm with a spectral resolution ranging from 70 000 to 86 000. The entrance slit width projected on two CCD pixels is 82 μm ($0''.6$) at the blaze angle. The light loss on the slit is about 50% if the seeing is $1''$. The length of the spectral orders is about 40 Å around 5500 Å. The CCD format allows to record 12 such orders in one exposure. The pixel size corresponds to about 1900 m s^{-1} in radial velocities. The vignetting in the image centre is about 16% and increases towards the edges (68%).

3. The short optical camera is a meniscus system (two menisci and two mirrors) has an effective focal length of 348 mm and provides a spectral resolution from 25 000 to 30 000 with the entrance slit width of 236 μm ($1''.73$) projected on two CCD pixels. There is virtually no light loss on the slit since it is wider than the average seeing. The light loss occurs mostly on the slit decker which is reduced for the camera as compared to the others for better order separation in cross-dispersion. The spectral format of the camera allows to record all spectral orders in one image from 20 to 67 with the length of one

order being around 120 Å at 5500 Å. Two such exposures are necessary to get the complete overlap and full wavelength coverage of all spectral orders. The pixel size corresponds to 5700 m s^{-1} in radial velocities. The vignetting of the camera is 22% in the image centre and 92% at the edges is due to the large secondary mirror.

The parameters of the first two optical cameras are given in the following table (units are mm); the optical diagram of the third camera is given in the original paper of Pronik (1995):

$N_{\rm cam}$	$f_{\rm cam}$	R_1	R_2	e_1^2	e_2^2	D_1	D_2	d_1	d_2
1	2079	-852.05	-216.36	1	2.2957	160	40	-340	420.05
2	1000	-937.50	-635.30	1.247	12.2233	160	60	-300	356.00

where $f_{\rm cam}$ is the focal length, R is the radius of the mirror curvature, e^2 is the eccentricity, D is the diameter of the mirror, d_1 is the distance between the mirrors, and d_2 is the distance between the focal plane and the secondary mirror.

Each camera is equipped with a focussing mechanism which is a turnable threaded ring to offset the image formed on the CCD along the optical axis whilst the positions of the optical elements of the camera remain unchanged. The CCD camera is attached to the optical camera via a bayonet adapter which preserves the CCD adjustment after re-installation of the optical and CCD cameras. The bayonet connectors are equipped with adjustment screws to align the CCD pixels with respect to the cross-dispersion direction.

Two similar Astromed-3200 CCD cameras (8) in Fig. 1.2 make use of two UV-coated EEV CCDs: P88100 (1152 × 298 pixels) and P88200 (1152 × 770 pixels) which are housed in liquid nitrogen cooled dewars and operated at a temperature of 150 K. The pixel size is $22.5 \times 22.5\,\mu$m^2. The dewar window is made of Spectrosil B fused silica, 50 mm in diameter and 2 mm in thickness. The first one, the larger format CCD camera, is used with the long and short cameras, the second one, the smaller format CCD, is used with the medium resolution camera.

1.4 Efficiency of the spectrograph

The overall efficiency of the system including telescope and spectrograph is defined as the fraction of the photons entering the main mirror which is detected by the CCD.

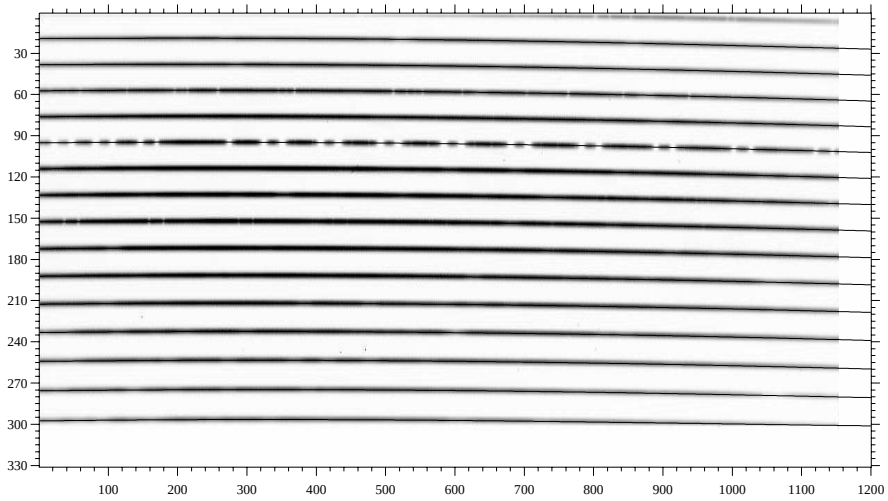

Figure 1.4: An échelle image of the RS CVn star IM Peg obtained with the medium camera; $R = 80\,000$ in the 6173 & 6563 Å spectral region. The spectral orders located during data reduction are shown. The wavelengths of the spectral orders increase from bottom to top. The O_2 atmospheric bands at 7600 Å are clearly seen in the 5th order from the top.

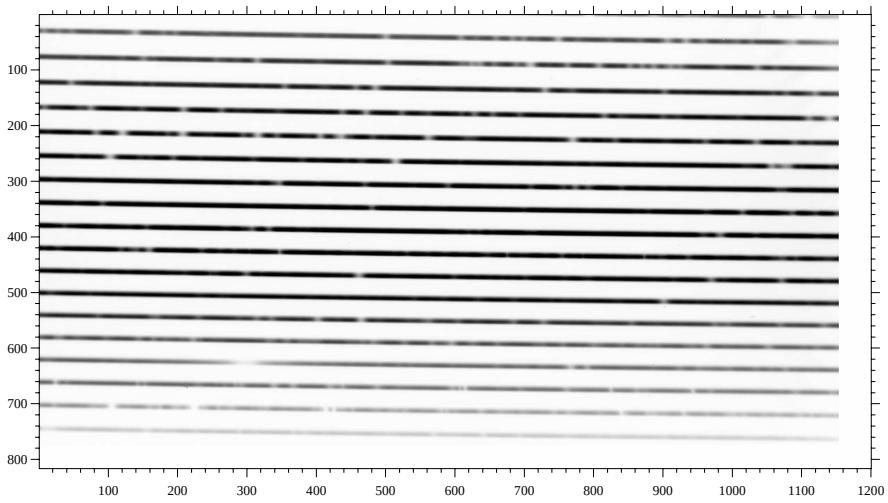

Figure 1.5: A raw échelle image of α Tau obtained with the long optical camera; $R = 160\,000$ in the 6427 & 7516 Å spectral region. The wavelengths of the spectral orders increase from top to bottom.

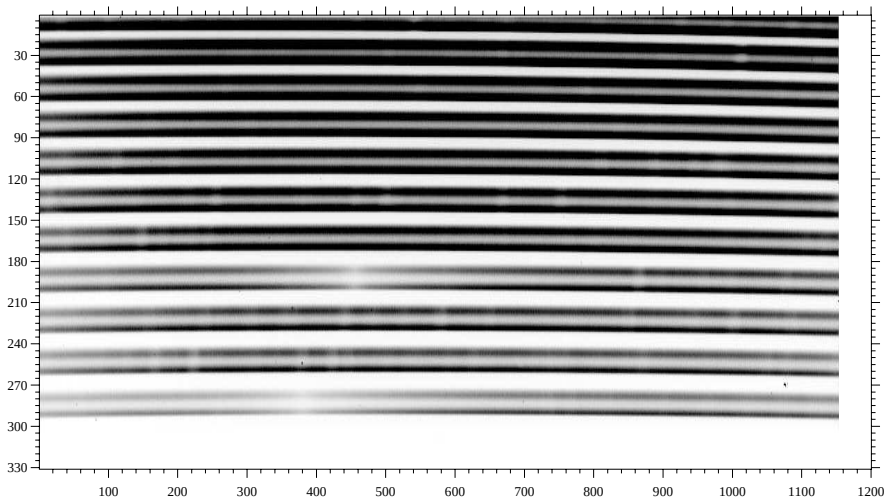

Figure 1.6: A raw échelle image of the magnetic Ap star α^2 CVn recorded with the Zeeman analyzer with the medium optical camera $R = 80\,000$ around 4500 Å. The doubled spectral orders are the left and right polarized beams.

1.4.1 The direct measurement of the efficiency

Measurements of the spectrograph efficiency are usually done by observing stars with known energy distributions at different wavelengths, e.g. the set of bright secondary standard stars for flux calibration given in Taylor (1984) and Hamuy et al. (1992). Instead of the standard method, we used the programme observations of two G-type stars obtained during different observing runs at a range of zenith distances and meteorological conditions to estimate the efficiency in the red.

The central CCD order was used where the vignetting effect is minimal. The width of the cross-dispersion profile was used as the estimate of the seeing condition during the exposure. Assuming that the seeing profile is a Gaussian, the relative transmittance of the slit is given by

$$T = \mathrm{erf}\left(\frac{w\sqrt{\ln 2}}{\mathrm{FWHM}}\right), \tag{1.1}$$

where the seeing profile width is given by FWHM, and w is the slit width. The transmittance is plotted as a function of the width ratio in Fig. 1.9. The measured signal-to-noise ratio (SNR) at the selected order, corrected for the slit effect, and reduced to the same exposure time was plotted in logarithmic units with respect to the airmass of the observations. The upper envelope of the points was used for linear extrapolation to the zenith.

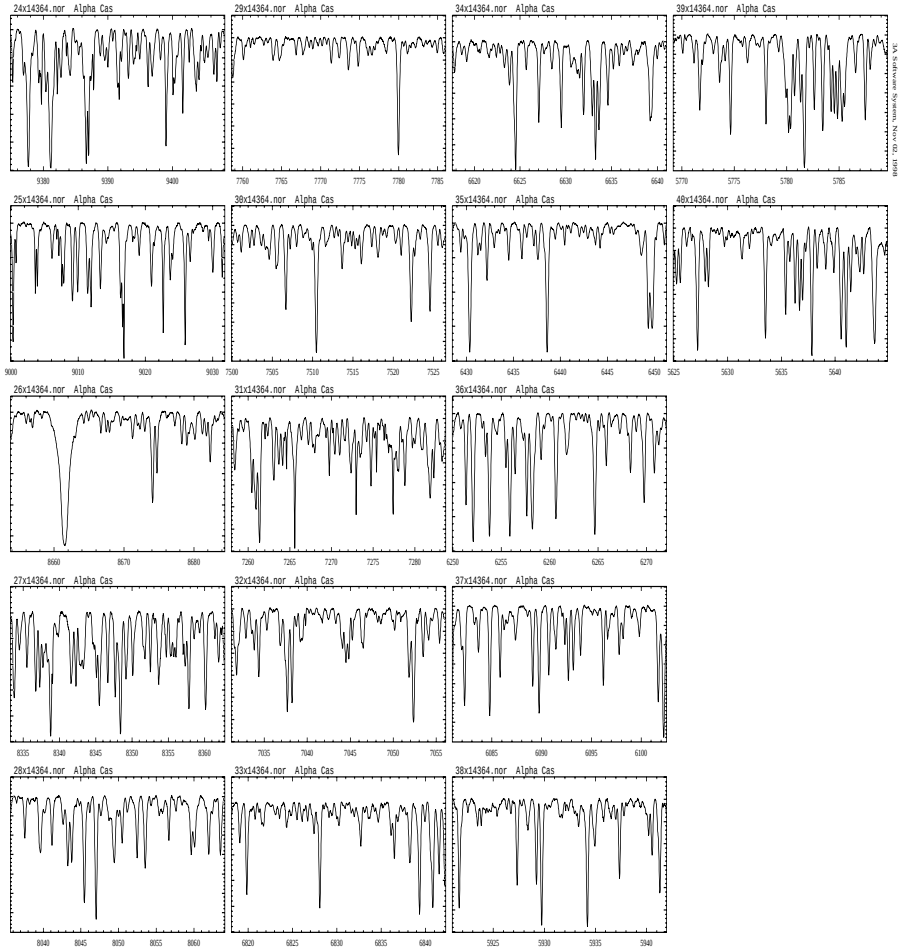

Figure 1.7: The reduced spectra of α Cas (V=2.20, K0 IIIa) with resolution $R = 160\,000$ in the 6427 & 7516 Å spectral region.

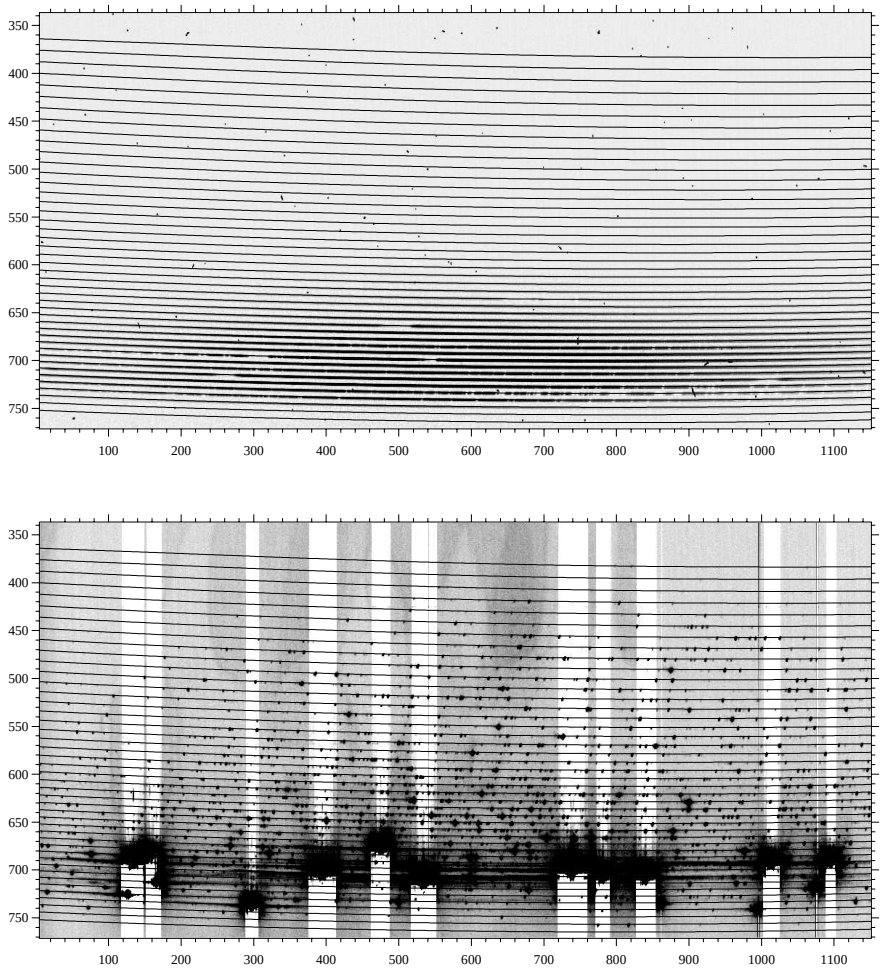

Figure 1.8: Echelle images taken with the low resolution $R = 30\,000$ optical camera. The horizontal curves indicate the position of the spectral orders found during data reduction. *Top:* preprocessed image with the scattered light surface subtracted prior to the weighted extraction of the spectral orders of the 20 min exposure of the FU Ori star V1057 Cyg (V=10) which gave a signal-to-noise ratio around 100 in the continuum at Hα. *Bottom:* The corresponding ThAr comparison spectrum image taken in the same spectral region. The bright Thorium lines in the red are overexposed to allow a large number of fainter lines to be seen and used for the calibration. The saturated lines produce vertical white "tails" areas, i.e. of depressed bias level.

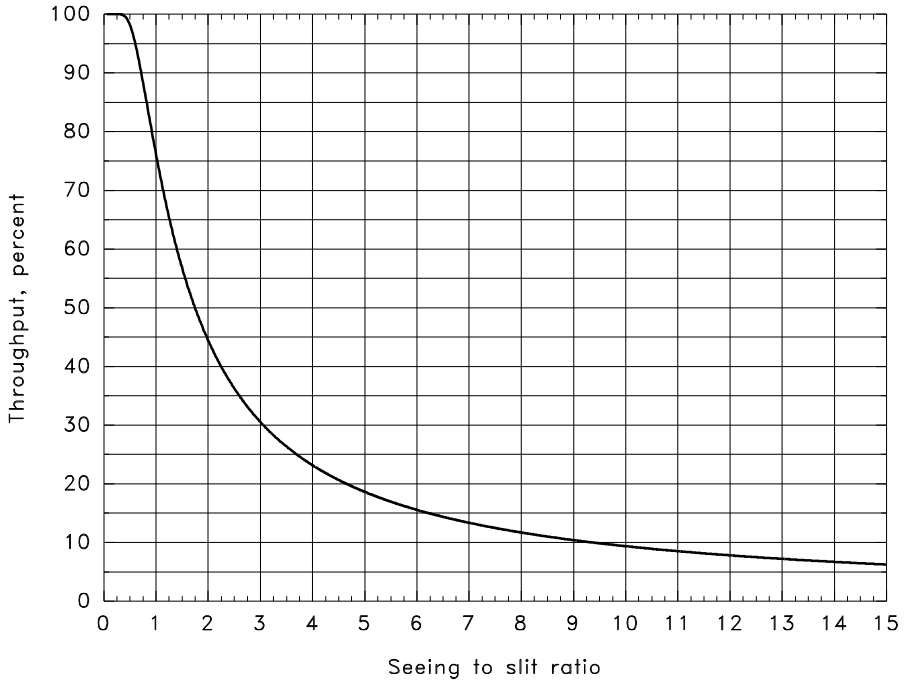

Figure 1.9: Throughput of the slit illuminated by a Gaussian seeing image. The horizontal axis is the ratio of the FWHM of the Gaussian seeing profile and the slit width.

58 observations of 31 Aql (V=5.20, G7 IV) were made with the long camera with the slit width 37 μm (0.″27) which gives the resolution $R = 160\,000$ ($\Delta\lambda$=0.020 Å per pixel) in the central order 35 at 6440 Å. Extrapolation to the zenith estimates SNR to be 470 in 10 min of exposure time without the light loss on the slit. The flux outside of the Earth atmosphere expected for the star is 1100 photons cm^{-2} s^{-1} Å^{-1} (interpolated from Allen 1976, p. 207). The monochromatic Earth atmosphere extinction at 6440 Å is 0.057 per airmass (the extinction coefficients for the La Palma Observatory were provided by the Carlsberg Meridian Telescope). For the given diameters of the telescope mirrors (256 and 51 cm respectively), the expected SNR of the star at zenith is 2260. Hence, the efficiency for the long camera is estimated to be 4.3%.

92 observations of HD 199178 (V=7.24 G2 III) were made with the medium camera with the slit width 81 μm (0.″60) which provides the resolution $R = 76\,000$ ($\Delta\lambda$=0.042 Å per pixel) in the central order 32 at 7000 Å. Extrapolation to the zenith estimates SNR to be 300 in 10 min of exposure time without the light losses on the slit. The extra-atmosphere flux for the star is about 970 photons cm^{-2} s^{-1} Å^{-1}.

The atmospheric extinction at 7000 Å is 0.033 per airmass, hence the expected SNR of the star at zenith is 1220 which gives the efficiency for the medium camera of about 6%.

1.4.2 The expected efficiency

The efficiency can also be estimated by calculating the transmissions of all optical surfaces of the spectrograph. The results of these detailed calculations are given in Tab. 1.1. The telescope reflectance is given by direct measurements after the cleaning of the mirrors. The reflectance on a surface at normal incidence is calculated according to the Fresnel formula:

$$r = \left(\frac{n-1}{n+1}\right)^2, \tag{1.2}$$

where the refractive index n is 1.51 at 7000Å for BK7 glass. The internal transmittance of BK7 is 0.99988 per mm (Optics Guide, Melles Griot Co. 1988). The échelle reflectance was provided by its specification. The reflectance of all SOFIN mirrored surfaces aluminized in 1990 is estimated to be 0.8.

The overall efficiency of the spectrograph and CCD is 6.8%. By including the telescope, the efficiency is reduced to 4%, which is in good agreement with the direct measurements.

For comparison, the coudé échelle spectrometer at the 2.7 m telescope of the McDonald Observatory has an estimated efficiency of the spectrograph of 16%, mainly because of the silver coated surfaces (97.5% reflectance), and the higher CCD efficiency (77%).

A similar design échelle spectrograph at the 4 m telescope of CTIO has an efficiency ranging from 4–8% depending on the optical system setup.

1.5 Model of the spectrograph

Present day CCDs which are used in the spectrograph are too small to cover the whole spectral range of the échelle image. Hence, the observations are carried out in selected settings of the échelle and prism angles with limited spectral coverage. It is a matter of importance to have an appropriate means to select the configuration of spectral lines (Fig. 1.10) and the pointing model of the spectrograph which transforms the coordinates of the spectral setting into the instrumental units of échelle and prism.

Table 1.1: The transmission table of the optical elements of the SOFIN spectrograph. The total transmission coefficients for each subsection are given in the rightmost column.

Telescope main mirror	reflection	0.786	
secondary mirror	reflection	0.782	0.60
Filter	surface	0.96	
	single pass, 3 mm	0.99963	
	surface	0.96	0.92
Compensating glass	surface	0.96	
	single pass, 3 mm	0.99963	
	surface	0.96	0.92
Diagonal mirror	reflection	0.8	
Collimator	reflection	0.8	
Echelle	reflection	0.67	
	vignetting	0.87	0.37
Cross-dispersion prism	surface	0.96	
	first pass, 39 mm	0.9953	
	reflection	0.8	
	second pass, 39 mm	0.9953	
	surface	0.96	0.73
Camera main mirror	reflection	0.8	
secondary mirror	reflection	0.8	0.64
CCD window	surface	0.96	
	single pass, 3 mm	0.99963	
	surface	0.96	0.92
UV-coated EEV CCD	QE at 7000 Å		0.50

1.5.1 Spectral mosaic

The échelle grating equation is

$$\sin\alpha + \sin\beta = N\,k\,\lambda \tag{1.3}$$

with

$$\alpha = \theta + \gamma + \epsilon \quad \text{and} \quad \beta = \theta - \gamma + \epsilon + \delta, \tag{1.4}$$

where α and β are the angles of incidence and diffraction, γ is the fixed angle of 4° (2γ is the angular separation of collimator and prism), θ is the blaze angle, ϵ is the échelle deflection angle with respect to the blaze, δ is the field angle varying around

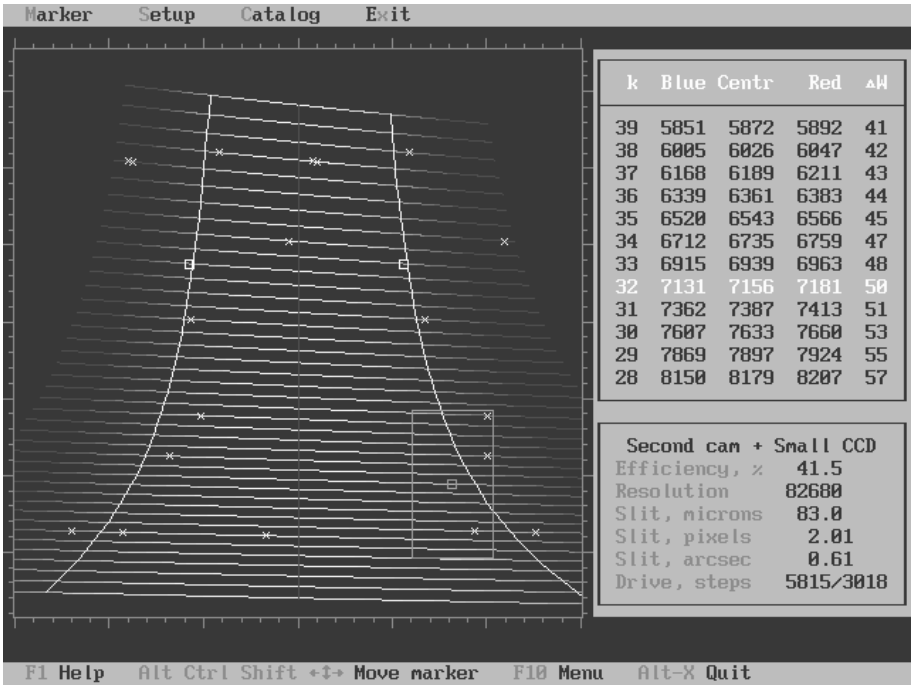

Figure 1.10: The model of the focal plane of the spectrograph as seen on the computer screen: the red orders are at the bottom and the blue orders are at the top. The blaze axis is at the centre, the two white curves at 41% of the échelle efficiency indicate the interval of the full wavelength overlap. The CCD box and the wavelength coverage correspond to the medium optical camera in 6173 & 6563 Å spectral region. The positions of some hydrogen and Ca lines are marked with crosses and boxes.

the image centre in dispersion direction, N is the number of grooves per mm, k is the spectral order number, and λ is the wavelength. The incidence and diffraction angles are in the same plane for this spectrograph (various configurations of échelle spectrographs were extensively discussed in Schroeder & Hilliard 1980).

The cross-dispersion prism equation describes the fact that the monochromatic ray crosses the surface two times at different angles and becomes internally reflected on the rear mirrored surface:

$$\arcsin\left(\frac{\sin\alpha_p}{n}\right) + \arcsin\left(\frac{\sin\beta_p}{n}\right) = 2\,\theta_p, \tag{1.5}$$

where α_p and β_p are the angles of incidence and refraction, θ_p is the prism apex angle. The refraction angle is given by the following sum:

$$\beta_p = \alpha_p + \gamma_p + \delta_p, \tag{1.6}$$

where $\gamma_p = 30^\circ$ is the fixed angular separation between the échelle and the optical camera, and δ_p is the field angle varying around the image centre in cross-dispersion direction.

The refractive index n of BK7 is approximated by

$$n^2 = A_1 + A_2\lambda^2 + A_3\lambda^{-2} + A_4\lambda^{-4} + A_5\lambda^{-6} + A_6\lambda^{-8} \tag{1.7}$$

with the wavelength λ given in μm, and the polynomial coefficients (Pronik 1995)

$$\begin{array}{ll} A_1 = 2.2699804 & A_2 = -9.8250605 \times 10^{-3} \\ A_3 = 1.10172030 \times 10^{-2} & A_4 = 7.6606834 \times 10^{-5} \\ A_5 = 1.16169520 \times 10^{-5} & A_6 = 5.81309000 \times 10^{-7}. \end{array}$$

The image formed in the focal plane is calculated in the coordinate system (ϵ,β_p) of the échelle deflection and the prism refraction angles as a function of ϵ and order number k:

$$\alpha_p(\lambda) = \alpha_p(\lambda(\epsilon, k)) \tag{1.8}$$

in the image centre with the field angles $\delta = \delta_p = 0$. A box in the focal plane which reflects the CCD format is calculated in the angular units according to the scaling factor of the selected optical camera. The CCD box can be positioned to the different angles of échelle ϵ and prism β_p. The corresponding table of the wavelength coverage is calculated with the two angles fixed at the selected position and the field angles δ and δ_p are varying within the CCD image:

$$\delta_p(\lambda) = \delta_p(\lambda(\delta, k)). \tag{1.9}$$

1.5.2 The échelle efficiency

The échelle grating has its maximum reflectance at the blaze angle which decreases as the angle changes. Also, as the incidence angle increases, the projected area of the grating is reduced which results in a beam area reduction. The total effect is calculated allowing to estimate the light collection efficiency at the given spectral setting.

The light reflectance with respect to the blaze intensity ($\epsilon = 0$) is

$$I_\lambda = \left(\frac{\sin u}{u}\right)^2, \quad \text{where} \quad u = \pi\left(k - \frac{\lambda_1}{\lambda}\right). \tag{1.10}$$

The quantity $\lambda_1 = 225\,885.77\,\text{Å}$ is the wavelength in order $k = 1$ at the blaze angle ($N\,\lambda_1 = 2\sin\theta\,\cos\gamma$).

The transmittance of the light due to the change of the illumination area of the échelle by the collimated beam as a function of the grating angle is given by the ratio of the two areas $S_{\rm ech}/S_{\rm col}$:

$$\frac{1}{4}S_{\rm ech} = (\sin 2\rho + 2\rho)\,D_{\rm col}^2 - \pi\,D_{\rm obs}^2, \qquad \frac{1}{4}S_{\rm col} = \pi D_{\rm col}^2 - \pi D_{\rm obs}^2 \tag{1.11}$$

with

$$\rho = \frac{L_y}{D_{\rm col}}\cos\alpha,$$

where L_y is the length of the longest échelle side (across the grooves), $D_{\rm col}$ is the diameter of collimator, and $D_{\rm obs}$ is the diameter of the diagonal flat mirror, which obscures the central part of the collimated beam. It is assumed that the collimated beam size equals the width of the échelle $D_{\rm col} = L_x$. The transmittance decreases from 94% to 77% from the blue to the red side of the order; additionally, the resolution increases from blue to red.

The overall efficiency is shown in Fig. 1.11 as obtained by the multiplication of the blaze function with the transmittance. The maximal efficiency at the blaze angle is about 86%.

1.5.3 The resolving power

The resolving power $R = \lambda/d\lambda$ is one of the basic parameters of the spectrograph and describes its ability to resolve narrow spectral lines. For the given focal length of the optical camera, the resolution is a function of the échelle angles and it changes along spectral orders. Qualitatively, it is obvious that with the increase of the angle of incidence, the projected density of the grooves becomes higher, which results in a larger dispersion.

The wavelength size $d\lambda$ of the resolution element formed by the slit projection onto the CCD is

$$N\,k\,d\lambda = \cos\beta\,d\beta, \quad \text{where} \quad d\beta = \frac{p}{f_{\rm cam}} \tag{1.12}$$

is the angular size of the resolution element given by the projected slit width p on the CCD and the focal length of the camera $f_{\rm cam}$. Then the resolving power is

$$R = \frac{\lambda}{d\lambda} = \frac{\sin\alpha + \sin\beta}{\cos\beta}\cdot\frac{f_{\rm cam}}{p} \tag{1.13}$$

which is a function of the échelle deflection angle ϵ, field angle δ, and the projected slit width p (the entrance slit width also depends on the above two angles). For the CCD centre at $\delta = 0$ it becomes

$$R = \frac{2\,\tan(\theta+\epsilon)}{1+\tan(\theta+\epsilon)\,\tan\gamma}\cdot\frac{f_{\rm cam}}{p}. \qquad (1.14)$$

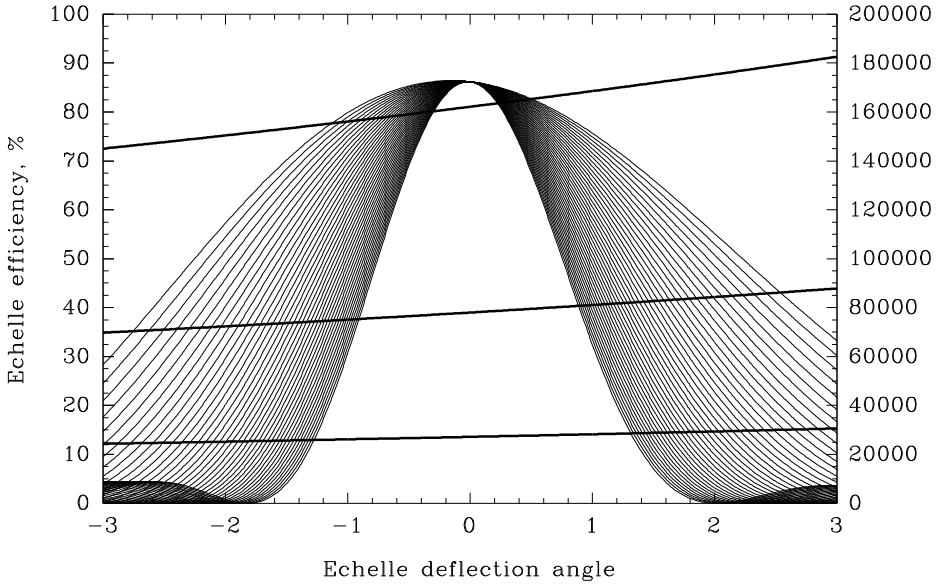

Figure 1.11: The échelle plus collimator efficiency is plotted with respect to the deflection angle in degrees. The uppermost curve corresponds to the red 20th order, and the innermost curve is for the blue 60th order. The resolving power is calculated for the three optical cameras for a resolution element of two pixels of the CCD.

1.5.4 The optimal slit width

The slit is called optimal when its image in the focal plane is optimally sampled by the CCD pixels. For the ordinary observing mode, the sampling interval is equal to one CCD pixel, which implies that the spatial cutoff (or Nyquist) frequency corresponds to two pixels on the CCD. The slit width which corresponds to an instrumental profile of two pixels FWHM is used for observations to provide the maximal resolving power for the given settings of the spectrograph.

The projected slit image is a convolution of three main profiles: the geometrical projection of the rectangular entrance slit, the aberration profile of the camera,

and the diffractional profile of the monochromatic beam on the collimated pupil. To calculate the resulting width, it is assumed that the profiles are Gaussians, hence, their widths can be added in squares:

$$p^2 = \left(\frac{f_{\rm cam}}{f_{\rm col}} \cdot \frac{\cos\alpha}{\cos\beta} \cdot w\right)^2 + A^2(\lambda) + \left(\frac{\lambda}{D_{\rm col}} f_{\rm cam}\right)^2 . \qquad (1.15)$$

The last term describes the diffraction broadening of the slit image. The middle term is the camera aberration as a function of image position; for simplicity, the aberration spot size is set constant and equal to $8\,\mu$m for all three optical cameras. The first term consists of the three factors: the magnification factor of the spectrograph, the angular magnification on the échelle, and the entrance slit width w. The magnification by the échelle follows from Eq. (1.3): $\cos\alpha\, d\alpha + \cos\beta\, d\beta = 0$.

The essential setup parameters for the three optical cameras are given in the following table for the central 40th order at 5647 Å at the blaze. The slit width w, given in μm, corresponds to two pixels on the CCD. The slit relative throughput T in percent is calculated for $1''$ seeing. $\delta\lambda$ and δv are the pixel width in wavelength (mÅ) and radial velocities ($\mathrm{m\,s^{-1}}$). $\Delta\lambda$ and Δk are the length in Å and the number of spectral orders in the CCD image.

No.	Camera	R	w	$w_{\rm sky}$	T	$\delta\lambda$	δv	$\Delta\lambda$	Δk
1	long	161 000	38	$0\farcs28$	25	17	930	20	16
2	medium	76 000	82	$0\farcs60$	50	37	1970	42	14
3	short	27 000	236	$1\farcs73$	100	104	5550	120	40

1.5.5 The pointing model of the spectrograph

The échelle and the cross-dispersion prism position angles are controlled by stepping motors. The pointing model establishes the relation between the step numbers and the position in wavelengths and order numbers for the centre of the CCD image and is used for the selection of spectral regions (Fig. 1.10).

To obtain the reference points, a series of comparison spectrum images were made in a grid of 5×7 different positions in dispersion direction and across the orders for the three optical cameras. The images were processed to obtain the central order number and its wavelength. Bivariate polynomial linear least-squares fits were used to approximate the échelle deflection angle ϵ in Eq. (1.3) and the central order number k as functions of the step motor numbers x and y as follows

$$\epsilon(x,y) = \mathbf{q}'(y)\mathbf{E}\,\mathbf{p}(x) \quad \text{and} \quad k(x,y) = \mathbf{q}'(y)\mathbf{C}\,\mathbf{p}(x), \qquad (1.16)$$

where $\mathbf{E}_{1\times2}$ and $\mathbf{C}_{4\times1}$ are the matrices of polynomial coefficients associated with the vectors of the Chebyshev polynomials $\mathbf{q}(y)$ and $\mathbf{p}(x)$ of the corresponding

degrees. The polynomial coefficients were found sufficient for the SOFIN spectrograph to describe the surface with an appropriate accuracy, although, a more dense grid in the cross-dispersion direction would provide an accuracy similar to that achieved in the dispersion direction.

1.6 Stability of the spectrograph

As the alt-azimuth mounted telescope tracks the position of a star, the spectrograph mounted on the rotating adapter is changing its orientation which is described by the parallactic angle. The parallactic angle between the hour circle and the vertical circle (Woolard & Clemence 1966, p. 55) is calculated from

$$\begin{aligned} \sin z \sin q &= \cos\phi \ \sin h \\ \sin z \cos q &= \sin\phi \ \cos\delta - \cos\phi \ \sin\delta \cos h, \end{aligned} \tag{1.17}$$

where q is the parallactic angle, z is the zenith distance, ϕ is the latitude of the telescope in the northern hemisphere, δ is the declination of the object, and h is its hour angle. Fig. 1.12 shows how the rotator parallactic angle and the zenith distance of an object are changing in time. For a star with $\delta \approx \phi$ the rotator angle is changing very fast but the zenith distance is not. Apart from this declination, the slower change of the rotator angle is compensated by the near constancy of the zenith distance at the meridian. The most critical parts are on the east and west where both angles are changing very rapidly.

A change of the spectrograph orientation unavoidably results in a drift of spectral line positions, an effect known as the flexure of Cassegrain mounted spectrographs. Different optical components may change their positions in a different way as the spectrograph changes its orientation which makes the overall effect very complicated.

To evaluate the amplitude and the behaviour of the line drifts, an experiment was made in December 1997 for the long 1st and medium 2nd optical cameras as follows. To ensure that the ambient temperature changes are minimal, the experiment was carried out during a cloudy night with the telescope dome closed and the air conditioning system switched on. The altitude of the telescope was gradually decreased from 90° to 20°; at each altitude the rotator was turned from $-90°$ to $+90°$, and at each rotator angle an exposure of the comparison spectrum was made. Then the whole sequence was repeated for the other camera. The line displacements were measured with respect to a group of lines at the image centre of the very first exposure with the cross-correlation technique. The results of the measurements are shown in Fig. 1.14, and the corresponding surfaces are shown in Fig. 1.15 and Fig. 1.16 which were approximated by a bivariate smoothing spline.

As was expected, the 1st camera traces show a twice larger amplitude due to

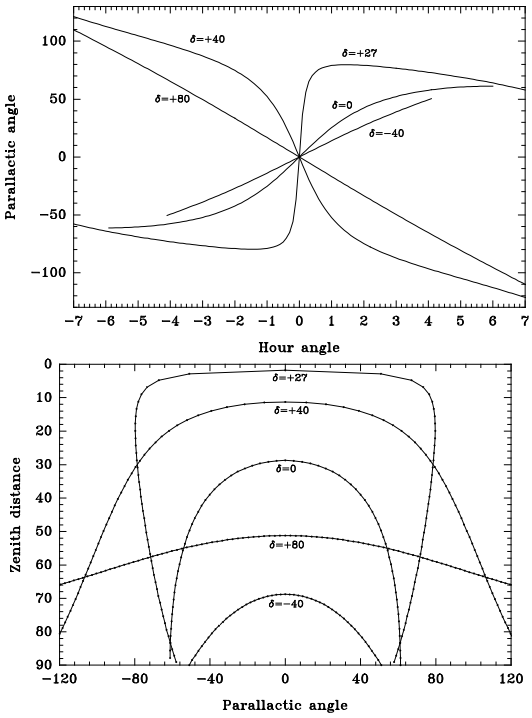

Figure 1.12: Change of the parallactic angle of the telescope rotator as function of hour angle (left) and zenith distance (right) at the latitude $\phi = 28.76°$ of the NOT for stars with different declinations. The length of the curves is defined by the visibility of a star above the horizon. The time interval between two dots in the right panel is 10 min of hour angle.

the doubled focal length as compared to the other camera. At each trace when the altitude is fixed there is a turning point at which the drift in the direction of rows (the dispersion direction) is minimal and is at $+30°$ of the rotator angle for the 1st camera and $-30°$ for the 2nd. This is simply explained by the fact that the angle between the échelle-prism axis and the optical camera is 30°: at the corresponding rotator angle the camera is exactly in the plane of the vertical circle, therefore its bending is minimal (Fig. 1.13). As the zenith distance is changing, the lines are moving back and forth in the dispersion direction. The minimal change of the drift occurs at 30° zenith distance. There is no feasible explanation why it happens at this angle: probably there are some changes in the resulting vector of forces in the échelle turnable frame drawn out by the braced springs, but at 30° of zenith distance the angle between the échelle plane and the vertical is only 30°. The échelle stands vertical at a zenith distance of 60°, hence, the échelle unit counteracts the springs.

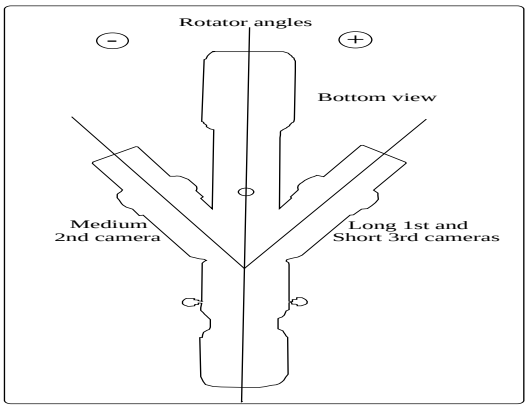

Figure 1.13: The bottom view of the spectrograph mounted on the telescope rotator adapter. Clockwise rotation corresponds to negative angles, and anticlockwise rotation corresponds to positive angles of the rotator. The angle between the optical cameras is 60°. When the rotator angle is $-30°$ the medium 2nd camera is oriented in the plane of the vertical circle of the telescope.

The change of the spectral line width from one exposure to the other is shown in the surface fits. These surfaces are less conclusive but show that the focussing of the optical camera is degrading at certain orientations of the spectrograph and it is definitely degrading with increase of the zenith distance. One conclusion that can be made is that at the rotator angles ($\pm 30°$), where the drift in the dispersion direction is minimal, the change of the focus is maximal.

The results of this experiment have merely practical consequences: to minimize the drift in the dispersion direction during observations the rotator angle for the long 1st camera should be around $+30°$ (the same is true for the short 3rd camera where the measurements were not made but the mechanical configuration is the same), and $-30°$ for the medium 2nd camera.

In order to obtain the optimal quality (stable lines and maximal resolution) long exposures should be subdivided into a series of short ones depending on the object position, with subsequent correction of the shifts.

1.6.1 Line broadening due to flexure

The drift of a spectral line across the CCD pixels during the integration results in an apparent shift of the line centre from where it is expected and leads to the increase of the line width. If the line shape can be described by a rectangular profile, then apparently, a shift of such a line by the amount Δ increases the line width by the same amount. Most of the real spectral lines can be described as

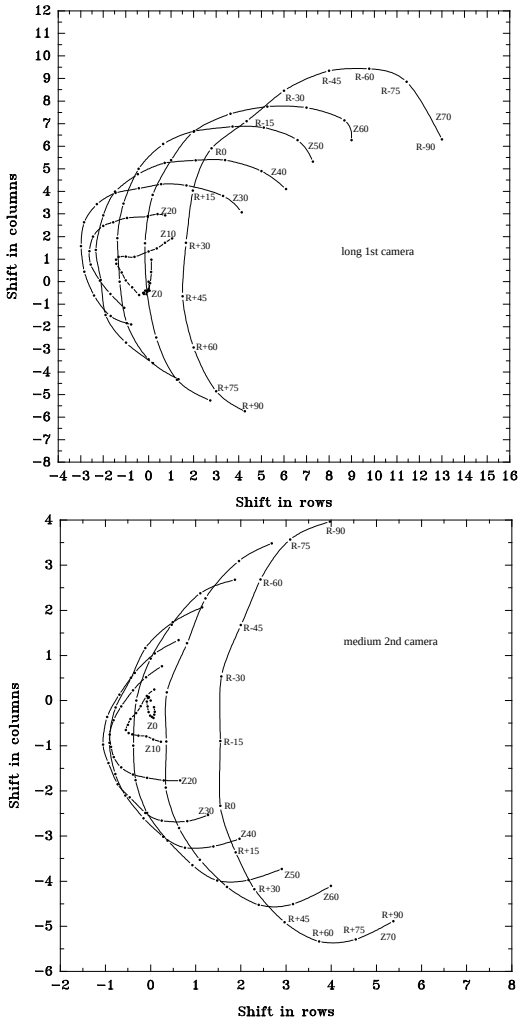

Figure 1.14: The line drift in two optical cameras as a function of the spectrograph spatial orientation. The shift in rows is along the dispersion direction and the shift in columns is in the cross-dispersion direction. The telescope rotator angle (R) is changing from $-90°$ to $+90°$ and the zenith distance (Z) is changing from $0°$ to $70°$. The scale size for the medium camera plot is half that for the long camera plot.

Gaussian profiles; in the latter case the increase of the width due to the shift is less significant.

The whole process can be described as a convolution of the true line profile $p(x)$

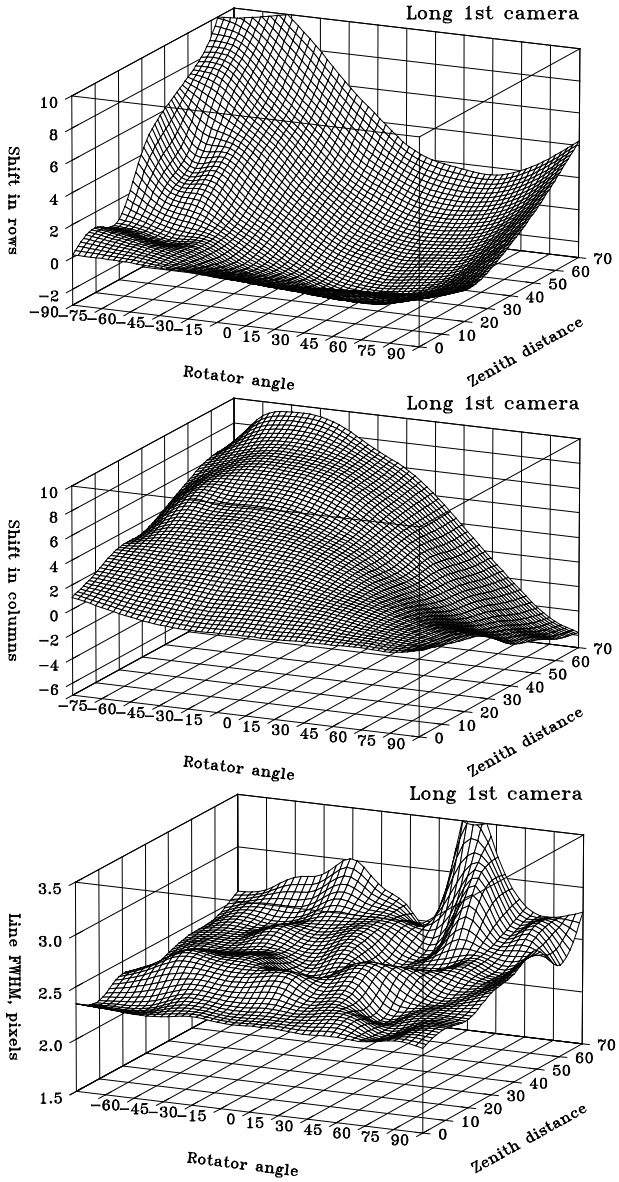

Figure 1.15: The surface fit shows the drift of a spectral line in the dispersion direction (upper panel), in the cross-dispersion direction (middle panel), and the change of the line FWHM as a function of zenith distance and rotator angle for the long 1st optical camera.

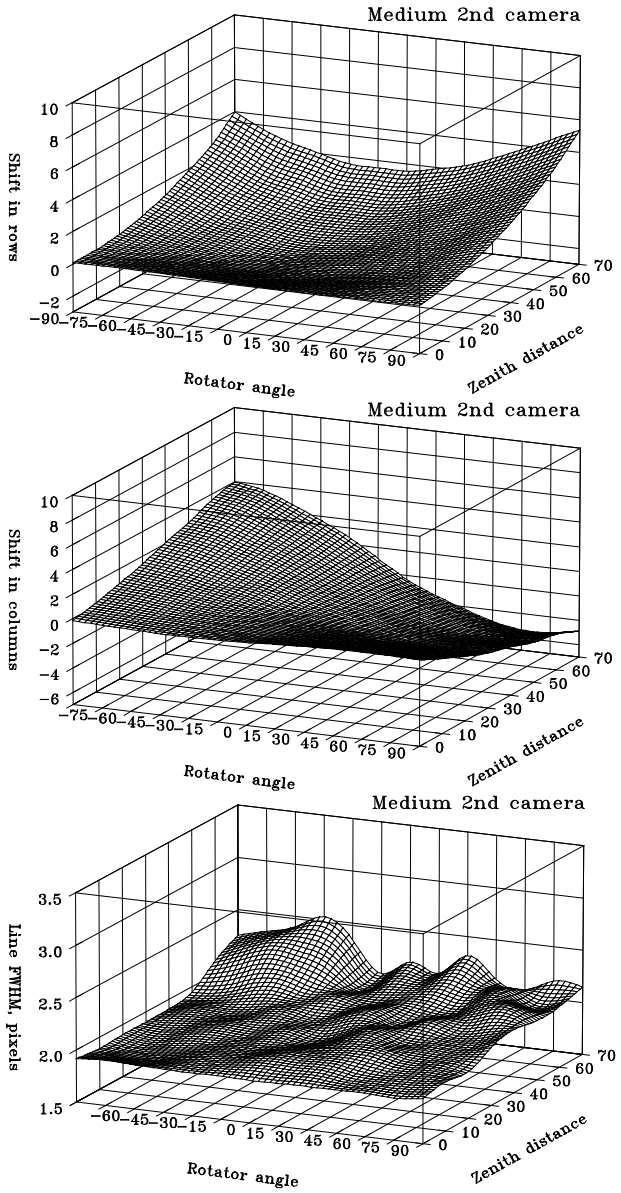

Figure 1.16: The surface fit shows the drift of a spectral line in the dispersion direction (upper panel), in the cross-dispersion direction (middle panel), and the change of the line FWHM as a function of zenith distance and rotator angle for the medium 2nd optical camera.

with the shift function $s(x)$ which results in the smeared profile $f(x)$. Assume that the shift function is a rectangular profile of the width Δ, i.e. the shift of the line is constant in time:

$$s(u) = \begin{cases} 1, & -\Delta/2 < u < +\Delta/2 \\ 0, & \text{otherwise.} \end{cases} \tag{1.18}$$

Let the line $p(u)$ be a Gaussian profile of the width σ, then the resulting profile is

$$f(x) = \int_{-\infty}^{+\infty} p(u)\, s(x-u)du = \int_{x-\Delta/2}^{x+\Delta/2} p(u)du = \int_{x-\Delta/2}^{x+\Delta/2} e^{-u^2/\sigma^2}du = \frac{\sqrt{\pi}}{2}\sigma\ (y_2 - y_1) \tag{1.19}$$

where

$$y_1 = \mathrm{erf}\left(\frac{x-\Delta/2}{\sigma}\right) \quad \text{and} \quad y_2 = \mathrm{erf}\left(\frac{x+\Delta/2}{\sigma}\right). \tag{1.20}$$

The resulting profile is not a Gaussian anymore but the difference of two error function profiles. The resulting full width w_f is calculated at half amplitude of the profile and plotted with respect to the width w_p and the shift Δ in the following form:

$$\frac{w_f}{w_p} = F\left(\frac{\Delta}{w_p}\right). \tag{1.21}$$

A more simple but less realistic case is when the shift function can be described by a Gaussian profile, i.e. the line position is a normally distributed random number with a mean equal to the expected line position and the width σ_2 (similar to the width Δ of the rectangular shift function). Then, the resulting profile is a convolution of the two Gaussians:

$$f(x) = \int_{-\infty}^{+\infty} p(u)\, s(x-u)du = \int_{-\infty}^{+\infty} e^{-u^2/\sigma_1^2} e^{-(x-u)^2/\sigma_2^2}du = \sqrt{\frac{\pi}{\sigma_1^2+\sigma_2^2}} \cdot \sigma_1\sigma_2 \cdot e^{-x^2/(\sigma_1^2+\sigma_2^2)}. \tag{1.22}$$

The resulting curves for the two shift functions are shown in Fig. 1.17. A rectangular shift of a Gaussian profile of 2 pixels FWHM by two pixels would increase its width by 25%; a shift by four pixels doubles the line width.

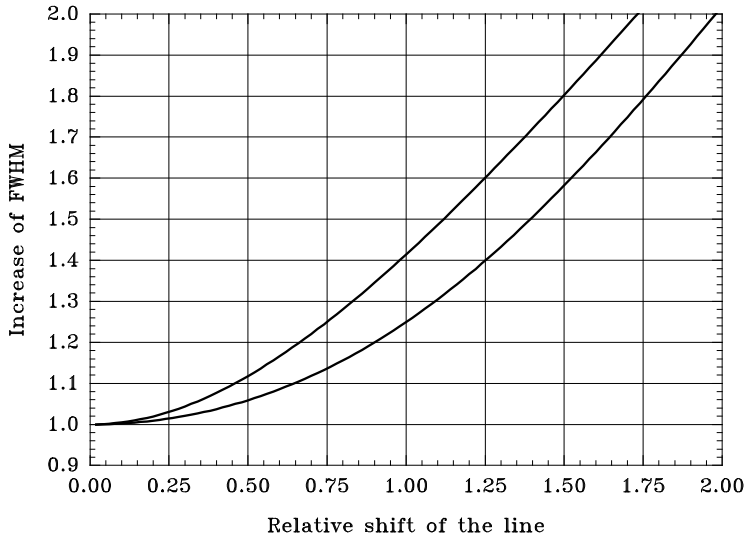

Figure 1.17: Relative increase of a Gaussian profiles FWHM as a function of the line shift with respect to its width. The bottom curve corresponds to a rectangular shift function, and the upper curve is for a Gaussian shift function.

To verify this in practice, we made an observation of α Cyg (A2 I) whose spectrum has very narrow interstellar absorption features in the Na I doublet. The observation was made with the 1st camera when the telescope was normally tracking the star and then when the telescope rotator was turned by 50° during the exposure. The comparison lines shifted by 0.5 pixels ($425\,\mathrm{m\,s^{-1}}$) during the exposure. The width of narrow absorption lines is about 4–5 pixels. The two spectra are shown in Fig. 1.18. No increase of the line width due to the shift was found in this experiment, because the expected increase of the line width is less than 1%.

1.6.2 Statical stability of the spectrograph

In this section we give an investigation of the statical stability of the spectrograph when the external long-term factors of the flexure due to telescope tracking are excluded. The importance of such a test is dictated by the need of understanding the nature of the positional instability of spectral lines due to instrumental effects. This is especially important when we study short term variations of spectral line profiles (e.g. non-radial pulsations or other monitoring programmes) where the physical effect could be compatible in amplitude with the effects of instrumental nature. On the other hand, slow variations (tens of minutes) of the line positions due to environmental effects give us additional suggestions of the proper operational modes of the SOFIN spectrograph which can be used to minimize the

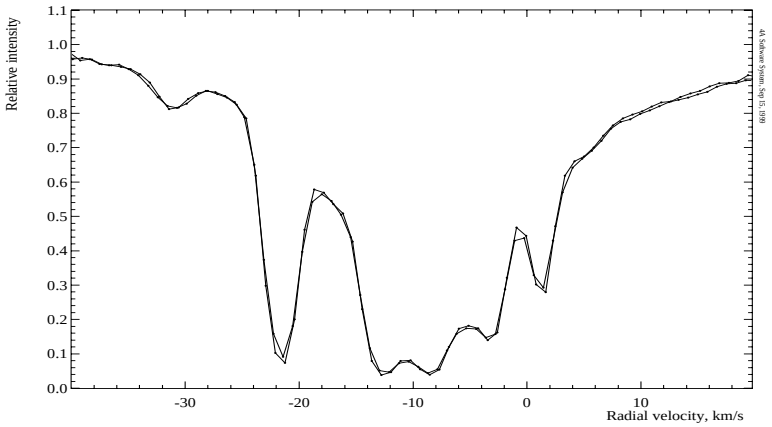

Figure 1.18: The reduced spectrum of α Cyg (V=1.25 A2 Iae) taken with the long 1st camera (R=176 000 at this spectral region) showing the profile of the interstellar Na I D_2 at 5889.9512 Å. The two spectra were taken under different conditions: when the telescope was only tracking, and when the rotator was turned from 0° to +50° step by step during its 5 min exposure at the zenith distance of 20°. The rotation caused a shift of the comparison spectrum lines by 0.5 pixels (one pixel is 850 m s^{-1}). No apparent change of the width in the profile components is seen. The decomposition of the line profile onto a number of Gaussians also gives the same widths for the two spectra.

instrumental instability during observations and taken into account during data reduction.

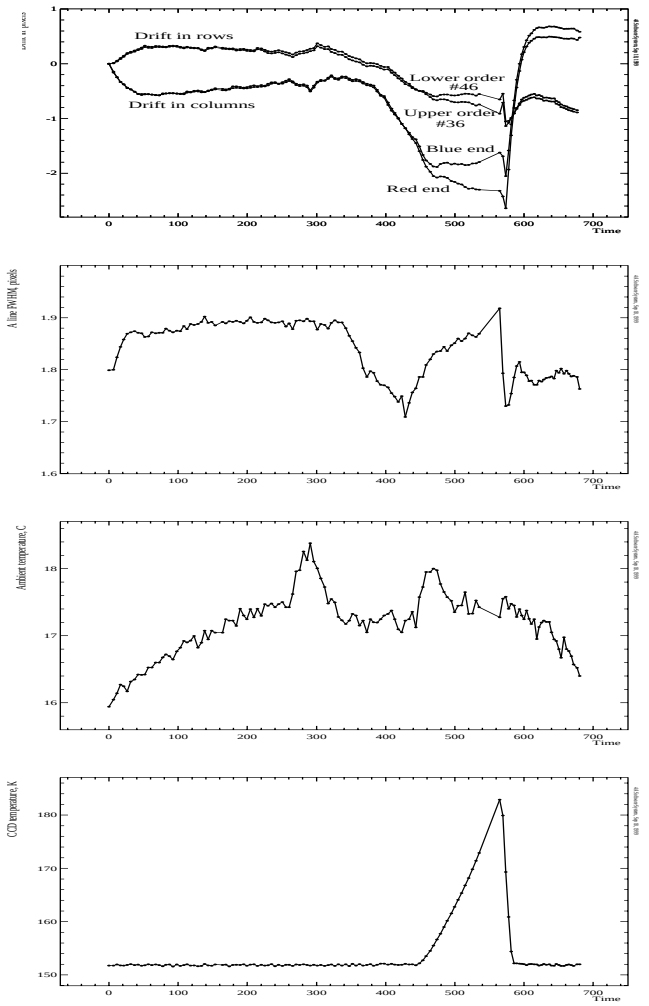

Figure 1.19: The stability test of the spectrograph in stand-by position. The horizontal axis is time in minutes. The panels from top to bottom are the image drift in CCD rows and columns, line FWHM, the ambient temperature in C, and the CCD temperature in K.

Chapter 2

The instrumental profile

2.1 The instrumental profile

The instrumental profile of a spectrograph defines its resolving power, a key parameter which determines the ability of the spectrograph to resolve narrow spectral lines. The resolving power is measured from the core of the profile, and its extended wings define the amount of scattered light of the spectrograph. This is another important parameter which can tell us how much the apparent line intensities differ from the true values and, therefore, defines the precision with which e.g. the equivalent widths of the lines can be measured.

2.1.1 Obtaining the instrumental profile

Following the prescriptions of Tull et al. (1995), Diego et al. (1995) and Barlow et al. (1995), the instrumental profile of SOFIN was measured in November 1998 for the 1st and the 2nd optical cameras. A HeNe laser was used as a source installed in front of the entrance slit. A small milk glass diffuser of the appropriate size was installed between the slit and the laser to ensure that the convergence of the entrance beam is $f/11$ and, therefore, the camera is uniformly illuminated. The spectral settings of the two cameras were adjusted so that the 6328 Å laser line appears close to the centre of the CCD image. The best focus was found prior to the series of exposures. The exposure times for the two cameras were set differently (10 s and 1 s, respectively) to achieve 25 000–30 000 ADUs per pixel at the maximum of the HeNe line profile (the dynamical range of the CCD is 65535 ADUs). A series of 200 exposures was carried out for the 1st and 2nd cameras giving a total signal-to-noise ratio at the line maximum of 10 000 and 5 500, respectively.

A similar measurement of the instrumental profile was carried out in April 2000 for the low resolution 3rd camera. A series of 150 exposures was obtained which yields a total signal-to-noise ratio of 3500.

A CCD bias column, averaged from the overscan in columns, was obtained and subtracted from every image separately to ensure that bias variations would not introduce any systematics. The photon noise is estimated from the Poisson statistics for the known CCD gain factor. A standard unweighted integration across the order was done to obtain the spectra of the line. The series of exposures took from 1 to 2 hours, therefore, a change of the ambient temperature and the CCD dewar weight due to liquid nitrogen evaporation could shift the line position. To eliminate the effect, the spectra were cross-correlated with respect to the first profile and the apparent shift in pixels was removed from each spectrum. The image in Fig. 2.1 shows a sum of all debiased individual images of the 1st camera, co-aligned in the dispersion direction.

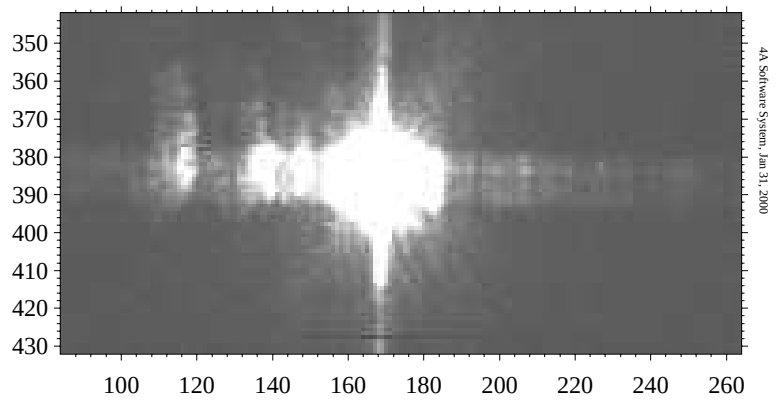

Figure 2.1: An image of the HeNe 6328 Å line obtained with the 1st camera. The image is a sum of 200 individual exposures co-aligned with each other.

We found that the immediate summation of all spectra results in an apparent increase of the core width of the resulting profile. The effect is well understood taking into account that due to the line drift and only a few pixels present in the line core, the undersampling of the core is severe, i.e. cannot be well described with the large pixel size. The increase of the line width will otherwise lead to the underestimation of the resolving power of the spectrograph. Therefore, we used the change of the line position in order to improve the sampling of the profile as follows.

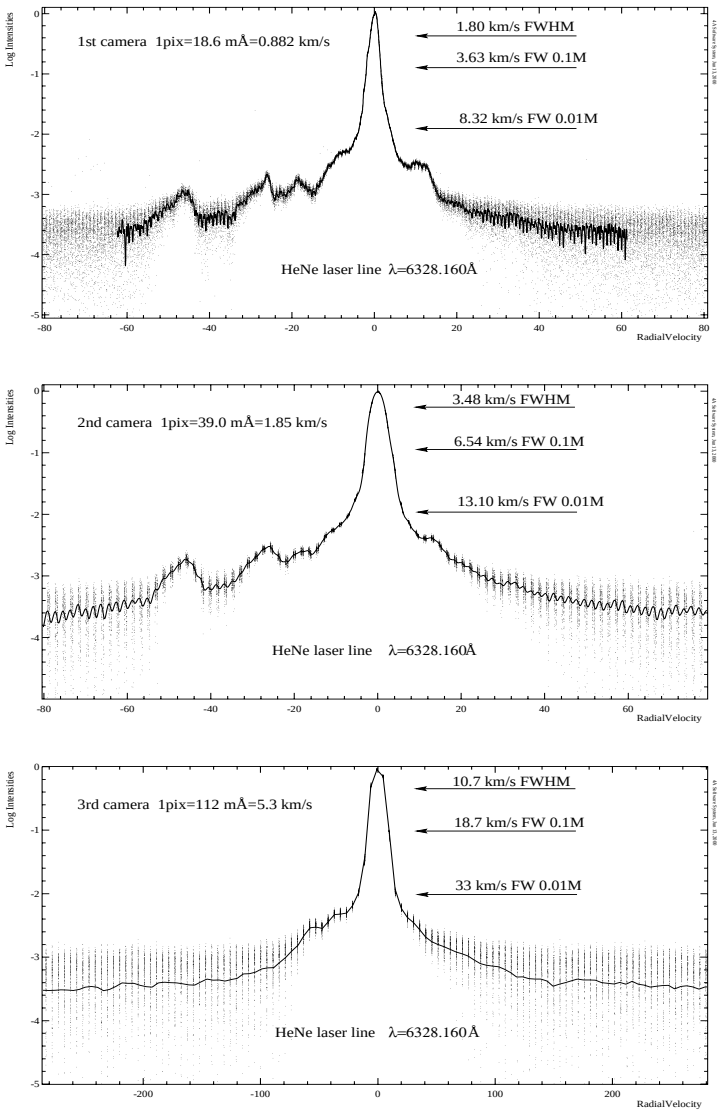

Figure 2.2: The instrumental profiles for the three optical cameras. The dots show the overlaid pixels of individual spectra coaligned to each other due to the line drift during the run of exposures. A spline fit is shown as a thin line for the camera 1 and 2. A jagged thin line in the camera 3 plot is the sum of individual spectra. The widths at the three intensity levels are indicated with arrows.

In order to exclude the effect of changes of the line intensity during the run due to variations of the exposure time and laser instability, the spectra were rescaled to the first spectrum. The linear scaling coefficients are determined by the cross-correlation method at the maximum of the cross-correlation function. The wavelength calibration was established from a ThAr comparison spectrum, the image of which was obtained before the series. The wavelengths of the spectra were transformed into radial velocities with respect to the line centre at 6328.160Å. The spectra overlaid (interleaved) with each other in radial velocities show the structure of the profile at a number of pixels which were drifted over the time span of the run. The resulting profile was obtained by fitting a smoothing spline to the pixels obtained as a weighted average over a small interval in velocity scale (about $25\,\mathrm{m\,s^{-1}}$).

The result of such a procedure is shown in Fig. 2.2 for the 1st and the 2nd cameras. In the case of camera 1, the overall line drift during the run is almost one pixel which resulted in the complete overlapping of the pixels. In the case of camera 2, the overall line drift was essentially smaller but well enough for the spline approximation. Unfortunately (for this application), the relative stability of the short camera is a few times higher than that of the other two. The corresponding pixels of the line profile were fixed to almost the same position during the run, giving no possibility to improve the sampling interval. Therefore, a sum of the cross-correlated spectra with small drifts corrected was calculated with the subsequent wavelength and radial velocity transformations.

2.1.2 The measurement of the resolving power

The resolving power definition involves the measurement of the line width. The line width for the 1st and 2nd camera was measured directly from the well-sampled profile. For the undersampled 3rd camera spectrum, the FWHM was measured from the weighted fit of a Gaussian to the core of the profile. Since only a few pixels are present in the core, the narrowest Gaussian was selected among all possible combinations of the pixels involved in the fit. The minimal number of pixels used for the fit is 4. This procedure is justified, because the very central part of the profile can be described by a Gaussian shape, as discussed later. In this section we assume, in the first approximation, that the internal line width of the HeNe laser line is negligible.

For the high resolution 1st camera, according to the model, the expected resolving power at this wavelength is $R = 168\,000$ ($R = \lambda/\Delta\lambda = c/v$) per resolution element of 2 pixels FWHM on the CCD. The measured width of the HeNe line is $1.80\,\mathrm{km\,s^{-1}}$ FWHM (2.04 pixels), which gives $R = 167\,000$. The 2nd camera profile yields a line width of $3.48\,\mathrm{km\,s^{-1}}$ FWHM (1.88 pixels) which results in $R = 86\,200$. The resolving power according to the model is $R = 81\,000$ for the 2 pixels FWHM resolution element. The width obtained with the low resolution 3rd camera is

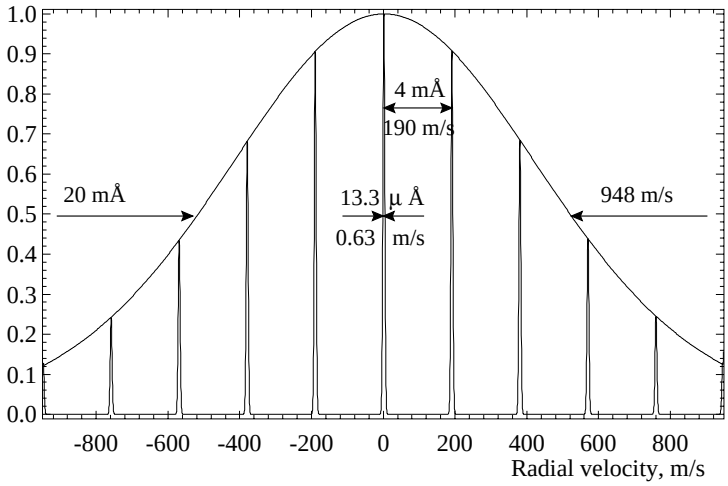

Figure 2.3: A schematic diagram of the fine structure of the HeNe laser 6328.16 Å line which was used for the instrumental profile calibration. The Doppler profile width is 1500 MHz ($T = 400$ K), the resonance mode spacing is 300 MHz (50 cm cavity length), and the single mode width is 1 MHz (this width is exaggerated 10 times for clarity). The width of the picture corresponds to two pixels ($2 \times 882\,\mathrm{m\,s^{-1}}$) of the high resolution 1st camera.

$10.7\,\mathrm{km\,s^{-1}}$ FWHM (2.02 pixels) and corresponds to $R = 28\,000$, which is close to the expected value $R = 28\,000$ for 2 pixels.

2.1.3 The natural width of the HeNe laser 6328 Å line

The natural width of the HeNe 6328 Å is assumed to be negligible for medium resolutions. According to Bloom (1966), the Doppler width of the line is at most 1.7 GHz, Melles Griot (1988) uses a typical value of 1.4 GHz (18.7 mÅ or $886\,\mathrm{m\,s^{-1}}$)[1]. This value agrees with the direct measurements of Tull (1972) obtained with an échelle spectrograph and scanner (they used a $R = 60\,000$ spectrograph). On the other hand, Barlow et al. (1995) refer to a width of 0.03 mÅ or $1.4\,\mathrm{m\,s^{-1}}$. Their measurements of the instrumental profile with the Ultra High Resolution Facility (UHRF) at AAT ($R = 10^6$) yields a core width of $300\,\mathrm{m\,s^{-1}}$ which implies that the natural width of their laser is indeed very small.

[1]For the frequency interval transformation, we use the differential equality $\Delta\lambda = \lambda^2 c^{-1} \Delta\nu$ which follows from $\lambda\nu = c$.

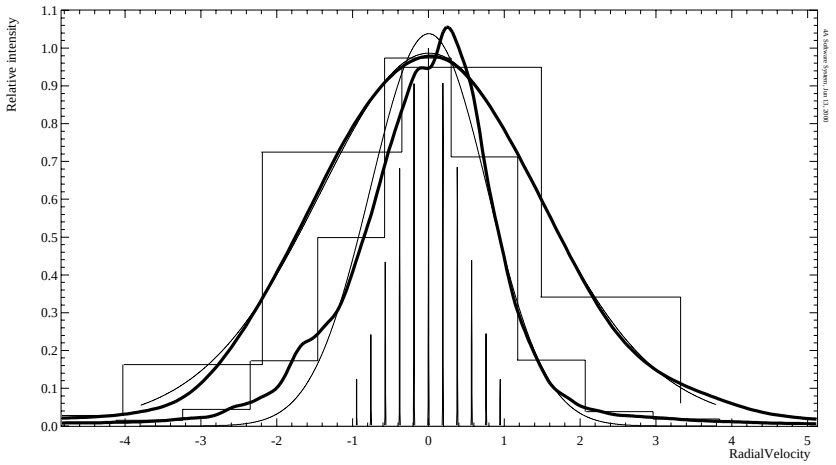

Figure 2.4: Shown in the middle is the comb of the HeNe laser line fine structure, its convolutions with a Gaussian profile (thin curves), where the narrow profile is for camera 1, the wider is for camera 2, the measured profiles approximated by a spline (thick curves), and the step functions which are the undersampled profiles calculated as the sum of the individual spectra (given for comparison).

To clarify the question of the true shape of the HeNe laser line, we refer to excellent introductions by Siegman (1971) and Svelto & Hanna (1989), some details are also given in Gray (1992, Ch.12). Fig. 2.3 shows the fine structure of the HeNe 6328.16 Å line, which consists of a number of single modes superimposed on a Doppler broadened profile. The width of a single mode is defined by the internal width of an atomic transition and is typically 1 MHz FWHM (13.3 μÅ) for a HeNe laser. The mode spacing, or cavity resonance function, is defined by $\Delta\nu = c/2L$ and is caused by the multiple passing of the light packet between the two cavity mirrors of the laser, the distance between them is denoted by L. The shorter the cavity, the less modes are present (a laser with a very short cavity, $L < 15$ cm, operates in a single mode). In our case, $L \approx 50$ cm which implies that the spacing is about 300 MHz or 4 mÅ. The intensities of the resonance modes are distributed with a thermal Doppler broadening function (a Gaussian profile), which depends on the gas temperature and its atomic number. For Ne (m=20) at 6328 Å and for the gas temperature $T = 400$ K, a width of 1500 MHz or 20 mÅ FWHM for the thermal profile is obtained. All unstabilized HeNe lasers are subject to mode sweeping, an effect caused by thermal changes of the cavity length. The most important thing is, that it is a long term effect as the cavity length changes with the ambient temperature which may result in variations of the mode spacing and their frequencies.

The described structure of the HeNe line would now explain the fact that the natural width is laser specific. For such a measurement when the natural width is comparable with the spectrograph resolution, a laser with a short cavity working in a single mode would be required.

Now, when we established the model of the line structure, we obtained the possibility to exclude it from the measurements by deconvolution of the laser comb. Instead, we convolve the laser profile with Gaussians of different widths and compare it with the measurements. Here, we have to assume that the convolution function has a Gaussian shape, resulting from the geometrical slit width, diffraction, and aberrations. The convolutions of the laser comb with Gaussians of 1.7 pixels FWHM for the two cameras are shown in Fig. 2.4. The corresponding widths in velocities are 1.5 and 3.2 $\mathrm{km\,s^{-1}}$ which yield a higher resolving power of $R = 200\,000$ and 93 000 for the pure Gaussian shape assumption for the 1st and 2nd cameras, respectively.

2.1.4 The features

The core of the instrumental profile of SOFIN can be approximated by a Gaussian profile. Fig. 2.5 shows the degree of deviation of the core from a Gaussian. Comparison with the profile of the 2nd and 3rd cameras shows a similar behaviour. Down to the level of 10% of the central intensity the Gaussian is a good approximation to the instrumental profile, but at the level, where the Gaussian reaches 1% of the central intensity, the instrumental profile still has about 3–4% intensity.

The extended wings of the profile constitute the amount of scattered light added to the spectrum in the dispersion direction. For the 2nd camera profile, for instance, the contribution is about 0.1% of the central intensity at $30\,\mathrm{km\,s^{-1}}$ (0.6 Å) from the line centre. Examination of the original image shows that there is no difference in the amount of scattered light along and across the dispersion around the central peak. The scattered light across the spectral orders can be approximated within the interorder gaps and removed from the image. This is not the case for the scattering in the dispersion direction, as was discussed in Gray (1992, Ch.12).

The scattered light intensity differs by a factor of 2 for the two cameras (the ratio of their focal lengths) over the whole range of $\pm 100\,\mathrm{km\,s^{-1}}$ as could be seen from the ratio of the two profiles. Griffin (1969) pointed out by using a log-log plot that the wings exhibit an inverse-square decline. The fit of a Lorentzian profile to the extended wings shows that the shape of the whole profile (except the satellites) can be well approximated by the sum of the two (but not with a Voigt profile which involves the convolution of the two). The FWHM of the Lorentzian profile is two times less than the FWHM of the Gaussian which fits the core. For the accurate convolution or deconvolution of the spectral lines, the instrumental profile should be used with the scattered light (far wings) subtracted from it. In practice, however, it is nearly impossible to distinguish between the scattered light and true

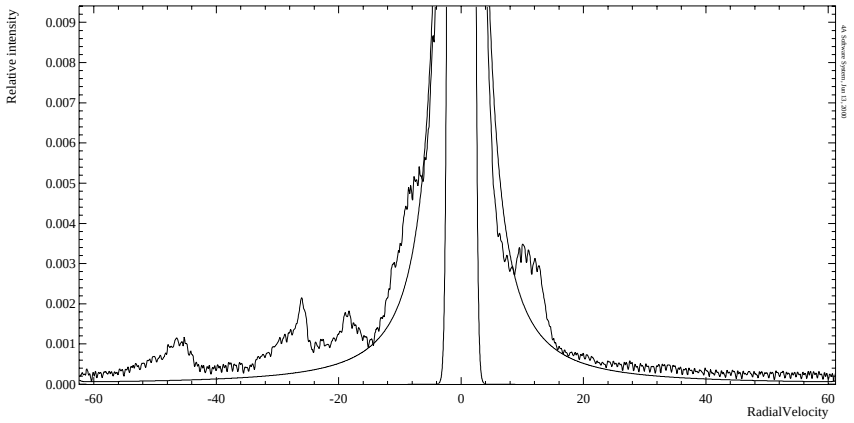

Figure 2.5: Comparison of the instrumental profile for the 1st camera with the best fit of a Gaussian profile (1.90 km s^{-1} FWHM) to the line core and a Lorentzian profile (0.95 km s^{-1} FWHM) to the extended wings.

features of the instrumental profile. Fortunately, for SOFIN, the scattered light contribution is so low, that it can be neglected.

Griffin (1969) distinguishes the following components of the instrumental profile:

1. The main peak (has been discussed above).
2. Rowland ghosts. This feature should be symmetrical with respect to the main peak. Most likely, they are absent in the observed profiles.
3. Diffracted wings. The diffraction maxima are unresolved in our case: the position of the first minimum is at 0.4 km s^{-1}, i.e. within one resolution element. The maximum $N = 30$ at 12 km s^{-1} has only 0.01% of the central intensity.
4. Small-angle scattering in the optical system.
5. Halation and scattering in the photographic emulsion (not present here).
6. True scattered light. Has been attributed above to the broad scattering wings.

Tull et al. (1995) add a number of new items:

7. Internal reflections and interference in the CCD. The two instrumental profiles were obtained by using two different CCDs (but of the same type). The

structure of the wings obtained is much the same, so that this component can be neglected.

8. Widening due to CCD transparency; the same argument as in the previous item.

9. Charge transfer inefficiency, which makes a characteristic tail in the direction of parallel (along the dispersion) or serial transfers (depending on which of these two registers is not fully optimized). The CCDs being used are optimized and specially tested for the effect.

10. External reflections (stray light images). This is the most plausible explanation for the satellites in the scattering wings. The equal positions of the satellites for the two cameras imply that the effect is taking place before entering the elements of the optical camera. Filling the collimator pupil would make external reflections on the collimator and échelle frames. Small-angle back-reflections on the optical elements are also possible. One of the features of SOFIN is a small flat mirror situated in the collimated beam. The mirror is a key element of the spectrograph design: it turns the light beam emerging from the slit by a right angle and renders it to the collimator; the use of the mirror reduces the size of the spectrograph and, therefore, improves its mechanical stability. However, the design has its drawback: the mirror is situated in the collimated beam which allows small-angle reflections back to the rear of the slit which results in the appearance of additional off-axis beams. The reflections which occur in the direction of the slit width will be seen as the displaced features in the dispersion direction, i.e. the satellites in the instrumental profile. The rear of the slit is protected from the back-illumination effect by a black metal shield with a hole, although, the size of the outlet leaves room for the small-angle back reflections. One other possibility for back-reflections in SOFIN is a filter installed between the slit and the flat mirror. The filter is composed of two pieces separated by a spacer: an "ideal" optical element to generate off-axis beams.

It has been a long discussion in the literature (e.g. Griffin 1969), that the instrumental profile obtained in the laboratory may differ from that obtained on the telescope. This important issue depends on the design of the spectrograph. Typically, the way how the collimator is illuminated is different for the calibration source and for the stellar image. In the former case, the collimator is uniformly illuminated, in the latter case, a central shadow area is present due to the secondary mirror of the telescope, hence, a difference in the shape of the profile may be expected, as well as a possible systematic shift in the line positions from the two sources. In the case of SOFIN, the diagonal flat mirror reduces the effect: the secondary mirror of the NOT is 20% of the primary in diameter, the flat mirror is 25% of the collimator. Therefore, the shadow from the telescope mirror is completely inside the shadow due to the flat mirror and one should not expect

any geometrical difference in the collimator illumination from the calibration and stellar sources. A non-uniform illumination of the collimator by the stellar source, which is also subject to temporal variations as opposed to the uniform illumination by the calibration source, causes the difference between the instrumental profiles obtained in the two cases.

2.1.5 Comparison with the solar spectrum

In this section we apply the measured instrumental profile to real observations. The solar spectrum is used and compared with the McMath FTS Solar Atlas (Kurucz et al. 1984), which has a resolving power of about 400 000 and a noise level below 0.1%. Another advantage is that the solar spectrum obtained with FTS is free of most instrumental effects, like the scattered light, and it is more accurate unlike a synthetic spectrum which may contain uncertainties in the line parameters.

The solar spectra of day light were obtained with the 1st and 2nd optical cameras in July 1996 in the spectral region around 5620 Å. The telescope was pointed without tracking to the sky with the dome and mirror opened. Pointing to the sky ensures that the collimator illumination is similar to the calibration or laser source. The exposure times were 15 and 8 min, yielding the signal-to-noise ratios 400 and 500 for the 1st and 2nd camera, respectively. The spectrum with the 3rd camera was obtained in similar conditions in June 1997 with the signal-to-noise ratio 260 in 8 min of exposure time.

A standard data reduction procedure was applied to the spectra including scattered light removal and wavelength calibration. No corrections to the wavelength scale other than the heliocentric correction were applied. The solar FTS spectrum was convolved with the measured instrumental profiles of the 1st, 2nd, and 3rd cameras in radial velocity scale. The continuum was derived by fitting a spline to the ratio of the observed spectra and the convolved FTS spectra.

The two spectra for the 1st camera are shown in Fig. 2.6: an excellent agreement with the two spectrographs at different line depths and consistency with the instrumental profile derived two years later. The difference between two spectra shows a scatter of 0.4% rms (depends on how many lines are present in the spectrum) which is higher than noise level of 0.25% due to photon statistics. The largest systematic deviations in the blue part of the spectrum occur possibly because of some small uncertainties in the wavelength scale. The comparison of the instrumental profile with a Gaussian in the previous sections shows that there is a systematic deviation at levels below 10% of the peak intensity. To check how significant the deviation is, we convolved the FTS spectrum with a number of Gaussians of different widths. For a convolution with 2 pixels FWHM all line profiles are 5% deeper than the observed spectrum. The best fit can be achieved with 4 pixels FWHM as far as the line depth is concerned, although the convolved line widths are then 10%

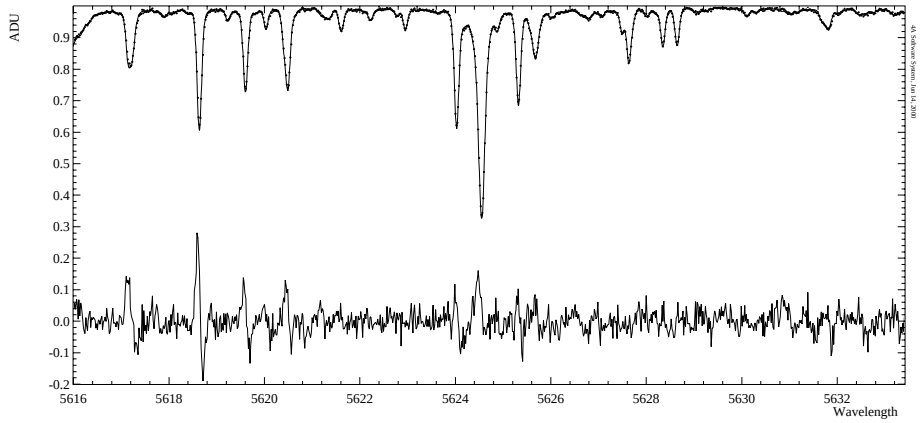

Figure 2.6: Comparison between the solar spectrum obtained with the 1st camera (dots) and the FTS spectrum convolved with the HeNe instrumental profile (thin line). The difference spectrum enlarged 10 times is plotted at the bottom. The mean difference is 0.4% rms, the maximal deviation is 2.8%.

larger than in the observed spectrum. Hence, it can be inferred that the profile wings below 0.1 are important and one should expect systematic deviations when using a pure Gaussian profile for the convolution with the synthetic data.

In the case of the 2nd camera, the observed spectrum is in best agreement with the convolved FTS spectrum (Fig. 2.7). The noise level in the difference spectrum 0.3% rms is almost completely due to the statistical noise level of 0.2%. However, a contribution to the excess could possibly be due to the fine structure of HeNe laser line present in the instrumental profile.

The comparison between the convolved FTS spectrum and the observed one with the camera 3 is given in Fig. 2.8. The convolved spectrum shows small, but systematical deviations of the line widths and depths from the observations: the lines are more narrow and shallow than in the observed spectrum, especially at the edges of the image.

2.1.6 The real resolving power

The above comparison with the observed spectra proves that the measured instrumental profile almost corresponds to the real profile. The core of the profile is broader due to the fine structure of the HeNe line but the near and far scattering wings are introducing a real effect when convolved with the FTS spectrum. The resolving power was measured from the deconvolved core of the profile and is in

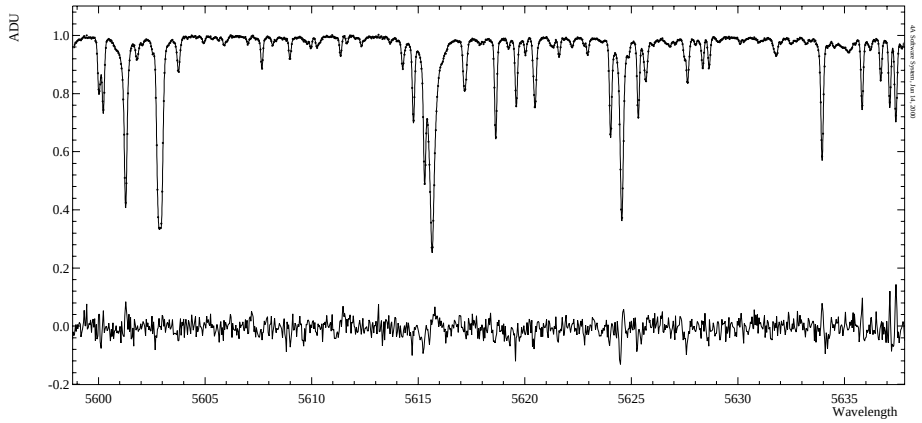

Figure 2.7: The solar FTS spectrum is convolved with the instrumental profile of the 2nd camera (thin line) and overplotted with the observed spectrum (dots). The difference spectrum enlarged 10 times is plotted at the bottom. The mean difference is 0.3% rms, the maximal deviation is 1.3%.

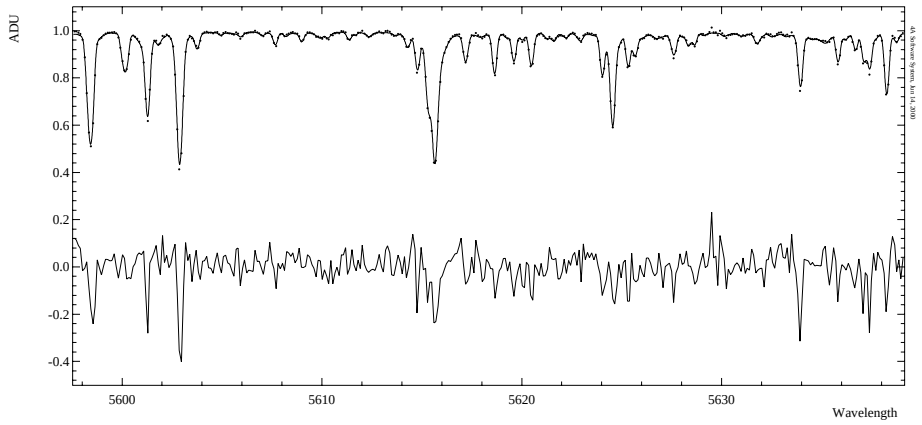

Figure 2.8: The solar spectrum observed with the 3rd camera (dots) and the FTS spectrum convolved with the HeNe laser instrumental profile. The difference spectrum enlarged 10 times is plotted at the bottom. The mean difference is 0.7% rms, the maximal deviation is 4%.

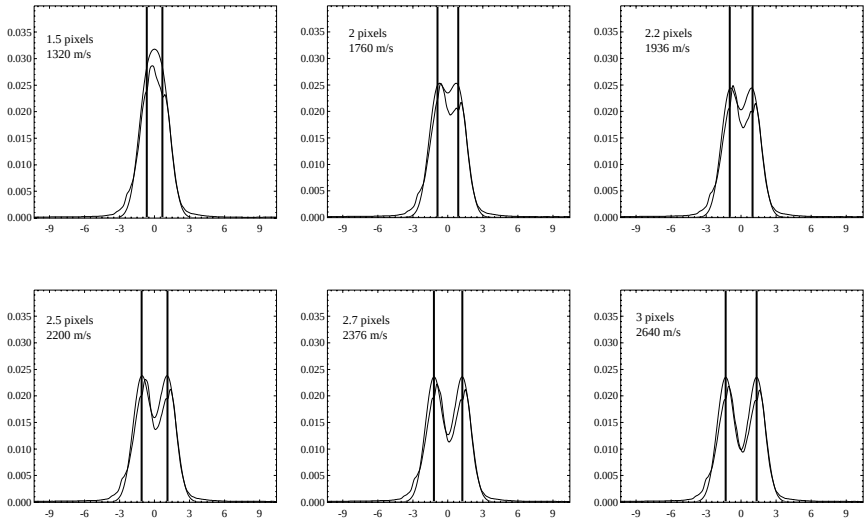

Figure 2.9: The convolution of two delta-functions of different separations with a Gaussian and with the instrumental profile of the 1st camera. The width of the convolved Gaussian profile is 2 pixels FWHM. The 1st camera instrumental profile is able to resolve two sharp features separated by less than 2 pixels ($1.8\,\mathrm{km\,s^{-1}}$) which corresponds to the resolving power better than $R = 167\,000$. The asymmetry and shift of the convolved instrumental profile with respect to the Gaussian is apparent; this could lead to a systematical error in radial velocities.

a good agreement with the expected values. A matter of practical considerations, is whether the real profile with its features is able to resolve narrow spectral lines and what is the real resolving power.

Two delta-functions were created in velocity scale with different separations to mimic narrow spectral features (Fig. 2.9). A convolution with a Gaussian profile of 2 pixels FWHM is given for comparison. The resolution can be defined as the minimal distance between two narrow features at which the convolved profile can be still numerically separated. The numerical separation involves either decomposition of the two profiles or deconvolution with the known instrumental function. The visual separation tells us that the convolved profile is still resolved at 2 pixels separation of the delta-functions.

One other test for the resolving power involves observation of interstellar clouds towards α Cyg (this spectrum was also used in Sec. 1.6.1 to demonstrate the effect of line broadening due to mechanical flexure). The spectrum of interstellar Na I D_2 at 5889.9512 Å was taken with the 1st camera ($R = 176\,000$ at this spectral region)

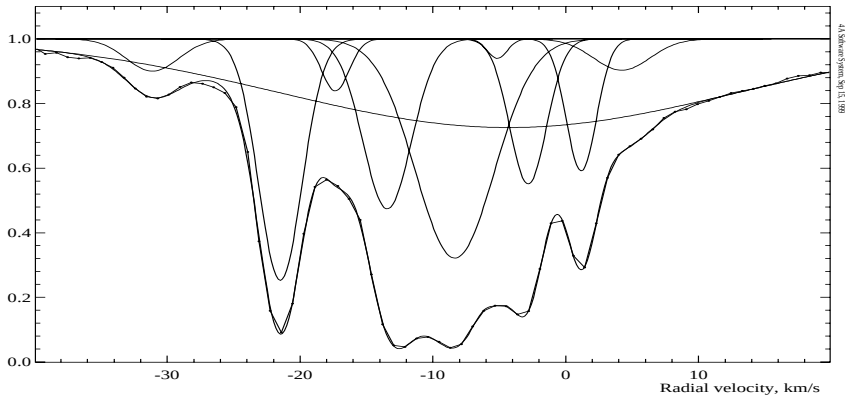

Figure 2.10: The spectrum of α Cyg (V=1.25 A2 Iae) taken with the 1st camera (R=176 000 at this spectral region) showing the profile of interstellar NaI D_2 at 5889.9512 Å. The profile is decomposed into 10 Gaussians. The line at $-31\,\mathrm{km\,s^{-1}}$ with FWHM=$4.6\,\mathrm{km\,s^{-1}}$ is a telluric line.

and is shown in Fig. 2.10. The profile was decomposed into 10 Gaussians (χ^2_ν = 7.7) and compared with observations of Wayte et al. (1978) and Blades et al. (1980), made with a Michelson interferometer ($R = 500\,000$). They have resolved a hyperfine structure of the interstellar profile on the line of sight in a number of narrow $\approx 1\,\mathrm{km\,s^{-1}}$ components. The component at $+1\,\mathrm{km\,s^{-1}}$ is a blend of two narrow profiles separated by $1\,\mathrm{km\,s^{-1}}$ with the total width $2\,\mathrm{km\,s^{-1}}$. Convolution with a two pixels Gaussian instrumental profile (the width is determined from the ThAr comparison spectrum lines) gives FWHM=$2.6\,\mathrm{km\,s^{-1}}$ which is exactly the width of the decomposed component.

2.1.7 Discussion

The above analysis has shown that the measured resolving power is consistent with that which is expected according to the design parameters. However, the estimated resolving power is higher than expected especially after the fine structure of the laser line was eliminated. The reduction of the profile width can be interpreted in different ways as follows.

Firstly, the observed line width could be narrower if the collimated beam does not fill the pupil completely, which results in only partial illumination of the optics of the spectrograph, i.e. the aberration spot becomes narrower. This problem was overcome by using a light diffuser situated at a certain distance above the slit. Secondly, there might be some uncertainty in the estimate of the aberration spot

for the optical cameras which is involved into the calculation of the slit width. And the last uncertainty may come from the slit calibration which is possibly resulting in a slit which is narrower than expected in linear scale. Nevertheless, the obtained instrumental profile is legitimate for the CCD image centre and for the optimal focus of the spectrograph.

The measured instrumental profiles show the typical shape common to all grating spectrographs (Dravins 1993). The core of the profiles can be approximated by a Gaussian down to 10% of its maximal intensity. Different kinds of estimations of the convolution width based on the sum of squares of widths remain valid up to the above accuracy. For higher accuracies, the real measured instrumental profile should be used for the convolution with the template (synthetic) spectrum to achieve the maximal correspondence to the observed spectrum. One should not use a Gaussian approximation of the PSF for the convolution.

Chapter 3

Optimization of CCD performance

3.1 Introduction

In this chapter we will consider some results of the practical work with the CCDs which were obtained during years of work with the Astromed CCD cameras used with SOFIN. In the first two sections, some prescriptions concerning the accurate flat fielding are given. Some preliminary results concerning the non-linearity effects as consequences of the charge transfer inefficiency are given in the following section. We proceed by describing a variant of the photon transfer technique which we employed to estimate the gain of the CCD system, and also to correct for the effects of non-linearity. Once the method has been developed and implemented, we managed to optimize the CCDs and make them linear, therefore, the method remains unused until future projects. Some general details about the mask method used for the optimization are given in the last section of the chapter.

3.2 Noise of the ideal CCD

The registered signal in a single CCD pixel can be expressed according to the following simplified model:

$$x_i = ys_i + b, \tag{3.1}$$

where y is the spatially uniform illumination level of the CCD in photoelectrons, x_i is the random number of photoelectrons registered in pixel number i. The function

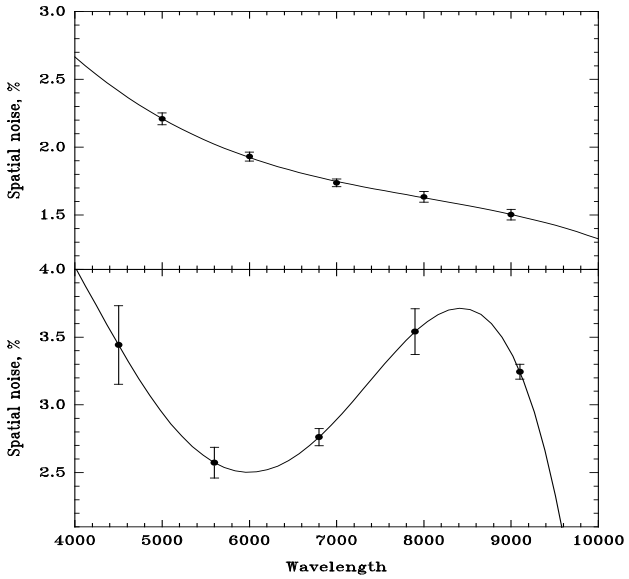

Figure 3.1: The behaviour of the high frequency pixel-to-adjacent-pixels spatial noise as a function of wavelength for two different CCDs. The upper panel shows the behaviour for the EEV P8600 576×385 CCD, and the lower panel is for the 580×520 virtual phase Electron Corp. CCD (from Shcherbakov et al. 1995) Note, that for the EEV CCDs, the pixel inhomogeneities are rather higher in the blue than in the red.

s_i describes the relative sensitivity of individual pixels and is often referred to as the high frequency spatial noise, pixel-to-adjacent-pixel noise, or fixed pattern noise of the CCD. The function is described by the mean $s = 1$ and its variance σ_s^2. The amplitude of this noise σ_s is typically 1–6% and is constant for a given CCD across the chip. The amplitude varies from one CCD to another depending on its type and optimization quality. This noise is also wavelength dependent (see Fig. 3.1). The random number b describes the additive component to the signal and is associated with the electronic bias subtracted from the raw image, hence, its mean $b = 0$, and $\sigma_b^2 = \sigma_{\rm ron}^2$ is the readout noise of the CCD in photoelectrons (e^-).

The total noise of the registered signal over a large sample of the CCD image is estimated using error propagation:

$$\sigma_x^2 = \sigma_y^2 s^2 + y^2 \sigma_s^2 + \sigma_{\rm ron}^2, \tag{3.2}$$

which after division by y^2 yields the total relative noise of the registered signal:

$$\delta_x^2 = \delta_y^2 s^2 + \sigma_s^2 + \frac{\sigma_{\rm ron}^2}{y^2} = \frac{1}{y} + \sigma_s^2 + \frac{\sigma_{\rm ron}^2}{y^2}, \tag{3.3}$$

where in the first term the noise distribution of y is assumed to be Poissonian and the mean of $s^2 = 1$. Fig. 3.2 demonstrates the contributions of the three components to the total relative noise.

At the first crossing point $y = \sigma_{\rm ron}^2$, the contributions of the readout noise and photon noise are equal (but dominating over the spatial noise) and limit the detectability of a very low signal with the CCD below this level. At the middle crossing point $y = \sigma_{\rm ron}^2/\sigma_s$, the contributions from the additive and multiplicative noise components are equal, but the photon noise is dominating. The last crossing point is at $y = 1/\sigma_s^2$ where the readout noise has become negligible, but the accuracy of the measured signal is determined merely by the spatial noise. Hence, the final accuracy of the measured signal is based on the quality of the spatial noise correction. Some special pre-requirements for the flat fielding procedure are discussed in the next section.

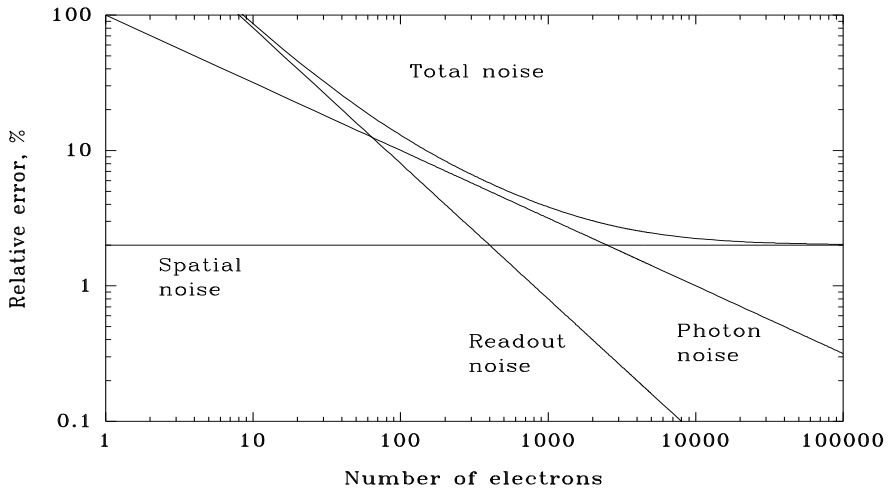

Figure 3.2: The three basic components of the total noise of the CCD. The amplitude of the spatial noise is set to $\sigma_s = 2\%$ and the readout noise to $\sigma_{\rm ron}^2 = 8\,e^-$. For the given parameters, the readout noise becomes dominant over the photon noise at light levels below $64\,e^-$ while the spatial noise dominates at the levels above $2500\,e^-$.

3.3 Correction for the high frequency spatial noise

The fixed pattern noise is a multiplicative component of the image structure, hence the correction is straightforward by division of the object image by an uniformly illuminated flat field image. The noise of the object image after the division may entirely depend on the noise level of the flat field image because of the statistical error of the accumulated flux: a poor flat fielding can significantly degrade the accuracy of the object image. Consider the amount of photoelectrons (e^-) accumulated in the object image y and in the flat field ny, where n is some number which implies that the flat field image is the sum of several individual exposures. The squared relative error of the ratio of two random independent variables is

$$\delta_r^2 = \delta_y^2 + \frac{1}{n}\delta_y^2, \tag{3.4}$$

where the readout noise contribution was neglected for simplicity. The following ratio of the relative errors is the accuracy reduction factor due to flat fielding and describes the achieved accuracy with respect to the one expected (which is equivalent to the ratio of the signal/noise of the two images):

$$\frac{\delta_r}{\delta_y} = \sqrt{1 + \frac{1}{n}}. \tag{3.5}$$

The following table gives for a range of flux ratios the corresponding accuracy reduction factors:

n	1	3	10	50	100
$\delta_r/\delta_y - 1$, %	41	15	5	1	0.5

If the fluxes are equal ($n = 1$), the signal/noise degradation of the object image is $\sqrt{2}$ which is equivalent to the loss of half the exposure time. The use of 50 flat fields will degrade the resulting signal-to-noise ratio by 1% only.

To accumulate the flux ny sufficient for accurate flat-fielding, a series of flat field images of the same level can be obtained with the subsequent co-addition of all of them to form the master flat field.

The intensity level of the individual images should be, in fact, close to that of the object exposure in the case of CCD linearity problems. The amplitude of the fixed pattern may be different at high levels as compared to lower levels of the object exposure. Apparently, this can introduce spurious systematical deviations in the noise level of the corrected image. The ideal solution to the problem is to correct the image intensities with the intensity transfer function to make their response linear, and then perform the flat field division.

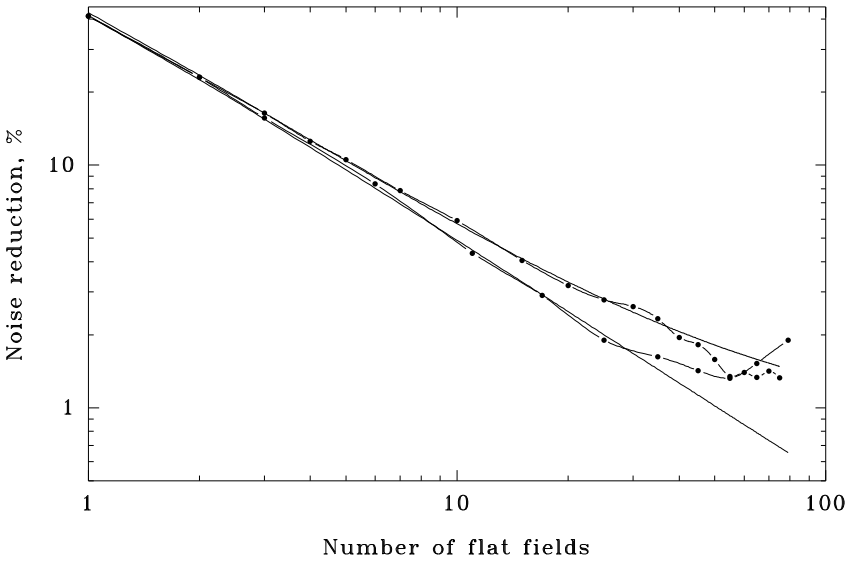

Figure 3.3: The accuracy reduction as a function of the number of co-added flat fields. Two different accumulation levels of $25000\,e^-$ (the lower curve) and $130\,e^-$ (the upper curve) were used. The solid curves are the expected accuracy reductions according to Eq. (3.7). The measurements were carried out in March 1996 with the P88100 CCD.

In the above equations the readout noise was neglected. Co-addition of many weak CCD images increases the noise component due to readout noise. The relative noise of the image divided by the sum of k flat fields, where the intensity of each individual image is a multiple n of the intensity of the source image, is given by:

$$\delta_r^2 = \delta_y^2 \left(1 + \frac{1}{nk}\right) + \frac{\sigma_{\rm ron}^2}{y^2}\left(1 + \frac{1}{n^2 k}\right), \tag{3.6}$$

which leads to the accuracy reduction equation:

$$\frac{\delta_r}{\delta_y} = \sqrt{\left(1 + \frac{\sigma_{\rm ron}^2}{y}\right) + \frac{1}{n^2 k}\left(n + \frac{\sigma_{\rm ron}^2}{y}\right)}. \tag{3.7}$$

The first term reflects the readout noise component of the total noise of the source image and the second term is the contribution of the sum of the flat fields.

It is always useful to compare theory and practice. In our experiment we used the EEV P88100 1152×298 pixels CCD, uniformly illuminated by a red diode. 80 similar flat field images were obtained for two illumination levels. After the

bias subtraction, the first image was divided by the sum of the flat fields and the relative error was measured in some selected area of the corrected image. A plot of the measured and expected noise levels as a function of the number of flat fields is shown on Fig. 3.3. Unfortunately, the environmental conditions changed at the end of the experiment (the humidity in the NOT dome was about 100%) which spoiled the last images. Otherwise, this experiment shows that the accuracy reduction follows the prediction and no other additional noise sources are present.

3.4 Charge transfer efficiency

The efficiency of the charge transport during readout is measured in both directions of the parallel and the serial transfer. The basic method to calculate the overall efficiency is the so-called *extended pixel edge response* (EPER). The CCD is illuminated to get a uniform response with the subsequent readout of a number of trailing pixels which is more than the physical number of pixels in the CCD in order to obtain overscan areas in both directions. The amount of charge (the sum) spilled out of the last column/row, or equivalently, the amount of *deferred charge* is measured with respect to the bias level.

The charge transfer efficiency describes the fraction of the charge transferred from one pixel to the other:

$$\mathrm{CTE} = 1 - \frac{d}{c \cdot n}, \tag{3.8}$$

where c is the intensity level of the uniform area in ADU (analogue-to-digital units), n is the number the CCD transfers, i.e. the number of times the charge loss was suffered in the direction of parallel or serial transfers, and d is the amount of measured deferred charge. The quantity (1–CTE) is called the *charge transfer inefficiency* (CTI).

The charge transfer inefficiency is one of the sources of CCD non-linearity: the charge trapped in a single pixel is accumulated until it is co-added to the next charge packet (column brightening), or in the case of a single event, it appears as a tail of the spilled charge opposite to the direction of the transfer. Since the charge is co-added to the other pixels, the ratio of the pixel intensities becomes dependent on the amount of the trapped charge as a function of the distance between pixels.

The above method of measuring CTE is the relative method. The absolute method is employed in CCD labs and uses an X-ray source with the known number of equivalent optical photoelectrons per single event (e.g. a Fe^{55}+Mn source has $1620\,e^-$/event). A plot of intensities versus column number shows the amount of charge lost as the number of transfers increases (e.g. Janesick 1997).

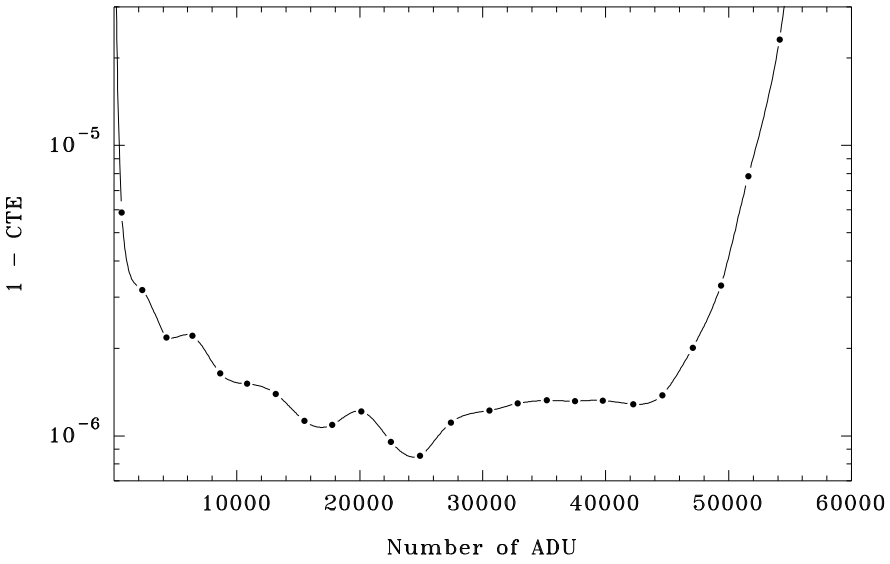

Figure 3.4: The charge transfer inefficiency 1–CTE in the direction of parallel transfer at different illumination levels of the P88100 CCD (December 1995). An average of two flat fields and 200 overscanned columns were used for the measurements.

Usually, the CTE of a CCD is characterized by a single number. We found that the CTE is not constant over a range of intensities (at least for our CCDs), and therefore cannot be expressed as a single number. In Fig. 3.4 we used the EPER technique at different flat field illumination levels. As can be seen, the minimal charge losses occur in the central part of the dynamical range. The systematical change of the CTE reflects the shape of the potential well. In principle, the structure of the well can be reconfigured with a fine tuning of the substrate bias voltage (VSS). The other reason for the increase of CTI at low light levels is a too high level of the output gate voltage (VOG) which controls the height of the potential barrier when the next charge packet is transferred into the output node of the serial register (this is valid at least for the EEV CCDs). A too high level of the barrier can cause a complete blockage of the signal, and a partial trapping of the signal results in the appearance of a "fat zero" effect which also can be seen in the linearity curve (Thorne et al. 1987).

3.5 The intensity transfer function of the CCD

In this section we consider a method for correction of the CCD non-linearity effects in a qualitative way, i.e. the problem is to reconstruct the intensity transfer function

which can be used to correct the raw pixel intensities. The importance of the problem and possible ways to its solution were extensively discussed in ESO CCD-related works, the most relevant is Gosset & Magain (1993).

The method described here is an extension of the known photon transfer technique (Janesick 1997) in the sense that the measured quantities are based on the analysis of the variance of the detected signal. This is the principal difference to the absolute methods which employ X-ray sources. In the following considerations we are going to find the exact solution to the problem and, if possible, to eliminate many of the assumptions used in the photon transfer technique. However, our experience of using the method described below shows that a more complex model of the CCD signal transfer equation is needed which should include an additive component due to the charge transfer inefficiency. Nevertheless, we proceed with the simplified model similar to that already introduced.

We shall consider the CCD as a non-linear system with the signal transformation according to the model:

$$x_i = p(y)s_i + b, \tag{3.9}$$

where y is the mathematical expectation of the input signal to the system in photoelectrons and its variance is $\sigma_y^2 = y$, x_i is the signal measured in pixel i in ADUs, $p(y)$ is the unknown signal transformation function of the CCD amplifier and the digitizing circuit, s_i is the fixed pattern noise with the mean $s = 1$ and the variance σ_s^2. The subtracted bias offset b is assumed to have the mean $b = 0$ and the variance $\sigma_b^2 = \sigma_{\rm ron}^2$ in ADUs to be known.

Two identical exposures of the uniformly illuminated CCD yield two images which have almost the same average level but never the same due to small deviations from the average in shutter response, light source brightness, etc. The division of the two debiased images by each other yields a ratio image, which is used to obtain two quantities: the average ratio r and its variance σ_r^2 by using a large enough area of the CCD. We use the ratio of the two images (not the difference as in Janesick 1997) in order to eliminate the multiplicative fixed pattern noise. Recalling the relative error identity for the ratio of two independent random numbers, we have:

$$\frac{\sigma_r^2}{r^2} = \frac{p_1'^2 y_1 s^2 + \sigma_{\rm ron}^2}{x_1^2} + \frac{p_2'^2 y_2 s^2 + \sigma_{\rm ron}^2}{x_2^2}, \tag{3.10}$$

where $p_1' \equiv p'(y_1)$ and $p_2' \equiv p'(y_2)$ are the first derivatives of the unknown function $p(y)$, y_1 and y_2 are the unknown "true" numbers of photoelectrons, x_1 and x_2 are the measured average of the signal registered on the same CCD area of the two identical exposures (*not* to be confused with the signal at the pixel number 1 and 2), and the factor $s^2 = 1$ is omitted hereafter.

In order to exclude unnecessary variables, namely x_2 and y_2, two assumptions

have to be made at this point, the first one is that

$$r = \frac{x_1}{x_2} \tag{3.11}$$

implying that the measured averages of the registered signals are not biased by the fixed pattern noise over a large sample, and the second one is that the unknown function $p(y)$ must be simple (Occam's approach is in action), i.e. within a small interval of intensities $[y_1, y_2]$ it can be approximated by a straight line:

$$x_2 - x_1 = p'(y_2 - y_1), \tag{3.12}$$

where the notation is $p' = p'_1 = p'_2$.

Applying these assumptions and after multiplication of both sides of Eq. (3.10) by x_1^2, we get

$$\frac{\sigma_r^2}{r^2} x_1^2 = p'^2(y_1 + r^2 y_2) + \sigma_{\text{ron}}^2(1 + r^2) \tag{3.13}$$

and finally, after omitting the index referring to the first image of two identical exposures $x \equiv x_1$ and $y \equiv y_1$, it follows:

$$p'^2 \cdot \frac{y}{x} = \frac{\sigma_r^2 x}{r^2(1 + r^2)} - p' \cdot \frac{r(1 - r)}{1 + r^2} - \frac{\sigma_{\text{ron}}^2}{x}, \tag{3.14}$$

which is a general form of the intensity transfer equation as a function of the number of different illumination levels measured as x.

3.5.1 The CCD gain function

Let us make a further simplification of the intensity transfer function, namely that it is

$$p(y) = \frac{y}{g(x)}, \tag{3.15}$$

i.e. the number of detected photoelectrons is $y = xg(x)$, where $g(x)$ is the gain function of the system in e^-/ADU units. This implies that $p'(y) = 1/g(x)$ and after some transformations we get the solution

$$g(x) = \frac{xr^2(1 + r)}{x^2\sigma_r^2 - \sigma_{\text{ron}}^2 r^2(1 + r^2)}. \tag{3.16}$$

The function, defined in the interval of different values of x over the dynamical range of the CCD, can be derived from the measurements of x, r, σ_r^2, and $\sigma_{\rm ron}^2$ obtained from a number of identical exposures. This approximation and the derived solution will be used later for the proposed "mask" method of the CCD quick characterization. Also, by neglecting the ratio term by setting $r = 1$ and for fluxes $x \gg \sigma_{\rm ron}^2$, one will get a simple estimate of the gain factor:

$$g(x) = \frac{2}{x\sigma_r^2}. \tag{3.17}$$

3.5.2 Integration of the transfer equation

To restore the shape of the function $p(y)$ we need to integrate the differential equation Eq. (3.14). In fact, we are finally interested to restore the inverse function of $p(y)$, namely a generalization of the gain function:

$$y = xg(x) \tag{3.18}$$

which would give us the true, corrected for the non-linearity effects, number of the photoelectrons y detected from the measured number x of ADUs. Eq. (3.14) is a differential equation which is quadratic in $p'(y)$. To lower the degree and simplify the derivations, we approximate the term $p'(y)$ on the right hand side in Eq. (3.14) by a constant number $1/g_0$, which is the inverse gain of the system, Eq. (3.16). An estimate of g_0 can be obtained as a preliminary step prior to the integration. Then, the right hand side of Eq. (3.14) reads

$$f(x) = \frac{\sigma_r^2 x}{r^2(1+r^2)} - \frac{1}{g_0}\frac{r(1-r)}{1+r^2} - \frac{\sigma_{\rm ron}^2}{x}, \tag{3.19}$$

which is a discrete function of the measurements at a number of different fluxes x. The variables are separated and integrated in parts as follows:

$$\int_0^y \frac{dy}{\sqrt{y}} = \int_0^x \frac{dx}{\sqrt{xf(x)}}, \tag{3.20}$$

where we write $p'(y) = dx/dy$. The integration can be done with the Runge-Kutta method in the case when the integration function is a smooth (and possibly an analytical) function. Here, we used two types of approximation of the integrated function depending on the complexity of its shape.

Polynomial approximation

Suppose, that the integration function can be approximated by a polynomial of degree n:

$$\frac{1}{\sqrt{f(x)}} = \sum_{k=0}^{n} c_k x^k; \tag{3.21}$$

after the integration it becomes

$$\sqrt{x} \sum_{k=0}^{n} \frac{c_k}{2k+1} x^k = \sqrt{y}. \tag{3.22}$$

Then, the unknown function is

$$g(x) = \frac{y}{x} = \left[\sum_{k=0}^{n} \frac{c_k}{2k+1} x^k \right]^2. \tag{3.23}$$

Smoothing spline approximation

Suppose, that the function $f^{-1/2}(x)$ cannot be well described by a polynomial but is approximated by a smoothing spline (the details of the implementation are given in Ilyin 2000). The smoothing cubic spline is defined on each interval $[x_i, x_{i+1}]$ of the data $i = 0, 1, \ldots, n$, and together with its derivatives is written as follows:

$$\begin{aligned} q(p) &= a_i + b_i p + c_i p^2 + d_i p^3 & q''(p) &= 2c_i + 6d_i p \\ q'(p) &= b_i + 2c_i p + 3d_i p^2 & q'''(p) &= 6d_i, \end{aligned} \tag{3.24}$$

where

$$p = \frac{x - x_i}{h_i} \qquad \text{and} \qquad h_i = x_{i+1} - x_i. \tag{3.25}$$

The unknown polynomial coefficients of the cubic spline are calculated from its second derivatives y_i'':

$$\begin{aligned} d_i &= \frac{h_i^2}{6}(y_{i+1}'' - y_i''), & c_i &= \frac{h_i^2}{2} y_i'', \\ b_i &= y_{i+1} - y_i - (d_i + c_i), & a_i &= y_i \end{aligned} \tag{3.26}$$

where the derivatives y_i'' are obtained from the solution of a system of linear equations and y_i are the *smoothed* points of the tabulated function. The integral

$$I_i(x) = \int_{x_i}^{x} \frac{1}{\sqrt{xf(x)}} dx \tag{3.27}$$

is defined on each interval $x \in [x_i, x_{i+1}]$. Integrating by parts, one can obtain:

$$\frac{I_i(x)}{2\sqrt{x}} = q(p) - \frac{2}{3}\left(\frac{x}{h_i}\right) q'(p) + \frac{4}{15}\left(\frac{x}{h_i}\right)^2 q''(p) - \frac{8}{105}\left(\frac{x}{h_i}\right)^3 q'''(p) \tag{3.28}$$

and the total integral $[0, x]$ consists of the sum:

$$J(x) = \int_0^x \frac{1}{\sqrt{xf(x)}} dx = \left[\sum_{i=0}^{k-1} I_i(x_{i+1})\right] + I_k(x), \tag{3.29}$$

where the index k is chosen from the interval where $x_{k-1} \leq x < x_k$. Finally, the unknown integrated function is

$$g(x) = \frac{y}{x} = \frac{J^2(x)}{4x}. \tag{3.30}$$

3.6 The mask method

With the variation of the photon transfer technique as described above to obtain the CCD linearity curve, a series of pair exposures of different exposure times (or by changing the light source intensity) with the CCD uniformly illuminated is obtained. Each pair consists of two exposures of the same accumulated level. In practice we usually do about 10–30 pairs of exposures which, with the subsequent image processing (to obtain r and σ_r^2 for a number of selected image regions), takes an hour to obtain the linearity curve. Consequently, a faster method was invented to speed up the process and make the trial-and-error CCD optimization process efficient and practically applicable.

The proposed *mask* method is used which is less accurate but is much faster in the sense, that only two exposures are needed to obtain the linearity curve at once. The idea behind it is that the CCD is illuminated fairly non-uniformly which results in an image with a large range of accumulated ADUs. If the CCD is linear, the ratio of such two images should be approximately a constant. The noise level of the ratio gives an estimate of the gain factor as a function of ADUs (Eq. (3.16)). The ratio of two exposures at different illumination levels can reveal

possible non-linear effects of the CCD, and can be used as a merit function for the CCD optimization process.

The mask is a PostScript programmed image and printed on a transparent film with a 300 dpi PS-printer. Fig. 3.5 shows the mask and the associated code which can be found in the "PostScript Language Manual" (Adobe Systems Inc., Wesley).

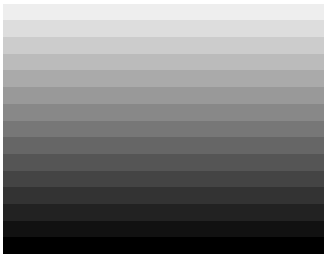

```
%!PS-Adobe-2.0
/DataString 256 string def
/mask{gsave translate scale
      image grestore} bind def
0 1 255 {DataString exch dup put} bind for
1 256 4 [1 0 0 256 0 0] {DataString}
120 100 20 70 mask
showpage
```

Figure 3.5: The mask (here printed with 600 dpi) used to obtain a non-uniformly illuminated CCD image and its corresponding code in PostScript. The numbers `120 100` in front of the `mask` command define the width and height of the mask and `20 70` are its lower-left position on the sheet in PostScript point units.

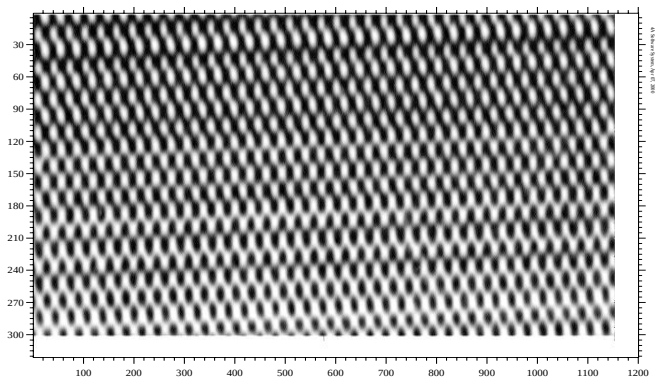

Figure 3.6: An image obtained through the mask installed in front of the CCD and uniformly illuminated by a light source. The actual CCD size is smaller than that of the mask shown in the previous figure. Thus, the fine structure results from light falling through the gaps between the dots which make up the "homogeneous" stripes in the mask. This installation was used for the P88100 CCD gain reconfiguration in October 1999. The range of pixel intensities is 10000–40000 ADUs.

The following figures show the results of the method and the success of the optimization procedure.

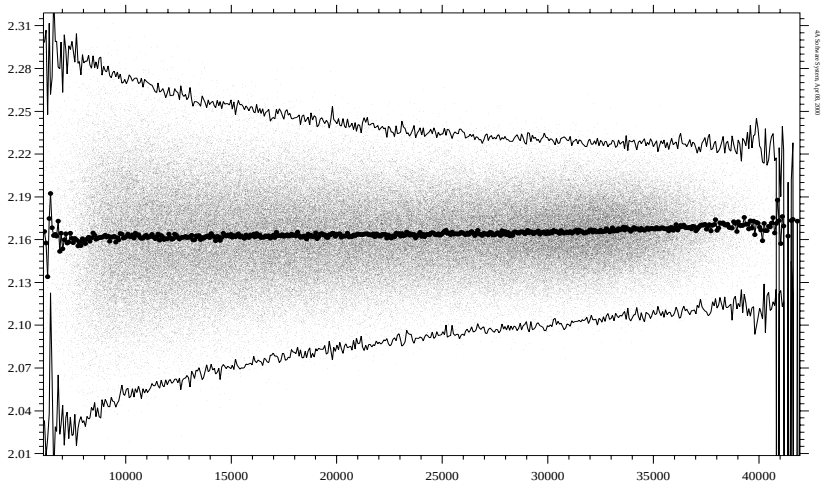

Figure 3.7: The ratio of two images taken with different fluxes versus intensity of the first image. Each point is the ratio of the intensities of the same pixels in two images. The mean and variance curves are calculated within every bin of 1/500 of the intensity range.

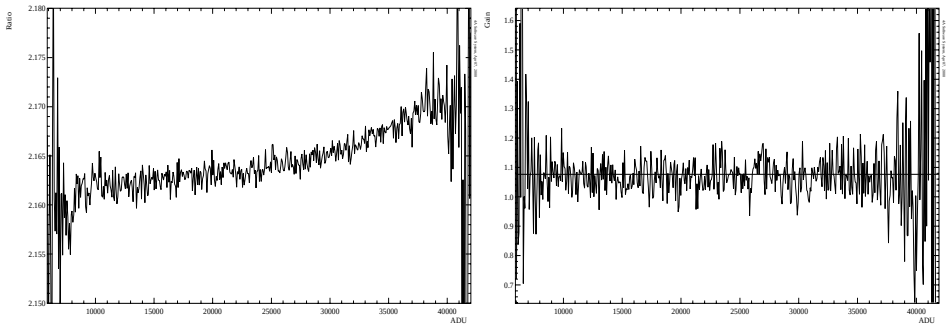

Figure 3.8: The ratio curve, enlarged from the previous figure, and the gain factor as functions of intensity. The ratio curve should be constant; it is tilted by only 0.3% within the range of intensities. Despite the tilt of the ratio, the gain factor curve is constant and the mean is $1.07\,e^-$/ADU for the reconfigured P88100 CCD camera with the adjusted parameters VOD=14, VRD=3.5, VRSPH=–7.8, and PGAIN=8.

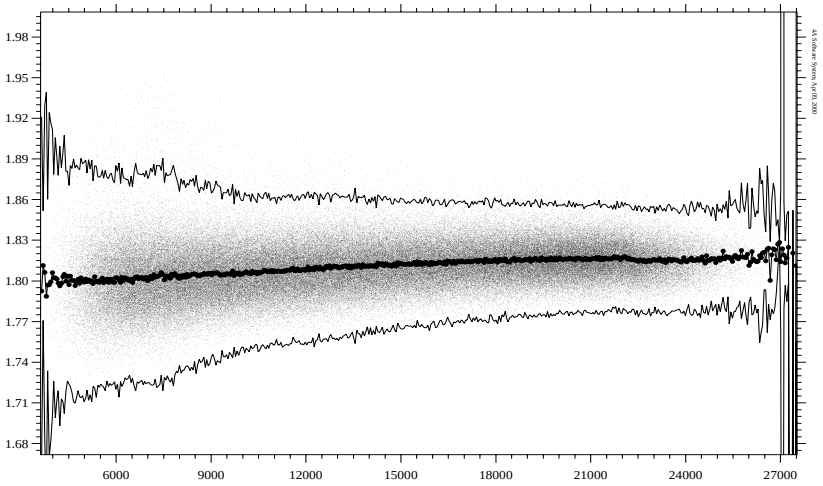

Figure 3.9: An example of the ratio plot of two CCD images with the incorrect voltage setup.

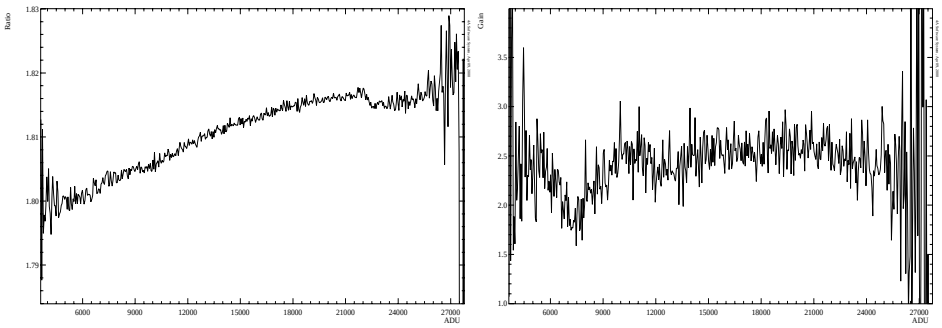

Figure 3.10: The enlarged ratio curve from the previous figure, the tilt is about 1.1%. The corresponding gain curve shows some tilt and breaks; the maximum non-linearity is about 30%. This was used as an indication that the the trial voltage parameters are wrong: VOD=16, VRD=7, VRSPH=–3, PGAIN=8.

Chapter 4

Processing astronomical spectra

4.1 The 4A software package

The Advanced Acquisition, Archiving, and Analysis (4A) software package is the main tool for providing observations with a remotely controlled spectrograph as well as the subsequent reduction and analysis of the data.

The package provides the software to control the SOFIN spectrograph and the CCDs which are used to register the échelle spectra.

The images and spectra are written as separate files stored in the FITS format, selected records of their headers constitute the contents of a database. Instead of using a command line prompt, file names, and shell scripts, like other data reduction facilities in astronomy, an interactive facility allows to operate with the data by its context as it is seen in the database. The procedures can be run interactively for a single image or spectrum for immediate evaluation of the result, or in an automatic, sequential mode for a number of images selected from the database.

The database facility allows to add new files to the database, copy or move them to another directory. New fields can be added, edited, and removed from the database. A number of mathematical operations, including time transformation routines, are incorporated to manipulate with the fields of the database, and, thus, records in the FITS headers.

One of the main features of the package is that it gives in the resulting spectra not only intensities but also errors of the intensities and pixel positions. All the routines are propagating the variances, which are ultimately based on the photon

noise statistics of the raw images.

Two groups of filters are implemented: the ranked filters with median and trimmed mean (including moving average filter), and the convolutional filters with the Gaussian, Lorentzian, and stellar rotational profiles. The approximation facility implements a weighted smoothing spline and polynomials; a clip-and-fit algorithm allows e.g. to approximate the outer envelope of the data or the interactive exclusion of intervals from the fit and facilitates reshaping the spectra e.g. during continuum normalization.

The software is written in the C language and contains about 100 000 lines of the source code (2.6 MB in total). It includes a graphical user interface, a number of mathematical routines (Ilyin 2000), the programs for the spectrograph and CCD control, data reduction and analysis facilities developed solely by the author. The total number of such programs is 140. Some standard mathematical routines were implemented from Press et al. (1992) and a number of routines for time and ephemeris transformations was coded from basic astronomical handbooks. Although the software is developed in MS-DOS, it is running in Linux and Windows-98 software emulation environments.

It a frequently asked question why not to use other standard data reduction packages, like IRAF, MIDAS, AIPS, Figaro, or Starlink, instead of 4A. The answer is that they indeed can be used for the reduction of the SOFIN échelle spectra without any problems. But our (limited) experience with the other packages shows that 4A does it better and in a more efficient way. However, most of the procedures are common, some of them are based on rather different approaches, like the flat field correction of échelle spectra. The criterion for the efficiency is that the observer can now leave the telescope with his data completely reduced, somehow similarly to the pipeline data reduction in MIDAS and IRAF.

4.2 Reduction of CCD échelle spectra: an overview

The process of spectrum reduction involves a number of procedures to correct for the spectrograph and CCD instrumental effects and to extract the calibrated stellar spectra from the raw images. The following constitutes a short overview; a more technical desription of the individual steps is given in the Appendix.

A very first step of any CCD reduction is the subtraction of the bias frame, an image obtained with a zero exposure time. If the bias is not uniform across the image but constant in time, the average of many such images is subtracted. However, if the bias is variable in time, then the overscan area of the same CCD image is used which involves the subtraction of the averaged and smoothed bias trace from the whole image.

Once the zero point of the intensity is removed and the images are trimmed at the edges, the estimation of the pixel variances is performed. The estimate of the pho-

ton noise is based on the known CCD gain factor and the amplitude of the readout noise. The variance of every pixel will then follow the intensity transformations at each and all subsequent steps of the data reduction.

The CCD pixels intrinsically have different sensitivities which vary within several percent depending on the CCD. The image of the pixel sensitivity can be obtained from the master flat field, which is made up by a sum of a large number of flat field exposures. Division of the images being processed by the master flat field can significantly reduce the apparent noise of the spectra.

Prior to the échelle order integration, the scattered light has to be subtracted from the image to ensure that the depth of the spectral lines remains undisturbed. The structure of the scattered light is usually very complex and results from the light diffusion and backwards reflections on the optical elements of the spectrograph. The background structure is difficult to describe in terms of a model, hence, an empirical approximation of the inter-order structure is used to retrieve the scattered light surface e.g. by means of a clip-and-fit smoothing spline in two dimensions.

The spectral orders of the échelle image are tilted and curved with respect to the regular grid of CCD pixels. The order definition involves recognition of the spectral orders in the image and approximation of the order positions with a bivariate polynomial.

The spectral orders are integrated at each wavelength pixel by using a weighted fit of the spatial profile to the intensity distribution of the pixels across the dispersion. Since the fit is linear, it allows to distinguish between good pixels and those which are affected by cosmic ray events. The latter are excluded from the fit. The image of the spatial profiles of the spectral orders is derived by smoothing the normalized intensities along the CCD columns in the dispersion direction.

The integrated spectra are usually curved due to the difference in illumination levels in the centre of the focal plane and in the edges. To correct for the vignetting function, flat field spectra are used which generally show the same shape in intensity. Appearance of interference fringes in the stellar spectra due to varying thickness of the CCD UV-coating film can also be accounted for with the aid of the flat field spectra.

The wavelength calibration of the stellar spectra is derived from the images of a ThAr comparison spectrum. The images are debiased, trimmed, and the variances are estimated. The background of the comparison images is obtained e.g. by a median filtration in the dispersion direction.

The bivariate polynomials of the spectral orders are used from the neighbouring object or flat field images. The position of the curves may not coincide with the centres of the spectral orders of the comparison image because of a drift between the two images. The exact position is obtained by fine tuning of the bivariate polynomial curves to the cross-dispersion profiles of the comparison spectrum image.

After integration of the spectral orders, the central positions of the lines are determined by fitting Gaussian profiles. To find the wavelengths of lines in a single order, a search algorithm is used which compares the positional configuration of the lines in the spectrum with the wavelength configuration of lines in a catalogue.

A fit of the line positions in pixels to their wavelengths defines the dispersion polynomial for a single order. The wavelength identification of the other spectral orders is done in a first approximation using the constancy of the ratio between échelle order numbers and wavelengths at a given pixel in the dispersion direction. The exact wavelength for every line of all other spectral orders is found by picking the nearest value from the catalogue of spectral lines.

Combination of hundreds of spectral lines into one fit based on the appropriate model significantly improves the accuracy of the wavelength calibration. Such a model is based on a bivariate polynomial fit of the line position in the dispersion direction as a function of wavelength and its position in cross-dispersion direction. The complexity of the model is justified by the fact that the dispersion of the spectral orders is changing non-linearly due to aberration effects in the optical cameras, misalignment of the optical elements, and centring errors due to possible asymmetry of the spectral lines. Furthermore, two subsequent comparison spectrum images exhibit a drift of the spectral line positions with respect to each other in either direction due to variations of the above factors in time as a function of the spectrograph's spatial orientation on the telescope and the ambient temperature in the dome. The model is capable to trace the temporal changes of the dispersion coefficients by inclusion of the third, the time dimension into the model, if at least two images are obtained at different times.

The pupil of the comparison spectrum is formed by uniform illumination of the slit. The pupil of the stellar image is defined by the width of the seeing profile. Any slit spectrograph is subject to the slit error which results in a small and random shift of the stellar lines with respect to the comparison spectrum lines. The amplitude of the effect depends on the relative sizes of the slit and the seeing profile, on the exposure time, and how accurately the stellar seeing image is centred onto the slit. The shift can be corrected using telluric lines which are very often present in some orders of the stellar spectra. The correction for the slit error is incorporated into the wavelength calibration model since the telluric lines obey the same dispersion relations as the comparison spectrum. A low order bivariate polynomial is added to the above 3D-polynomial and describes the deviation of the telluric line positions from the wavelength solution. A zero-order polynomial would specify a constant shift of all telluric lines with respect to the comparison lines.

Instead of rebinning the spectra into the wavelength scale, a wavelength table is added to the spectra giving the wavelength and its error for each pixel. The heliocentric wavelength correction and possible removal of the stellar radial velocity does a simple transformation of the wavelength table for every pixel. The spectra

are rebinned into the same wavelength scale when the weighted average or the sum of many spectra is calculated. The variances of the rebinned spectrum are calculated taking the variances of the pixel intensities and their wavelength errors into account.

The spectra are normalized to a continuum estimated from a synthetic or mean spectrum using a smoothing spline or polynomials. The clip-and-fit algorithm together with the interval selection feature (masking the pixels) facilitates the continuum approximation.

The cross-correlation facility is a tool to determine the position of a spectrum with respect to a template. Due to the non-linearity of the wavelength scale, the shift between two spectra can be determined in three different scales: pixels, wavelengths, and radial velocities. The weighted linear regression at each offset accounts for the variances of the spectra and their positional errors.

As a matter of fact, the cross-correlation is also used very often internally in many algorithms at different steps of the data reduction. The error of the offset is used in many instances as a weight for subsequent steps or as a significance level when the program should make a decision. Therefore, in the next section the details of the cross-correlation technique are described. In the last section of this Chapter some details of the radial velocity scale transformations are given which are related to the implementation of the cross-correlation method.

4.3 The cross-correlation offset determination

4.3.1 The cross-correlation method

Let $t(x_i)$, $i = 1, 2 \ldots, N$ be a noise-free template spectrum and $p_i \equiv p(x_i)$ a programme spectrum given with the variance for each pixel σ_i^2. The shift δ is determined as the offset at which the match between the spectra is best, i.e. the merit function is minimal:

$$\chi^2(a, b, \delta) = \sum_i \left(\frac{a + b \cdot t(x_i + \delta) - p_i}{\sigma_i} \right)^2, \tag{4.1}$$

where a and b constitute the intensity transformation of the template spectrum $t(x_i + \delta)$ to the programme spectrum p_i at the trial offset δ. The index i is ranging within the overlapping regions of the two spectra for the given δ with possible exclusion of masked features in the two spectra, which implies that the number of used pixels n is also a function of the offset δ. Since the template spectrum is given noise-free, the values of $t(x_i + \delta)$ can be interpolated for the offset equal to any fractional part of the step size. As it is seen from the model, the noisy programme spectrum $p(x_i)$ is not interpolated between pixels.

The above non-linear least-squares fit in general has no unique solution since in the case of stellar spectra the minimization function may consist of several minima at different offsets produced by similar spectral lines. Therefore, the problem must be solved in two steps: the first includes the solution of the linear fit to determine the parameters a and b for every trial offset δ, and the second one is to find the appropriate minimum of the $\chi^2(\delta)$ as a function of one variable.

The solution of the linear problem leads to the following transformation of the minimization function:

$$\chi^2(\delta) = \left(1 - r^2(\delta)\right) \cdot \sum \omega_i (p_i - \bar{p})^2, \tag{4.2}$$

where $\omega_i = 1/\sigma_i^2$ are the weighting factors as the inverse variances of the programme spectrum, r is the cross-correlation coefficient as a function of the offset:

$$r(\delta) = \frac{\sum \omega_i (p_i - \bar{p})(t_i(\delta) - \bar{t}(\delta))}{\sqrt{\sum \omega_i (p_i - \bar{p})^2 \cdot \sum \omega_i (t_i(\delta) - \bar{t}(\delta))^2}} \tag{4.3}$$

and the weighted averages are:

$$\bar{p} = \frac{\sum \omega_i p_i}{\sum \omega_i} \quad \text{and} \quad \bar{t}(\delta) = \frac{\sum \omega_i t_i(\delta)}{\sum \omega_i} \tag{4.4}$$

with the notation $t_i(\delta) \equiv t(x_i + \delta)$ for simplicity.

Since the latter term in Eq. (4.2) is constant, the minimum of the function can be found by choosing the appropriate peak of the cross-correlation function and using a centring algorithm to determine the position of the maximum. The variance of the parameter δ will then be defined as the inverse of the curvature matrix of $\chi^2(\delta)$ times the variance of the linear fit:

$$\sigma_\delta^2 = \frac{\chi^2(\delta)}{n-2} \cdot 2 \left(\frac{d^2\chi^2}{d\delta^2} \right)^{-1}. \tag{4.5}$$

The second derivative of $\chi^2(\delta)$ is

$$\frac{d^2\chi^2}{d\delta^2} = -2 \left[\left(\frac{dr}{d\delta} \right)^2 + r \, \frac{d^2 r}{d\delta^2} \right] \cdot \sum \omega_i (p_i - \bar{p})^2, \tag{4.6}$$

where the first derivative vanishes when the function is at minimum. Therefore

$$\frac{d^2\chi^2}{d\delta^2} = -2r \, \frac{d^2 r}{d\delta^2} \cdot \sum \omega_i (p_i - \bar{p})^2 \tag{4.7}$$

and, finally, replacement of the weighted sum of the residuals from Eq. (4.2) gives:

$$\sigma_\delta^2 = -\left(\frac{d^2 r}{d\delta^2}\right)^{-1} \cdot \frac{1-r^2}{r\,(n-2)}, \tag{4.8}$$

where r is the amplitude of the cross-correlation peak at the offset δ, n is the number of the overlapped pixels of the two spectra at the given offset, and the inverse curvature of the peak can be determined with the selected centring algorithm.

The first component of the above formula describes the accuracy of the offset limited by the width and depth of the line(s): the shallower the line, the flatter the cross-correlation peak, hence, the larger the uncertainty of the offset. The second term describes both random and systematical components of the linear regression between the template and observed spectrum. The error of the centring of the cross-correlation peak and that of the curvature determination are small compared to the terms in Eq. (4.8) and, therefore, are neglected.

4.3.2 The accuracy for Gaussian profiles

Now, let us construct a simple example to gain some insight about the accuracy estimate. Let the program spectrum be a single Gaussian profile

$$p(x_i) = C\left(1 \pm d\exp\left[-\left(\frac{x_i - x_c}{\sigma_{\rm line}}\right)^2\right]\right) \tag{4.9}$$

centred at x_c with the width $\sigma_{\rm line}$, d is the relative line depth (strength), C is the continuum level. The spectrum is sampled with the step size $\Delta\lambda$ over n pixels. Let the normally distributed noise with the variance σ^2 be added to the spectrum $p(x)$. Let the template spectrum be the same profile but noiseless.

The cross-correlation of two Gaussians is equivalent to the convolution of the two profiles which results in a Gaussian shape:

$$r(\delta) = r_0 \exp\left(-\frac{\delta^2}{2\,\sigma_{\rm line}^2}\right), \tag{4.10}$$

which gives the curvature of the cross-correlation function at its maximum

$$\frac{d^2 r}{d\delta^2} = -\frac{r_0}{\sigma_{\rm line}^2}. \tag{4.11}$$

The sum of the weighted ($\omega_i = 1/\sigma^2$) squared deviations of the programme spectrum p_i from the mean $\bar{p}$ is obtained after the integration:

$$\sum \omega_i (p_i - \bar{p})^2 = \sqrt{\frac{\pi}{2}} \cdot \frac{C^2}{\sigma^2} \cdot \frac{d^2\,\sigma_{\rm line}}{\Delta\lambda} \left(1 - \frac{\sqrt{2\pi}\,\sigma_{\rm line}}{n\Delta\lambda} \right). \tag{4.12}$$

Neglecting the ratio in the brackets (if $n\Delta\lambda \gg \sigma_{\rm line}$) and introducing the signal-to-noise ratio in the continuum (SNR=C/σ), the integral reads

$$\sum \omega_i (p_i - \bar{p})^2 = \sqrt{\frac{\pi}{2}} \cdot \frac{d^2\,\sigma_{\rm line}}{\Delta\lambda} \cdot ({\rm SNR})^2. \tag{4.13}$$

The variance term in Eq. (4.5) will be

$$\frac{\chi^2(\delta)}{n-2} = 1 \tag{4.14}$$

in this model, since no systematical difference has been introduced between two equal Gaussians, therefore, the squared sum of weighted residuals $\chi^2(\delta)$ of the linear regression will be exactly equal to the number of degrees of freedom $n-2$. Then, expressing $\sigma_{\rm line}$ by FWHM and putting all terms together we obtain:

$$\sigma_\delta^2 = \sqrt{\frac{1}{2\pi \ln 2}} \cdot \left(\frac{1}{r_0 \cdot {\rm SNR} \cdot d} \right)^2 \Delta\lambda \cdot {\rm FWHM}. \tag{4.15}$$

The constant in front of the equation is about 0.48. The equation derived resembles to ones obtained by other authors (e.g. Brown 1990). The better the sampling interval, the deeper and narrower the line; the higher the signal-to-noise ratio, the better the accuracy of the cross-correlation. It was also derived but omitted here for simplicity, that the inclusion of m similar Gaussians into the model will decrease the variance to σ_δ^2/m accordingly.

4.4 Rebinning into radial velocity scale

The offset in radial velocity scale between two spectral lines depends on the wavelengths of the lines. In order to measure the offset in radial velocities, the spectra in wavelengths have to be rebinned to a scale with a constant step size in velocities according to the Doppler formula:

$$\frac{\Delta v}{c} = \frac{\Delta\lambda}{\lambda} = \Delta \ln \lambda, \tag{4.16}$$

where Δv is the radial velocity difference between two wavelengths separated by $\Delta\lambda$ around wavelength λ, c is the speed of light, and in this linear approximation $\Delta v \ll c$ and $\Delta\lambda \ll \lambda$.

The constant step size in velocities is achieved after the transformation of the wavelength scale to the constant step size in $\ln\lambda$, which results in the definition of the rebinning grid:

$$\ln\lambda_i = \ln\lambda_0 + i \cdot \Delta\ln\lambda \tag{4.17}$$

with λ_0 being the initial wavelength of the spectrum, the index $i = 0, 1, \ldots, n-1$. An ordinary rebinning in wavelengths implies that the difference in wavelengths in the new grid is constant, but in the case of radial velocities, the ratio between wavelengths in the new grid (in the subsequent nodes) must me constant.

It is more convenient than $\ln\lambda$ to have velocity units for describing the pixel positions. One should realize that the possibly high velocities resulting from this transformation do not have any physical meaning; only velocity differences between nearby ($\Delta v \ll c$) features in the same spectrum or between the same features in different spectra indicate the Doppler shift. The velocity scale is merely a reformulation of the commonly used $\ln\lambda$ scale.

One choice of the step size is a predefined velocity step size, the more flexible option is to select an average velocity as follows:

$$\Delta v = c \cdot \Delta\ln\lambda = c \cdot \frac{\ln\lambda_{n-1} - \ln\lambda_0}{n-1} = \frac{c}{n-1} \cdot \ln\frac{\lambda_{n-1}}{\lambda_0}. \tag{4.18}$$

The intensities of the spectrum are integrated

$$\hat{s_i} = \int_{\lambda^-}^{\lambda^+} s(\lambda_i) d\lambda \tag{4.19}$$

within the interval in wavelengths defined as

$$\lambda_i^{\pm} = \lambda_0 \cdot \exp\left[\frac{\Delta v}{c} \cdot (i \pm 0.5)\right]. \tag{4.20}$$

It is convenient to have a grid in the velocity scale common to different spectra. Since the grid is linear, the zero point can be established at the wavelength of a spectral feature λ_c common to a number of spectra. The initial velocity at the wavelength λ_0 of the first pixel of the spectrum and the velocity grid is therefore given by:

$$v_i = c \cdot \ln\frac{\lambda_0}{\lambda_c} + \Delta v \cdot i. \tag{4.21}$$

There is an alternative and intermediate way to transform into radial velocity scale without involving the rebinning procedure. This results in the unequally spaced

spectra with the linear velocity scale, i.e. the distance between two features caused by a radial velocity shift at different wavelengths remains constant. The procedure also involves the wavelength λ_c of a common feature of the spectra. The velocities for each pixel k in the spectrum are calculated according to

$$v_i = c \cdot \ln \frac{\lambda_i}{\lambda_c}. \tag{4.22}$$

The intensities of the spectrum remain unchanged in their pixels until a number of spectra have to be rebinned into the same grid for cross-correlation or arithmetical operations.

Chapter 5

Deconvolution of stellar spectra

5.1 Introduction

The observed stellar spectra are subject to broadening due to various instrumental and physical effects. If the effects are known and can be modeled then the true spectral profile can be recovered. Presence of noise in the spectra makes the problem of restoration ill-posed. The solution of the problem can be found by solving the inverse problem formulated in various ways. In this chapter we consider the restoration of the underlying spectrum and the broadening function. These inverse problems play a key role in the modern methods of the analysis of stellar spectra. The basic applications are highlighted as follows.

Deconvolution of the blurred spectra with the known point spread function (PSF) is the way to increase the spectral resolution and to resolve narrow features. Hereafter we refer to the term of the PSF caused only by the spectrograph, i.e. it is the instrumental profile. Deconvolution with e.g. the known rotational profile would refine the exact position and the structure of the interior of the spectral lines.

Deconvolution of the observed low resolution spectrum with the PSF obtained with a smaller step size (and a higher resolution) results in a spectrum of a higher resolution. The increase factor depends on the sample length. Another way to increase the resolution keeping the sample length fixed is to use a different observing technique known as dithering (Lauer 1999, where it is applied to the WFPC images of the HST) to obtain spectra shifted with respect to each other by a multiple of the pixel size. Such a number of spectra interleaved in the wavelength scale decreases the step size but not the resolution (Gray 1986 uses a dithering device to produce the interleaved spectra to improve the accuracy of the line bisectors).

Deconvolution with the proper PSF will increase the resolution of the observed spectra.

The restoration of the broadening function depends on the template spectrum. Several different cases can be summarized:

1. The template spectrum is of the same kind as the observed one, but obtained with a higher resolution and preferably with a higher signal-to-noise ratio (SNR). One natural choice is to use the solar spectrum obtained with the spectrograph and the FTS solar spectrum (Kurucz et al. 1984). The restoration of the PSF made with these spectra for several spectrographs was described by Valenti et al. (1995), who also used a spectrum of an iodine cell. The restoration is an alternative way to obtain the PSF of the spectrograph instead of its direct measurement with the use of a laser or telluric lines (Griffin 1969). The use of a synthetic spectrum is also possible but increases uncertainty of the restoration due to an additional freedom in the choice of the stellar parameters and the broadening function.

2. The template spectrum consists of a number of delta functions with their positions and intensities corresponding to the spectral line list. The restoration of the broadening function gives a mean spectral profile of the observed spectrum which is de-blended from the delta functions but includes the PSF. The use of many spectral lines, which is possible with échelle spectra, can increase the accuracy of the restored stellar profile. The use of the delta-spectrum convolved with the known PSF as a template in the deconvolution results in a mean profile free of the instrumental effects. The method has become known as the least-squares deconvolution (LSD) and was implemented by Donati et al. (1997) and Collier Cameron (1999).

3. The template is calculated by the integration of the local line profiles over the stellar disk weighted with a limb-darkening function. In the case of a rotational broadening mechanism, the restored broadening function will represent the true rotational profile, including effects like asymmetric macroturbulence. This true profile can then be used to deblend lines which cannot be modeled reliably. The deconvolved profile is free from the assumptions made in modeling the rotational profile (Gray 1992, Ch.17).

4. Restoration of the blended profiles of binary systems as a function of the orbital phase involves a template spectrum of a single star. The method was successfully used by Rucinski (1999) to resolve the double components of the observed profile. It was demonstrated that the deconvolution has a certain advantage as compared to the widely used cross-correlation technique.

One related problem, where many of the same techniques used in deconvolution problems can also be applied, is the restoration of the distribution of stellar parameters across the star's surface. A range of techniques has been developed, known in

general as the Doppler imaging technique, to solve the ill-posed inversion problem to restore the stellar surface from a time series of one-dimensional stellar spectra (Vogt et al. 1987, Piskunov et al. 1990, Collier Cameron 1992, and Berdyugina 1998).

5.2 Formulation of the problem

The convolution of the known true spectrum $t(x)$ with the unknown kernel $p(x)$, which is the instrumental PSF or a broadening function, results for the continuous case in the blurred function $s(x)$ co-added with the known function of the random noise $\epsilon(x)$

$$s(x) = \int_{-\infty}^{+\infty} t(x-u)\, p(u) du + \epsilon(x) \tag{5.1}$$

which is the first problem: the reconstruction of the unknown function $p(x)$. The convolution of the unknown true spectrum $t(x)$ with the known kernel $p(x)$

$$s(x) = \int_{-\infty}^{+\infty} p(x-u)\, t(u) du + \epsilon(x) \tag{5.2}$$

is the second problem: the reconstruction of the true spectrum $t(x)$.

5.3 The sampling matrix

The convolution process becomes discrete once it is sampled and integrated (recorded) with the CCD. For simplicity, let the CCD pixels be adjacent (no gaps) and have a flat response within each pixel (Jorden et al. 1993 showed that this assumption is not very accurate). Furthermore, assume that either $t(u)$ or $p(u)$ are known on a sampling grid finer than the actual CCD pixel size. To match the spectra, we need to resample the convolved function to the pixel size of the observed spectrum.

The length of the restored function depends on the sampling rate, an *integer* multiple r of the sampling interval of $t(u)$ or $p(u)$ which equals the sampling interval of $s(x)$:

$$r = \frac{\Delta x}{\Delta u}. \tag{5.3}$$

The equal step size of the observed spectrum remains unchanged but the template (profile) is rebinned with the new step size $\Delta x/r$ according to the following scheme:

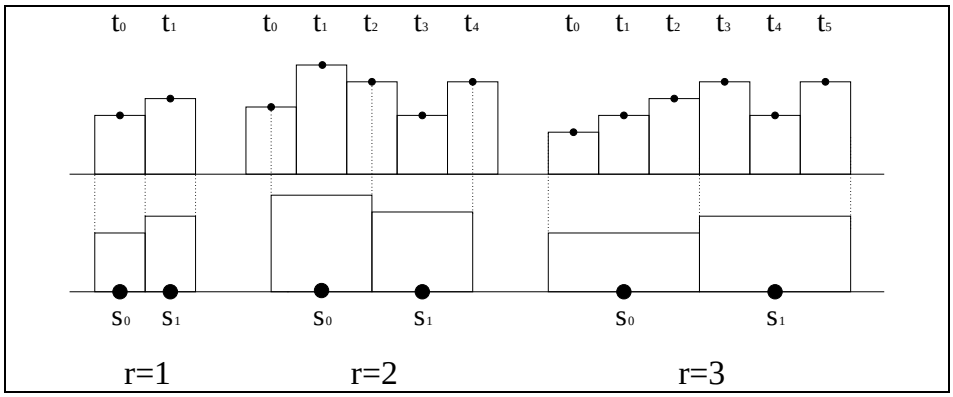

The choice for the configuration of the template pixels for even r is more complicated than e.g. Valenti et al. (1995); it is employed in order to minimize the loss of resolution. Therefore, we use a more sophisticated scheme where the centre of one of the template pixels coincides with that of the observed pixel.

The integration of a single pixel is described by the sampling row-vector $\mathbf{h}_{1\times q}$ so that[1]

$$s_i = \sum_{k=0}^{q-1} h_k \, t_{i\cdot r+k} \tag{5.4}$$

and the number of pixels involved in the integration over one pixel in the observed spectrum is

$$q = \frac{r}{2} \cdot 2 + 1, \tag{5.5}$$

where the ratio is an *integer* division. The normalized elements of the sampling vector are

$$\mathbf{h}_{1\times q} = [h_i] = \frac{1}{r} \begin{cases} (0.5 \quad 1 \quad \ldots \quad 1 \quad 0.5), & r \text{ is even}, \\ (1 \quad 1 \quad \ldots \quad 1 \quad 1), & r \text{ is odd}. \end{cases} \tag{5.6}$$

The resampling of the whole spectrum $\mathbf{t}_{l\times 1}$ into $\mathbf{s}_{n\times 1}$ is described by the product with the sampling matrix $\mathbf{H}_{n\times l}$:

$$\mathbf{s}_{n\times 1} = \mathbf{H}_{n\times l} \cdot \mathbf{t}_{l\times 1} \tag{5.7}$$

[1] In this Chapter indices run from zero.

where the elements of the matrix are the sampling vectors shifted row-wise by the sampling rate r and given by:

$$\mathbf{H}_{n\times l} = [H_{i,ir+k}] = h_k, \qquad k = 0, 1, \ldots q-1, \quad i = 0, 1, \ldots n-1. \tag{5.8}$$

The number of pixels of the template spectrum $\mathbf{t}_{l\times 1}$ satisfies the following condition:

$$l = \begin{cases} qn, & r \text{ is odd}, \\ (q-1)n+1, & r \text{ is even}. \end{cases} \tag{5.9}$$

The following is the illustration of the sampling matrix with $r = 3$, $n = 2$, $l = 6$:

$$\begin{pmatrix} h_0 & h_1 & h_2 & 0 & 0 & 0 \\ 0 & 0 & 0 & h_0 & h_1 & h_2 \end{pmatrix} \begin{pmatrix} t_0 \\ t_1 \\ t_2 \\ t_3 \\ t_4 \\ t_5 \end{pmatrix} = \begin{pmatrix} s_0 \\ s_1 \end{pmatrix}.$$

5.4 Deconvolution of the PSF

The formation of the observed spectrum with the known true or expected spectrum in the discrete case is given by:

$$\mathbf{s}_{n\times 1} = \mathbf{H}_{n\times l} \cdot \mathbf{T}_{l\times m} \cdot \mathbf{p}_{m\times 1} + \boldsymbol{\epsilon}_{n\times 1}, \tag{5.10}$$

where $\mathbf{s}$ is the observed spectrum and $\boldsymbol{\epsilon}$ is the vector of its random noise, $\mathbf{H}$ is the sampling matrix, and $\mathbf{T}$ is the offset matrix of the template spectrum $\mathbf{t}_{l\times 1}$. Its length is defined by the sampling matrix

$$l = \begin{cases} qn, & r \text{ is odd}, \\ (q-1)n+1, & r \text{ is even}, \end{cases} \tag{5.11}$$

and $\mathbf{p}$ is the unknown PSF of length m. The *odd* number of pixels m can be less than that of the template spectrum and should be selected from the interval $q \ll m \leq l$. The elements of the matrix $\mathbf{T}$ are constructed by shifting the template spectrum $\mathbf{t}_{l\times 1}$ and the elements are:

$$\mathbf{T}_{l\times m} = [T_{ik}] = \begin{cases} t_{i-m/2+k}, & 0 \le i - m/2 + k < l \\ 0, & \text{otherwise.} \end{cases} \tag{5.12}$$

The following example illustrates the contents of the matrices for $r = 2$, $n = 3$, $m = 5$, and $l = 7$:

$$\begin{pmatrix} h_0 & h_1 & h_2 & 0 & 0 & 0 & 0 \\ 0 & 0 & h_0 & h_1 & h_2 & 0 & 0 \\ 0 & 0 & 0 & 0 & h_0 & h_1 & h_2 \end{pmatrix} \begin{pmatrix} 0 & 0 & t_0 & t_1 & t_2 \\ 0 & t_0 & t_1 & t_2 & t_3 \\ t_0 & t_1 & t_2 & t_3 & t_4 \\ t_1 & t_2 & t_3 & t_4 & t_5 \\ t_2 & t_3 & t_4 & t_5 & t_6 \\ t_3 & t_4 & t_5 & t_6 & 0 \\ t_4 & t_5 & t_6 & 0 & 0 \end{pmatrix} \begin{pmatrix} p_0 \\ p_1 \\ p_2 \\ p_3 \\ p_4 \end{pmatrix} = \begin{pmatrix} s_0 \\ s_1 \\ s_2 \end{pmatrix}.$$

The design matrix of the convolution model is the product

$$\mathbf{A}_{n\times m} = \mathbf{H}_{n\times l} \cdot \mathbf{T}_{l\times m} \tag{5.13}$$

and the PSF profile can be found by solving the least-squares problem:

$$\mathbf{s}_{n\times 1} = \mathbf{A}_{n\times m} \cdot \mathbf{p}_{m\times 1} + \boldsymbol{\epsilon}_{n\times 1}. \tag{5.14}$$

The obtained system of equations should be well conditioned if $n \gg m$ and can be solved with the standard methods of least-squares with the use of e.g. the Cholesky decomposition for the inversion. Since, in general for the applications described, $\mathbf{A}$ is not well-behaved, we shall proceed with the ill-posed solutions as described in Sec. 5.6.

5.5 Deconvolution of the spectrum

The formation of the observed spectrum convolved with the known PSF in the discrete case is given by:

$$\mathbf{s}_{n\times 1} = \mathbf{H}_{n\times m} \cdot \mathbf{P}_{m\times m} \cdot \mathbf{t}_{m\times 1} + \boldsymbol{\epsilon}_{n\times 1}, \tag{5.15}$$

where $\mathbf{s}$ is the observed spectrum of length n and $\boldsymbol{\epsilon}$ is the vector of its random noise, $\mathbf{H}$ is the sampling matrix, $\mathbf{P}$ is the offset matrix of the known PSF vector $\mathbf{p}_{l\times 1}$. The length l is an *odd* number, $\mathbf{t}$ is the unknown deconvolved spectrum and its length is defined by the sampling matrix:

$$m = \begin{cases} qn, & r \text{ is odd}, \\ (q-1)n+1, & r \text{ is even}. \end{cases} \tag{5.16}$$

The elements of the matrix $\mathbf{P}$ are constructed by shifting the elements of the PSF vector $\mathbf{p}$:

$$\mathbf{P}_{m\times m} = [P_{ik}] = \begin{cases} p_{l/2+k-i} \,/\, \sum_k p_k, & 0 \le l/2+k-i < l \\ 0, & \text{otherwise} \end{cases} \tag{5.17}$$

and the elements in each row are normalized to their sum in order to preserve the intensities of the deconvolved spectrum at its edges.

The following example illustrates the contents of the matrices for $r = 2$, $n = 3$, $m = 7$, $l = 5$, not showing the profile normalization:

$$\begin{pmatrix} h_0 & h_1 & h_2 & 0 & 0 & 0 & 0 \\ 0 & 0 & h_0 & h_1 & h_2 & 0 & 0 \\ 0 & 0 & 0 & 0 & h_0 & h_1 & h_2 \end{pmatrix} \begin{pmatrix} p_2 & p_3 & p_4 & 0 & 0 & 0 & 0 \\ p_1 & p_2 & p_3 & p_4 & 0 & 0 & 0 \\ p_0 & p_1 & p_2 & p_3 & p_4 & 0 & 0 \\ 0 & p_0 & p_1 & p_2 & p_3 & p_4 & 0 \\ 0 & 0 & p_0 & p_1 & p_2 & p_3 & p_4 \\ 0 & 0 & 0 & p_0 & p_1 & p_2 & p_3 \\ 0 & 0 & 0 & 0 & p_0 & p_1 & p_2 \end{pmatrix} \begin{pmatrix} t_0 \\ t_1 \\ t_2 \\ t_3 \\ t_4 \\ t_5 \\ t_6 \end{pmatrix} = \begin{pmatrix} s_0 \\ s_1 \\ s_2 \end{pmatrix}$$

The design matrix of the convolution model is the product

$$\mathbf{A}_{n\times m} = \mathbf{H}_{n\times m} \cdot \mathbf{P}_{m\times m} \tag{5.18}$$

and the deconvolved spectrum $\mathbf{t}$ can be found by solving the inverse problem:

$$\mathbf{s}_{n\times 1} = \mathbf{A}_{n\times m} \cdot \mathbf{t}_{m\times 1} + \boldsymbol{\epsilon}_{n\times 1}. \tag{5.19}$$

The matrix $\mathbf{A}$ is an r-times underdetermined system of linear equations: no unique solution exists unless we use the solution of ill-posed problems described below. The solution to the problem is extensively described in Sec. 5.6.

5.6 The principal components regression

Modern methods of matrix factorizations give a new treatment of the linear least-squares problem (Watkins 1991, Stoer 1993, Golub & van Loan 1989). The classical method of least-squares is a perfect way to solve the problem, except in the case

when the matrix of normal equations $\mathbf{A}'\mathbf{W}\mathbf{A}$ is close to singular.[2] This may happen when the number of free parameters exceeds the number of observations, or/and when the parameters of the model chosen to describe the observed process are heavily correlated with each other. This results in a linear dependence of rows of the design matrix $\mathbf{A}$, reduction of its rank, and singularity of the inversion or plurality of the solution.

The problem can be solved in a different way based on the concept of orthogonal decomposition of the model which we use to describe the observations. This results in a new system of equations, which uses orthogonal functions (i.e. a new orthogonal design matrix), and in a new set of unknown parameters, known as the *principal components*, which are independent of and uncorrelated with each other. The least-squares solution of the orthogonal system of equations to the observations gives the unknown principal components parameters.

The independence of the parameters will allow us to test the statistical significance of the terms in a simple manner to decide which of them can be eliminated from the fit. The vector from which the insignificant components have been eliminated comprises the *reduced principal components*. The original set of unknowns is then obtained by back composition of the truncated set of the independent parameters with a matrix which describes the linear dependence of the original parameters. Due to the cancellation of the insignificant principal components the solution in terms of the original unknown parameters is not unique, and forms a family of parameter sets. The size of the family can be reduced by imposing additional linear constraints on the problem.

One can see a similarity between the spectral decomposition by Fourier transformation and the above orthogonal functions. The difference is that the Fourier harmonics are the trigonometric functions while here, the orthogonal functions are not specified, except that they satisfy the orthogonality condition. The trigonometric functions are orthogonal only for continuous data; they are in general not orthogonal on a given data window; the construction of the principal components ensures that their associated basis functions are orthogonal given the observations. The same approach is used when a set of orthogonal polynomials is constructed.

The solutions to ill-conditioned and singular linear systems was described and discussed in many papers and monographs, some of them were used here: Hocking (1976), who reviewed the solutions based on the principal components and rigid estimators, Jackson (1991), Hansen (1997), and Dunteman (1989). The principal components solution is similar to the truncated least-squares (TLS) developed by Golub & van Loan (1980) for solving overdetermined systems of linear equations, who have also extended it to the total TLS approach where the variances of the variables of the model are incorporated into the minimization functional. Neumaier (1998) discussed the problem in terms of the truncated singular value decomposition (SVD), together with many other aspects of the inversion problems.

[2] $\mathbf{A}$ is the design matrix, $\mathbf{A}'$ is its transposed, and $\mathbf{W}$ is the weight matrix.

Let the linear model, describing an observed process, be given in the form:

$$\mathbf{y} = \mathbf{A}\mathbf{p} + \boldsymbol{\epsilon}, \tag{5.20}$$

where $\mathbf{y}_{n\times 1}$ is the observations and $\boldsymbol{\epsilon}_{n\times 1}$ is the vector of their random noise, $\mathbf{A}_{n\times m}$ is the design matrix, and $\mathbf{p}_{m\times 1}$ is the vector of unknown parameters or underlying function. The number of unknown parameters m could be less or greater than the number of observations n. The noise in the observations is characterized by the positively definite and symmetric dispersion matrix $\mathcal{E}(\boldsymbol{\epsilon}'\boldsymbol{\epsilon}) = \mathcal{D}(\mathbf{y})$.

In order to satisfy the orthogonal condition of the decomposition of $\mathbf{A}$, we need to decompose the variance matrix into two matrices. If the variance matrix is not diagonal, the Cholesky factorization results in a lower triangular matrix $\mathbf{S}$:

$$\mathcal{D}(\mathbf{y}) = \sigma^2\mathbf{W}^{-1} = \sigma^2\mathbf{S}\mathbf{S}', \tag{5.21}$$

where it is assumed that the dispersions are known up to some scaling factor σ^2. To obtain the weighting matrix we need to invert the dispersion matrix:

$$\mathbf{W} = \sigma^2\mathcal{D}^{-1}(\mathbf{y}) = (\mathbf{S}^{-1})'(\mathbf{S}^{-1}) = \mathbf{V}'\mathbf{V}. \tag{5.22}$$

The inversion of the lower triangular $\mathbf{S}$ is straightforward (Press et al. 1992). In the case of uncorrelated noise in the observations, the diagonal elements of $\mathbf{V}$ are simply the inverse of the standard deviations: $\mathbf{V} = [\sigma_{ii}^{-1}]$.

The orthogonal basis of the matrix $(\mathbf{VA})_{n\times m}$ can be obtained with the QR factorization (Golub & van Loan, 1989) or with the SVD (the algorithm in Press et al. 1992 is based on Golub & van Loan, 1989). The latter factorization is more suitable for the current problem and decomposes the matrix into three components:

$$\mathbf{VA} = \mathbf{BCD}', \tag{5.23}$$

where the matrix $\mathbf{B}_{n\times m}$ contains the orthonormal *basis* vectors ($\mathbf{B}'\mathbf{B} = \mathbf{I}_{m\times m}$, but $\mathbf{B}\mathbf{B}' \neq \mathbf{I}$), the diagonal matrix $\mathbf{C}_{m\times m}$ contains the *singular* values of the decomposition, and the orthonormal $\mathbf{D}_{m\times m}$ is the linear *dependence* matrix ($\mathbf{D}'\mathbf{D} = \mathbf{D}\mathbf{D}' = \mathbf{I}_{m\times m}$).

The elements of $\mathbf{C} = \mathrm{diag}(c_0, c_1, \ldots, c_{m-1})$ are $c_0 \geq c_1 \geq \ldots \geq c_{m-1} \geq 0$ and the rank of $\mathbf{VA}$ equals the number of non-zero singular elements.

The columns of $\mathbf{B}$ are the eigenvectors and $\mathbf{C}^2$ are the eigenvalues of

$$(\mathbf{VA})(\mathbf{VA})' = \mathbf{BC}^2\mathbf{B}'$$

The columns of $\mathbf{D}$ are the eigenvectors and $\mathbf{C}^2$ are the eigenvalues of

$$(\mathbf{VA})'(\mathbf{VA}) = \mathbf{A}'\mathbf{W}\mathbf{A} = \mathbf{DC}^2\mathbf{D}'$$

The approximated function becomes

$$\tilde{\mathbf{y}} = \mathbf{A}\mathbf{p} = \mathbf{V}^{-1}\mathbf{B}\mathbf{C} \cdot \mathbf{D}'\mathbf{p} = \mathbf{T} \cdot \mathbf{q} \tag{5.24}$$

i.e. expressed in the new terms

$$\mathbf{T} = \mathbf{V}^{-1}\mathbf{B}\mathbf{C} \qquad \text{and} \qquad \mathbf{q} = \mathbf{D}'\mathbf{p} \tag{5.25}$$

of the new design matrix $\mathbf{T}$ which is orthogonal with the weights of observations $\mathbf{T}'\mathbf{W}\mathbf{T} = \mathbf{C}'\mathbf{C} = \mathbf{C}^2$, and of the vector $\mathbf{q}$ of uncorrelated unknowns, known as the principal components of the vector $\mathbf{p}$.

Denoting the vector of the residuals of the fit as $\mathbf{r} = \mathbf{y} - \tilde{\mathbf{y}}$, the minimization functional becomes

$$\sigma^2\chi^2(\mathbf{q}) = \mathbf{r}'\mathbf{W}\mathbf{r} = (\mathbf{y} - \mathbf{T}\mathbf{q})'\,\mathbf{W}(\mathbf{y} - \mathbf{T}\mathbf{q}) \tag{5.26}$$

The minimum of the norm $(\mathbf{A}\mathbf{x} - \mathbf{y})'(\mathbf{A}\mathbf{x} - \mathbf{y})$ is at $\mathbf{x}$ obtained from the normal equations $\mathbf{A}'\mathbf{A}\mathbf{x} = \mathbf{A}'\mathbf{y}$.

The system of normal equations is

$$\mathbf{T}'\mathbf{W}\mathbf{T}\,\mathbf{q} = \mathbf{T}'\mathbf{W}\mathbf{y} \tag{5.27}$$

which then becomes

$$\mathbf{C}^2\mathbf{q} = \mathbf{C}\mathbf{B}'\mathbf{V}\mathbf{y} \tag{5.28}$$

and readily gives the solution for the principal components

$$\mathbf{q} = \mathbf{C}^{-1}\mathbf{B}'\mathbf{V}\mathbf{y}. \tag{5.29}$$

The original parameters, or the underlying function, is a linear combination of the principal components:

$$\mathbf{p} = \mathbf{D}\mathbf{q}. \tag{5.30}$$

The diagonal of the dispersion matrix of the principal components is:

$$\mathcal{D}\,(\mathbf{q}) = \mathbf{C}^{-1}\mathbf{B}'\mathbf{V} \cdot \mathcal{D}\,(\mathbf{y}) \cdot \mathbf{V}'\mathbf{B}\mathbf{C}^{-1} = \sigma^2\,\mathbf{C}^{-2} \tag{5.31}$$

and the dispersion matrix of the original parameters is

$$\mathcal{D}\,(\mathbf{p}) = \mathbf{D}\,\mathcal{D}\,(\mathbf{q})\,\mathbf{D}' = \sigma^2\mathbf{D}\mathbf{C}^{-2}\mathbf{D}'. \tag{5.32}$$

And finally, the approximated function is

$$\tilde{\mathbf{y}} = \mathbf{A}\mathbf{p} = \mathbf{T}\mathbf{q} = \mathbf{V}^{-1}\mathbf{B}\mathbf{C}\mathbf{q}. \tag{5.33}$$

The dispersion matrix of the fit is

$$\mathcal{D}(\tilde{\mathbf{y}}) = \mathbf{T}\mathcal{D}(\mathbf{q})\ \mathbf{T}' = \sigma^2(\mathbf{V}^{-1}\mathbf{B}) \cdot (\mathbf{V}^{-1}\mathbf{B})' = \sigma^2\mathbf{S}\mathbf{B}\mathbf{B}'\mathbf{S}', \tag{5.34}$$

where $\mathbf{V}^{-1} = \mathbf{S}$ as it was introduced for the standard deviations of the additive random noise of the observations in (5.21) and (5.22).

5.7 Selection of the principal components

To find a stable solution to the problem, we have to eliminate the $m - k$ smallest principal components in $\mathbf{q}$ which have the largest variances and contribute noisy components to $\mathbf{p}$. A number of tests can be used which results in a vector of the *reduced principal components* $\tilde{\mathbf{q}}$ with the last $m - k$ terms are set to zero. This causes also the corresponding terms of the singular values in $\mathbf{C}$ to become zero.

5.7.1 The F-test

The squared sum of the residuals of the fit (RSS) is

$$\mathbf{r}'\mathbf{W}\mathbf{r} = \mathbf{y}'\mathbf{W}\mathbf{y} - \sigma^2\mathbf{q}'\mathcal{D}^{-1}(\mathbf{q})\,\mathbf{q} = \mathbf{y}'\mathbf{W}\mathbf{y} - \mathbf{q}'\mathbf{C}^2\mathbf{q}, \tag{5.35}$$

which is the series of the terms

$$\mathrm{RSS}_m = \mathbf{y}'\mathbf{W}\mathbf{y} - \sum_{k=0}^{m-1} q_k^2 c_k^2 = \sum_{i=0}^{n-1} \omega_i y_i^2 - \sum_{k=0}^{m-1} q_k^2 c_k^2 \tag{5.36}$$

and obeys the recurrence relation:

$$\mathrm{RSS}_k = \mathrm{RSS}_{k-1} - q_k^2 c_k^2. \tag{5.37}$$

Since the principal components $\mathbf{q}$ are linearly (hence, statistically) independent, each of them can be tested for its statistical significance in the fit.

A standard F-test can be applied to the principal components by evaluating the change of the RSS as a function of the index k. The null hypothesis $H : q_k = 0$ is tested against its alternative $H_1 : q_k \neq 0$ to check the significance of q_k. If the hypothesis is true, then it follows that $\mathrm{RSS}^H = \mathrm{RSS}_{k-1}$, and the F statistics is

$$F_k = \frac{\mathrm{RSS}_{k-1} - \mathrm{RSS}_k}{\mathrm{RSS}_k/(n-k)} = \frac{q_k^2 c_k^2}{\mathrm{RSS}_k/(n-k)}. \tag{5.38}$$

The hypothesis is accepted if the probability for F_k being as small as it is obtained,

$$P(F > F_k) = Q(F_k, 1, n-k) > 1 - \alpha, \tag{5.39}$$

is higher than some level given by the significance of the fit α which is e.g. 95%. If the hypothesis H is accepted, then the element k is considered insignificant and all subsequent $m - k$ components are set to zero. In many practical cases, the statistics F may show a wiggly or noisy behaviour superimposed on the obvious decaying trend as the index k increases. Therefore, a careful analysis based on several consecutive components is needed to decide where it crosses the significance level.

5.7.2 Goodness of the fit

The reduced χ^2 of the minimization functional is a function of the number k of the principal components (χ^2 is also the correction coefficient for the sample variance σ^2):

$$\chi^2_{n-k} = \sigma^2 = \frac{\mathrm{RSS}_k}{n-k}, \tag{5.40}$$

where the index $k = 0, 1 \ldots r$ and $r = \mathrm{rank}(\mathbf{VA})$ is a number of the non-zero singular values $r \leq \min(n, m)$. If the variances of the observations are known exactly ($\sigma^2 = 1$), then the number of the principal components can be selected when χ^2_{n-k} as a function of k descends to the unity level, or any other pre-defined level if the variances are not exactly known.

A visual inspection of the plot of χ^2_{n-k} as a function of the index k is also useful for the subjective definition of the number of components at some kink or sudden drop of the function.

5.7.3 Analysis of variance

As it was shown, the sum of the diagonal elements of the dispersion matrix of the original parameters equals the total sum of variances of the principal components:

$$\mathrm{tr}\mathcal{D}\,(\mathbf{p}) = \mathrm{tr}\mathcal{D}\,(\mathbf{q}) = \mathrm{tr}\mathbf{C}^{-2} \tag{5.41}$$

i.e. this defines the third stopping criterion to select the number of components for which the sum of variances is less than a predefined threshold for the maximally

allowed sum of variances of the original parameters. The criterion described by Kendall (1975) is based on the analysis of the sum of the minimal singular values $\mathbf{C}$ which obeys the χ^2 distribution.

5.8 The constrained principal components solution

The solution to the constrained linear least-squares problem is detailed in Ilyin (2000):

$$\begin{aligned} \mathbf{y} &= \mathbf{A}\mathbf{p} + \boldsymbol{\epsilon} \qquad \text{subject to:} \qquad \mathbf{G}\mathbf{p} \geq \mathbf{c} \\ \mathbf{y} &= \mathbf{A}\mathbf{p} + \boldsymbol{\epsilon} \qquad \text{subject to:} \qquad \mathbf{G}\mathbf{p} \leq \mathbf{c}, \end{aligned} \tag{5.42}$$

where $\mathbf{G}_{l\times m}$ is the linear condition matrix, $\mathbf{c}_{l\times 1}$ is the vector of constants constraining the solution $\mathbf{p}_{m\times 1}$, and the number of the constraints $l \leq m$.

The use of the principal components does not change essentially in the solution, although, the form of the Lagrangian solution is slightly modified:

$$\mathbf{p} = \tilde{\mathbf{p}} - \left(\mathbf{D}\mathbf{C}^{-2}\mathbf{D}'\right)\mathbf{G}' \cdot \left(\mathbf{G}\left(\mathbf{D}\mathbf{C}^{-2}\mathbf{D}'\right)\mathbf{G}'\right)^{-1} \cdot \left(\mathbf{G}\tilde{\mathbf{p}} - \mathbf{c}\right), \tag{5.43}$$

where $\tilde{\mathbf{p}} = \mathbf{D}\tilde{\mathbf{q}}$ is the unconstrained reduced principal components solution.

As an example it is demonstrated how it works in one particular case often met in practice when we need to find the solution whose sum is equal to some predefined number

$$\sum_{k=0}^{m-1} p_k = c, \tag{5.44}$$

or, in the other words, the solution is normalized. The matrix $\mathbf{G}_{1\times m} = (1, 1, \ldots 1)$ is a unity row, and the constant sum is $\mathbf{c}_{1\times 1} = c$. Denoting the elements of the dispersion matrix $\mathcal{D}(\mathbf{p})\,\sigma^{-2} = \mathbf{D}\mathbf{C}^{-2}\mathbf{D}' = [\sigma_{ik}^2]$, we form a vector

$$\mathbf{v}_{m\times 1} = [v_i] = \sum_{k=0}^{m-1} \sigma_{ik}^2, \tag{5.45}$$

i.e. the sums of the dispersions in each row. Then the elements of the vector of the constraint solution is

$$p_i = \tilde{p}_i - \frac{v_i}{\sum v_k} \cdot (\sum \tilde{p}_k - c), \tag{5.46}$$

which shows that the difference between the obtained and expected sums is applied via the multiple correlation coefficient to correct the solution. One can also see that in the constrained solution $\sum p_i = c$.

5.9 Linear regularization methods

The principal components analysis is, in fact, a particular method of a more general class of minimization problems known as the regularization methods of the inverse problem.

The orthogonal decomposition of the design matrix, described in the previous sections, is equivalent to spectral decomposition of the observed process. The set of orthogonal functions is the set of discrete spatial harmonics, which describe the data, and comprises the columns of the matrix $\mathbf{T}$ and the principal components $\mathbf{q}$ are interpreted as their amplitudes. Selection of the reduced set of the components acts as a spatial filter which is a trade-off between the amplitude of the smallest spatial harmonics and the noise. Generally speaking, such a compromise can be established in many inverse problems where the amplitude of the smallest spatial harmonic is well distinguished from the low level noise, i.e. it works very well for the broad features in a spectrum with high signal-to-noise ratio. For a lower signal-to-noise the principal components cannot distinguish between the harmonics and the random noise, hence, they tend to pick noisy features of the solution (one possible remedy to the problem is to obtain these harmonics with a higher accuracy by extending the length of the data sample, i.e. use of many spectra instead of one for deconvolution, for example). This is the insufficiency of the method and leads to the addition of external conditions which can control, e.g. the shape of the solution. The additional conditions are invoked into the minimization functional which controls the shape of the solution and the strength of this control is attributed to a regularization parameter (a Lagrangian multiplier).

5.10 The standard formulation

In brief, the regularization solution to the underdetermined least-squares problem ($n < m$) can be obtained as follows (Craig & Brown, 1986). Find the solution $\mathbf{p}$ which minimizes the functional of the modified least-squares, or ill-posed problem:

$$\chi^2(\mathbf{p}) = \frac{1}{\sigma^2}\,\mathbf{r}'\mathbf{W}\mathbf{r} + \alpha\,\mathbf{p}'\mathbf{R}\mathbf{p} \tag{5.47}$$

where the residuals are $\mathbf{r} = \mathbf{y} - \mathbf{Ap}$, the regularization parameter is $\alpha > 0$, and $\mathbf{R}$ is a symmetric and positively definite regularization matrix which controls the solution depending on the definition of the matrix. The equation of the minimum of the functional $\partial\chi^2(\mathbf{p})/\partial\mathbf{p} = 0$ is

$$\mathbf{A'WA\,p} - \mathbf{A'Wy} + \lambda\,\mathbf{Rp} = 0 \tag{5.48}$$

where $\lambda = \frac{1}{2}\alpha\sigma^2$. The solution is

$$\mathbf{p} = (\mathbf{A'WA} + \lambda\,\mathbf{R})^{-1} \cdot \mathbf{A'Wy} \tag{5.49}$$

The standard methods to obtain the solution of the regularized inverse problems is a normal matrix inversion (Press et al. 1992). The LU or Cholesky decomposition can be used for the inversion since the matrix is not singular due to the presence of the non-zero regularization matrix $\mathbf{R}$.

Several types of the regularization matrices can be used. The simplest is the zeroth order regularization matrix $\mathbf{R} = \mathbf{I}$, i.e. the product $\mathbf{p'Rp} = \mathbf{p'p}$ is the minimization of the sum of squares of the solution. The first, second, etc. order regularization matrices are minimizing the total square of the first, second, etc. derivatives of the solution, $\mathbf{R} = \mathbf{H}$, where $\mathbf{H} = \mathbf{H_1'H_1}$ or $\mathbf{H} = \mathbf{H_2'H_2}$. The matrices $\mathbf{H_1}$ and $\mathbf{H_2}$ are called the difference matrices and are given in Press et el. (1992). For completeness, we have them also here.

The first difference matrix has the following elements:

$$(\mathbf{H_1})_{(m-1)\times m} = \begin{pmatrix} -1 & 1 & & & & 0 \\ & -1 & 1 & & & \\ & & \cdots & & & \\ & & & -1 & 1 & \\ 0 & & & & -1 & 1 \end{pmatrix} \tag{5.50}$$

and its quadratic form is a three band-diagonal matrix:

$$(\mathbf{H_1'H_1})_{m\times m} = \begin{pmatrix} 1 & -1 & & & & & & 0 \\ -1 & 2 & -1 & & & & & \\ & -1 & 2 & -1 & & & & \\ & & \cdots & \cdots & & & & \\ & & & -1 & 2 & -1 & & \\ & & & & -1 & 2 & -1 & \\ 0 & & & & & -1 & 1 & \end{pmatrix} \tag{5.51}$$

The second difference matrix has the elements:

$$(\mathbf{H_2})_{(m-1)\times m} = \begin{pmatrix} -1 & 2 & -1 & & & & 0 \\ & -1 & 2 & -1 & & & \\ & & & \cdots & & & \\ & & & -1 & 2 & -1 & \\ 0 & & & & -1 & 2 & -1 \end{pmatrix} \tag{5.52}$$

and its quadratic form is a five band-diagonal matrix:

$$(\mathbf{H_2'H_2})_{m\times m} = \begin{pmatrix} 1 & -2 & 1 & & & & & 0 \\ -2 & 5 & -4 & 1 & & & & \\ 1 & -4 & 6 & -4 & 1 & & & \\ & 1 & -4 & 6 & -4 & 1 & & \\ & & & \cdots & \cdots & & & \\ & & 1 & -4 & 6 & -4 & 1 & \\ & & & 1 & -4 & 6 & -4 & 1 \\ & & & & 1 & -4 & 5 & -2 \\ 0 & & & & & 1 & -2 & 1 \end{pmatrix} \tag{5.53}$$

5.11 Regularized principal components solution

The regularization method was initially developed to solve the problem of the matrix inversion in ill-posed problems by means of biasing of its diagonal with a small amount of positive additive to improve the matrix condition number and therefore to avoid its singularity during the inversion.

Similarly, the singularity in the inversion is avoided when the solution is obtained with the principal components where the last $m - k$ presumably small singular values are eliminated or truncated according to the selected stopping criteria. Hence, the reduced principal components can be formulated as the solution to the minimization problem:

$$\chi^2(\mathbf{q}) = \frac{1}{\sigma^2}\,\mathbf{r'Wr} \quad \text{subject to:} \quad \mathbf{q}_i = 0 \quad \text{for} \quad i = k, k+1, \ldots, m-1 \tag{5.54}$$

i.e. it acts as a uniform cut-off filter to the vector $\mathbf{q}$. The regularization of singular linear systems stabilizes the solution by controlling its smoothness, i.e. it has filtering properties.

The solution $\mathbf{p}$ of a singular linear system was expressed in terms of the orthogonal decomposition of the design matrix. Therefore, we can also formulate and solve the regularization problem in terms of the principal components. It has also an advantage that once the principal components solution is obtained, it can be further improved, in terms of smoothness, by means of the regularization. The use

of different regularization matrices and various regularization functionals allows to control the smoothness and the shape of the principal components in a number of different ways. This results in a number of solutions for the original parameters, and the choice of the correct solution has to be done from the specific formulation of the minimization problem.

The regularization problem can be formulated as follows: find the solution $\mathbf{q}$ which minimizes the functional

$$\chi^2(\mathbf{q}) = \frac{1}{\sigma^2}\,\mathbf{r}'\mathbf{W}\mathbf{r} + \alpha\,\mathbf{q}'\mathbf{R}\mathbf{q}, \tag{5.55}$$

where the same notations are used as before, but the vector of the residuals is $\mathbf{r} = \mathbf{y} - \mathbf{T}\mathbf{q}$. The equation of the minimum of the functional $\partial\chi^2(\mathbf{q})/\partial\mathbf{q} = 0$ is

$$\mathbf{T}'\mathbf{W}\mathbf{T}\,\mathbf{q} - \mathbf{T}'\mathbf{W}\mathbf{y} + \lambda\,\mathbf{R}\mathbf{q} = 0, \tag{5.56}$$

where $\lambda = \frac{1}{2}\alpha\sigma^2$. The equation becomes

$$(\mathbf{C}^2 + \lambda\,\mathbf{R})\,\mathbf{q} = \mathbf{C}^2\hat{\mathbf{q}}, \tag{5.57}$$

where the normal principal solution is denoted as

$$\hat{\mathbf{q}} = \mathbf{C}^{-1}\mathbf{B}'\mathbf{V}\mathbf{y}. \tag{5.58}$$

The *regularized principal components* solution is

$$\mathbf{q} = (\mathbf{C}^2 + \lambda\,\mathbf{R})^{-1}\cdot\,\mathbf{C}^2\hat{\mathbf{q}}, \tag{5.59}$$

or, in the alternative form

$$\mathbf{q} = (\mathbf{I} + \lambda\,\mathbf{C}^{-2}\mathbf{R})^{-1}\cdot\,\hat{\mathbf{q}} \tag{5.60}$$

as a function of the regularization parameters λ. The dispersion of the regularized solution has become

$$\mathcal{D}\,(\mathbf{q}) = \sigma^2\,(\mathbf{C}^2 + \lambda\,\mathbf{R})^{-1}\cdot\,\mathbf{C}^2\cdot\,(\mathbf{C}^2 + \lambda\,\mathbf{R})^{-1}. \tag{5.61}$$

The parameter λ can be estimated in the first approximation from the equality of the two components of the sum:

$$\lambda = \alpha\sigma^2 = \frac{\mathrm{tr}\mathbf{C}^2}{\mathrm{tr}\mathbf{R}}. \tag{5.62}$$

Then, the parameter λ should be decreased until

$$\frac{1}{\sigma^2}\mathbf{r}'\mathbf{W}\mathbf{r} < \delta, \tag{5.63}$$

i.e. the weighted sum of the residuals reaches some level δ. Another method of choosing the regularization parameters is the cross-validation method and the L-curve criterion discussed in Fierro et al. (1997).

The regularized solution of the original parameters is as before

$$\mathbf{p} = \mathbf{D}\mathbf{q}. \tag{5.64}$$

The product in front of $\hat{\mathbf{q}}$ in Eq. (5.59) can be interpreted as a damping filter which suppresses the noisy components of the vector: the smaller the square of the singular values in $\mathbf{C}$, the stronger the dumping of the components of $\hat{\mathbf{q}}$. The degree of the suppression depends on the regularization parameter λ, and the shape of the filter is defined with the regularization matrix $\mathbf{R}$. Here we can apply different regularization matrices to $\mathbf{q}$ to obtain a class of various regularized solutions to $\mathbf{q}$, $\mathbf{p}$, and to the fitting function $\tilde{\mathbf{y}}$.

5.11.1 Regularization of the principal components

I Minimum squares of $\mathbf{q}$, i.e. $\mathbf{R}$=$\mathbf{I}$. The solution to the problem is

$$\mathbf{q} = (\mathbf{C}^2 + \lambda\mathbf{I})^{-1} \cdot \mathbf{C}^2\hat{\mathbf{q}}. \tag{5.65}$$

Since the inversion matrix is diagonal, the components of the vector are

$$q_k = \frac{c_k^2}{c_k^2 + \lambda} \cdot \hat{q}_k. \tag{5.66}$$

The filtering properties of this solution are obvious: the larger the parameter λ, the stronger the suppression of the noise in $\hat{\mathbf{q}}$ as the singular values $c_k \to 0$ along with their variances $\sigma_{q_k} \to 1/\lambda$. The variances of the solution are given by

$$\sigma_{q_k}^2 = \frac{c_k^2}{(c_k^2 + \lambda)^2}. \tag{5.67}$$

Fierro et al. (1997) investigated the filtering properties of this solution applied to the problem of total truncated least-squares.

H Maximal smoothness of the solution $\mathbf{q}$, i.e. $\mathbf{R}$=$\mathbf{H}$. The solution to the problem is

$$\mathbf{q} = (\mathbf{C}^2 + \lambda\mathbf{H})^{-1} \cdot \mathbf{C}^2\hat{\mathbf{q}}. \tag{5.68}$$

At zero singular values $c_i \equiv 0$, where $i \geq r = \min(n, m)$, the submatrix of the inversion matrix becomes singular because the regularization matrix $\mathbf{H}$ itself is not positively definite (i.e. $\mathbf{x}'\mathbf{H}\mathbf{x} > 0$ is not true for all $\mathbf{x}$, in particular, it is zero for the unity vector $\mathbf{x}$). The solution to $\mathbf{q}$ should be found for the vector and the inversion matrix truncated to the rank r with zero singular values excluded from the inversion.

5.11.2 Regularization of the original parameters

The problem is to find the solution $\mathbf{q}$ which minimizes the functional

$$\chi^2(\mathbf{q}) = \frac{1}{\sigma^2}\mathbf{r}'\mathbf{W}\mathbf{r} + \alpha\,\mathbf{p}'\mathbf{R}\mathbf{p} = \frac{1}{\sigma^2}\mathbf{r}'\mathbf{W}\mathbf{r} + \alpha\,\mathbf{q}'\,\mathbf{D}'\mathbf{R}\mathbf{D}\,\mathbf{q}, \tag{5.69}$$

i.e. controls the shape and the smoothness of the original parameters. The regularization matrix to $\mathbf{q}$ is now $\mathbf{D}'\mathbf{R}\mathbf{D}$ and the solution to the problem is

$$\mathbf{q} = (\mathbf{C}^2 + \lambda\,\mathbf{D}'\mathbf{R}\mathbf{D})^{-1} \cdot \mathbf{C}^2\hat{\mathbf{q}}. \tag{5.70}$$

I Minimum squares of $\mathbf{p}$, i.e. $\mathbf{R}$=$\mathbf{I}$. The solution to the problem is

$$\mathbf{q} = (\mathbf{C}^2 + \lambda\mathbf{I})^{-1} \cdot \mathbf{C}^2\hat{\mathbf{q}} \tag{5.71}$$

the same as in Eq. (5.65).

H Maximal smoothness of the solution, i.e. $\mathbf{R}$=$\mathbf{H}$. The solution to the problem is

$$\mathbf{q} = (\mathbf{C}^2 + \lambda\,\mathbf{D}'\mathbf{H}\mathbf{D})^{-1} \cdot \mathbf{C}^2\hat{\mathbf{q}}. \tag{5.72}$$

5.11.3 Regularization of the fitting function

Find $\mathbf{q}$ which controls the smoothness of the fit weighted with the variances of the observations, i.e. which minimizes the functional

$$\chi^2(\mathbf{q}) = \frac{1}{\sigma^2}\mathbf{r}'\mathbf{W}\mathbf{r} + \alpha\,(\mathbf{V}\tilde{\mathbf{y}})'\,\mathbf{R}\,(\mathbf{V}\tilde{\mathbf{y}}) = \frac{1}{\sigma^2}\mathbf{r}'\mathbf{W}\mathbf{r} + \alpha\,\mathbf{q}' \cdot \mathbf{C}\mathbf{B}'\mathbf{R}\mathbf{B}\mathbf{C} \cdot \mathbf{q}, \tag{5.73}$$

where the orthogonal decomposition Eq. (5.24) of the fitting function was used. The regularization matrix to $\mathbf{q}$ is $\mathbf{C}\mathbf{B}'\mathbf{R}\mathbf{B}\mathbf{C}$ and the solution to the problem is

$$\mathbf{q} = (\mathbf{C}^2 + \lambda\,\mathbf{CB}'\mathbf{RBC})^{-1} \cdot \mathbf{C}^2\hat{\mathbf{q}}. \tag{5.74}$$

I Minimum squares of the fit, **R=I**, then

$$\mathbf{q} = \frac{1}{1+\lambda}\,\hat{\mathbf{q}}, \tag{5.75}$$

i.e. scaling the principal components changes the amplitude of the fit, hence its total square.

H Maximal smoothness of the fit, i.e. **R=H**, then

$$\mathbf{q} = (\mathbf{C}^2 + \lambda\,\mathbf{CB}'\mathbf{HBC})^{-1} \cdot \mathbf{C}^2\hat{\mathbf{q}}, \tag{5.76}$$

or, in a similar form

$$\mathbf{Cq} = (\mathbf{I} + \lambda\,\mathbf{B}'\mathbf{HB})^{-1} \cdot \mathbf{C}\hat{\mathbf{q}} \tag{5.77}$$

5.12 Regularized differential solution

In the regularization functionals considered so far, the solution was formed in the arbitrary basis of all possible solutions. In the case $\mathbf{R} = \mathbf{H}$, the solution is smoothed by minimizing the differences of subsequent pixels and the differential nature of the matrix does not change the norm of the solution. This is not the case for the zeroth-order regularization matrix $\mathbf{R} = \mathbf{I}$, which minimizes the norm of the solution as the factor λ increases. This limits the application of the zeroth-order regularization to these data which are around zero, i.e. this regularization suppresses the wildly oscillating solutions around zero by controlling their amplitude. On the other hand, the use of the zeroth-order regularization is the most simple from the computational point of view, since it operates with diagonal matrices, and it has the simplest functional form which is easy to interpret in order to understand more complex problems. One of such insights is that the zeroth order regularization implicitly uses the *a priori* information about the solution assuming that it should be around zero. This leads us to the inclusion of the *a priori* information in a more general functional which will seek for the solution closest to any predefined function or any other deterministic information about the solution. The solution obtained with the known *a priori* information will be called the *regularized differential solution*.

This is, on the other hand, the basis for the solution to the pattern recognition problem where the goodness of the fit is used as a criterion to make the decision. The regularized differential solution is also widely-known as *Occam's inversion*.

The English fourteenth century philosopher William Occam wrote that *it is vain to do with more what can be done with fewer*, which has become known as Occam's razor - a fundamental tenet of modern science: hypotheses should be neither unnecessarily complicated nor unnecessarily numerous (Constable et al. 1987, who have first applied Occam's principle to the inversion).

The minimization functional in terms of the orthogonal decomposition is

$$\chi^2(\mathbf{q}) = \frac{1}{\sigma^2}\,\mathbf{r}'\mathbf{W}\mathbf{r} + \alpha\,(\mathbf{q}-\tilde{\mathbf{q}})'\mathbf{R}\,(\mathbf{q}-\tilde{\mathbf{q}}), \tag{5.78}$$

where $\tilde{q}$ is an *a priori* known function. In the absence of the *a priori* information, the reduced principal components solution $\tilde{q}$ can be used instead as the first guess to the solution. After derivations similar to the ones above, the minimization equation becomes

$$\mathbf{C}^2\mathbf{q} + \lambda\,\mathbf{R}(\mathbf{q}-\tilde{\mathbf{q}}) = \mathbf{C}^2\hat{\mathbf{q}} \tag{5.79}$$

and the solution is given by

$$\mathbf{q} = (\mathbf{C}^2 + \lambda\,\mathbf{R})^{-1}\cdot(\mathbf{C}^2\hat{\mathbf{q}} + \lambda\,\mathbf{R}\tilde{\mathbf{q}}), \tag{5.80}$$

where $\hat{q}$ is the principal components solution as before.

I Let the regularization matrix be of zeroth order $\mathbf{R} = \mathbf{I}$. The components of the vector $\mathbf{q}$ become

$$q_i = \frac{c_i^2\hat{q}_i + \lambda\tilde{q}_i}{c_i^2 + \lambda}. \tag{5.81}$$

Once again, the vector of the reduced principal components solution has the elements:

$$\tilde{q}_i = \begin{cases} \hat{q}_i, & i = 0, 1, \ldots k-1 \\ 0, & i = k, k+1, \ldots m \end{cases} \tag{5.82}$$

therefore the regularized differential solution has the elements

$$q_i = \begin{cases} \hat{q}_i, & i = 0, 1, \ldots k-1 \\ \dfrac{c_i^2}{c_i^2+\lambda}\cdot\hat{q}_i, & i = k, k+1, \ldots m. \end{cases} \tag{5.83}$$

That is exactly what we often need in practice: to keep the real part of the spatial harmonics of the solution and smooth its noisy tail with the chosen parameter λ. This solution, in turn, does not require an additional inversion of the matrix.

H In case we need to determine that solution whose residuals with respect to the *a priori* solution are smooth, the regularization matrix of the higher orders should be used: $\mathbf{R} = \mathbf{H}$. The solution becomes

$$\mathbf{q} = (\mathbf{C}^2 + \lambda\,\mathbf{H})^{-1} \cdot (\mathbf{C}^2\hat{\mathbf{q}} + \lambda\,\mathbf{H}\tilde{\mathbf{q}}). \tag{5.84}$$

The solution should be found for the truncated inversion matrix when $c_i > 0$ as it was discussed for Eq. (5.68).

Similar is the case when the reduced principal components solution in the original parameters space $\tilde{\mathbf{p}} = \mathbf{D}\tilde{\mathbf{q}}$ is used as the *a priori* information:

$$\chi^2(\mathbf{q}) = \frac{1}{\sigma^2}\,\mathbf{r}'\mathbf{W}\mathbf{r} + \alpha\,(\mathbf{p} - \tilde{\mathbf{p}})'\mathbf{R}\,(\mathbf{p} - \tilde{\mathbf{p}}), \tag{5.85}$$

which has the solution given by

$$\mathbf{q} = (\mathbf{C}^2 + \lambda\,\mathbf{D}'\mathbf{R}\mathbf{D})^{-1} \cdot (\mathbf{C}^2\hat{\mathbf{q}} + \lambda\,\mathbf{D}'\mathbf{R}\mathbf{D}\,\tilde{\mathbf{q}}). \tag{5.86}$$

In the case $\mathbf{R} = \mathbf{I}$, the solution is the same as in Eq. (5.83), and for $\mathbf{R} = \mathbf{H}$ it is obtained by straightforward substitution of the regularization matrix.

5.13 Astronomical example

In this section we give an example of the deconvolution applied to real observations. We use the solar spectrum which was used in Sec. 2.1 for the comparison with the FTS solar spectrum convolved with the instrumental profile. Here, we use the same spectrum obtained with the high resolution 1st camera and the measured HeNe laser instrumental profile for deconvolution and compare it with the original FTS spectrum.

The process of deconvolution is demonstrated with a number of figures. The weighted design matrix of the convolution model Eq. (5.18) is constructed from the offset instrumental profile and the sampling matrix with the sampling rate $r = 1$, and is shown in Fig. 5.1.

The result of its SVD factorization (Eq. (5.23)) is shown in Fig. 5.2 where the two matrices $\mathbf{B}$ and $\mathbf{D}$ are given. One can see from the images that the orthogonal functions in the columns of the matrices have rather different spatial frequencies from the left to the right. The vector of singular values $\mathbf{C}$ is given in Fig. 5.1. The solution of the least-squares problem results in the vector of the principal components $\mathbf{q}$ (Eq. (5.29)), which is plotted in Fig. 5.3. The best solution was selected, in this particular study case, from the plot of χ^2_ν (Fig. 5.3), which describes the mismatch error of the fit. The number $k = 450$ of the first significant principal

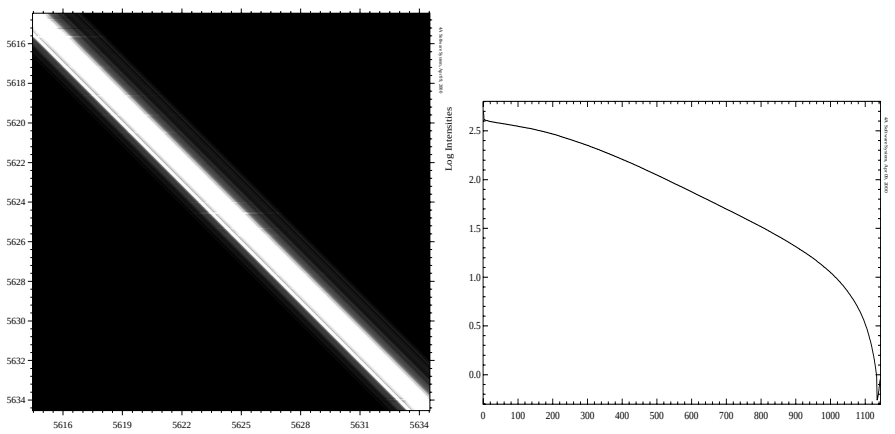

Figure 5.1: The image of the weighted design matrix **VA** and the vector of singular values of the diagonal of **C** in log scale.

components was selected where $\chi^2_\nu = 1$, and all other components were set to zero. The particular solution in the original parameter space (the deconvolved spectrum) is obtained by using Eq. (5.30) and shown in Fig. 5.5. The covariance matrix for the selected solution is shown in Fig. 5.4, which gives us the degree of correlation between neighbouring pixels of the solution.

To ensure that the selected solution is indeed the best, we create an image (Fig. 5.4) of the family of solutions, where the deconvolved spectra are given in each row; the number of the reduced principal components increases from top to bottom. We see that the inclusion of the first few tens of the principal components gives a rough estimate of the spectrum, the further down the more details are reproduced, and towards the end the noise magnification occurs.

The deconvolved spectrum shown in Fig. 5.5 is overplotted with the FTS spectrum. The difference spectrum reveals a quite good agreement between the spectra.

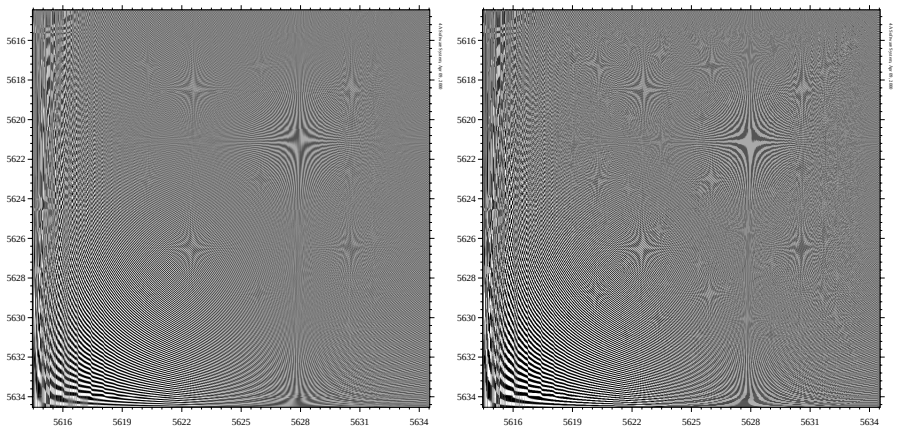

Figure 5.2: The image of the orthogonal matrices **B** and **D** of the weighted design matrix **VA**.

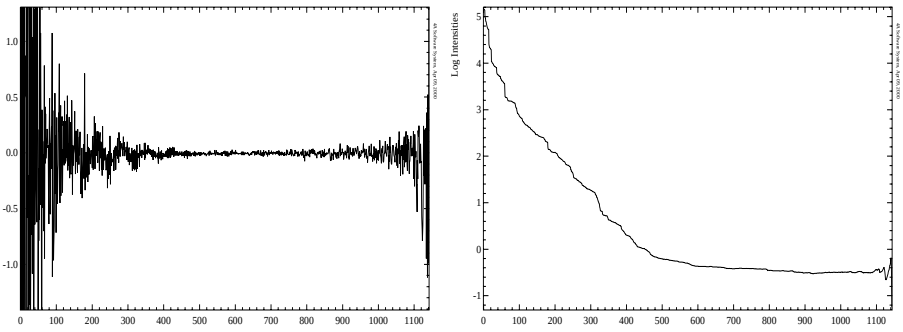

Figure 5.3: The vector of the principal components **q** and the run of $\log \chi^2_{n-k}$ as a function of the number of principal components k. The best solution is at $k = 450$ when $\chi^2_{n-k} = 1$.

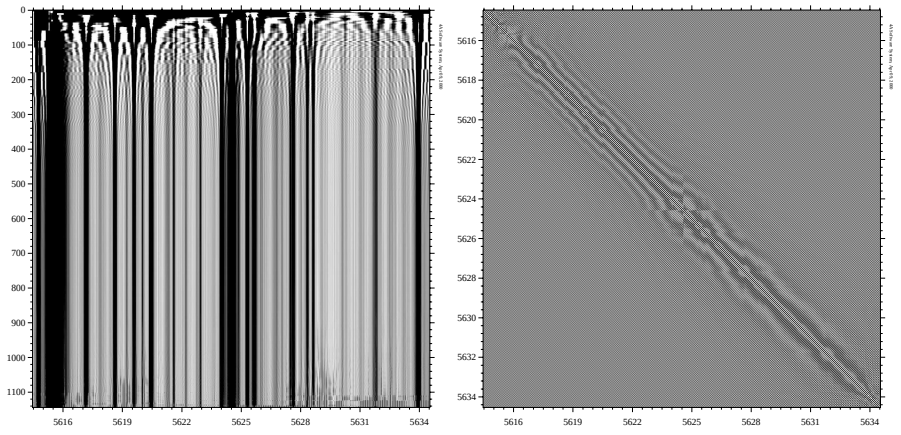

Figure 5.4: The image containing all principal solutions and the covariance matrix of the selected solution.

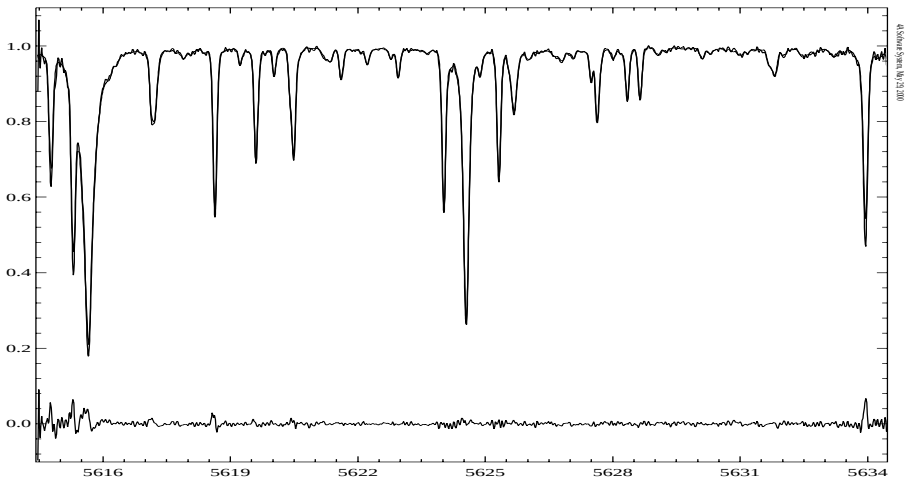

Figure 5.5: Comparison of the deconvolved spectrum and the FTS solar spectrum. The difference between the spectra is shown at the bottom. The rms of the difference is 0.4%.

Chapter 6

Line profile variations of the binary star α And

6.1 Introduction

α And (HR 15, HD 358) is a well-known peculiar bright double-lined binary system which has a mercury-magnesium primary component (B8 IVpMnHg). The primary component is the hottest ($T_{\rm eff}$=13800 K) star among its class and shows abundances of Mn, Hg, P, and Ga which are 4–5 orders of magnitude higher than in the Sun (Ryabchikova et al. 1999). The spectral variability of the line profiles has been known for a long time. Rakos et al. (1981) reported the detection of variations in the UV Si II line profiles (1100–1300Å) with a period of around $3^{\rm h}$ based on Copernicus observations. The variations of the continuum level in the lineless 3431Å region show a period of $23^{\rm h}$. The presence of such different variations complicates the explanation of the abundance anomalies by diffusion. In this study, we concentrate on the profile variability of the Hg II 3984 Å line which was earlier suspected to show some variations (Ryabchikova et al. 1999). The observations and subsequent analysis yield that the line indeed shows variations of its shape modulated by the stellar rotation, and the most plausible explanation is the presence of two strong Hg spots on the stellar surface.

6.2 Observations and data reduction

The observations of α And were obtained with the SOFIN spectrograph at the 2.56 m Nordic Optical Telescope (NOT) at Roque de los Muchachos Observatory, La Palma, Spain. A total number of 68 observations was obtained during 21 nights

in May, June, August, September, October, and November 1999 covering a time span of 180 days. The entrance slit width was set to 82 μm (0.″6 on the sky) providing the resolution element of 2 pixels FWHM and the resolving power of 80 000 at the spectral setting centred on 3984 Å at order number 57. The spectra were recorded with an Astromed-3200 CCD camera providing a spectral coverage of 10 échelle orders (51–60) of about 30 Å in length from 3766 Å to 4450 Å. Exposure time varied from 1 to 10 min depending on the seeing conditions, the signal-to-noise ratio achieved ranges from 80 to 350. Typically, one to three observations were made per night, within the time span of 2–3 hours given the unknown periodicity of the Hg II 3984 Å line on short (hours) and long (days) time-scales. Each observation comprises one to three individual exposures to avoid possible CCD overflow in the reddest spectral orders.

The spectra were reduced with the 4A package. This involved standard procedures of bias subtraction, estimate of the variance of the flux, master flat field correction, scattered light subtraction with the aid of 2D-smoothing splines, spectral order definition, and weighted integration of the flux with cosmic spikes elimination. The wavelength calibration was done with the use of a ThAr comparison spectrum, each of them taken before and after each individual object exposure to eliminate any temporal changes in the spectrograph during an exposure. The wavelength solution incorporates Gaussian-centred positions, wavelength, and time of all detected spectral lines from the two images bracketing the stellar image. The wavelength for every pixel in the stellar spectrum is calculated for the time of its mid-exposure. The corrections of the spectra for the vignetting function and for the Earth's orbital motion constitute the final steps.

6.3 Radial velocity measurements

The Hg II 3984 Å line shows variations of the line profile superimposed on the orbital motion of the primary stellar component due to the secondary. Hence, to remove the stellar radial velocity, we used relative measurements of the velocity with respect to the mean of the three neighbouring spectral orders 53 (4264–4294 Å), 54 (4185–4214 Å), and 55 (4109–4138 Å). The three orders show no conspicuous trace of the secondary stellar component. A cross-correlation technique was used to measure the velocity of each individual spectrum with respect to the mean with the velocity error determination involving variances of the pixel fluxes and the curvature of the cross-correlation peak. A polynomial of 4th degree was used to determine the centre and the curvature. Depending on the spectral order and the signal accumulated, the typical error is about 100–400 $\mathrm{m\,s^{-1}}$.

The parameters of the orbit was prevously published by Pan et al. (1992), Tomkin et al. (1995), and Ryabchikova et al. (1999). A Keplerian orbital fit (Ilyin 2000) to our measurements of the primary component is shown in Fig. 6.1 and the parameters obtained are given in Tab. 6.1. The limited time span of the observations

γ, $\mathrm{m\,s^{-1}}$	5539 ± 96	T_{peri},	$2451\,532.92 \pm 0.26$
K, $\mathrm{m\,s^{-1}}$	32976 ± 118	$T_{\mathrm{RV\,max}}$,	$2451\,526.17 \pm 0.20$
P, days	96.884 ± 0.12	T_{conj},	$2451\,533.79 \pm 0.23$
ω, degrees	77.5 ± 0.48		
e	0.5342 ± 0.0025	N_{free}	204
rms, $\mathrm{m\,s^{-1}}$	651	χ^2_ν	10.5

Table 6.1: The set of the orbital parameters of the Keplerian fit. The moments of time are given as HJD.

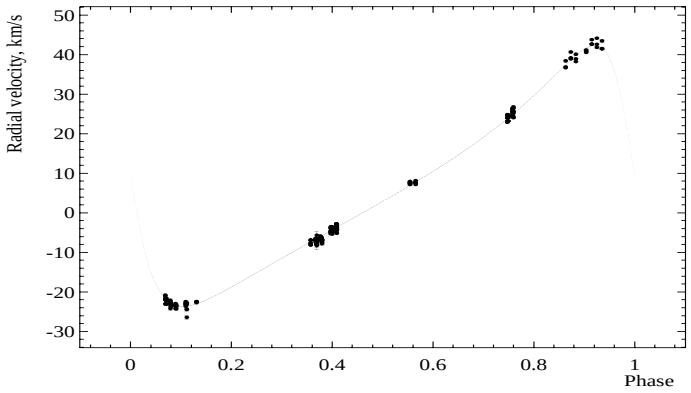

Figure 6.1: The orbital solution to the relative radial velocities of the primary component.

did not allow for an improvement of the period compared to that obtained by the other authors. The radial velocity of the order number 57 containing the line Hg II 3984 Å was removed by using the orbital fit.

6.4 The period of the line profile variations

The line of interest, Hg II 3984 Å, shows remarkable changes of its shape from night to night. In order to understand the behaviour of the process, we first investigated the periodogram of the line profile for each wavelength (pixel) of the profile. A Lomb-Scargle periodogram (Press et al. 1992) was calculated for an image of spectra resampled to the same stepsize in wavelengths, separately for

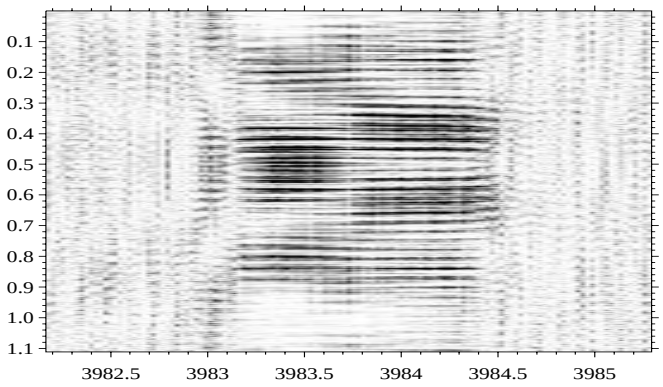

Figure 6.2: The gray-scale image of the periodogram of the Hg II 3984 Å line profile variations. The vertical axis units are frequencies in d^{-1}. The maximum corresponding to the rotational period $2\overset{\mathrm{d}}{.}38$ is at $0.42\,\mathrm{d}^{-1}$.

each pixel. The periodogram image is shown in Fig. 6.2 and a sample of one column is given in Fig. 6.3. As we see from Fig. 6.3, the maximum is at $0.42\,\mathrm{d}^{-1}$ which corresponds to $2\overset{\mathrm{d}}{.}38$. This frequency is persistent over the whole line profile in Fig. 6.2, unlike the other peaks which are present only in parts of the profile. The associated window function of the observations is shown in Fig. 6.4, which peaks at the one day frequency.

The period can also be justified because it is very close to the rotational period of the main component of α And from the following considerations. Pan et al. (1992) derived the inclination of the orbit of $i = 105\overset{\circ}{.}66 \pm 0\overset{\circ}{.}22$; Ryabchikova et al. (1999) estimated $v \sin i = 52\,\mathrm{km\,s^{-1}}$, and the stellar radius was estimated by Shallis et al. (1995) to $R = 2.7\,R_{\odot}$. Given the parameters, the estimate for the rotational period is $P_{\mathrm{rot}} = 2\overset{\mathrm{d}}{.}53 \pm 0\overset{\mathrm{d}}{.}05$ taking into account the error in the inclination and assuming that the error in the rotational velocity is $1\,\mathrm{km\,s^{-1}}$.

To refine the period of the line profile variations estimated from the periodogram, we could use a cross-correlation of the individual profiles with respect to the mean spectrum and fit a model to the resulting changes (e.g. RVs). The disadvantage of this approach is that the cross-correlation technique assumes a similarity of the spectra being used which is not the case for this profile. Instead, we used a non-linear least-squares fit of a single period to all wavelength pixels of the profile versus time allowing to vary the offset, amplitude, and phase shifts along the line profile

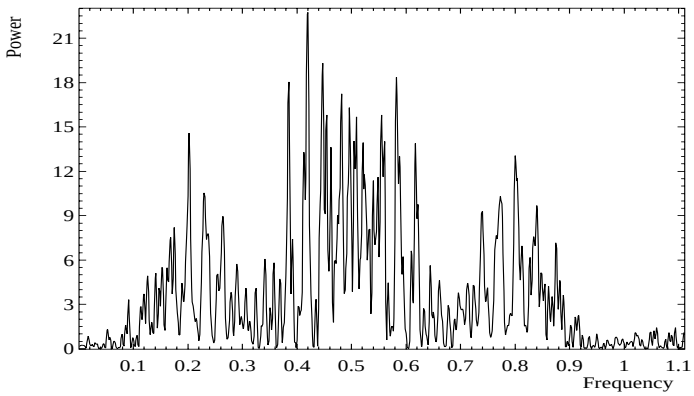

Figure 6.3: The periodogram of the line profile at $\lambda\,3983.5\,$Å. The frequencies are in d^{-1}.

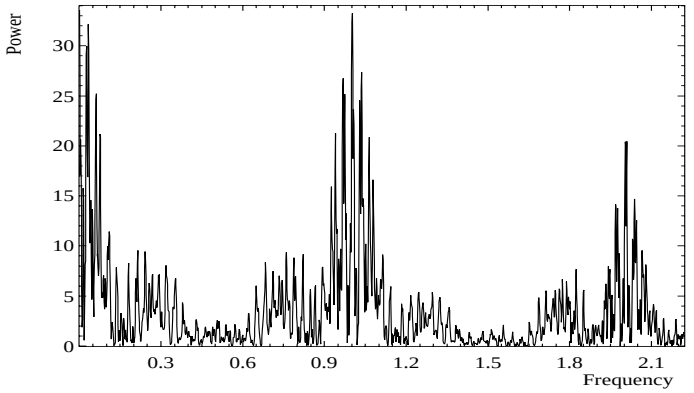

Figure 6.4: The window function of the observations calculated for an extended range of frequencies.

$$y_{ik} = b_i + a_i \cos 2\pi \left(\frac{t_k}{p} + \phi_i \right)$$

where y_{ik} is the image of spectra versus time t_k, $k = 1, 2, \ldots N$, and wavelength $i = 1, 2, \ldots M$. The free parameters along the profile are the offset (bias) b_i, the amplitude of variations a_i, and phase shifts ϕ_i, as well as the period of the variations p. The Levenberg-Marquardt method (Press et al. 1992) was used to find the parameters; the initial guesses for b_i, a_i, and ϕ_i were obtained from a linear least-squares solution for the period estimated from the periodogram

The period found by using this model is $P = 2\overset{\mathrm{d}}{.}38257 \pm 0.00024$ with the goodness of fit values rms=0.0081 and $\chi^2_\nu = 3.15$. The change of the bias, amplitude, and phase is shown in Fig. 6.5 together with their error bars. The image shows the profile phased with $t_k/p + \phi_i$. Clearly, two features separated by half a period at phases 0.3 and 0.8 are present. A more convenient image is shown in Fig. 6.6 where no phase shift was applied. The second, smaller feature is not so well shaped as compared to the other one, because the observations are not very dense at phases 0.6–0.8. The average within every 0.1 phase bin of the line profile is also shown in Fig. 6.7.

The time scale of the variability modulated by the stellar rotation and the different strengths of the two features rule out the hypothesis of non-radial pulsations for the star. The expected time scale of non-radial pulsations for this star could be about 10–20 hours as it is for the stars of similar type and spectral class. The most plausible interpretation, hence, is the presence of two Hg II patches separated by 180° in longitude. According to the slope in the phase diagram, the latitudes of the two spots are almost the same.

The model could not completely describe the variability of the line profile, especially in the case of two spots. The spot configuration and their geometry should be included. The inconsistency of the model is indicated by the excess of χ^2_ν. Indeed, the model, aimed to find the period, is the simplest model one can apply without involving any stellar spot geometry configuration.

6.5 Variability of other spectral lines

To check whether spectral lines in other spectral regions of the échelle image show variability, we analyzed a variance spectrum for each spectral order with the orbital motion of the primary component removed. The result is shown in Fig. 6.8: the weighted average of the order is shown at the top of each panel and the spectrum of the standard deviation (magnified by a factor of 100) is at the bottom. No strong variations as much as in Hg II 3984 Å is seen. The excess variance at 4200, 4045, and 3849 Å was analyzed with the Lomb-Scargle periodogram as above. The most significant peaks at these regions are very close to the orbital period $96\overset{\mathrm{d}}{.}8$

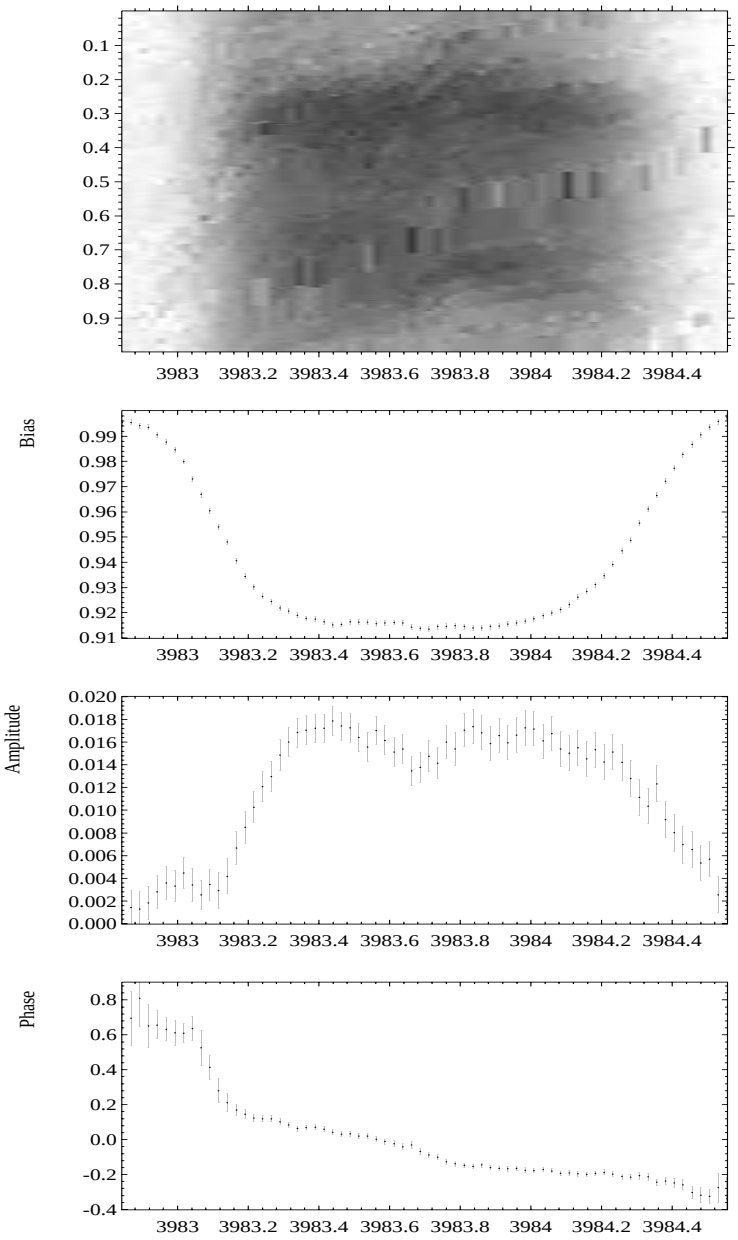

Figure 6.5: The image shows a phase diagram where the drift of the features in wavelength with phase is removed. The plots below are the intensity level, amplitude, and the phase shifts of the fit to the line profile.

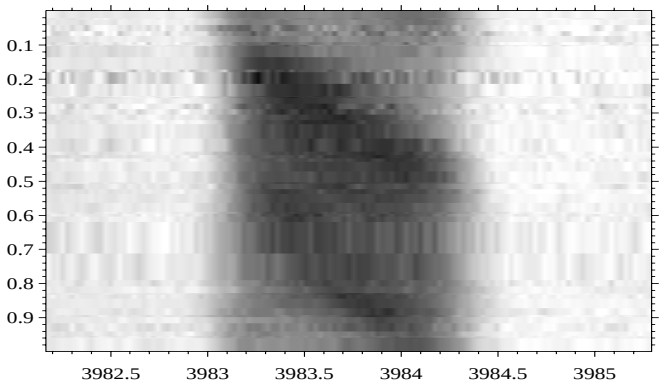

Figure 6.6: The line profile phased with the rotational period.

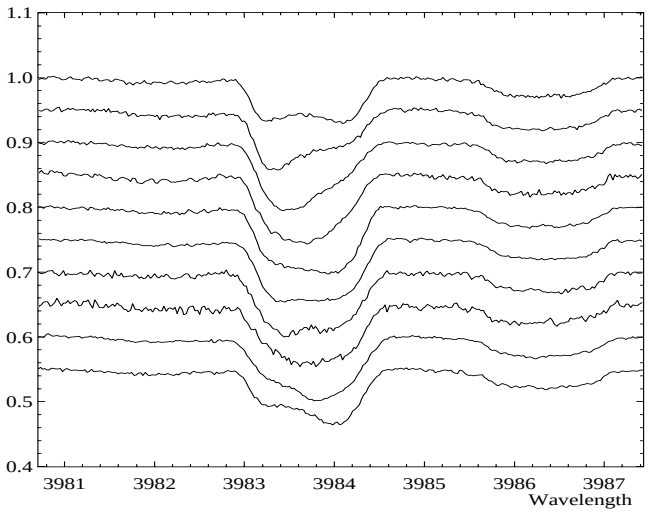

Figure 6.7: The individual spectra averaged in bins of the rotational phase $0.0 - 0.1, 0.1 - 0.2, \ldots, 0.9 - 1.0$. The phase increases from top to bottom with the displacement 0.05 in intensities between spectra.

of the binary system, hence, these features, most likely, belong to the secondary component.

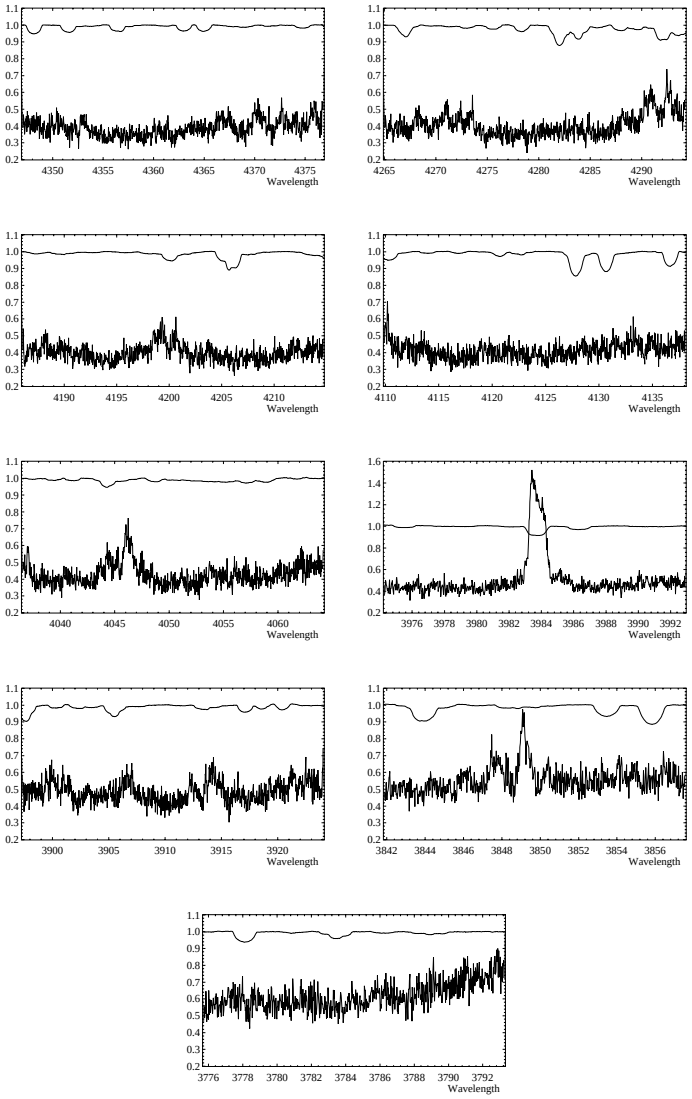

Figure 6.8: The averaged line profiles and the variance spectrum×100 for the échelle orders 52 – 60 left to right and top to bottom. The orders 57, 59, and 60 are truncated to avoid strong Hydrogen lines.

Appendix A

Reduction of SOFIN CCD échelle spectra: a user guide

A.1 Introduction

Unlike many other data reduction packages used in astronomy, where most of the procedures are built into a few integrated tasks, the 4A data reduction consists of a number of elementary steps. This approach is more flexible, it gives a better feeling for the data, but makes the whole procedure more complex.

In this chapter the description of the data reduction sequence is given from the point of view of a user, who is familiar to work with 4A. The detailed description of the 4A facilities is given in the "Reference Guide for 4A". The present user's guide gives the explicit commands in the normal sequence of échelle spectra reduction. The numerical parameters given in the guide are typical for SOFIN spectra but should be always adjusted for the particular set of data.

A.2 The essential steps of the data reduction

1. Removal of the electronic bias from the CCD images.
2. Variance estimation.
3. Correction for the master flat field.
4. Evaluation and removal of the scattered light surface from the images.
5. Definition of the spectral orders.

6. Weighted extraction of the spectral orders.

7. Correction of the object spectra for the vignetting function.

8. Background subtraction from the comparison spectrum images and spectral order extraction.

9. Wavelength calibration based on comparison and telluric lines.

10. Transformation of the object spectra into the wavelength scale.

11. The heliocentric and radial velocity transformations of the wavelength scale.

12. The continuum normalization of the object spectra.

A.3 Removal of the CCD bias

Overscan selection

For the object and flat field images use the overscan in columns at the bottom of the image, and for the saturated comparison spectra (especially in case of the 3rd camera images) use the overscan in rows on the right of the image. Display the image and position the marker box to the overscan area. Move the box to exclude the first 1–3 CCD edge pixels (they may create a problem later during filtration). Create a new record in the list of regions (`Process` menu): the extraction function should be `avrcols` for the overscan in columns, and `avrrows` for the overscan in rows. The template for the file name is `ccd00000.bss` or similar (Fig. A.1). Ensure that the record in the list is highlighted (and none of the others). Mark the images and extract the averaged biases (`FITS/Extract regions`). Repeat the region selection and the extraction for the images with the overscan in rows in necessary.

Bias smoothing

Smooth the averaged biases with a trimmed mean filter with the window parameters 33-5-5 (the window length is 33, and the highest/lowest 5 pixels are rejected). In case of apparent fringes in the bias (which is due to electrical interference on the CCD), use a filter with the smaller window size (11-3-3 for instance), or a Gaussian filter with the window length 3. Ensure that cosmic spikes do not affect the filtration.

Bias subtraction

Mark the smoothed biases and subtract them from the marked images (`Reduction/Bias removal`), where the option `column` applies to the overscan in columns. The resulting images will have the extensions `.col` and `.row`, respectively. Check that the averaged level in the overscan area of the subtracted images is around zero by inspecting the averaged cross-cut or making a histogram. Move the original images to the trash can (usually a `DUMP` subdirectory in the working directory).

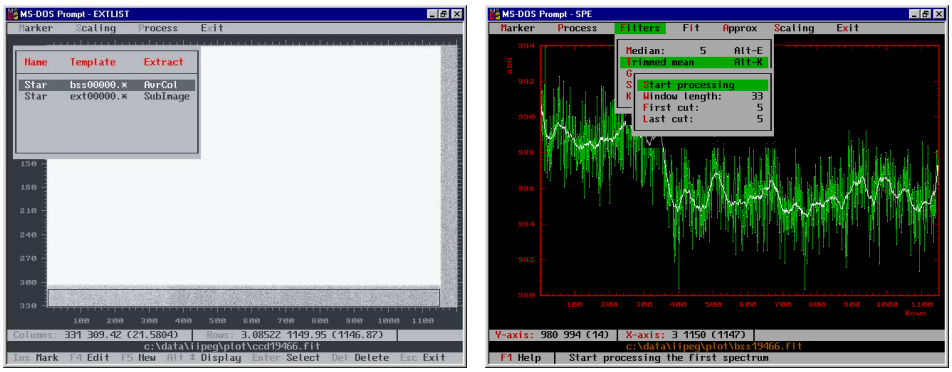

Figure A.1: *Left*: An image with the selected overscan area in the CCD columns shown as the marker box. The position of the box is given in the highlighted record of the opened list of regions. *Right*: An averaged bias column containing a jump in it due to CCD electronics stabilization problem is shown. A trimmed mean filter is used to eliminate the readout noise and preserve the variations. The smoothed bias is subtracted from every column of the original image.

Trimming the images

Select an area with the marker box which is the same for all images: the region should exclude the two overscans and the first few edge pixels in columns and rows which are usually bad. Create a record in the list of regions with the template file name `ext00000.*` and the extraction function `Subimage`. Unmark the bias records. Mark the debiased images and extract the subimages. Move the original images `.col` and `.row` out of the working directory.

Estimation of the photon noise

Mark *all* debiased, trimmed images in the database and start the estimation of the photon noise command in `Process/Variances`. This operation will not change the image name but it changes its size. The number of dimensions of the images

is increased by one, and the third dimension is used to store the estimated variances. Check that the error bars appear in a cross-cut of the image when changing the plotting mode or by plotting the variances (`Scaling` menu). The procedure requires two FITS records to be present: `GAIN` is the CCD gain factor in e^-/ADU and `RON` is the readout noise in ADU. These records should be added to the FITS header, if not present.

A.4 Flat field correction

Master flat field normalization

The easiest way to calculate the trend in the master flat field is to use a trimmed mean filter with the window parameters 41-11-11. Unfortunately, for some dark pixels and dust particles the smoothed function may follow these features. Use a weighted spline with the smoothing factor ranging from 0.05 to 0.0001 and the rejection level ± 40. In the particular case of camera 3 the parameters are $\pm 80/0.001$. Take the ratio between the original and smoothed images. If the normalized image is still disturbed in the areas around the dark pixels, then the pixels should to be masked out in the original image.

An alternative way to mask out the dark and sharp features is to use the clipping facility in `Process/Variances`: smooth the master flat with a median filter of 40–50 rows in length, sort the database, so that the original and smoothed records appear together, and clip the pixels which deviate from the median more than $40\,\sigma$.

Division by the master flat

Mark the object and night flat field images and divide them by the master flat which creates `.dvd` files by default. Check the noise reduction: take a cross-cut of one column in the night flat field before and after the division. Calculate statistical parameters in a flat region of the spectrum: the `Stdev/Mean` ratio gives the measured signal/noise ratio. In case there is no such flat part in the spectrum, then smooth the spectrum by a spline, take the ratio, and measure the variance. The estimated signal/noise should be the same as the expected one, which is obtained by displaying the signal/noise spectrum (`Scaling/PlotSNR`). Move the original images `.col` and the master flats out of the working directory.

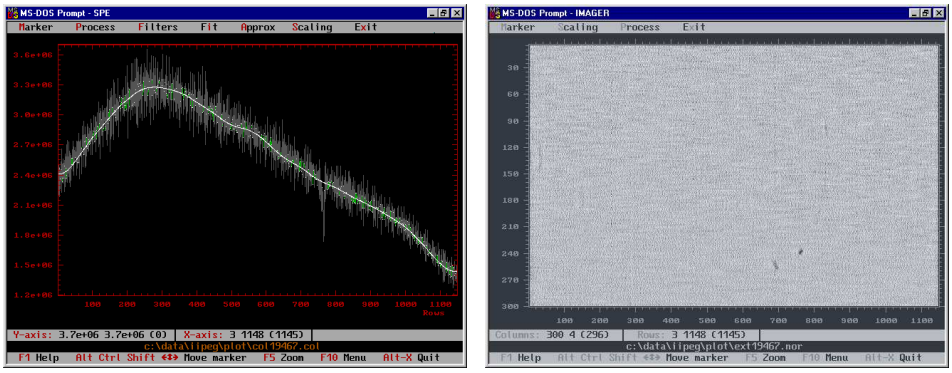

Figure A.2: *Left*: A column of the master flat field smoothed by a spline with the factor 0.01. In order to avoid sharp features, the sigma-clipping parameter is set to 40, hence the pixels deviating more than 40σ of the photon noise are rejected, which is, in this particular case, approximately the level of the CCD pixel-to-pixel noise. The clipped pixels are shown in gray. *Right*: The master flat field image after the normalization. The dark features are well preserved during the spline smoothing. The signal-to-noise ratio of the image is about 1100.

A.5 Scattered light removal

The scattered light surface is calculated in two steps: the surface of the interior of the spectral orders is approximated using a weighted spline in the clip-and-fit mode along rows, then the resulting surface is smoothed by a spline in columns.

1st camera. Smoothing in rows is done by a weighted spline with the smoothing factor 600 and the clipping parameters 2 (above) and 0 (below). The image extension could be set to `.pol`. Smoothing in columns is done with an unweighted spline of factor 600. The resulting image extension is `.bgn`.

2nd camera. Use a weighted spline in rows with the smoothing factor 10 and the clipping parameters 2 (above) and 0 (below). Use an unweighted spline in columns with the factor 1000.

3rd camera. Use a weighted spline in rows with the smoothing factor 1 and the clipping parameters 2 (above) and 0 (below) and an unweighted spline in columns with the factor 10.

A sometimes difficult problem for images of the 3rd camera is the undersampling effect in cross-dispersion which produces conspicuous ripples in the scattered light images in the dispersion direction. Subtraction of such a surface introduces the ripples into the stellar spectra. By using larger smoothing factors the ripples can be reduced, however, the scattered light level could still be overestimated.

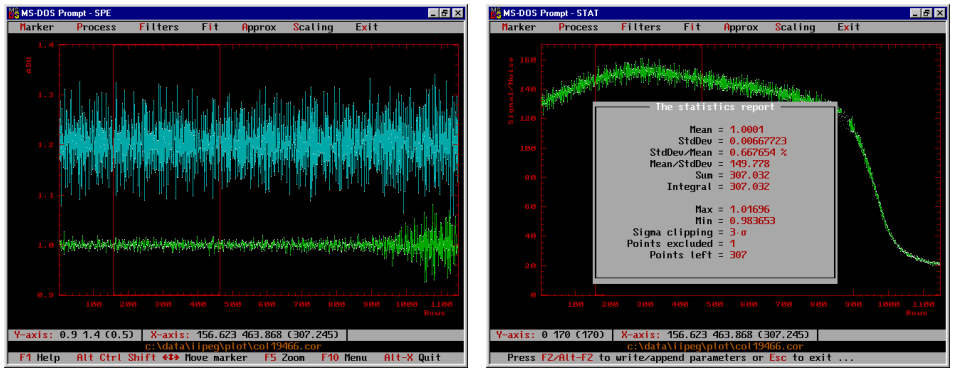

Figure A.3: *Left*: Decrease of the noise in the same column of the night flat field image before (upper, 6%) and after (lower, 0.6%) the master flat division. The columns are normalized to their trends. The amplitude of the high frequency spatial noise of the CCD used for the 2nd camera is about 6% rms and is constant for any illumination levels. The increase of the noise at the lower right is due to the lower light intensity level. *Right*: Check of the signal/noise ratio consistency by using the same single flat field column after the master flat correction. The plot shows the expected signal/noise ratio along the column (obtained with the `Alt-N` command in `Scaling/Plot SNR`). The opened statistical window gives a similar signal/noise (about 150) calculated for the selected region of the marker box. The shape of the signal/noise plot reflects the shape of the trend removed from the column and is due to order curvature.

In case the scattered light surface is disturbed by bad pixels in the original image, they can be masked out by clipping around a median image (filtered with window length 60 rows) with the clipping levels 100 (above) and 5 (below).

In the case when the ripples on the background are present due to electrical interference on the CCD, choose a small factor of the smoothing spline of the order of 1–5. This will allow to remove the wavy pattern from the image during the background subtraction.

Sort the database by file names and extensions and subtract the scattered light surfaces from the original images by using the pair operation command. The result should look like the left image in (Fig. A.4). The flat field corrected images `.dvd` and the background images can be moved out of the working directory.

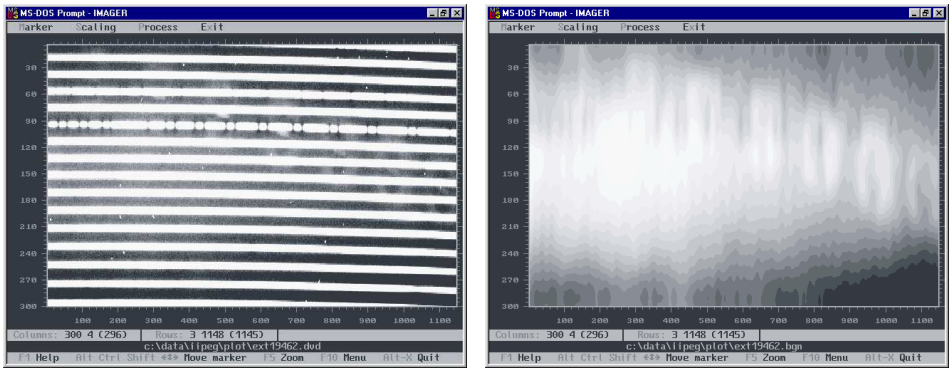

Figure A.4: *Left*: An image prior to the scattered light correction. A structure is seen between the spectral orders. *Right*: The scattered light surface of the image in the previous picture. The surface was obtained by approximation of the interorder gaps by a spline with the smoothing factor 10 and the rejection of pixels above 2σ along each row of the image in cross-dispersion. Then, the resulting image was smoothed along each column in the dispersion direction with an unweighted spline of the factor 100.

A.6 Definition of spectral orders

Order detection

Two parameters can be changed for the detection procedure: the median filter length and the detection probability. A filter length of 5 pixels is sufficient for most of the images; the more cosmic particles in the image the longer the filter. The detection probability should be 100% for the short 3rd camera and 1–10% for the others. The parameter can be as small as 10^{-20} in order to eliminate the detection of spurious spectral order-like features in the interorder gaps in the blue.

Mark the scattered light subtracted images and run the detection of orders program. The order definition polynomials are stored in separate binary (non-FITS) files with the extension `.spp`.

Order assignment

Displaying image by image, give the correct échelle order numbers to the spectral orders detected (Fig. A.6). For the 2nd camera the order numbers are increasing downwards (blue is at the bottom of the image) and the order number which is set in the program should be positive. For the 1st and 3rd cameras the order numbers are decreasing downwards (red is at the bottom of the image), therefore, the order number should be negative.

The order number can be identified from a known feature (Hα, for instance) and retrieved from the focal plane map program. If there is no such feature, the corresponding spectral order in the comparison spectrum can be identified (see wavelength identification, Sec. A.9.1) and the wavelength interval compared to the model of the focal plane.

If a number of images are very similar to each other (the same camera, the same spectral setting, and the spectral orders are approximately at the same positions during monitoring observations), the order assignment can be done with a single command. Firstly, give the order number to the first image, mark all images of the same kind, and secondly, run the `Reduction/Count orders` command from the database of images. The program will ask to point to the first reference image. Press `Enter` to start the procedure to enumerate the échelle order numbers for the marked images. Inspect the last images to ensure that the order numbers are correct (in case of a shift in the cross-dispersion).

A.7 Optimal extraction of spectra

Parameter adjustment

Check whether the default parameters are suitable for the images being processed. For a single object image run the weighted extraction with the spline smoothing parameter 0, which creates the unsmoothed version of the spatial profile image (`.sp`). Take a cross-cut of a column and check at what smoothing factor the spline fits the data. Use a weighted spline fit without clipping (both values are reset to zero). The higher the factor the less flexibility for the spline to fit small curvatures.

The default parameters for the smoothing factors are 10^9 for the 1st camera images, 10^8 for the 2nd, and 10^6 for the 3rd. The median filter length can be around 11 and the threshold is 3.

Inspection of the images

Mark the object and night flat field images and run the extraction procedure. It will create two new images for every original one. The first image contains the spatial profiles (`.sp`), which can be inspected and deleted. The extracted spectra and their variances are packed into one image with the column number equal to the order number (Fig. A.6). The cosmic spikes detected can be inspected in the original images: the hits are masked by changing the signs of their variances. The original images should all be inspected by displaying them with the `Marker/Masked pixels` switched on.

The scattered light subtracted images `.sub` can be moved out of the working directory.

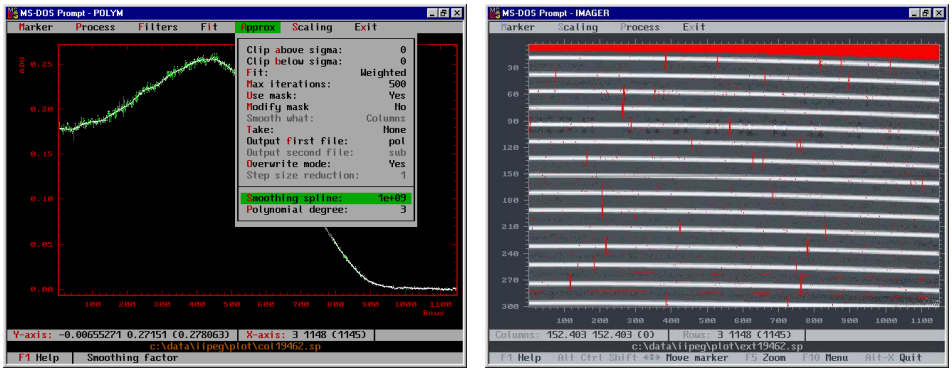

Figure A.5: *Left*: A column of the raw spatial profile of the image. A smoothing spline of factor 10^9 is used to obtain the filtered image of the spatial profile for the optimal extraction. *Right*: A smoothed spatial profile image with patches on it which are rejected from the spline approximation.

A.8 Correcting the shape of the spectra

Smoothing flat fields

Use a weighted spline with a smoothing factor 0.1 and possibly no clipping to smooth the images of the flat field packed spectra column by column (which are now the spectral orders). Any appearance of interference waves in the smoothed orders should be carefully inspected and compared with the corresponding spectra of the object. If the amplitude and phase of the waves are the same, then the interference can be removed from the object spectra. Otherwise, the effect can be enhanced several times. In this case, any interference appearance in the flat field spectra should be smoothed out by the spline approximation.

Normalize to the mean

In order to keep a similar number of ADUs in the object spectra, the smoothed flat fields can be approximated by a polynomial of zeroth degree in columns taking the ratio. The number of ADUs in the bluest orders of 3rd camera images is usually very low, which leads to singularities after the normalization. These orders can be patched by 1.

Reshaping the spectra

Mark the corresponding packed object images and divide them by the normalized flat fields. Check that the object spectra become flattened (Fig. A.7). This is often

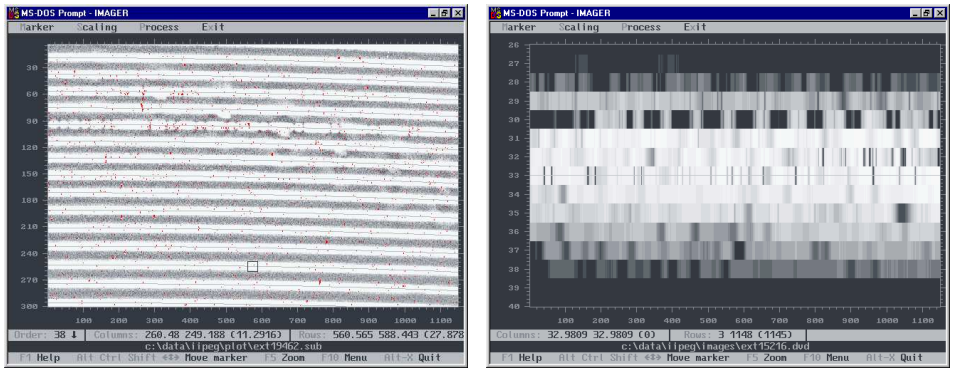

Figure A.6: *Left*: The image with the scattered light subtracted and used for the optimal extraction. After the extraction the detected cosmic spikes are marked on the image and seen as red patches after entering the mode `Alt-F6`. The amount of detected spikes is controlled by the sigma-clipping parameter of the optimal extraction algorithm. The curves of the located orders are shown. The bottom status bar indicates the échelle order numbers resulting after the orders assignment: the small marker box (in the third order from the bottom) indicates the position of the order number 38. *Right*: The image of the packed spectral orders after the optimal extraction.

not the case for 3rd camera spectra due to possible differences in the shapes of the object and flat field spectra. Remove all flat fields and the original object images from the working directory.

A.9 Wavelength calibration

Background removal

Mark all comparison spectrum images and apply a median filter with a window length of about 33 rows over one column and take the difference. This will create new images with the median background subtracted on a column by column basis. Delete the median images `.med` and move or delete the original images.

The other way to remove the background is to use a smoothing spline in the clip-and-fit weighted mode. One set of typical parameters are: the smoothing factor is 1, clip above is 2, and below is 10 (to avoid cold pixels due to overexposed comparison lines). Fit the images in columns and take the difference. This procedure works much slower that the median filtration, but gives a more smooth solution. The important advantage is that the median may slightly disturb the central position of a blend of lines which is wider than the filter length. On the other hand,

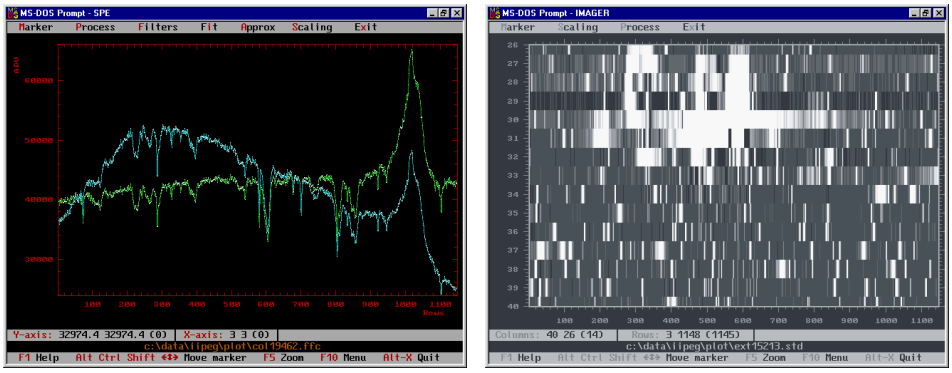

Figure A.7: *Left*: Two spectra are shown before and after the division by the night flat field which results in reshaping of the continuum. *Right*: An image of the packed spectral orders of the comparison spectrum image.

the smoothing spline may be sensitive to the clipping parameters in certain cases of line configuration, e.g. broad overexposed features, many cold pixels, etc. The remedy is to mask out these features by using a median filter and then to use the spline to fit and subtract the background. In the case of using the spline approximation, the images with the subtracted background should be unmasked (`Process/Variances/Absolute variances`) prior to any further operations.

Order tuning

The spectral orders for the comparison spectrum image should be taken from the nearest object or flat field images (`Reduction/Orders assignment`). The orders of these images may not be at the same positions as these of the comparison image. To align the orders to the actual position of the cross-profile, use the `Reduction/Orders tuning` command which works with marked images. For a single image the order tuning can be done from the imager program (`Process/Orders tuning`) with the input parameter which gives the initial offset of the orders in the cross-dispersion direction. For small offsets the parameter is zero. Run the procedure and check that the polynomial curves are adjusted to the centre of the spectral orders. The parameter equal to the distance between two adjacent orders in pixels will offset the polynomial curves down to the next spectral order. The actual offset of the curves is displayed in the bottom status bar.

In many cases, the strong overexposed spectral lines may disturb the order tuning procedure. The areas around strong lines can be masked out to be excluded from the fit: use the `Scaling/Mask region` command for individual images, or for a number of images it can be done from the list of regions: select the areas and use the function `MaskRegion`. Run the command `FITS/Extract regions` from the

database of images to mask out the selected areas of the marked images.

After the run, add two FITS records created by the program to the database: `CROFFS` is the offset of the spectral orders in cross-dispersion direction and `ECROFFS` is its error. Check that the orders in those images with large offsets are aligned correctly and their order numbering remains the same as in other images.

A.9.1 The wavelength solution of the comparison spectrum

Wavelength identification

For the first comparison spectrum in a series, do the standard extraction which creates an image of the packed spectral orders (Fig. A.7). Unpack the image to create a separate spectrum for each spectral order. Select an order with a known wavelength range and run the spectral line parameters program (`Reduction/Spectral lines/Line parameters`).

Locate the positions of spectral lines given so that at this stage the strongest lines should be selected for identification purposes. The location is simply done by putting the horizontal line of the graphical marker at the top of the background noise level and pressing `Enter`. All lines above the level will be detected and Gaussian profiles fitted to their profiles. The parameter given in `Graph/Gaussian zero` specifies the continuum level of the Gaussians. If the spectrum is used for the first time, the parameter is calculated as the median of the spectrum.

Select the catalogue of ThAr spectral lines named `tharkpno.cat`. Run the wavelength identification (`Table/Search in catalog`) by specifying the possible range of wavelengths for the blue end of the spectrum and the range of possible lengths of the order. The program gives a number of different identification choices: select the one with the maximal number of lines included. Select the `PosWav` function and make a fit. Exclude the most deviating points: use the `Ins` command to exclude a single line from the table, `Ctrl-Ins` to exclude a group of lines whose deviates are within the marker box positioned in the plot of residuals from the fit, or `Alt-E` to exclude a group of lines whose deviates are outside the marker box.

If the identification is wrong for all choices, i.e. the rms is too large everywhere, repeat the whole procedure with a reduced amount of lines included (delete all lines in the table, repeat the line locating with a raised level, so that only the strongest lines are selected).

A larger number of identified lines may result if the catalogue is changed to `tharpen.cat`. The wavelengths in the table are updated from the previous search by the command `pickup from catalogue`.

Make the fit and remove deviating points. The rms should be around 1–10 mÅ. Run the `Adjacent orders` command to calculate approximate dispersion curves for all adjacent orders of the image.

Run the line parameters program for every order in that image to locate the positions of spectral lines, and to pick up the wavelengths from the catalogue. Make the fit and exclude the most deviating points (this can be also done later during the global fit). The parameters of the spectral lines including their wavelengths are stored in separate binary (non-FITS) files for each spectral order with the extension `.slp`.

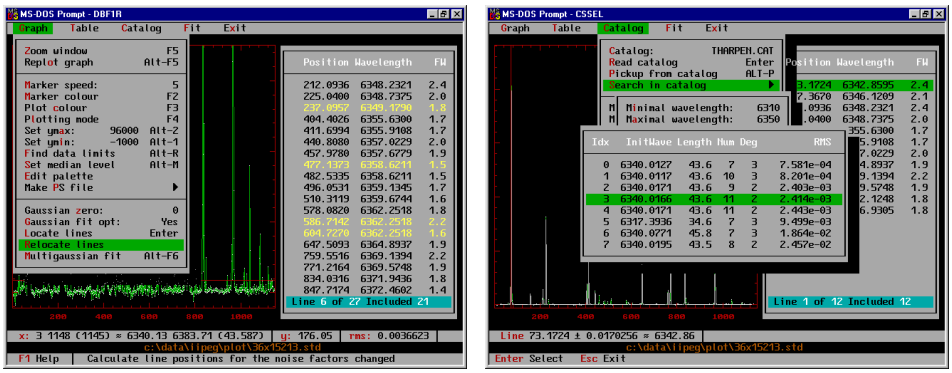

Figure A.8: *Left*: The comparison lines location window commands. The background level is set to zero, the horizontal marker box is positioned above the noise and used to locate all the lines above it. The wavelengths of the lines located are picked up from the catalogue of ThAr lines according to the dispersion polynomials obtained from another order. *Right:* The initial step to find the wavelength of the lines located. Give the approximate wavelength range of the blue (left) end of the spectrum and its length, obtained from the focal plane model of the spectrograph. A number of solutions is shown. The two solutions which have the same initial wavelength and most of the lines included (field `Num`) are the correct solutions.

Wavelength solution

Run the `ArcLamp solution` command on the packed comparison spectrum image with the wavelengths identified. It displays the global fit in two projections: along the central row and along the dispersion direction in wavelengths scaled to some reference order number. The default value for this order number is 40. Remove the most deviating points with the marker box. For a single comparison image, typical degrees (along time × columns × wavelengths), rms, and the fit error for the image centre are (the units are $\mathrm{m\,s^{-1}}$):

Camera	Degrees	rms	FitErr
1st	$0 \times 1 \times 3$	70	10
2nd	$0 \times 2 \times 4$	120	15
3rd	$0 \times 1 \times 4$	600	35

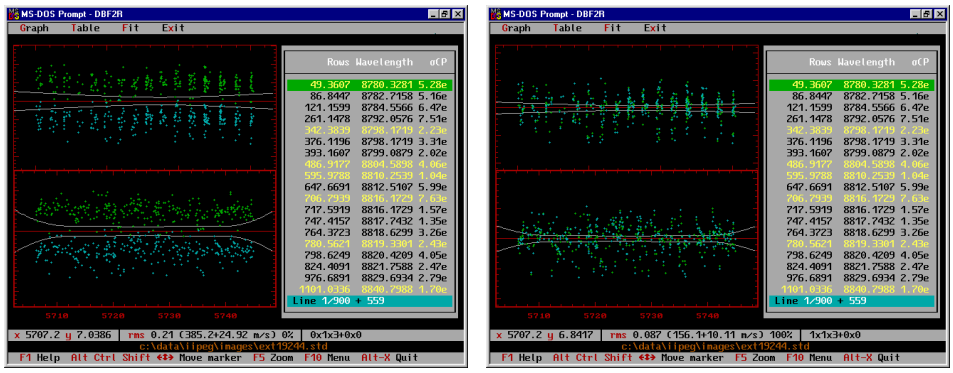

Figure A.9: *Left*: Two comparison spectra images, taken before and after the stellar exposure, are merged into the global fit. The effect of the drift of the line positions is seen. *Right*: The same as in the previous picture after the fit versus time is performed. The polynomial dispersion degree across the rows is 3, the divergence degree across the columns is 1, and in time it is 1 since only two images are involved.

Multiple wavelength identification

After the wavelength scale is established for a single reference comparison image, the wavelength scale can be established for all other images of the same spectral region and camera. Mark the images, run the `Coalign spectra` command, and point to the reference comparison spectrum. The parameter p specified in the menu command is the search interval ($\pm p$) of the cross-correlation range which is used to define the shift between the spectra.

When the procedure has succeeded, unmark all records selected, and run the comparison spectrum wavelength solution for each image to inspect the fit and to remove the most deviating points. The procedure creates a binary (non-FITS) file of the dispersion coefficients with the extension `.was`.

Multiple wavelength solutions

In order to exclude any effects related to the instability of the spectrograph, two or more comparison spectrum images which were taken before and after the object

exposure can be combined into one wavelength solution. Mark the images and run the program. Increase the time degree in the fit. Combination of two images should improve the rms of the fit by a factor $\sqrt{2}$. The dispersion coefficients for multiple comparison spectra are stored with the name of the first image.

Transformation into wavelength scale

At this stage the object spectra can be transformed into the wavelength scale if the telluric correction will not be applied. The wavelength scale command asks for the comparison image and the object image. The object spectra (orders) are transformed into the wavelength scale and stored as separate files.

A.9.2 The telluric wavelength solution

Creation of the telluric image

Mark the object images and apply a weighted spline with the smoothing factor 0.001 or so and the clipping factors 2 (below) and 0 (above) with taking the difference. The file extension for the difference could be `.atm`. The image with the difference should contain mostly the sharp telluric lines while the broader stellar lines are filtered out (see Fig. A.10).

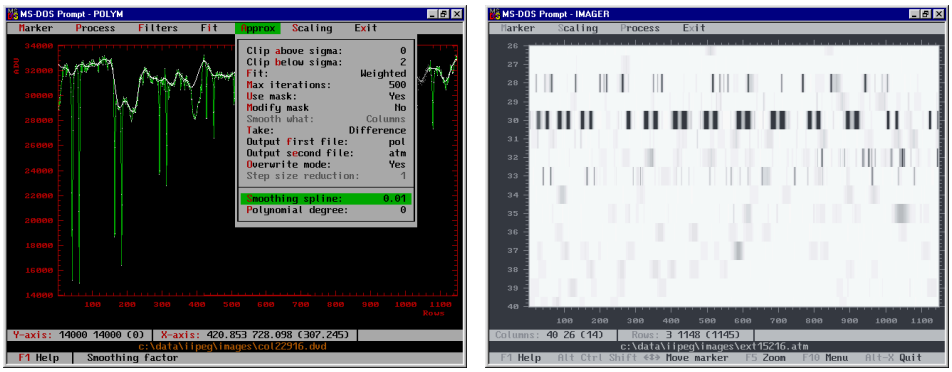

Figure A.10: *Left*: A spectral order with the telluric lines. The smoothness of the spline is adjusted to filter the stellar lines out and leave the sharp telluric features. The difference of the two constitutes the telluric image. *Right*: The telluric image of the packed spectral orders after most of the stellar lines were filtered out.

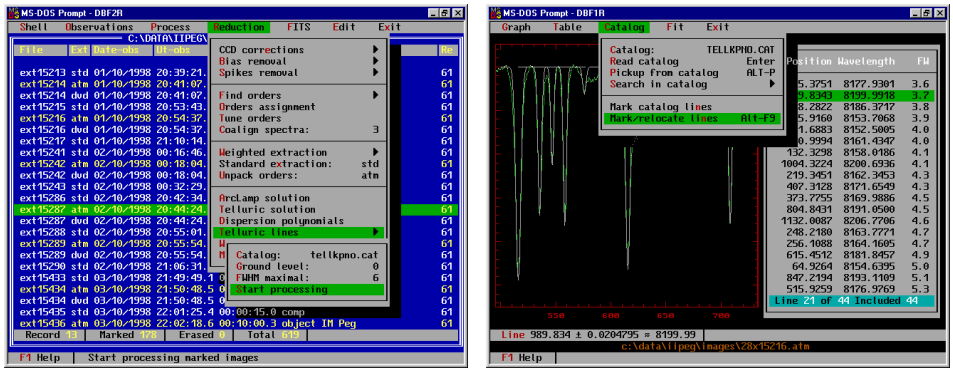

Figure A.11: *Left*: The telluric line identification menu. The selected images `.atm`, the catalogue specified, the continuum level, and the maximal FWHM of the lines to be selected are shown. *Right*: A fragment of the unpacked spectral order containing the identified telluric lines for the image. The same result can be obtained in order-by-order basis with use of the `Mark/Relocate lines` command as shown in the open menu.

Dispersion polynomials

In order to make the identification of the telluric lines possible, one should know the wavelength scale of the telluric images. Then, the program can guess the wavelength of the detected feature and find its exact wavelength from the catalogue of the telluric lines. The dispersion polynomials for each order and every telluric image have to be generated. Resort the database of images, so that they are in order of time. The comparison spectrum images should have the wavelength solution at the time. Run the `Reduction/Dispersion polynomials` command. In the bottom prompt line it will be indicated what to enter: first, it asks to point to the comparison spectrum, then to the telluric image. Once it is done, the program calculates the polynomials for every order of the image (binary non-FITF files with the extension `.fps`). Then enter the next pair of images. To exit from the cycle, press `Esc`. In case there are many telluric images and a single comparison spectrum, the procedure can be done faster by marking these images and entering only the comparison image.

Identification of the telluric lines

Open the menu of `Reduction/Telluric lines` and specify the catalog which should be `tellkpno.cat`: a catalog of the telluric lines derived from the Solar Photographical Atlas. Specify the background level: the intensity of the continuum. In case the difference was taken, the continuum level is zero, in case of

normalization, it is one. Specify the maximal width of the telluric lines: the program will reject all choices where the identified line is broader than the specified limit. The value depends on the resolving power and a good choice is 2–6 pixels FWHM. Run the procedure for the selected packed images (see Fig. A.11).

In case of having some problems, the identification can be inspected for individual orders step-by-step (Fig. A.11). To do that, unpack the image of the telluric lines and run the spectral line parameters program for an order where telluric lines are expected (5000–9000 Å). The dispersion polynomials are assumed to be prepared. The presence of the dispersion polynomial is indicated in the status bar: as the graphical marker is moved it displays the approximate wavelength for the marker position. Change the catalog name to `tellkpno.cat`. Run the `Mark/Relocate` command, which makes an initial guess about the line positions based on the dispersion polynomials and the wavelength from the catalog, and relocates the lines to the observed spectrum (it means that it tries to fit a Gaussian to the spectrum at the position where the telluric line is expected). The lines wider than 3 pixels FWHM are deleted. Inspect the Gaussian fit for every line, make a dispersion curve fit, and remove the most deviating lines. A potential pitfall of the procedure is that the telluric lines can be confused with narrow stellar lines which is then difficult to recognize because of the small number of lines.

Make a global fit of the telluric image by using the comparison spectrum wavelength solution and remove deviates.

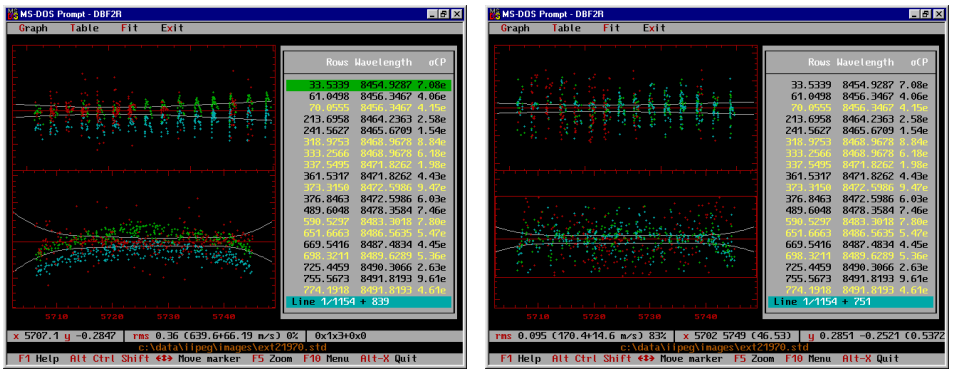

Figure A.12: *Left*: The combined fit of two comparison spectrum images and telluric lines prior to the exclusion of the deviating lines. In spite of the large scatter of the telluric lines, they tend to cluster around a curve. *Right*: The combined fit after the deviating points are excluded (with help of the exclusion out of the box command `Alt-E`).

Wavelength solution

The telluric solution allows to combine one or two comparison spectra and the telluric spectrum into one global fit. The final wavelength solution for the object images is made by obtaining the telluric solution for every observation. Mark the two (or the first, if the second does not exist) comparison images, run the `telluric solution` command, and select the record with the telluric image. Make the fit by `F7`. If there are many telluric lines, they should cluster around a curve. Many deviating lines can be excluded by using the `Alt-E` command, which excludes all lines outside of the marker box.

Change the degree in rows from 0 to 1 or higher and check the significance of the fit. In most cases, the zeroth degree in rows is enough. Use the `Partial` option to display the behavior of the telluric lines curve with respect to the comparison spectrum lines. This may help to estimate the degree of the telluric polynomial according to its curvature.

Typical values based on the telluric solution with two comparison images are (the degrees are along time × columns × wavelengths for the comparison image + columns × rows for the telluric image; the units are $\mathrm{m\,s^{-1}}$):

Camera	Degrees	rms	FitErr
1st	$1 \times 1 \times 3 + 0 \times 1$	80	12
2nd	$1 \times 2 \times 4 + 0 \times 1$	120	20
3rd	$1 \times 1 \times 4 + 0 \times 1$	800	75

The dispersion coefficients are written to a non-FITS file with the extension `.was` and the name of the telluric image.

Transformation into the wavelength scale

The transformation into the wavelength scale is done as described before in Sec. A.9.1, except that the "comparison spectrum image" is now the telluric image.

A.10 The wavelength transformations

Heliocentric correction

The correction for the Earth's motion is done by removing its projected radial velocity from the wavelength table of the marked spectra by running the `Remove Radvel` command in the `Reduction/Wavelength transformation` menu. Specify the output files extension, the usual choice is `.hwl`. The `Add error` option is

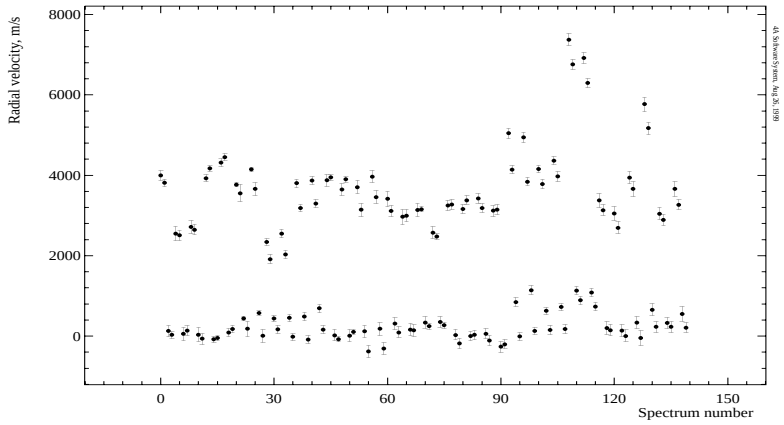

Figure A.13: The plot shows the effect of the slit error correction made for 35 different observations of Ap stars with the short 3rd camera. The vertical axis is the radial velocity in $\mathrm{m\,s^{-1}}$ and the horizontal is the spectrum number. Two water-line rich orders (#27 and #31) were used for the comparison. The upper part shows the comparison of telluric line positions with respect to an artificial spectrum prior to the correction. A significant offset of all spectra by about 0.7 pixels (the pixel size is 5400 $\mathrm{m\,s^{-1}}$) is evident. The lower part shows the same comparison after the combined telluric solution was applied. The average level is 260 $\mathrm{m\,s^{-1}}$. The most deviating points around spectrum number 110 are from a bright star which was difficult to centre accurately onto the slit. The larger the centring error, the larger the difference between the dispersion polynomials of the comparison spectrum and the telluric lines, which results in an incomplete correction of the slit effect.

irrelevant for this procedure. The velocity in $\mathrm{m\,s^{-1}}$ is given in the FITS header by `EARTHVEL` and used by the command as an argument.

If the record is not present, run the `Target` command on the marked spectra to update the header records. Spectra co-added prior to the heliocentric correction have no `EARTHVEL` parameter since the midpoint of the sum has changed. These spectra have to be updated with the `Target` procedure.

Stellar radial velocity rest frame

Similarly, the correction for the stellar radial velocity is done by removing the radial velocity given in a specified FITS keyword; again, a new copy of each spectrum with the specified extension, `.swl` for instance, is created. The stellar velocity FITS record should be created with the `FITS/Modify record` command: enter

a name, select the floating-point format, and the value in $\mathrm{m\,s^{-1}}$. The velocity will be removed from the spectrum, which means that the red-shifted spectrum should have the positive velocity. The procedure assumes that the spectra are in the wavelength scale. The wavelengths of the resulting spectra are modified for each pixel according to the velocity given: $\lambda_i \cdot (1 - v/c)$.

The `Add error` option requires also an error of the radial velocity to be given in the FITS record with the prefix `E` in the name of the velocity keyword name. The option affects the variance of the pixel intensities.

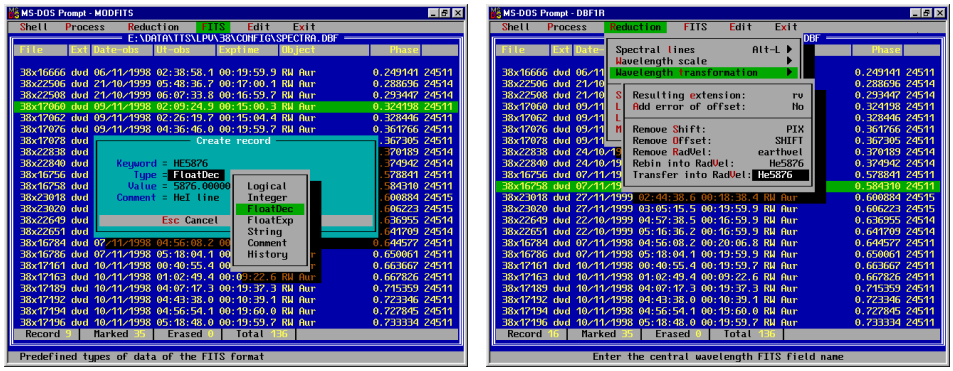

Figure A.14: *Left*: The picture shows how the FITS keyword is created to specify the wavelength of a line. The dialog window is opened from the `Fits/Modify record` menu. The new FITS record will be appended to the headers of the spectra marked in the database. *Right*: The transfer to radial velocity scale dialogue window: the resulting file extension `.rv` and the FITS keyword having the central wavelength as its value are shown.

Rebinning into radial velocity

The procedure rebins the selected spectra into the radial velocity scale with respect to the wavelength which is given in the specified FITS record. It creates a new set of spectra with the file extension as specified in the menu window. The spectra are rebinned into the same step size in the velocity scale ($\Delta\lambda \cdot c/\lambda = \mathrm{const}$ for any part of each spectrum). The zero velocity corresponds to the reference wavelength chosen. The distance between two lines in velocity scale will not depend on their wavelength. The rebinning procedure involves modification of the spectrum intensities and their variances.

If the `Add error` option is set to `Yes`, then the error of the wavelength calibration is involved into the calculation of variances of rebinned pixels.

The rebinned spectra can be used for radial velocity measurements, although the

cross-correlation procedure itself does the rebinning from wavelength into radial velocities in case the `Radvel` option is selected.

Transformation into radial velocity

The procedure is similar to the previous one, but no rebinning of the intensities is performed. The wavelengths are transformed into radial velocity scale with respect to the central wavelength specified in the FITS record: $v_i = c \cdot \ln(\lambda_i/\lambda_c)$. This creates a table of unequally spaced radial velocities for each pixel of the spectrum. The spectra can be used for the cross-correlation in `Wavelength` rebinning mode.

The `Add error` option has no effect for this procedure.

Remove offset in pixels

The procedure removes an offset in pixel scale and the value is given in the specified FITS record. The type of the spectrum argument units is irrelevant. A shift by one pixel moves the pixel position (wavelength number, radial velocity, etc.) from the original pixel to the new one which results in the shift of the spectrum leftwards with respect to the original one. A shift by half a pixel results in a spectrum where the pixel position is calculated as the mean of the positions of two adjacent pixels.

The `Add error` option requires also an error of the offset given in the FITS record with the prefix `E` in the name of the pixel shift keyword name. The option affects the variance of the pixel intensities.

Remove offset in wavelength

The procedure removes the offset given in axis units which can be wavelength, radial velocity, pixels, etc. and results in modification of pixel positions.

The `Add error` option requires also an error of the offset given in the FITS record with the prefix `E` in the name of the wavelength offset keyword name. The variance of the pixel intensities are modified according to the error of the wavelength scale (if the spectra are in wavelength scale) and the error of the specified offset.

A.11 Continuum normalization

The continuum normalization involves fitting of a smoothing spline or a polynomial to the area of the spectrum free of spectral lines. The procedure requires the presence of the variances in the spectrum (to check it, display the spectrum and run the plot variance command in `Scaling` menu `Alt-V`). If for some reason no

variances are present, make an estimation of the photon noise or set the variances to a constant in the `Process/variances` menu of the database of spectra.

The fitting of the curve is done from the `Approximation` menu after the spectrum is displayed. Use the `Gray-` key to mask pixels out or `Gray+` key to unmask them (the masked pixels are displayed in a gray colour). The pixels around spectral lines being masked out are not used for the approximation. Open the `Approximation` window, select `Weighted` fit, set clipping levels to 0, and use a spline of the specified smoothing factor or a polynomial of a certain degree. Normally it generates a curve which overplots the spectrum. The curve is automatically saved as a FITS file with the same name as the spectrum and the extension `.pol`. The file is added to the last records of the database and can be retrieved later. In order to generate and display the normalized spectrum on the same screen, choose the option `Take` as `Ratio` by pressing `Enter` on the command (the other choice are `Difference` and `None`). Set up the output normalized spectrum extension in the `Second output` command, `.nor`, for instance. Run the fit again to generate the normalized spectrum which is automatically saved as a FITS file and added to the database. The option `Overwrite mode` prevents overwriting the existing file. For the trial-and-error fit, the option should be set to `Yes`. To display the normalized spectrum in the same scale as the original, change the scaling factor in `Scaling/Scale Alt-F7` to the value, for instance, of 1.5 times of the original spectrum intensity. The normalized spectrum will be enlarged on the screen by this amount (the spectrum intensities are not modified). Change the mask, if necessary, by (un-)masking pixels and tune the fit parameters to satisfy a good continuum.

To facilitate the continuum fitting, the procedure can be used in a clip-and-fit mode to exclude from the fit narrow absorption lines. Set the `Clip below` parameter to 2 and make a fit. The features below 2σ of the standard deviation are masked out and the remaining pixels are used for the fit. In fact, the procedure does a number of iterative fits subsequently masking the deviating pixels before it converges to the some curve. Broad spectral features or emission lines can be excluded from the fit by hand with the `Gray-` command. The resulting normalized spectrum inherits the position of the masked pixels (they are seen in gray): in order to restore them to the normal mode use unmask pixels commands `Gray +`, or it can be done at once for many spectra by running the `Process/Variances/Absolute variances` command from the database of spectra (the spectra should be marked).

The described normalization can also be done for many spectra at the same time if the spectra are similar to each other and cover the same wavelength range. The original marked spectra are displayed on the same screen with the `Alt-Enter` command and the above masking and normalization will be performed for every spectrum at the same time. A useful command for this purpose is `Fit/Transfer intervals`, which masks the same pixels of all displayed spectra as in the first spectrum. A non-interactive fit and continuum normalization can be also done for a number of marked spectra from the `Process/Polynomial approximation`

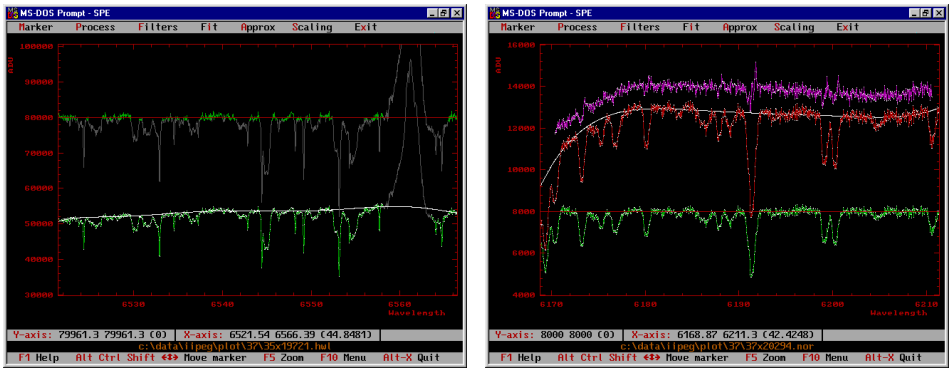

Figure A.15: *Left*: A spectrum normalized to a polynomial continuum of 7th degree in the fit-and-clip mode, where a 2σ clipping of features below the continuum was used. The normalized spectrum was scaled by 80000 to be seen in the same scale as the original spectrum. The broad emission Hα line was excluded from the fit by masking its pixels out with the `Gray-` command, as it is seen on the original spectrum by its gray colour. *Right*: A spectrum normalized to the continuum of the mean spectrum. Shown are the original spectrum, the ratio to the mean spectrum (shifted upwards for clarity), and its polynomial curve which is the continuum. The resulting normalized spectrum is scaled to 8000. In the ratio, a number of small but sharp features are due to line profile variability.

menu of the database of spectra. This can be useful for a large amount of spectra when there are no features to mask out, or the masking has been done with the `Transfer intervals` command.

The other way to normalize to a continuum is to use a mean spectrum. Mark the spectra and make the sum. Fit a continuum to the summed spectrum and normalize to it. Divide every original spectrum by the normalized mean spectrum. In the ratio, non-variable spectral lines are canceled and the shape of the continuum remains. Fit a curve to these divided spectra: the `Take` option should be set to `None`, and all variable line features should possibly be masked out. Divide the original spectra by the smooth curves which constitutes the continuum normalization. To do that, sort the database of spectra by file name and extension, and use pair operations in the `Process` menu to divide the spectra. A synthetic spectrum can be used as well instead of the mean normalized spectrum.

A.12 Cross-correlation of spectra

Select the spectra being used for the cross-correlation and display them simultaneously on the screen with the `Alt-Enter` command. The first spectrum in the

sequence is used as the reference or template spectrum. To change the order of the sequence, use the `Alt-D` or `Alt-Q` commands from the `Marker` menu. The name of the first spectrum in the sequence is displayed in the bottom status bar. Exclude parts of the spectrum which should not be used for the cross-correlation, if necessary, by masking pixels out with the `Gray-` command. From the `Fit` menu run the cross-correlation `Alt-F10`. Three modes for the lag calculations are incorporated: pixels, wavelengths, and radial velocities. Change the calculation mode in the `Marker` menu, the range of the lags, and the number of points of the cross-correlation function within this range. The change of the number of points starts the calculations and displays the function. To interrupt the process press `Esc`.

The cross-correlation function in the pixel scale is calculated regardless of the axis units: the offsets are applied in index units. In the wavelength mode it is calculated in axis units, so that the spectra are rebinned with the same step size in axis units. In the radial velocity mode the spectra are rebinned with the same step size in velocity scale assuming that the axis unit is wavelength. The option `Marker/Position error` is used to take into account the error of the wavelength calibration when calculating the error of the cross-correlation offset determination and is used when the axis unit of the spectra is wavelength.

To find the position of the maximum use the commands from the `Search` menu: the `Parabolic search` command estimates the centroid position based on the curvature of the uppermost points, the `Polynomial fit` command estimates the position of the maximum from a polynomial fit of specified degree, and the `Gaussian fit` command is used to fit a Gaussian to the cross-correlation peak. The centroid positions can be determined individually by going through the table of the offsets, or it can be done at once for all of them. The table includes the following items: the spectrum file name, the position of the function maximum `Offset`, the error of the centroid determination `StdDev` (based on the variances of the spectra and the curvature of the peak), the amplitude of the peak `Rmax`, χ^2_ν of the regression fit `Rchi2`, and the two coefficients of the linear regression `c0` and `c1`. These parameters can be saved into the FITS header of the spectra from the `Exit` menu. Select a FITS keyword to be used to identify these parameters and save the changes. The keyword can be used later to shift the spectra, i.e. to remove the stellar orbital motion, from the `Wavelength transformation` menu as described above.

A.13 Decomposition of line profiles

Line profiles which consist of several components can be decomposed into a number of Gaussian profiles with the use of the `Reduction/Line parameters` procedure (`Alt-F7`). The decomposition function assumes that the variances of the spectrum are present. Enter the function and fit a number of Gaussians to the line profile: to fit an emission profile put the horizontal marker line above the continuum level and to fit an absorption line put the marker below. Press `Enter` to do the fit: firstly,

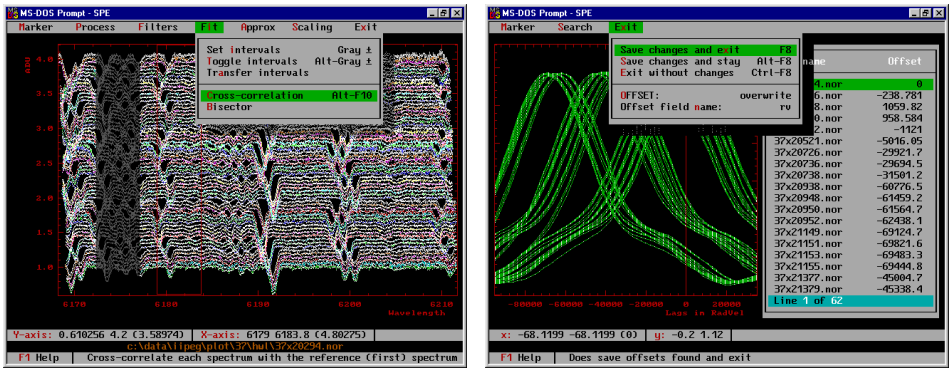

Figure A.16: *Left*: A number of spectra are displayed in order to run the cross-correlation facility. The spectra are offset in intensities and the reference spectrum is at the bottom of the plot. A number of pixels on the left are masked out to be excluded from the regression fit. *Right*: The cross-correlation function for every spectrum and the maximum positions displayed in the table. The lag unit is radial velocity. The opened `Exit` window shows the name of the FITS record used to save the offsets in the header of each spectrum.

it recognizes all the features above or below the marker level, and secondly, makes the fit of a Gaussian to each feature. To fit a Gaussian without minimization of the profile width, change the option in `Marker/Gaussian fit opt` to `No`. This creates a table of the initial guess for the multi-Gaussian fit. The table of the line parameters can also be edited using `Alt-F4`. To display the Gaussian profiles, press `F8` (`Table/Plot Gaussians`).

The next step is to tell the program which of these initial profiles will be used in the multi-Gaussian fit: being in the table of lines press `Alt-I` (`Table/Select line`). A line with the table record in pink indicates that it is included into the fit. In the same way a line can be excluded from the fit. Press `Alt-F6` (`Marker/Multi Gaussian fit`) to start the fit: it opens a window where the current parameters of the Gaussian profiles and the convergence of the fit are displayed. One of the parameters is `DeltaMax` which is the tolerance interval. The fit has converged when the tolerance is less than 10^{-11}. If the fit has converged, as indicated with a message at the bottom status bar, press `Enter` to accept the newly fitted parameters. By pressing `Esc`, the newly found parameters of the fit are discarded. If the fit has not converged, it indicates that the initial guess is too bad: try to fit new Gaussian profiles which describe the components in a more close way.

To display the sum of the decomposed Gaussians, use `Alt-F8` (`Table/Plot sum`). The individual Gaussians can be subtracted from the line profile with `Alt-S` (`Table/Subtract Gaussians`), the line record in the table is displayed in red.

It is useful in some cases, to subtract some of the components and do the fit to the remainders. In this case the subtracted profiles have to be excluded from the fit. The resulting composition of the Gaussians can be written into a separate file by the `Table/Write Gaussians` command. The variances of the function are the errors of the multi-Gaussian fit. It is also possible to modify the original line profile by subtracting one or several components: on exit (`Alt-X`), the program asks whether to save the changes (press `Enter`) or not (press `Esc`). Subtraction of a component changes the variances of the initial line profile.

The resulting parameters in the table from the multi-Gaussian fit are the line position and its error (`Position` and σ`(Pos)`), the amplitude and FWHM of the Gaussian (`Intensity` and `FWHM`), and the equivalent width with its error (`EWG` and σ`(EWG)`). The table of the parameters can be exported into a text file by using the `Table/Print table` command.

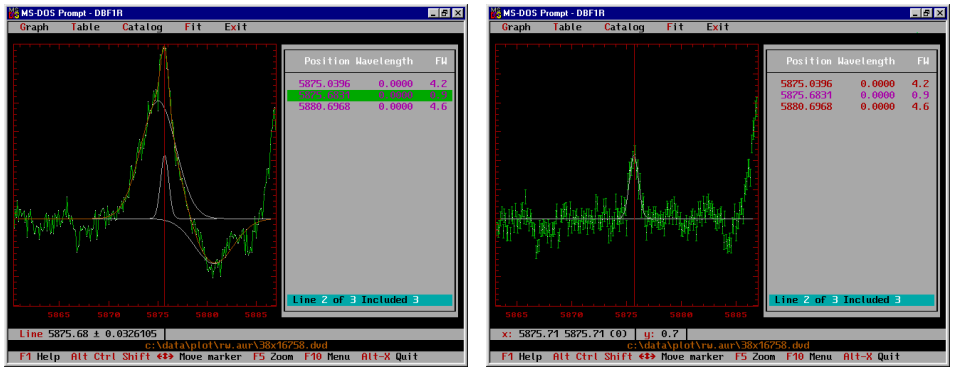

Figure A.17: *Left*: A line profile decomposed onto three Gaussians. The line profile, the individual components, and their sum are shown. *Right*: After the fit, the two broad components are subtracted leaving the narrow component. The plotting mode is changed to show the error bars of the pixels.

References

Allen, C.W. 1976, Astrophysical Quantities, 3rd ed. (University of London, Athlone: London)

Barlow, M.J., Crawford, I.A., Diego, F., Dryburgh, M., Fish, A.C., Howarth, I.D., Spyromilio, J., Walker, D.D. 1995, MNRAS 272, 333

Berdyugina, S.V. 1998, A&A 338, 97

Berdyugina, S.V., Berdyugin, A.V., Ilyin, I., Tuominen, I. 1998, A&A 340, 437

Blades, J.C., Wynne-Jones, I., Wayte, R.C. 1980, MNRAS 193, 849

Bloom, A.L. 1966, Appl. Opt. 5, 1500

Brown, T.M. 1990, in: CCDs in Astronomy (ed. G.H.Jacoby), PASPC 8, p. 335

Bukach, A.B., Zlotnikov, L.F. 1995, Bull. Crimean Astrophys. Obs. 89, 138

Collier Cameron, A. 1992, in: Surface Inhomogeneities on Late-type Stars (eds. P.B.Byrne & D.J.Mullan), (Springer-Verlag: Berlin) p. 33

Collier Cameron, A. 1999, in: Precise stellar radial velocities, IAU Coll. 170 (eds. J.B.Hearnshaw & C.D.Scarfe), PASPC 185, p. 233

Constable, S.C., Parker, R.L., Constable, C.G. 1987, Geophysics 52, No. 3, 289

Craig, I.J.D., Brown, J.C. 1986, Inverse Problems in Astronomy (Hilger: Bristol)

Diego, F., Fish, A.C., Barlow, M.J., Crawford, I.A., Spyromilio, J., Dryburgh, M., Brooks, D., Howarth, I.D., Walker, D.D. 1995, MNRAS 272, 323

Donati, J.-F., Semel, M., Carter, B., Rees, D.E., Collier Cameron, A. 1997, MNRAS 291, 1

Donati, J.-F., Semel, M. 1990, Sol. Phys. 128, 227

Dravins, D. 1993, "The Impact of Long-Term Monitoring on Variable Star Research", NATO workshop (eds. C.Sterken & M.de Groot)

Dunteman, G.H. 1989, Principal components analysis (SAGE: Newbury Park, California)

Fierro, R.D., Golub, G.H., Hansen, P.C., O'Leary, D.P. 1997, SIAM J. Sci. Comput. 18, No. 4, 1223

Golub, G.H., van Loan, C.F. 1980, SIAM J. Numer. Anal. 17, 883

Golub, G.H., van Loan, C.F. 1989, Matrix computations (Johns Hopkins University Press: Baltimore)

Gosset, E., Magain, P. 1993, ESO Messenger 73, 13

Gray, D.F. 1986, in: Instrumentation and Research Programmes for Small Telescopes, IAU Symp. 118 (eds. J.B.Hearnshaw & P.L.Cottrel), (Reidel: Dordrecht), p. 401

Gray, D.F. 1988, Lectures on spectral-line analysis: F, G, and K stars (Arva: Ontario)

Gray, D.F. 1992, The observation and analysis of stellar photospheres, 2nd ed. (Cambridge University Press: Cambridge)

Griffin, R.F. 1969, MNRAS 143, 319

Hamuy, M., Walker, A.R., Suntzeff, N.B., Gigoux, P., Heathcote, S.R., Phillips, M.M. 1992, PASP 104, 533

Hansen, P.C. 1997, Rank-Deficient and Discrete Ill-Posed Problems: Numerical Aspects of Linear Inversion (SIAM: Philadelphia)

Hocking, R.R. 1976, Biometrics 32, 1

Ilyin, I.V. 1995, Bull. Crimean Astrophys. Obs. 89, 127

Ilyin, I.V. 1996, Remote control observations with the SOFIN spectrograph and reduction of CCD échelle spectra. Licentiate Dissertation, University of Oulu

Ilyin, I.V. 2000, Numerical methods of data analysis – A collection of notes to 4A algorithms. (Unpublished)

Jackson, E. 1991, A User's Guide to Principal Components (Wiley: New York)

Janesick, J. 1997, SPIE 3019, 70

Jorden, P., Deltorn, J.-M., Oates, P. 1993, RGO Gemini 41, 1

Kendall, M. 1975, Multivariate analysis (Griffin: London)

Kurucz, R.L., Furenlid, I., Brault, J., Testerman, L. 1984, National Solar Observatory Atlas No. 1 (Tucson, NSO)

Lagutin, A.F. 1995, Bull. Crimean Astrophys. Obs. 89, 127

Lang, K.R. 1974, Astrophysical Formulae (Springer-Verlag: Berlin)

Lauer, T.R. 1999, PASP 111, 227

Melles Griot Co. 1988, Optics Guide 4

Neumaier, A. 1998, SIAM Rev. 40, 636

Pan, X., Shao, M., Colavita, M.M., Armstrong, J.T., Mozurkewich, D., Vivekanand, M., Denison, C.S., Simon, R.S., Johnston, K.J., 1992, ApJ 384, 624

Petrov, P.P., Zajtseva, G.V., Efimov, Yu.S., Duemmler, R., Ilyin, I.V., Tuominen, I., Shcherbakov, V.A. 1999, A&A 341, 553

Piskunov, N.E., Tuominen, I., Vilhu, O. 1990, A&A 230, 363

Plachinda, S.I., Tarasova, T.N. 1999, ApJ 514, 402

Press, W.H., Teukolsky, S.A., Vetterling, W.T., Flannery, B.P. 1992, Numerical Recipes, 2nd ed. (Cambridge University Press: Cambridge)

Pronik, V.I. 1995, Bull. Crimean Astrophys. Obs. 89, 111

Rakos, K.D., Jenkner, H., Wood, J. 1981, A&AS 43, 209

Rucinski, S. 1999, in: Precise stellar radial velocities, IAU Coll. 170 (eds. J.B.Hearnshaw & C.D.Scarfe), PASPC 185, p. 82

Ryabchikova, T.A., Malanushenko, V.P., Adelman, S.J. 1999, A&A 351, 963

Schroeder, D.J., Hilliard, R.L. 1980, Appl. Opt. 19, 2833

Shallis, M.J., Baruch, J.E.F., Booth, A.J., Selby, M.J. 1995, MNRAS 213, 307

Shcherbakov, A.G., Shcherbakova, Z.A., Ilyin, I., Tuominen, I. 1995, in: New developments in array technology and applications (eds. D.Philip, K.A.Janes, A.R.Upgren), IAU Symp. 167

Siegman, A.E. 1971, An introduction to lasers and masers (McGraw-Hill: New York)

Stoer, J. 1993, Introduction to numerical analysis (Springer: New York)

Svelto, O., Hanna, D.C. 1989, Principles of Lasers, 3rd ed. (Plenum Press: New York)

Taylor, B.J. 1984, ApJS 54, 259

Thorne, F.J., Jorden, P.R., Waltham, N.R. 1987, Proceedings of ESO-OHP workshop "The Optimization of the Use of CCD Detectors in Astronomy", ESO Conf. Proc. No. 25

Tomkin, J., Pan, X., McCarthy, J.K., 1995, AJ 109, 780

Tull, R.G. 1972, in: ESO/CERN Conference on Auxiliary Instrumentation for Large Telescopes (eds. S.Laustsen & A.Reiz), p. 269

Tull, R.G., MacQueen, P.J., Sneden, C., Lambert, D.L. 1995, PASP 107, 251

Tuominen, I. 1992, NOT News, No. 5, p. 15

Valenti, J.A., Butler, R.P., Marcy, G.W. 1995, PASP 107, 966

Vogt, S.S., Penrod, G.D., Hatzes, A.P. 1987, ApJ 321, 496

Wahlgren, M., Dolk, L., Kalus, G., Johansson, S. 1999, submitted to ApJ

Watkins, D.S. 1991, Fundamentals of matrix computations (Wiley: New York)

Wayte, R.C., Wynne-Jones, I., Blades, J.C. 1978, MNRAS 182, 5P

Woolard, E.W., Clemence, G.M. 1966, Spherical Astronomy (Academic Press: New York)

Part II

Publications

Appendix B

Publications based on SOFIN observations

In this chapter a list of publications is given where the observing and reduction methods presented in the thesis were used.

The publications are divided into three groups, the first two (T Tau and RS CVn stars) contain results of the research project "Late type stars and interstellar matter: activity, magnetism, and turbulence" at the University of Oulu. The third group gives the papers of other works to which the author has contributed. Selected publications, marked with a bullet in the list, are presented in the subsequent part of this thesis.

The author's contributions in most of the papers are observations and data reduction. This has given the possibility to develop the observing technique and data analysis, and to obtain a unique set of scientific observations. Frequent observations, analysis of various instrumental effects, the CCD optimization, development of the specific observing approach to the spectrograph resulted in high quality spectra as compared to the earliest observations with SOFIN or with other spectrographs we have used. The data reduction facility, as it is described in this thesis, was not created at once but was continuously developed during the past years with the raw material in hands. The most essential procedures which determine the quality of spectra reduction were recreated in some cases several times to achieve the maximum efficiency and stability. All this has resulted in excellent scientific output.

A demand to observe and analyze small effects of the line profile position and shape, which we see in the spectra of e.g. extra-solar planetary systems and stars which undergo non-radial pulsations, was a next step in the development of the data analysis facility including the error propagation in the data reduction, ad-

vanced cross-correlation, multi-period analysis, and the spectrum/PSF deconvolution facilities. The work is still going on and many new results are not included in the present thesis.

B.1 T Tau stars

Refereed journals:

Petrov, P.P., Gullbring, E., Ilyin, I., Gahm, G.F., Tuominen, I., Hackman, T., Lodén, K. 1996, "The gas flows of SU Aurigae", A&A 314, 821

Gullbring, E., Petrov, P.P., Ilyin, I., Tuominen, I., Gahm, G.F., Lodén, K. 1996, "Line profile variations of the classical T Tauri star BP Tauri", A&A 314, 835

Zajtseva, G., Petrov, P.P., Ilyin, I., Duemmler, R., Tuominen, I. 1996, "RY Tauri at high brightness", IBVS 4408

- Petrov, P., Duemmler, R., Ilyin, I, Tuominen, I. 1998, "Increase of emission and shell features in the spectrum of the FUor V1057 Cyg", A&A 331, L53

- Petrov, P.P., Zajtseva, G.V., Efimov, Yu.S., Duemmler, R., Ilyin, I.V., Tuominen, I., Shcherbakov, V.A. 1999, "Brightening of the T Tauri star RY Tauri in 1996. Photometry, polarimetry and high-resolution spectroscopy", A&A 341, 553

Conference proceedings:

Gahm, G.F., Petrov, P., Tuominen, I., Gullbring, E., Ilyin, I. 1995, "High-resolution spectroscopy of T Tauri stars", 4th MUSICOS workshop (eds. L.Huang, D.S.Zhai, C.Catala, B.H.Foing), p. 237

Petrov, P.P., Gullbring, E., Gahm, G.F., Lodén, K., Ilyin, I., Tuominen, I., Hackman, T. 1995, "Wind, accretion and spots of the T Tau star SU Aurigae", Stellar surface structure (ed. K.Strassmeier), IAU Symp. 176, Poster Proceedings, p. 217

Zajtseva, G., Efimov, Yu., Petrov, P., Ilyin, I., Duemmler, R., Tuominen, I. 1998, "Brightening of the T Tauri star RY Tau in 1996", Cool Stars, Stellar Systems, and the Sun, 10th Cambridge Workshop, (eds. J.A.Bookbinder & R.A.Donahue), PASPC 154, p. 1808

B.2 RS CVn stars

Refereed journals:

- Duemmler, R., Ilyin, I., Tuominen, I. 1997, "A new radial velocity curve for the RS CVn star σ Gem. Constraints on its physical parameters.", A&AS 123, 209

- Berdyugina, S.V., Jankov, S., Ilyin, I, Tuominen, I., Fekel, F.C. 1998, "The active RS Canum Venaticorum binary II Pegasi. I. Stellar and orbital parameters", A&A 334, 863

- Berdyugina, S.V., Berdyugin, A.V., Ilyin, I., Tuominen, I. 1998, "The active RS Canum Venaticorum binary II Pegasi. II. Surface images for 1992-1996", A&A 340, 437

Korhonen, H., Berdyugina, S.V., Hackman, T., Duemmler, R., Ilyin, I.V., Tuominen, I. 1999, "Study of FK Comae Berenices. I. Surface images for 1994 and 1995", A&A 346, 101

- Berdyugina, S.V., Ilyin, I., Tuominen, I. 1999, "The long-period RS Canum Venaticorum binary IM Pegasi. I. Orbital and stellar parameters", A&A 347, 932

- Berdyugina, S.V., Ilyin, I., Tuominen, I. 1999, "The active RS Canum Venaticorum binary II Pegasi. III. Chromospheric emission and flares in 1994-1996", A&A 349, 863

- Berdyugina, S.V., Berdyugin, A.V., Ilyin, I., Tuominen, I. 1999, "The active RS Canum Venaticorum binary II Pegasi. IV. The spot activity cycle", A&A 350, 626

- Berdyugina, S.V., Berdyugin, A.V., Ilyin, I., Tuominen, I. 2000, "The long-period RS Canum Venaticorum binary IM Pegasi. II. First surface images", accepted by A&A

Conference proceedings:

Shcherbakov, A.G., Fernandez-Figueroa, M.J., Martin-Parra, F., De Castro, E., Cornide, M., Montes, D., Ilyin I., Tuominen I. 1995, "The He I 10830Å and Ca II H observations of the RS CVn system ζ And", Stellar surface structure (ed. K.Strassmeier), IAU Symp. 176, Poster Proceedings, p. 181

Berdyugina, S., Ilyin, I., Tuominen, I. 1998, "II Peg: Stellar and Orbital Parameters", Cool Stars, Stellar Systems, and the Sun, 10th Cambridge Workshop, (eds. J.A.Bookbinder & R.A.Donahue), PASPC 154, p. 1384

Berdyugina, S., Ilyin, I., Tuominen, I. 1998, "II Peg: New Surface Images for 1992-1996", Cool Stars, Stellar Systems, and the Sun, 10th Cambridge Workshop, (eds. J.A.Bookbinder & R.A.Donahue), PASPC 154, p. 1952

Berdyugina, S., Ilyin, I., Tuominen, I. 1998, "II Peg: Quiescent Chromospheric Emission and Flares in 1994-1996", Cool Stars, Stellar Systems, and the Sun, 10th Cambridge Workshop, (eds. J.A.Bookbinder & R.A.Donahue), PASPC 154, p. 1477

Aarum, V., Berdyugina, S.V., Ilyin, I.V. 1999, "Doppler imaging of UX Ari", Proceedings of Astrophysics with the NOT (eds. H.Karttunen & V.Piirola), University of Turku, p. 222

Korhonen, H., Berdyugina, S.V., Duemmler, R., Hackman, T., Ilyin, I.V., Tuominen, I. 1999, "Surface imaging of FK Comae Berenices", Proceedings of Astrophysics with the NOT (eds. H.Karttunen and V.Piirola), University of Turku, p. 234

Berdyugina, S., Ilyin, I., Tuominen, I. 2000, "II Peg: the spot activity cycle", Cool Stars, Stellar Systems, and the Sun, 11th Cambridge Workshop, (eds. M.R.Zapatero Osorio, R.García López & R.Rebolo), PASPC (in press)

Berdyugina, S., Berdyugin, A.V., Ilyin, I., Tuominen, I. 2000, "IM Peg: first surface images", Cool Stars, Stellar Systems, and the Sun, 11th Cambridge Workshop, (eds. M.R.Zapatero Osorio, R.Garsia Lopez & R.Rebolo), PASPC (in press)

Berdyugina, S., Ilyin, I., Tuominen, I. 2000, "LQ Hya: surface images for 1993-1999", Cool Stars, Stellar Systems, and the Sun, 11th Cambridge Workshop, (eds. M.R.Zapatero Osorio, R.García López & R.Rebolo), PASPC (in press)

Piskunov, N., Vincent, A., Duemmler, R., Ilyin, I., Tuominen, I. 2000, "Doppler imaging of the eclipsing binaries ER Vul and TY Pyx", Cool Stars, Stellar Systems, and the Sun, 11th Cambridge Workshop, (eds. M.R.Zapatero Osorio, R.García López & R.Rebolo), PASPC (in press)

B.3 Other stars and topics

Refereed journals:

Polosukhina, N., Kurtz, D., Hack, M., North, P., Ilyin, I., Zverko, J., Shakhovskoy, D. 1999, "Lithium on the surface of cool magnetic CP stars I. Summary of spectroscopic observations with three telescopes", A&A 351, 283

Tautvaisiene, G., Tuominen, I., Ilyin, I. 1999, "M 67: an Exhibitor of Metal Abundant Core Helium-Burning Stars", Ap&SS 265, 285

Tautvaisiene, G., Edvardsson, B., Tuominen, I., Ilyin, I. 2000, "Chemical composition of evolved stars in the open cluster M 67", accepted by A&A

Conference proceedings:

Shcherbakov, A.G., Shcherbakova, Z.A., Ilyin, I., Tuominen, I. 1995, "Performance and astrophysical applications of EEV and Electron Corp. virtual phase CCDs in the near infrared He I 10830Å region", New developments in array technology and applications (eds. D.Philip, K.A.Janes, A.R.Upgren), IAU Symp. 167

Schulz, R., Arpigny, C., Manfroid, J., Ilyin, I., Rickman, H., Stüwe, J.A. 1997, "On the $^{13}CN/^{12}CN$ isotopic ratio in comet Hale-Bopp", Bull. AAS, 29th DPS meeting, No. 3, 37.09, p. 1048

- Ilyin, I.V., Duemmler, R. 1999, "Precise radial velocity measurements with a Cassegrain spectrograph. I. Wavelength calibration.", in: Precise stellar radial velocities, IAU Coll. 170 (eds. J.B.Hearnshaw & C.D.Scarfe), PASPC 185, 63

- Ilyin, I.V., Duemmler, R. 1999, "Precise radial velocity measurements with a Cassegrain spectrograph. II. Radial velocity determination and applications", in: Precise stellar radial velocities, IAU Coll. 170 (eds. J.B.Hearnshaw & C.D.Scarfe), PASPC 185, 68

Ilyin, I.V., Duemmler, R. 1999, "Precise radial velocities from the SOFIN Cassegrain échelle spectrograph", Proceedings of Astrophysics with the NOT (eds. H.Karttunen & V.Piirola), University of Turku, 242

Tuominen, I., Ilyin, I.V., Petrov, P.P. 1999, "High resolution spectroscopy with SOFIN", Proceedings of Astrophysics with the NOT (eds. H.Karttunen & V.Piirola), University of Turku, p. 47

Nielsen, K., Wahlgren, G.M., Ilyin, I.V. 1999, "Observations in the near-UV with the SOFIN", Proceedings of Astrophysics with the NOT (eds. H.Karttunen & V.Piirola), University of Turku, p. 248

Wahlgren, G.M., Plez, B., Ilyin, I. 2000, "Abundance analysis of luminous M-type stars using near-UV spectroscopy", Cool Stars, Stellar Systems, and the Sun, 11th Cambridge Workshop, (eds. M.R.Zapatero Osorio, R.García López & R.Rebolo), PASPC (in press)

Grinin, V.P., Kozlova, O., Rostopchina, A.N., Natta, A., Ilyin, I.V., Tuominen, I., Thé, P.S. 1999, "Spectral variability of the UX Ori type stars", Proceedings of Astrophysics with the NOT (eds. H.Karttunen & V.Piirola), University of Turku, p. 226

Tautvaisiene, G., Tuominen, I., Ilyin, I. 1998, "M67: an Exhibitor of Metal Abundant He-Core Burning Stars", Proceedings of Galaxy Evolution: Connecting the Distant Universe with the Local Fossil Record, Paris-Meudon Observatory

Tautvaisiene, G., Tuominen, I., Ilyin, I.V. 1999, "Evolutionary effects in atmospheres of metal abundant red horizontal branch stars", Proceedings of Astrophysics with the NOT (eds. H.Karttunen & V.Piirola), University of Turku, p. 214

Paper I & II

Ilyin, I.V., Duemmler, R. 1999, "Precise radial velocity measurements with a Cassegrain spectrograph. I. Wavelength calibration", in: Precise Stellar Radial velocities, IAU Coll. 170 (eds. J.B.Hearnshaw & C.D.Scarfe), PASPC 185, p. 63

Ilyin, I.V., Duemmler, R. 1999, "Precise radial velocity measurements with a Cassegrain spectrograph. II. Radial velocity determination and applications", in: Precise Stellar Radial velocities, IAU Coll. 170 (eds. J.B.Hearnshaw & C.D.Scarfe), PASPC 185, p. 68

Precise Stellar Radial Velocities
ASP Conference Series, Vol. 185*, 1999*
J.B. Hearnshaw and C.D. Scarfe, eds.

Precise radial velocity measurements with a Cassegrain spectrograph. I. Wavelength calibration

I.V.Ilyin, R.Duemmler

Astronomy Division, University of Oulu, FIN-90571, Oulu, Finland

Abstract. We briefly describe the instrumental effects which affect the accuracy of the radial velocity measurements. We have implemented several methods to correct for the instability effects and improve the accuracy of the measurements. These include modifications of the observational strategy and a time-dependent wavelength solution as well as a discussion of the error of the offset from cross-correlation. These methods are applied to observations obtained with the high resolution échelle spectrograph SOFIN mounted at the Cassegrain focus of the alt-azimuth 2.56 m Nordic Optical Telescope, La Palma, Canary Islands.

1. Introduction

To obtain the maximal achievable accuracy of the radial velocity measurements with a Cassegrain spectrograph we take into account the instrumental effects reviewed by Griffin & Griffin (1973), and analyzed quantitatively by Brown (1990).
Bending of the spectrograph as the telescope and its adapter change the spatial orientation, liquid nitrogen evaporation which causes change of the weight of the CCD dewar attached, temporal variations of the ambient temperature, and the refractive index of the air result in a systematical drift of the spectral lines during one exposure. Assuming that during a short period of time these effects are small, progressive, and changing linearly, one would prefer to take external calibration lamp spectra before and after each stellar exposure, and to divide one long stellar exposure into a series of shorter ones, long enough to accumulate sufficient signal-to-noise, which makes the sum of systematical and random errors minimal. To reconstruct the expected position of the stellar lines in wavelengths at the mid-point of the exposure we use a wavelength solution based on the three-dimensional model described below.
A second order effect of the drift is the broadening of spectral lines which would lead to spurious offsets of the radial velocity due to increased blending and distortions of the line profile. Fortunately, the effect is not too large if one considers that the progressive drift results in the convolution of spectral line profile with a rectangular profile. In our case, a drift by 0.3 pixels of a line of 2 pixels FWHM would increase its width by 1%. The smallness of this effect

implies that the effect on the radial velocities apart from the overall drift is negligible (see also Sect. 3.).
The way of setting the star on the slit of the spectrograph coupled with the effective seeing (including the accuracy of the guiding) results in random deviations of the stellar line positions in wavelengths from what was expected from the above correction. The effect comes from the non-uniform illumination of the slit which leads to an unequal filling of the collimator pupil and échelle, and is changing from one exposure to the other. The effect becomes magnified by better seeing; less accurate guiding smears the stellar image on the slit (in our case, the projected slit width is $1860\,\mathrm{m\,s^{-1}}$, $0\farcs25$ on the sky, and the median seeing is $0\farcs8$). To eliminate this effect we use telluric lines as an external reference source.
Furthermore, the effects outlined above are wavelength dependent, which makes these wavelength corrections functions of the spectral order number. The wavelength solution eliminates this dependency for the comparison spectrum with sufficient accuracy (see Fig. 1). But the stellar radial velocities reveal a remaining trend across the orders resulting from the difference in the slit illumination. Telluric lines, if well distributed across the orders, can also be used to correct for this tilt; otherwise, the stellar spectra themselves are used.

2. Wavelength solution

In a series of comparison images, for each spectral order the positions of the Th-Ar comparison lines are determined by non-linear weighted least-squares fits of Gaussian profiles. Let x_{ij} be the position along the CCD columns (the dispersion direction) of the line number i of the image number j, y_{ij} the position along the CCD rows, k_{ij} the spectral order number, λ_{ij} the wavelength, t_j the time (mid-point of the exposure) since the first image. Let the cross-dispersion axis $k\lambda$=const be tilted with respect to CCD rows due to imperfection of the CCD alignment, diverging due to optical distortions, and changing linearly with time, so that the angle of the axis is:

$$a_{ij} = b_0 + b_1\,t_j + (d_0 + d_1\,t_j)\,x_{ij} \tag{1}$$

Let Δ be the linear shift between images along x per time unit; then a coordinate transformation gives the positions u_{ij} in the undistorted system:

$$u_{ij} = (x_{ij} + \Delta \cdot t_j)\cos a_{ij} + y_{ij} \sin a_{ij} \tag{2}$$

Let k_c be the common order to which the wavelengths of all the others are translated, and n the degree of the dispersion polynomial:

$$\lambda_{ij}\frac{k_{ij}}{k_c} = \sum_{m=0}^{n} c_m\,u_{ij}^m \tag{3}$$

Therefore, the model to be fitted is

$$\lambda = F(x, y, t, k, k_c;\, \Delta, b_0, b_1, d_0, d_1, c_0, c_1 \ldots, c_n) \tag{4}$$

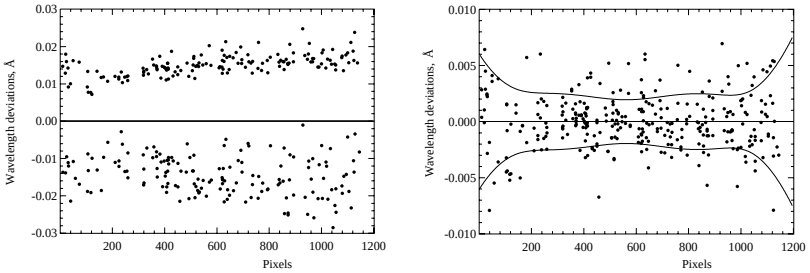

Figure 1. Wavelength solution of two comparison images selected to exaggerate the effects. *Left*: scatter plot of 363 spectral lines around a dispersion polynomial of 3rd degree prior to corrections. *Right*: after the optimization (the vertical scale enlarged three times) it converged to weighted rms=2.5 mÅ=130 m s^{-1} at 5635 Å. The two curves show the $10\,\sigma$ level of the error of the fit as a function of the pixel number. The wavelength error in the image center is σ=0.2 mÅ=10 m s^{-1} and steeply rises at the edges.

All other possible parameters can be neglected for our spectrograph. This model is optimized by the Marquardt method for non-linear least-squares. To get a more convenient function to be used for rebinning, the above function is subsequently approximated by two-dimensional Chebyshev polynomials on the regular grid of x as function of time for each order separately.

3. The error of the cross-correlation offset determination

For shift determination between spectra the cross-correlation method is used. A good knowledge of the error is essential, e.g. for proper weighting the radial velocity measurements in orbital fits.
The offset δ between the programme $p(x)$ and the template $t(x)$ spectrum is the offset at which the match between the spectra is best, i.e. the merit function

$$\chi^2(a,b,\delta) = \sum_{i=0}^{N} \left(\frac{a + b\,t(x_i+\delta) - p(x_i)}{\sigma_i} \right)^2 \qquad (5)$$

is minimal. Here, the free parameters a and b constitute the intensity transformation of the template to the programme spectrum for each trial offset δ, σ_i is the uncertainty of the intensity of $p(x_i)$, and the index i is ranging within the overlapping region of the two spectra for the given δ with possible exclusion of intervals containing unwanted features in the programme spectrum; this implies that N, the number of overlapping pixels, is a function of the offset. The offset can be any fractional part of the step size which implies that the template spectrum have to be noiseless to allow interpolation between pixels.

The merit function can be expressed as a function of only one variable:

$$\chi^2(\delta) = \left[1 - r^2(\delta)\right] \cdot \sum \omega_i (p_i - \bar{p})^2 \tag{6}$$

where the weighted cross-correlation function $r(\delta)$ is

$$r(\delta) = \frac{\sum \omega_i (p_i - \bar{p})(t_i(\delta) - \bar{t}(\delta))}{\sqrt{\sum \omega_i (p_i - \bar{p})^2 \cdot \sum \omega_i (t_i(\delta) - \bar{t}(\delta))^2}} \tag{7}$$

with the notations: $\omega_i = 1/\sigma_i^2$, $t_i(\delta) \equiv t(x_i + \delta)$, where the weighted averages:

$$\bar{p} = \frac{\sum \omega_i p_i}{\sum \omega_i} \quad \text{and} \quad \bar{t}(\delta) = \frac{\sum \omega_i t_i(\delta)}{\sum \omega_i} \tag{8}$$

The variances of the free parameters in least-squares is the inverse of the curvature matrix times the variance of the fit (Martin 1971):

$$\sigma_\delta^2 = 2 \left(\frac{d^2 \chi^2(\delta)}{d\delta^2} \right)^{-1} \frac{\chi^2(\delta)}{N-2} \tag{9}$$

which results in the formula:

$$\sigma_\delta^2 = - \left(\frac{d^2 r}{d\delta^2} \right)^{-1} \frac{1 - r^2}{r\,(N-2)} \tag{10}$$

where the variance incorporates both the random noise of the spectrum and the systematical error due to template mismatch.
The position of the cross-correlation maximum and its curvature is found by fitting a polynomial of degree 3–4 to the very top of the peak of $r(\delta)$ which is calculated within an interval of a few pixels, re-sampled with a subpixel step size. Our Monte-Carlo simulations show a complete agreement with the above error estimation.
The uncertainty (10) of the position difference of two similar Gaussians, one being noiseless, the other being with a signal-to-noise ratio SNR, with the depths d in continuum units, the widths FWHM, the sampling interval $\Delta\lambda$, becomes the well-known formula:

$$\sigma_\delta = (2\pi \ln 2)^{-1/4} \cdot \frac{\sqrt{\Delta\lambda \cdot \mathrm{FWHM}}}{r \cdot \mathrm{SNR} \cdot d} \tag{11}$$

In case when a noiseless template spectrum is not available, $r(\delta)$ could still be calculated if δ varies with the step size of the programme spectrum. Otherwise, a non-linear optimization of the full merit function, which includes the scaled uncertainties of the template spectrum, would be necessary to find the offset; the error of the offset then follows from the covariance matrix.

References

Brown, T.M. 1990, PASPC 8, 335
Griffin, R. & Griffin, R. 1973, MNRAS 162, 243
Martin, B.R. 1971, Statistics for Physicists (New York: Academic Press)

Precise Stellar Radial Velocities
ASP Conference Series, Vol. 185, *1999*
J.B. Hearnshaw and C.D. Scarfe, eds.

Precise radial velocity measurements with a Cassegrain spectrograph. II. Radial velocity determination and applications

I.V.Ilyin, R.Duemmler

Astronomy Division, University of Oulu, FIN-90571, Oulu, Finland

Abstract. We present our measurements of radial velocities of two stars suspected to have a substellar companion by using observations made with a Cassegrain échelle spectrograph. The stability issues and details of the data reduction are discussed in Ilyin & Duemmler (paper I, these proceedings). The results obtained here show that relatively high accuracy of radial velocity determinations is also attainable for Cassegrain spectrographs.

1. Observations

Spectra of τ Boo (HR 5185; F7V) and υ And (HR 458; F8V) were recorded with the spectrograph SOFIN mounted at the Cassegrain focus of the alt-azimuth 2.56 m Nordic Optical Telescope, La Palma, Canary Islands. The spectrograph is equipped with an R2 échelle and a cross-dispersion prism to separate spectral orders. A Thorium-Argon lamp is used for the comparison spectrum. One of the three optical cameras, which provides the highest resolving power of about 160 000 (930 $\mathrm{m\,s^{-1}}$ per one CCD pixel), was used for the radial velocity measurements. The spectral region was chosen around 6437 Å which gives 17 spectral orders, with a length of about 22 Å each, recorded simultaneously in one échelle image ranging from 5400 Å to 9400 Å. 16 observations of τ Boo with the average signal-to-noise ratio of 360 were obtained in April and June 1997. 44 observations of υ And with the average signal-to-noise ratio of 180 were obtained in December 1997 and March 1998.

2. Radial velocity determination

The wavelength calibration was done with the dispersion curve defined by the three-dimensional model, whenever it was possible, to reduce the instrumental effects (see paper I). The remaining small offsets were determined by cross-correlation of the telluric lines with an artificial spectrum for different spectral orders. The artificial telluric spectrum was created by computing Lorentzian profiles around the given wavelength (from Pierce & Breckinridge 1973) and by adjusting the intensities to the observed spectrum. The average offset was applied to all spectral orders of the same image.

The radial velocities were measured for each order with respect to the spectral orders of the same star having the best signal-to-noise. The whole spectral order is used for cross-correlation with the template with possible exclusion of intervals disturbed by telluric lines.
The dependence of the radial velocities on the order number is corrected by a weighted linear fit across the orders. The fitted value of the radial velocity and its error for a given image are taken from that central order where the error of the linear fit is minimal.
The error of the measurement is obtained by adding two terms in quadrature: the error of the mean of the telluric correction and the error of the above fit. The error of the zeroth term of the wavelength solution is canceled by the telluric correction, the errors of the other terms are included in the linear fit across the orders.
The internal accuracy of the radial velocities can be $2\,\mathrm{m\,s^{-1}}$ from 20 lines in a sharp-lined K-star and is not better than $20\,\mathrm{m\,s^{-1}}$ from 5 lines in a F-star with $v \sin i > 10\,\mathrm{km\,s^{-1}}$. The major uncertainty in the final radial velocity comes from the telluric correction which ranges from 10 to 100 $\mathrm{m\,s^{-1}}$ per spectral order, depending on the line strengths and the number of unblended lines.

3. Orbital solution

A Keplerian orbit (Heintz 1978) was fitted to the weighted relative radial velocities by using the Marquardt method for non-linear least-squares. The orbital solutions and their functions for both stars are given below. The errors of functions of the orbital parameters incorporate covariances between the parameters. The mass of the secondary component is estimated assuming that the mass of the primary is $1.2\,M_\odot$ consistent with the spectral types.
An F-test gives the significance level of the elliptical fit of τ Boo of only 52% which implies that our data are not sufficient to make the conclusion. The excess of the reduced χ^2_ν above 1 could imply that the data are not adequate for a Keplerian orbit. The minimal mass of a brown dwarf ($20\,M_{\mathrm{Jup}}$) as the maximal mass of the secondary constrains the inclination of the orbit to 10°. The inclination $i < 10°$ would occur in 1.5% cases of randomly oriented orbital planes, which implies that, apart from the selection effects, the companion could be a substellar object with a probability of 98.5%.
The significance level of the elliptical fit of υ And is 91%, therefore, more observations are necessary to support the issue that the orbit is not circular. For the mass of the secondary to be less than $20\,M_{\mathrm{Jup}}$ the inclination angle have to be more than 2°, which implies a probability of 99.94% that such an orbit occurs in randomly oriented orbital planes.

References

Butler R.P., Marcy G.W., Williams E., Hauser H. & Shirts P. 1997, ApJ 474, L115

Heintz W.D. 1978, Double Stars (Reidel: Dordrecht), p.80

Pierce A.K., Breckinridge J.B. 1973, The Kitt Peak Table of Photographic Solar Spectrum Wavelengths, Kitt Peak Contr. No. 559

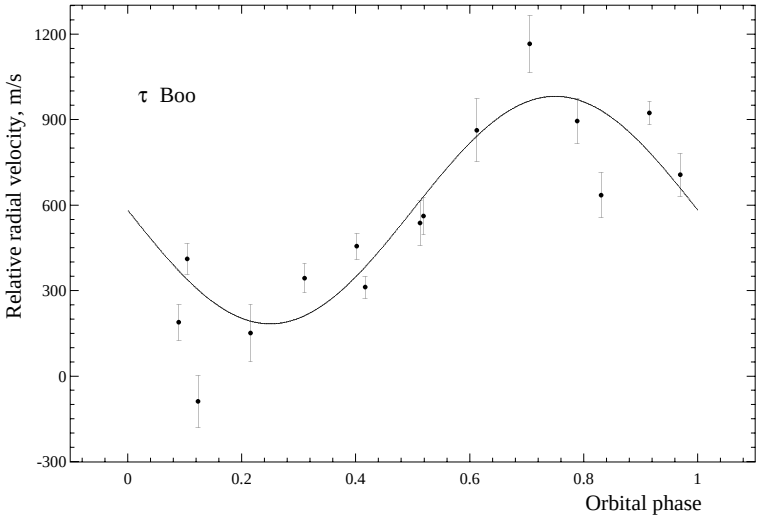

Figure 1. Relative radial velocity measurements of τ Boo and the circular orbit fit phased with respect to $T_{\rm conj}$. The average error of the measurements is 71 $\mathrm{m\,s^{-1}}$.

Table 1. Orbital elements of τ Boo

Parameter	Circular fit	Elliptical fit	Butler et al. (1997)
K_1, $\mathrm{m\,s^{-1}}$	399 ± 72	383 ± 71	469 ± 5
P, days	3.306 ± 0.025	3.301 ± 0.010	3.3128 ± 0.0002
ω, degrees		97 ± 55	254
e		0.28 ± 0.14	0.018 ± 0.016
$T_{\rm peri}$, HJD		$2\,450\,600.83 \pm 0.48$	
$T_{\rm maxRV}$, HJD	$2\,450\,599.89 \pm 0.07$	$2\,450\,600.24 \pm 0.13$	$2\,450\,235.41 \pm 0.2$
$T_{\rm conj}$, HJD	$2\,450\,600.71 \pm 0.07$	$2\,450\,600.80 \pm 0.22$	
$a_1 \sin i$, $R_\odot$	0.026 ± 0.005	0.024 ± 0.005	
$a_1 \sin i$, AU	$(1.2 \pm 0.2) \cdot 10^{-4}$	$(1.1 \pm 0.2) \cdot 10^{-4}$	$1.4 \cdot 10^{-4}$
$f(m)$, $M_\odot$	$(2.2 \pm 1.2) \cdot 10^{-8}$	$(1.7 \pm 1.0) \cdot 10^{-8}$	$3.45 \cdot 10^{-8}$
$m_2 \sin i$, $M_{\rm Jup}$	3.45 ± 0.62	3.18 ± 0.63	3.87
a_2, $R_\odot$	9.50 ± 0.002	9.50 ± 0.0008	
a_2, AU	$0.044 \pm 9 \cdot 10^{-6}$	$0.044 \pm 4 \cdot 10^{-6}$	0.0462
$\sigma_{\rm fit}$, $\mathrm{m\,s^{-1}}$	161	159	14
χ^2_ν	6.932	6.779	
Num. of RVs.	15	15	19
Time span	80 days	80 days	450 days

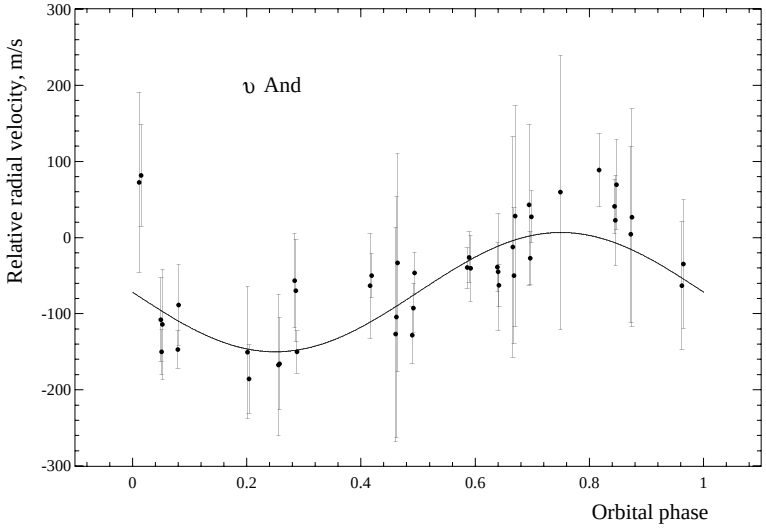

Figure 2. Relative radial velocity measurements of υ And and the circular orbit fit phased with respect to $T_{\rm conj}$. The average error of the measurements is 73 m s^{-1}.

Table 2. Orbital elements of υ And

Parameter	Circular fit	Elliptical fit	Butler et al. (1997)
K_1, m s^{-1}	78 ± 11	109 ± 18	74.1 ± 4
P, days	4.858 ± 0.054	4.855 ± 0.010	4.611 ± 0.005
ω, degrees		90 ± 16	314
e		0.46 ± 0.12	0.109 ± 0.04
$T_{\rm peri}$, HJD		$2\,450\,893.91 \pm 0.17$	
$T_{\rm maxRV}$, HJD	$2\,450\,892.59 \pm 0.12$	$2\,450\,893.38 \pm 0.17$	$2\,450\,088.64 \pm 0.3$
$T_{\rm conj}$, HJD	$2\,450\,893.81 \pm 0.12$	$2\,450\,893.91 \pm 0.12$	
$a_1 \sin i$, $R_\odot$	0.008 ± 0.001	0.009 ± 0.001	
$a_1 \sin i$, AU	$(3.5 \pm 0.5) \cdot 10^{-5}$	$(4.3 \pm 0.6) \cdot 10^{-5}$	$3.2 \cdot 10^{-5}$
$f(m)$, $M_\odot$	$(2.4 \pm 1.0) \cdot 10^{-10}$	$(4.7 \pm 1.8) \cdot 10^{-10}$	$2.18 \cdot 10^{-10}$
$m_2 \sin i$, $M_{\rm Jup}$	0.77 ± 0.11	0.96 ± 0.12	0.68
a_2, $R_\odot$	12.28 ± 0.001	12.27 ± 0.0002	
a_2, AU	$0.057 \pm 6 \cdot 10^{-6}$	$0.057 \pm 1 \cdot 10^{-6}$	0.057
$\sigma_{\rm fit}$, m s^{-1}	46	37	12
χ^2_ν	1.026	0.667	
Num. of RVs.	43	43	18
Time span	180 days	180 days	160 days

Paper III

Duemmler, R., Ilyin, I., Tuominen, I. 1997, "A new radial velocity curve for the RS CVn star σ Gem. Constraints on its physical parameters.", A&AS 123, 209

ASTRONOMY & ASTROPHYSICS
SUPPLEMENT SERIES
JUNE I **1997**, PAGE 209

Astron. Astrophys. Suppl. Ser. **123,** 209-218 (1997)

A new radial velocity curve for the RS CVn star σ Gem*

Constraints on its physical parameters

R. Duemmler, I.V. Ilyin, and I. Tuominen

Department of Geosciences and Astronomy, University of Oulu, Linnanmaa, P.O. Box 333, FIN–90571 Oulu, Finland

Received July 25; accepted September 25, 1996

Abstract. 26 high quality radial velocity measurements of the RS CVn star σ Gem taken in 1993, 1994, and 1995[1] are used in combination with older measurements to fit a new radial velocity curve. Essentially, the orbital parameters given by Bopp & Dempsey (1989) are confirmed. However, the orbit turns out to be circular. σ Gem is known as a single–lined binary, and also in the new spectra no trace of the secondary is found. However, combining the orbital with rotational parameters, constraints on the fundamental parameters can be found: the inclination, the radius and the two masses. The inclination is high; the mass of the primary seems to be normal for a K1 giant, its radius, however, seems to be too small.

Key words: stars: spectroscopic — stars: fundamental parameters — binaries: stars individual: σ Gem

1. Introduction

σ Gem (75 Gem = HR 2973 = HD 62044; $V \approx 4\overset{m}{.}2$) belongs to the class of RS CVn stars. These stars are close binaries with usually one evolved component (sub–giant or giant) with signatures of strong activity in one or both components. σ Gem is classified as K1 III and as a single–lined binary. These and a number of further parameters of the star are listed in Strassmeier et al. (1993, Star No. 73). For a RS CVn star, it has an untypically long period of 19.6 days, a fact that might lead to some other, untypical properties (Hatzes 1993).

The latest orbit calculations were done by Bopp & Dempsey (1989). They found a marginally eccentric orbit, but note that the orbit may be circular. They remark that there is no significant change of the orbit over the time span available to them (1902–1988).

Twenty–six new radial velocities (RVs) were obtained in 3 runs in 1993, 1994 and 1995. The SOFIN high resolution echelle spectrograph was used, yielding additional to the high resolution high S/N spectra (typically S/N > 200).

The new radial velocities offer some prospects: first, they extend the time base of RVs of σ Gem by another 7 years; thus, they allow for further improvement of the orbital period. They are far more accurate than any previously published radial velocities (see below). Thus, they are used to check the non-circularity of the orbit and to determine accurate values for all other orbital parameters. Furthermore, due to the high resolution and the high S/N ratio the spectra might allow for the detection of spectral lines belonging to the secondary. Additionally, some old RVs not used by Bopp & Dempsey are supplemented. Altogether, a new orbit determination is worthwhile, especially as a preparation of the spectra for surface (Doppler) imaging, where the shifts due to the orbital motion and the line profile distortions due to star spots need to be separated with high accuracy. Surface images from the SOFIN spectra will be discussed in a forthcoming paper.

2. Observations and reductions

For the purpose of surface imaging, very high–resolution (about 170 000 at 6173 Å), high S/N spectra (about 200 – 300) were obtained with the high–resolution echelle spectrograph SOFIN (Tuominen 1992) at the 2.56 m Nordic Optical Telescope (NOT) at Roque de los Muchachos Observatory, La Palma, Spain. The high resolution optical camera was used. The entrance slit width of 32 μm is adjusted to give a resolution element of about 2 pixels FWHM, corresponding to $0\overset{''}{.}23$ on the sky. The spectra were recorded with an Astromed–3200 CCD

Send offprint requests to: R. Duemmler;
e-mail: Rudolf.Duemmler@oulu.fi

* based on observations collected at the Nordic Optical Telescope (NOT), La Palma, Spain.

[1] Table 1 is also available in electronic form at the CDS via anonymous ftp to cdsarc.u-strasbg.fr (130.79.128.5) or via http://cdsweb.u-strasbg.fr/Abstract.html

camera (Mackay 1986) equipped with an EEV P88200 UV–coated 1152 × 770 CCD with a pixel size of 22.5 μm and operating at the optimal working temperature of 150 K. Three observing runs for σ Gem were conducted in late 1993, 1994 and 1995. Typical integration times were 30–40 minutes.

The reductions of the echelle spectra used the 3A–software package (Acquisition, Archiving and Analysis; Ilyin 1996).

The reductions involved the usual procedures of cosmic spike removal, bias subtraction, flatfielding, subtraction of scattered light, extraction of the curved echelle orders and wavelength calibration. The result is for each order the intensity normalized to the local continuum vs. heliocentric wavelength.

Two steps deserve a more detailed description. Flatfielding uses summed, merged flatfields, i.e. the slit height is so large that the orders of the flatfield spectra overlap; many of those images are summed in order to improve the S/N ratio in the flatfields. Fringing is usually of very low amplitude or absent. In some cases, however, an ordinary flatfield image is available, taken with the same parameters and immediately before or after the stellar exposure, which, after flatfielding and filtering to improve S/N and retain only the fringes, can be used to correct the corresponding stellar spectrum for fringing.

In order to obtain the highest possible accuracy in the wavelengths, a *two–dimensional* dispersion curve is determined from the Thorium–Argon comparison spectrum; this has the main advantage to use many comparison lines from many orders, as opposed to the sometimes very low number of comparison lines available in one individual echelle order. The determination proceeds as follows:

- Many orders from the comparison spectrum image are extracted in the same way as the orders from the stellar spectrum image and the backgrounds are subtracted.
- The positions of the comparison lines are determined by fitting of Gaussians.
- The wavelengths are identified semi–automatically using the Kitt–Peak Atlas for the Thorium–Argon–spectrum (Willmarth 1987).
- After determination of the two–dimensional positions $(x_i,\ y_i)$ for many $(100-200)$ comparison lines, all are transformed into one master order, using the $k\lambda$–law, i.e.

$$\lambda_0 = \lambda_i \frac{k}{k_0}, \tag{1}$$

  where k is the order number in which the line with wavelength λ_i has been measured and (k_0, λ_0) correspond to the master order.
- The merging of all lines in the master order is subsequently optimized according to the model:

$$\begin{aligned} p_i &= y_i \sin\alpha_i + x_i \cos\alpha_i \\ \alpha_i &= a + b\, x_i. \end{aligned} \tag{2}$$

  The first equation describes the rotation of the CCD rows with respect to the lines perpendicular to the dispersion direction. The rotation angle, and thus the curves $k\lambda$ = const., are modified due to the optical distortions as described by the second equation. It was found, that this simple model works very well for our spectrograph, where the incident and diffracted beams are in the same plane. a and b are optimized by minimizing the χ^2 of all merged comparison lines from a single polynomial describing the dispersion curve of the master order.
- The polynomial is then transported along the lines $k\lambda$ = const. into each of the orders of the original image, yielding a dispersion curve for each of them that is based on all the comparison lines distributed all over the original two–dimensional image.
- Finally, telluric lines are used to establish the accurate wavelength zero point, correcting for tiny geometrical shifts between the comparison and stellar images due to bending of the spectrograph.

The accuracy of the RVs is determined by the following factors:

- The *accuracy of the dispersion curve*: typically, about 150 comparison lines are taken into account. The dispersion curve within the master order is described by a polynomial of 2nd degree; the rms deviation of the lines from the final fit is generally about 2 mÅ at 6165 Å or 0.1 km s^{-1}. Since due to the large number of comparison lines used the error of the coefficients is much less than that, we conclude that the statistical error of the dispersion curve is negligible.
- The *stability of the RV across the chip*: any systematical error of the two–dimensional dispersion curve should show up as a systematical variation of the RV across the different orders. This was checked in the spectrum of the RV–standard β Oph: the RV is stable across the chip to within 0.03 km s^{-1}. Also for σ Gem with its much broader lines due to fast rotation the RV is stable to better than 0.1 km s^{-1}.
- The *accuracy of the wavelength zero point*: Each spectral image is shifted geometrically with respect to the image containing the comparison spectrum. Strong atmospheric O_2 and H_2O lines are used to establish the wavelength zero point. The standard wavelengths are taken from the solar catalogue by Pierce & Breckinridge (1973). In the present spectra, three different orders are available, each containing enough atmospheric lines to establish independently the wavelength zero point. They prove that there is no significant systematic variation of the shift across the image and allow an error estimate for the shift. Typically, the shift is determined with an accuracy of 0.1 to 0.2 CCD pixels. Since in echelle spectra in a good first approximation the dispersion is proportional to the wavelength this uncertainty transforms to a

systematic error of the RV from the whole image of about 0.1 to 0.2 km s^{-1}.

– The *accuracy of the template's RV*: The RV of σ Gem is measured by cross–correlating the wavelength region around 6175 Å with the same region of a spectrum of β Oph (K2 III), taken with the same equipment and reduced in the same way. The spectrum has been filtered to mimic the rotational broadening in the σ Gem spectra. β Oph is a radial velocity standard (see Astronomical Almanac 1995), a candidate for a list of primary standards; we can thus assume that both the constancy and the value of its RV are established to high accuracy. According to the Astronomical Almanac (1995) its RV = (-12.0 ± 0.1) km s^{-1}.
– The *accuracy of the cross–correlation*: At present, this cannot be determined independently. Therefore, we adopt an error of another 0.1 km s^{-1} from this procedure.

If we assume these error sources to be independent and add up the variances from the different contributions, the final RV–error is about 0.3 km s^{-1}. Note that although all the above error sources are also present in the template spectrum only the second to last source enters into the RV–error of σ Gem, since the literature value for the RV of β Oph is used to determine the RV from the cross–correlation.

The RVs measured from the SOFIN spectra are given in Table 1.

3. The radial velocity curve

3.1. The full data set

The radial velocities measured from the SOFIN spectra (Table 1) are supplemented by older measurements from the following sources (N is the number of RVs given):

Abt (1970), $N = 1$
Bopp & Dempsey (1989), $N = 110$
includes 19 values from Harper (1935)
Eker (1986), $N = 9$
Harper (1914), $N = 38$
Harper (1935), $N = 21$
includes 2 values from Harper (1914)
5 values from Moore (1928),
4 of which are revised from Reese (1903)
4 values from Jones (1928),
also listed by Lunt (1919).

An obvious misprint in one JD given by Harper (1935) has been corrected. Eker's RVs were not published before; he kindly made them available to us, and they are given in Table 2. The total number of RVs is thus 187 and the time interval covered by them ranges from 1902 to 1995.

The data are weighted, with the weight of an individual RV being the inverse of its variance. Since no individual errors for the older RVs are known, for each set of data a common mean standard deviation is adopted:

Table 1. The radial velocities (RVs) measured from the SOFIN spectra. The heliocentric Julian date is given for mid-exposure. A typical error of the individual RV is 0.3 km s^{-1}

date [dd.mm.yy]	HJD −2400000.0	RV [km s^{-1}]
26. 09. 93	49256.7404	39.5
27. 09. 93	49257.6758	28.7
28. 09. 93	49258.7281	19.6
29. 09. 93	49259.7266	13.6
30. 09. 93	49260.7196	10.0
02. 10. 93	49262.7492	12.3
03. 10. 93	49263.7351	20.5
04. 10. 93	49264.7213	27.5
05. 10. 93	49265.7339	40.9
06. 10. 93	49266.7125	51.8
03. 11. 93	49294.7532	52.1
13. 11. 94	49669.7733	24.9
14. 11. 94	49670.6763	17.8
15. 11. 94	49671.6859	12.1
16. 11. 94	49672.6892	10.0
18. 11. 94	49674.6961	15.9
18. 11. 94	49674.7486	16.3
19. 11. 94	49675.7660	24.1
21. 11. 94	49677.6992	44.4
22. 11. 94	49678.6537	54.5
15. 12. 94	49701.6142	78.9
15. 12. 94	49701.6714	79.1
18. 12. 94	49704.5654	70.3
20. 12. 94	49706.6310	50.2
01. 12. 95	50052.7725	69.8
02. 12. 95	50053.7750	75.9
03. 12. 95	50054.7828	77.5
04. 12. 95	50055.7708	76.8
05. 12. 95	50056.7620	73.5

Table 2. The previously unpublished RVs measured by Eker. The measurement procedure and the interpretation is given in Eker (1986). He estimates the RV error to be 0.5 km s^{-1}

date [dd.mm.yy]	HJD −2400000.0	RV [km s^{-1}]
23. 02. 84	45753.6713	11.6
29. 02. 84	45759.6119	71.5
03. 03. 84	45762.7217	78.2
07. 03. 84	45766.6354	48.8
09. 03. 84	45768.7292	23.8
23. 03. 84	45782.7120	75.7
26. 03. 84	45785.7147	50.8
01. 04. 84	45791.7071	11.3
06. 04. 84	45796.6927	50.2

Bopp & Dempsey (1989) estimate their RV–errors to be $0.9\,\mathrm{km\,s^{-1}}$, and they assign to the data given by Harper (1914, 1935) a weight of 0.5 with respect to their own measurements. This translates to a standard deviation of $1.3\,\mathrm{km\,s^{-1}}$, which is adopted here and also used for the RV given by Abt (1970). Eker (1986, see Table 2) gives an error of $0.5\,\mathrm{km\,s^{-1}}$. We estimate the error of the SOFIN RVs to be $0.3\,\mathrm{km\,s^{-1}}$(see above).

3.2. The fit and error determination

The data consisting of triples (t_i, RV_i, w_i) with the weights w_i are fitted (least–squares fit) by the function

$$\mathrm{RV}(t) = \gamma + K\,(\cos(v+\omega) + e\cos\omega), \tag{3}$$

(see e.g. Heintz 1978 for the derivation and the meaning of the symbols).

The parameters are determined with a non–linear least–squares fit using the simplex–algorithm (e.g. Caceci & Cacheris 1984; Press et al. 1994).

As an additional parameter derived from the fit–parameters, we compute the period in the rest frame of the system (corrected for the time dilation in the inertial frame moving with the velocity γ with respect to the sun, and to the increasing light travel–time between periastron passages due to γ). We use P_{rest} in the computation of $a\sin i$ and $f(m)$.

There are two ways to determine standard deviations for the fit–parameters.

1. The *formal error* of any fit–parameter p is given by

$$\sigma_p^2 = 2\left(\frac{\partial^2\chi^2}{\partial p^2}\right)^{-1} \tag{4}$$

(Bevington 1969) with the derivatives taken at the minimum of χ^2. With the fit–parameters and their formal errors known, the errors of the derived parameters can be obtained by the usual error propagation.

2. The *bootstrap errors* (see e.g. Efron & Tibshirani 1993) are computed from the actual residuals of the measurements from the fit. B bootstrap samples are constructed by randomly selecting from the residuals of the N real measurements N residuals, with replacement, and adding them to the computed RVs using the best fit parameters. Since the residuals of measurements having low weight are on average larger than those of measurements having high weight, each residual picked is accompanied by its original weight. For each set of these new "measurements" a fit of the RV curve is performed, resulting in a new set of fit–parameters and derived parameters. For large B the parameter errors are given by the standard deviations of the bootstrap parameters (both fit–parameters and derived ones) from their values obtained from the set of real measurements.

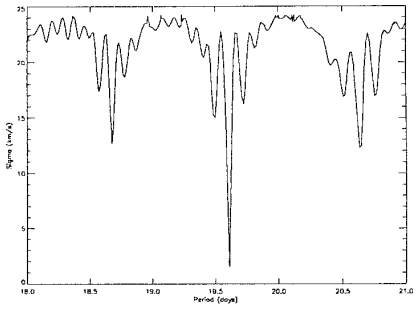

Fig. 1. Periodogram of the RV measurements of σ Gem. The only significant period is at 19.604471 days

3.3. The period search

Assuming the orbit to be circular, i.e. fixing $e = 0$ in the fits, and removing the last 3 measurements from Table 1 (see Sect. 3.4), the best orbital period was searched in the interval 18.0 to 21.0 days.

Figure 1 shows the periodogram obtained by varying the start value of the period in fits of RV curves to the data set. The plot gives the standard deviation σ_1 of an individual measurement of mean weight from the fit vs. the period. It is obvious that there is only one period close to the value given by Bopp & Dempsey (1989); all other minima have σ_1 exceeding $10\,\mathrm{km\,s^{-1}}$.

3.4. The radial velocity curve of σ Gem

The results of four different fits of radial–velocity curves are given in Table 3. Except for Solution 4, all allow for a non–zero eccentricity of the orbit. The formal parameter errors are only given for Solution 1: one can see that in most cases the formal and the bootstrap errors are very close to each other. The main exception is ω which has a very large bootstrap error. The bootstrap error is certainly more realistic due to the very small eccentricity. This relation between the formal and the bootstrap errors is the same for all fits; only the (more reliable) bootstrap errors are therefore given in the following.

A forced circular fit to all measurements excluding the last 3 SOFIN measurements (see below) yields a slightly different period than that given in Solution 1:

$$P = (19.604471 \pm 0.000022)\quad \mathrm{days}, \tag{5}$$

which is adopted as the final period. This period is kept fixed in fits leading to Solutions 2–4, because the limited time–coverage of the data sets used for them does not allow a reliable determination of the period.

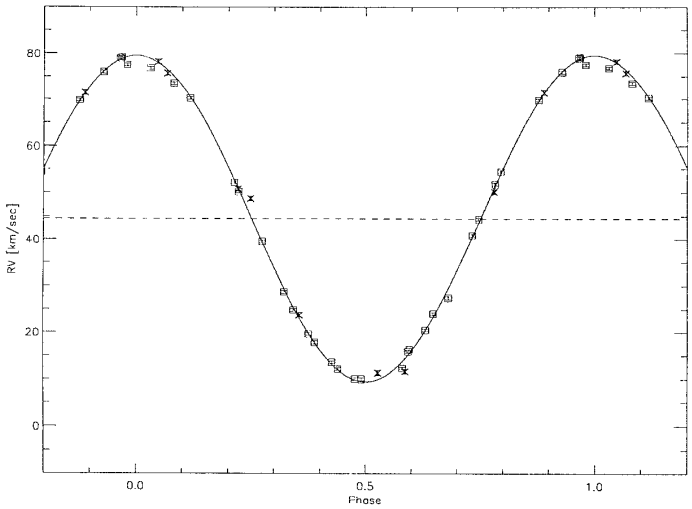

Fig. 2. The SOFIN measurements (squares) and Eker's measurements (crosses) with the radial velocity curve of Solution 4

The eccentricity of the orbital solution 1 is only half of what Bopp & Dempsey (1989) got. Solutions 2 and 3 are obtained with the aim to establish the significance (or otherwise) of this eccentricity. Only the data sets having the smallest velocity errors, i.e. the SOFIN and Eker's data sets (Table 1 and Table 2), are used. Solution 2 uses all of these data. The eccentricity has slightly decreased further. When computing the O–C from the orbit, the last 3 SOFIN measurements in Table 1 show systematical deviations from the fit. They range up to 2.6 kms^{-1}. Since these measurements are at a sensitive phase (close to the maximum RV, where there are also not many other measurements) they might be responsible for a large part of the eccentricity. For Solution 3, they are therefore removed from the data set. The eccentricity dropped again by a factor 2, now being only a 1 σ result and extremely small. We thus conclude (as was already suspected by Bopp & Dempsey 1989) that the orbit is in fact circular. Solution 4 is accordingly a forced circular fit to the data set used for Solution 3 (SOFIN + Eker, excluding the last 3 measurements in Table 1) and we adopt it as the final solution. The insignificant changes in the orbit parameters and in σ_1 from Solution 3 to Solution 4 support our conclusion of circularity. Note, that the period of the final orbital solution is still based on the whole data set covering the time interval 1902–1995; only all other parameters are derived from the limited, but most accurate data. As can be seen from Table 3 the parameters are very close to those given by Bopp & Dempsey (1989).

Figure 2 shows the measurements of SOFIN and Eker (1986) together with the fit of Solution 4. The systematic deviation of the last 3 SOFIN measurements close to phase 0 is clearly seen. These and the significant deviations of a few other data points are probably caused by strong distortions of the line profiles due to spot features.

4. The rotation parameters

4.1. The rotation period

Strassmeier et al. (1993) list a rotation period for σ Gem of $P_{\mathrm{rot}} = 19.410$ days. Henry et al. (1995) analyse long–term photometric data and interpret them in a two–spot model. They obtain for each spot a different period, most of them shorter than the orbital period, which is interpreted by them as differential rotation. They give a rotation period of the star $P_{\mathrm{rot}} = 19.54$ days. Jetsu (1996) analysed the same data as Henry et al. (1995). He finds that the data of σ Gem's light minima indicate the presence of active longitudes, which means a unique period. His period is $P_{\mathrm{rot}} = (19.606 \pm 0.023)$ days. This period is identical (within the quite large errors) with the orbital period given in Eq. (5). It thus seems that σ Gem's rotation is in fact synchronized with its orbit; this is consistent also with the finding above, that the orbit is circular. We adopt in the following $P_{\mathrm{rot}} = P_{\mathrm{orb}}$.

Table 3. The results of 4 different fits of radial velocity curves to the data. Solution 1 includes all data; the errors given in parentheses are the formal fit errors, the others bootstrap errors from $B = 1000$ bootstrap runs. For Solutions 2–4, only the bootstrap errors from $B = 1000$ runs are given. Solution 2 includes only the SOFIN data supplemented by Eker's RVs (Table 1 and Table 2). Solution 3 includes the same data as Solution 2 except the last 3 SOFIN measurements. Solution 4 is a circular fit to the data used for Solution 3. For Solutions 2–4 the period was kept fixed at 19.604471 days. For comparison, the parameters given by Bopp & Dempsey (1989) are given in the column BD89

		Solution 1	Solution 2	Solution 3
P	(days)	19.604462(±0.000038)±0.000023	19.604471±0.00	19.604471±0.00
γ	($\mathrm{km\,s^{-1}}$)	44.24(±0.11)±0.11	44.28±0.14	44.47±0.14
K	($\mathrm{km\,s^{-1}}$)	34.72(±0.16)±0.16	34.73±0.19	35.04±0.19
e		0.0120(±0.0045)±0.0045	0.0109±0.0053	0.0055±0.0052
ω	(deg.)	218.36(±0.26)±23.6	240.82±23.6	281.2±38.3
T_0	(HJD)	2447224.396(±0.014)±1.283	2447225.6±1.6	2447227.8±2.1
$T_{\max}$	(HJD)	2447232.063(±0.024)±0.035	2447232.048±0.042	2447232.082±0.036
T_{conj}[1]	(HJD)	2447227.150(±0.025)±0.030	2447227.174±0.036	2447227.222±0.035
P_{rest}	(days)	19.601570(±0.00033)±0.000023	19.601575±0.000009	19.601563±0.000009
$a \sin i$	($R_\odot$)	13.445(±0.061)±0.062	13.447±0.074	13.569±0.073
$f(m)$	($M_\odot$)	0.0850(±0.0012)±0.0012	0.0850±0.0014	0.0874±0.0014
σ_1	($\mathrm{km\,s^{-1}}$)	1.53	0.99	0.89

		Solution 4	BD89
P	(days)	19.604471±0.00	19.60447±0.00007
γ	($\mathrm{km\,s^{-1}}$)	44.48±0.14	43.78±0.17
K	($\mathrm{km\,s^{-1}}$)	35.06±0.19	34.79±0.25
e		0.0±0.0	0.0210±0.0069
ω	(deg.)	0.0±0.0	160±20
T_0	(HJD)	2447232.121±0.015	2447221.2±1.1
$T_{\max}$	(HJD)	2447232.121±0.015	
T_{conj}	(HJD)	2447227.220±0.015	2447227.08±0.02
P_{rest}	(days)	19.601562±0.000009	
$a \sin i$	($R_\odot$)	13.578±0.073	13.48±0.09
$f(m)$	($M_\odot$)	0.0875±0.0014	0.0857
σ_1	($\mathrm{km\,s^{-1}}$)	0.87	

[1] Conjugation time with primary in front.

4.2. The rotation velocity

For the projected rotational velocity $v \sin i$, Eaton (1990) gives $27\,\mathrm{km\,s^{-1}}$, a value used by Hatzes (1993) and Henry et al. (1995). Strassmeier et al. (1993) give $v \sin i = 25\,\mathrm{km\,s^{-1}}$ and remark that this value is better than the one given by Eaton.

Since $v \sin i$ is a very important observable concerning the constraints to be derived in the next section and a sensitive input parameter for the forthcoming surface imaging, a redetermination seems to be necessary. For this, we use the Fourier transform of the SOFIN spectra (see e.g. Unsöld 1955; Gray 1988, p. 2–1ff).

A mean spectrum is created from all 29 SOFIN spectra. For this, each spectrum has been shifted to $\mathrm{RV_{hel}} = 0$ using the orbital parameters of Solution 4 in Table 3. In order to minimize distortions due to noise and occasional spot features, a $\kappa\,\sigma$–clipping has been done (in 3 iterations remove for each wavelength those points that are deviating more than $\kappa = 2$ times the standard deviation from the mean). The power–spectrum obtained from the whole

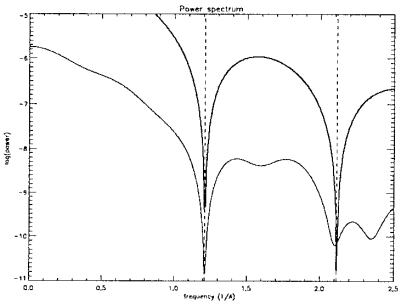

Fig. 3. Power spectrum of Fe I 6173 Å from the mean spectrum 1993-95, compared to that of a pure rotation profile computed with a linear limb–darkening of $\epsilon = 0.73$. $v \sin i$ for the model profile is $27.1\,\mathrm{km\,s^{-1}}$

wavelength range is dominated by the minima and maxima caused by the many blended lines. Only the features, whose main components are Fe I 6173 Å and Fe I 6180 Å, are sufficiently unblended to be used.

Figure 3 shows the power–spectrum obtained from Fe I 6173 Å. It is compared to that of a pure rotational profile computed with a linear limb–darkening coefficient $\epsilon = 0.73$ (obtained by interpolating to $T_{\rm eff} = 4500\,{\rm K}$, $\log g = 2.5$, $\lambda = 6175\,$Å in the tables given by Al–Naimiy 1978). It is obvious, that the second minimum is already heavily distorted by blending effects, so only the first minimum can be used (the same is true for Fe I 6180 Å). The mean projected rotational velocity determined from the two lines is

$$v \sin i = 27.0 \pm 0.2\,{\rm km\,s^{-1}}. \quad (6)$$

This is consistent with the value given by Eaton (1990) and will be used in what follows.

5. Constraints on the fundamental parameters

5.1. The minimum radius

The true rotation period $P_{\rm rot} = P_{\rm orb,rest} = 19\overset{\rm d}{.}601562$ combined with the projected rotational velocity $v \sin i = 27.0\,{\rm km\,s^{-1}}$ gives a lower limit for the radius of the star:

$$R \sin i = \frac{P_{\rm rot}}{2\,\pi}\, v \sin i = 10.5\, R_\odot. \quad (7)$$

This is only valid if the star is assumed to be spherical. Due to its relatively long rotation period it seems unlikely that the star is flattened by rotation; it might, however, approach its Roche–lobe limit and become distorted. The assumption of sphericity is thus equivalent to the assumption that the star does not fill its Roche–lobe. So far, there is no observation indicative of mass–transfer in the system, so this assumption seems to be justified. Note that here and in the following we do not distinguish between the inclination of the axis of rotation and that of the orbital axis. Since the orbit is circularized and the rotation is synchronized with the orbit it is natural to assume that these two axes are aligned. This is supported by the results of Stawikowski & Glebocki (1994).

5.2. The Roche–lobe limit

In the following the index 1 ("primary") indicates the visible component of the binary (the K1 III star) and the index 2 the secondary. The orbital parameters determine $a_1 \sin i$. If the primary would fill its Roche–lobe, the ratio of the effective radius of the Roche–lobe $R_{\rm rl}$, i.e. the radius of the sphere that has the same volume as the Roche–lobe, and the distance between the two stars, i.e. $a = a_1 + a_2 = a_1\,(1 + q)$ is entirely determined by the mass–ratio $q_{\rm rl} = m_1/m_2$ of the two components:

$$\frac{R_{\rm rl}}{a} = \frac{R_{\rm rl} \sin i}{a_1 \sin i (1 + q_{\rm rl})} = \frac{0.49\, q_{\rm rl}^{(2/3)}}{0.6\, q_{\rm rl}^{(2/3)} + \ln\left(1 + q_{\rm rl}^{(1/3)}\right)} \quad (8)$$

(Eggleton 1983). Since $R_1 < R_{\rm rl}$ and $R_{\rm rl}$ increases with $q_{\rm rl}$, we obtain a lower limit for the mass ratio q, if we replace $R_{\rm rl}$ by R_1 in Eq. (8):

$$q = \frac{m_1}{m_2} > q_{\rm rl} = 1.02. \quad (9)$$

5.3. The secondary

The mean SOFIN spectrum has been subtracted from each of the individual spectra and the residuals carefully examined. There are variations exceeding the noise, they are, however, inside the spectral features, i.e. their displacement with respect to the primary star is less than $27.0\,{\rm km\,s^{-1}}$. They cannot be due to the secondary, because from the limit of the mass-ratio it can be concluded that the displacement should reach sometimes at least $K_1 + K_2 = K_1(1 + q) > 70.8\,{\rm km\,s^{-1}}$. The variations are also not systematic over the whole 2 years period; they are thus most probably features caused by surface inhomogeneities.

Thus, even with the high–resolution, high S/N SOFIN spectra, no trace of the secondary (in this wavelength region) can be found. Since the S/N of the SOFIN spectra is generally well above 100, we can conclude, that the luminosity of the secondary does not exceed 1% of the luminosity of the primary. Adopting $M_V = 0\overset{\rm m}{.}3$ for the K1 III primary (Gray 1988, Appendix B), the secondary must be fainter than $M_V \approx 5^{\rm m}$, which would make it a main–sequence star of type G6 or later, or a compact object (white dwarf, neutron star). As a star of type G6 V or later, its mass would be less than $0.95\,M_\odot$, as a white dwarf less than the Chandrasekhar–limit of $1.4\,M_\odot$. Ayres et al. (1984) analyse the far–UV spectra of σ Gem and from the lack of any trace of a hot continuum conclude that the secondary is probably a late–type dwarf.

If we adopt for the secondary $m_2 < 0.95\,M_\odot$ and take into account the mass function from the orbital solution as well as the lower limit for the mass ratio from the Roche–limit, we obtain a stringent lower limit for the inclination:

$$\begin{aligned} \sin^3 i &= (1+q)^2 \frac{f(m)}{m_2} \\ &> (1 + \min(q))^2\, \frac{f(m)}{\max(m_2)} \\ \text{i.e.} \quad i &> 46\overset{\circ}{.}2. \end{aligned} \quad (10)$$

Here, $\min(x)$ and $\max(x)$ give the minimum and maximum of all possible values for x. This limit on i is interesting, because it means that σ Gem has a high inclination of its rotational axis and is therefore suitable for surface

imaging. The value of $i = 60°$ adopted for the interpretation of photometry of σ Gem e.g. by Poe & Eaton (1985) is perfectly consistent with this limit.

5.4. The limits on the mass of the primary

If we now combine $m_2 < 0.95\,M_\odot$ with the mass function and the upper limit for the inclination, $i < 90°$, we obtain an upper limit for the mass m_1:

$$\begin{aligned} m_1 &= m_2 \cdot \left(\sqrt{\frac{m_2 \sin^3 i}{f(m)}} - 1 \right) \\ &< \max(m_2) \cdot \left(\sqrt{\frac{\max(m_2)\max(\sin^3 i)}{f(m)}} - 1 \right) \end{aligned}$$

$$\text{i.e.} \quad m_1 < 2.2\,M_\odot. \tag{11}$$

A lower limit on m_1 results from the lower limit on q and $i < 90°$:

$$\begin{aligned} m_1 &= q^3 \cdot (1+q^{-1})^2 \frac{f(m)}{\sin^3 i} \\ &> \min(q) \cdot (\min(q)+1)^2 \, \frac{f(m)}{\max(\sin^3 i)} \end{aligned}$$

$$\text{i.e.} \quad m_1 > 0.4\,M_\odot. \tag{12}$$

Unfortunately, this limit is not very useful: a star of such low mass would probably not have become a giant yet in the 10 Gyr or so that the Galaxy exists. Probably, the mass of the primary is larger than 1 $M_\odot$.

5.5. The primary's gravity

The surface gravity g_1 of the primary can be written as:

$$g_1 = \frac{G\,m_1}{R_1^2} - \frac{(v \sin i)^2}{R_1 \sin i}. \tag{13}$$

The last term corrects for the influence of the centrifugal force, which is $v^2 \cos\phi / R_1 = v^2 \sin i / R_1$, if we adopt as a value for the observed g_1 that in the center of the stellar disk, which is at a latitude $\phi = 90° - i$. The correction for centrifugal forces consists thus only of observables and cannot be varied.

The limits for mass, radius and mass ratio then give also limits for the surface gravity:

$$\begin{aligned} g_1 &< G \frac{\max(m_1)}{\min(R_1^2)} - \frac{(v \sin i)^2}{R_1 \sin i} \\ \text{i.e.} \quad \log g_1 &< 2.73 \end{aligned} \tag{14}$$

$$\begin{aligned} \text{and } g_1 &= G \cdot q \cdot (1+q)^2 \frac{f(m)}{R_1^2 \sin^3 i} - \frac{(v \sin i)^2}{R_1 \sin i} \\ &> G \cdot \min(q) \cdot (1+\min(q))^2 \\ &\quad \cdot \frac{f(m)}{(R_1 \sin i)^2} \, \frac{1}{\max(\sin i)} - \frac{(v \sin i)^2}{R_1 \sin i} \end{aligned}$$

$$\text{i.e.} \quad \log g_1 > 1.91. \tag{15}$$

Note, that the lower limit corresponds to the lower limit for m_1, which is too low. If we assume $m_1 > 1\,M_\odot$, then

$$\begin{aligned} g_1 &= \frac{G\,m_1 \sin^2 i}{R_1^2 \sin^2 i} - \frac{(v \sin i)^2}{R_1 \sin i} \\ &> \frac{G \min(m_1) \min(\sin^2 i)}{R_1^2 \sin^2 i} - \frac{(v \sin i)^2}{R_1 \sin i} \end{aligned}$$

$$\text{i.e.} \quad \log g_1 > 2.08. \tag{16}$$

Therefore, the true gravity is very probably higher than $\log g_1 = 2$.

5.6. The mass–mass–plot of the allowed stellar parameters

In Fig. 4, the results of the previous paragraphs are presented in graphical form in the (m_1, m_2)–plane. The oblique lines to the left are the mass–ratios $q = 1.0$ (for orientation) and $q = q_{\rm rl}$. The curves are lines of constant radius of the primary, and since $R_1 \sin i$ is fixed, lines of constant inclination as well. Since the mass function is also fixed, each value of m_1 for given R_1 thus corresponds uniquely to a value of m_2. Lines $m_2 = 0.95\,M_\odot$ and $m_2 = 1.4\,M_\odot$ are also shown. Note, that if $0.95\,M_\odot < m_2 < 1.4\,M_\odot$ the secondary needs to be a white dwarf or low mass neutron star, because a main–sequence star would have been detected in the spectra, and above $1.4\,M_\odot$ it must be a neutron star. To emphasize the importance of the gravity, the lines of constant $\log g_1 = 2.0, 2.5, 3.0$ are added to the figure. We note, that the line $\log g_1 = 2.0$ is almost always above the Roche–limit $q = q_{\rm rl}$ and the line $\log g_1 = 3.0$ entirely in the region with $m_2 > 0.95\,M_\odot$. Note, that for a normal radius, $R_1 = 16\,R_\odot$ (Dyck et al. 1996), the secondary is most probably too massive to be a white dwarf.

6. Summary and discussion

New high quality radial velocity measurements of the RS CVn star σ Gem have been used to derive the orbital parameters of this single–lined binary. Essentially, the orbit given by Bopp & Dempsey (1989) is confirmed; however, the orbit is most probably circular.

The orbital parameters and the rotational parameters $P_{\rm rot} = P_{\rm orb}$ and the newly determined $v \sin i = 27.0\,{\rm km\,s^{-1}}$ (confirming the result by Eaton 1990) are combined to construct the region of allowed combinations of the inclination, the two masses and the gravity of the primary. A few plausible assumptions have to be made during this process:

- that the primary is spherical and does not fill its Roche–lobe;
- that the rotational axis of the primary and the orbital axis are parallel;
- that the secondary is less massive than $0.95\,M_\odot$.

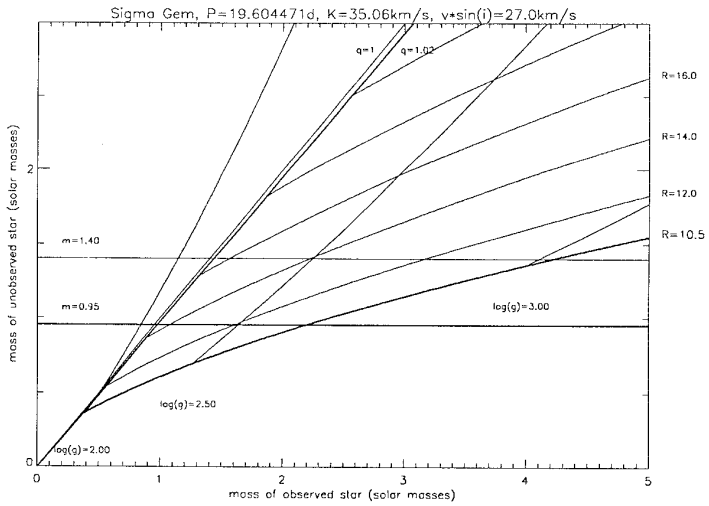

Fig. 4. The stellar parameters in the mass–mass–plane. See text for detailed explanation

The first assumption is made plausible by the fact that the RV curve is stable over the century of data, i.e. there seems to be no interaction between the components. The second assumption is based on the circularized orbit and the seemingly synchronized rotation; the third on the invisibility of the secondary in the high S/N SOFIN spectra and the additional assumption that it is a main–sequence star.

The inclination is high: $i > 46°$. The mass of the primary is between $0.4\,M_\odot$ (or more probably $1\,M_\odot$) and $2.2\,M_\odot$ which is normal for a K1–giant (Schmidt–Kaler 1982), at least when it belongs to the old disk population (Eker 1992; Eggen 1993). Its radius, however, seems to be smaller than the "normal" values for stars of this type.

The limits on the gravity are especially interesting: The gravity is in principle an observable; it can be obtained from careful modelling of the spectrum. As can be seen in Fig. 4 an accurate determination of the gravity leads to a very narrow range for the allowed values of m_1. Unfortunately, the atmospheric models are usually calculated in steps of $\delta \log g = 0.5$. Our limits here indicate, that practically the only gravity allowed is then $\log g_1 = 2.5$. The next lower gravity is almost certainly excluded, because the mass of the primary becomes too low for its spectral class or the Roche–lobe limit would be violated. Should we, however, find that a *higher* gravity is needed to describe the spectrum, this would also contradict our limits. The most uncertain assumption made is that the secondary is a main–sequence star. For a higher gravity in the primary, *both* stars have to be more massive. Since under these conditions the secondary cannot be a main–sequence star (otherwise it would have been seen at least in the SOFIN spectra) and it cannot be a white dwarf (Ayres et al. 1984) we need to conclude that the secondary had to be a neutron star. Note that this would also mean, that the primary's radius is then allowed to be at its normal value of $(16 \pm 2)\,R_\odot$ (Dyck et al. 1996, consistent with Schmidt–Kaler 1982). For $R_1 \approx 16\,R_\odot$ the inclination would only be $i \approx 41°$. This might be another check, because according to Piskunov et al. (1996) (largely) different i can be distinguished by the quality of surface imaging.

The fact that during the history of RV curves for σ Gem all new orbital solutions tend to confirm (with increasing refinement) the previous solutions is a sign that there is no interaction between the two stars. If the secondary would be a neutron star, there is therefore not much hope to see any sign of it. If, however, indirect evidence for it is found (e.g. by the necessity of a $\log g_1 \geqq 3$ to describe the spectrum), σ Gem would turn out to be indeed a very special RS CVn–star.

Acknowledgements. This work has made use of the SIMBAD data base, operated at CDS, Strasbourg, France. Z. Eker has kindly made his unpublished individual RV–measurements available to us. We thank the referee, B.W. Bopp, for his valuable comments. R.D. would like to thank A. Bruch for very

helpful discussions concerning the Roche–lobe limit; he gratefully acknowledges further discussions with S. Jankov and O. Vilhu. The project "Late–type stars: activity, magnetism, turbulence" is supported by the EC Human Capital and Mobility Network, No. ER–BCHRXCT940483.

References

Abt H.A., 1970, ApJS 19, 387
Al–Naimiy H.M., 1978, ApSS 53, 181
Ayres T.R., Simon L., Linsky J.L., 1984, ApJ 279, 197
The Astronomical Almanac for the year 1996, 1995, U.S. Government Printing Office, Washington, and HMSO, London, p. H43
Bevington P.R., 1969, Data Reduction and Error Analysis for the Physical Sciences. McGraw–Hill, New York, p. 245
Bopp B.W., Dempsey R.C., 1989, PASP 101, 516
Caceci M.S., Cacheris W.P., 1984, Byte 9, 340
Dyck H.M., Benson J.A., van Belle G.T., Ridgway S.T., 1996, AJ 111, 1705
Eaton J.A., 1990, IBVS 3460
Efron B., Tibshirani R.J., 1993, An lntroduction to the Bootstrap. Chapman & Hall, New York
Eggen O.J., 1993, AJ 106, 80
Eggleton P.P., 1983, ApJ 268, 368
Eker Z., 1986, MNRAS 221, 947
Eker Z., 1992, ApJS 79, 481
Gray D.F., 1988, Lectures on Spectral–Line Analysis: F, G, and K Stars. The Publisher, Arva, Ontario
Harper W.E., 1914, Publ. Dom. Obs. Ottawa 1, 265
Harper W.E., 1935, Publ. Dom. Astrophys. Obs. Victoria 6, 207 (see p. 224)
Hatzes A.P., 1993, ApJ 410, 777
Heintz W.D., 1978, Double Stars. Reidel, Dordrecht, p. 80
Henry G.W., Eaton J.A., Hamer J., Hall D.S., 1995, ApJS 97, 513
Ilyin I.V., 1996, latest edition of Acquisition, Archiving and Analysis (3A) Software Package – User's Manual, Observatory, University of Helsinki
Jetsu L., 1996, A&A 314, 153
Jones H.S., 1928, Ann. Cape Obs. 10, pt. 8 (see p. 170)
Lunt J., 1919, ApJ 50, 161
Mackay C.D., 1986, ARA&A 24, 255
Moore J.H., 1928, Publ. Lick Obs. 16 (see p. 117)
Pierce A.K., Breckinridge J.B., 1973, The Kitt Peak Table of Photographic Solar Spectrum Wavelengths, Kitt Peak Contr. No. 559
Piskunov N., Ryabchikova T.A., Tuominen I., 1996, A&A (submitted)
Poe C.H., Eaton J.A., 1985, ApJ 289, 644
Press W.H., Teukolsky S.A., Vetterling W.T., Flannery B.P., 1994, Numerical Recipes in C. Cambridge Univ. Press, Cambridge, 2nd ed., 2nd repr., p. 408ff
Reese H.M., 1903, ApJ 17, 308
Schmidt–Kaler T., 1982, in Landolt–Börnstein, New Series, Group VI, Vol. 2b, p. 1
Stawikowski A., Glebocki R., 1994, Acta Astron. 44, 393
Strassmeier K.G., Hall D.S., Fekel F.C., Scheck M., 1993, A&AS 100, 173
Tuominen I., 1992, NOT News, No. 5, p. 15
Unsöld A., 1955, Physik der Sternatmosphären. 2nd ed., Springer, Berlin, p. 513
Willmarth D., 1987, A CCD Atlas of Comparison Spectra: Thorium–Argon Hollow Cathode, Kitt Peak National Observatory, revised 1992

Paper IV

Petrov, P.P., Zajtseva, G.V., Efimov, Yu.S., Duemmler, R., Ilyin, I.V., Tuominen, I., Shcherbakov, V.A. 1999, "Brightening of the T Tauri star RY Tauri in 1996. Photometry, polarimetry and high-resolution spectroscopy", A&A 341, 553

Astron. Astrophys. 341, 553–559 (1999)

ASTRONOMY AND ASTROPHYSICS

Brightening of the T Tauri star RY Tauri in 1996⋆,⋆⋆

Photometry, polarimetry and high–resolution spectroscopy

P.P. Petrov[1,⋆⋆⋆], G.V. Zajtseva[2], Yu.S. Efimov[3], R. Duemmler[1], I.V. Ilyin[1], I. Tuominen[1], and V.A. Shcherbakov[3]

[1] Astronomy Division, University of Oulu, Linnanmaa, P.O. Box 333, FIN-90571 Oulu, Finland
[2] Sternberg Astronomical Institution, University pr. 13, 119899 Moscow, Russia
[3] Crimean Astrophysical Observatory, p/o Nauchny, 334413 Crimea, Ukraine

Received 7 September 1998 / Accepted 27 October 1998

Abstract. The T Tauri star RY Tau has increased its brightness from V= $10\overset{\mathrm{m}}{.}6$ to V= $9\overset{\mathrm{m}}{.}6$ in October–November 1996. By February–March 1997, the star has faded again to V= $10\overset{\mathrm{m}}{.}8$. High–resolution échelle spectra of RY Tau were obtained with the SOFIN spectrograph at the Nordic Optical Telescope (La Palma, Spain) at low and high brightness levels of the star. No significant changes in the photospheric lines, which are sensitive to temperature and gravity, were noticed. The spectral type of RY Tau is defined as G1–2 IV, which in combination with photometric data implies $A_{\mathrm{V}} = 1\overset{\mathrm{m}}{.}0 - 1\overset{\mathrm{m}}{.}3$. Polarimetric patrol of RY Tau during the fading of the star showed an increase of its intrinsic polarization from 0.5–1.0% at high brightness to about 2% at low brightness in the V, R and I bands. The flux radiated in Hα and the IR Ca II emission lines remained about the same, in spite of the one magnitude difference in the continuum flux. These results indicate that variable obscuration of the star by circumstellar dust clouds was responsible for the brightness change of RY Tau, and that the emission line source is mostly outside of the obscured region.

Key words: stars: circumstellar matter – stars: individual: RY Tau – stars: pre-main sequence

1. Introduction

RY Tau belongs to the classical T Tauri Stars (TTS), with irregular light variability and a moderate emission spectrum. The star has long been a target for photometric and spectroscopic observations, particularly after its brightening in 1983/84 from 11th to 9th magnitude in V (Herbst & Stine 1984, Zajtseva et al. 1985). The characteristic pattern of the photometric variability of RY Tau is the near constancy of its colours at different brightnesses. Therefore, the dependence of the colours on the brightness is not well expressed but somewhat similar to that of the UX Ori–type stars: the star becomes slightly redder when fading from V= $9\overset{\mathrm{m}}{.}5$ to $10\overset{\mathrm{m}}{.}0$, but then turns to be bluer when even fainter, with a large intrinsic dispersion in the colours (Zajtseva 1986, Gahm et al. 1993, Eaton & Herbst 1995, Kardopolov & Rspaev 1995).

The spectral classification is K1e IV,V(Li) (Herbig 1977, Cohen & Kuhi 1979) though the earlier spectral type G2 was estimated by Cabrit et al. (1990). The star has a low level of veiling, ≤ 0.1 in the visible region of the spectrum (Basri et al. 1991, Hartigan et al. 1995). No veiling was found in the blue (Valenti et al. 1993). The IUE spectrum shows weak Fe II emission and moderate far–UV excess (Herbig & Goodrich 1986). The equivalent width of the Hα emission is about 20 Å (which is not far from the conventional threshold of 10 Å between weak–line TTS and classical TTS), Hβ is sometimes in emission, sometimes in absorption, while higher Balmer line are always in absorption.

Contrary to other classical TTS, RY Tau is a rapid rotator; its $v \sin i$ was determined to about 50 km s^{-1} (see e.g. Bouvier 1990). It is an X–ray emitter with $\log L_{\mathrm{X}} = 29.71$ (erg s^{-1}) (Damiani et al. 1995), which is an average value for TTS in the Tau–Aur region.

RY Tau has a rather large level of intrinsic linear polarization of a few percent. The variability of the linear polarization was first discovered by Vardanyan (1964) and confirmed by Serkowski (1969). The wavelength dependence of the linear polarization indicates that most of the polarization arises in an external, circumstellar dust envelope which lies outside of the high–temperature, gas–emitting region (Bastien & Landstreet 1979). The dependence of the linear polarization on the brightness of the star is not unambiguous, however in the deep minima of the brightness the polarization was higher (Efimov 1980).

RY Tau has a remarkably flat distribution of energy in the far–infrared region (Bertout et al. 1988); it is also a strong source of millimeter continuum emission (Beckwith et al. 1990), but

Send offprint requests to: P. Petrov

⋆ based on observations collected at the Nordic Optical Telescope (NOT), European Northern Observatory, La Palma, Spain; at the 2.6m and the 1.25m telescopes of the Crimean Astrophysical Observatory; at the 60cm telescope of the Crimean Laboratory of the Sternberg Astronomical Institution.

⋆⋆ Tables 2 and 3 are only available in electronic form at the CDS via anonymous ftp to cdsarc.u-strasbg.fr (130.79.128.5) or via http://cdsweb.u-strasbg.fr/Abstract.html

⋆⋆⋆ on leave from Crimean Astrophysical Observatory
Correspondence to: Peter.Petrov@Oulu.Fi

was not detected at radio wavelengths in a search for molecular outflows (Edwards & Snell 1982, Calvet et al. 1983).

There were many attempts to find a periodicity in the light variations of RY Tau on both short and long timescales. Some periods were reported on timescales from 5 to 66 days, but none was confirmed later on (Herbst et al. 1987, Herbst & Koret 1988, Bouvier et al. 1993, Bouvier et al. 1993, Bouvier et al. 1995). It is fair to say that if there is any periodicity in the light curve of RY Tau, it is hidden in a larger amplitude irregular variation and/or not persistent on a long timescale.

The relative constancy of colours during large amplitude variations of brightness indicates that the photospheric parameters of the star remain unchanged. Indeed, RY Tau does not show variations of the TiO bands with brightness even in rather deep minima, which could be expected if a cool spot were the cause of the brightness variability (Herbst & Lavreault 1990).

The Hα line profile is variable on a timescale of days, showing transient blue– and red–shifted absorption components (Zajtseva et al. 1985, Petrov & Vilhu 1991, Johns & Basri 1995). The same transient absorption was observed in the line profiles of the sodium doublet, which was interpreted as trace of stellar prominences (Petrov 1990). The most detailed review on the high–resolution line profiles was given by Hamann & Persson (1992).

The dependence of the Hα flux on the brightness of the star is somewhat controversial. Holtzman et al. (1986) found from UBVRI and Hα photometry that the Hα flux generally decreases as the star fades, but can change independently of brightness by a factor of 3 or more. On the other hand, Vrba et al. (1993) reported that the Hα flux increases with decreasing brightness, although with poor correlation.

During the patrol photometric observations of TTS at the Crimean Laboratory of the Sternberg Astronomical Institution, we have discovered a new event of brightness increase of RY Tau at the end of 1996. The star went from V= $10\overset{\mathrm{m}}{.}6$ to V= $9\overset{\mathrm{m}}{.}6$ within about one month (Zajtseva et al. 1996). This offered a new opportunity to study the phenomena connected with the brightening in great detail. In this paper we present photometric, polarimetric and spectroscopic data obtained at different brightness levels of the star, and discuss possible causes of its variability.

2. Observations

UBV *photometry:* The 60 cm telescope and the pulse–counting photometer at the Crimean Laboratory of the Sternberg Astronomical Institution (Ukraine) has been used for the photometric monitoring of TTS, including RY Tau, since 1965. Comparison stars and their magnitudes are given in Zajtseva et al. (1974). The diaphragm used was 27″; the typical error of the measurements is about $0\overset{\mathrm{m}}{.}01$.

UBVRI *photometry and polarimetry:* The 1.25 m telescope equipped with a five–channel photometer–polarimeter at the Crimean Astrophysical Observatory (Ukraine) was used for observations of RY Tau from December 1996 to March 1997. The diaphragm was 10″. UBVRI magnitudes of RY Tau were determined with respect to the comparison star SAO 76567 = BD +27°657, for which we determined V= $9\overset{\mathrm{m}}{.}13$, B–V= $0\overset{\mathrm{m}}{.}90$, U–B= $0\overset{\mathrm{m}}{.}34$, V–R= $0\overset{\mathrm{m}}{.}71$, V–I= $1\overset{\mathrm{m}}{.}23$, using the photometric standard BD +24°659 (K3 V, V= $9\overset{\mathrm{m}}{.}42$) from the list of Neckel & Chini (1980).

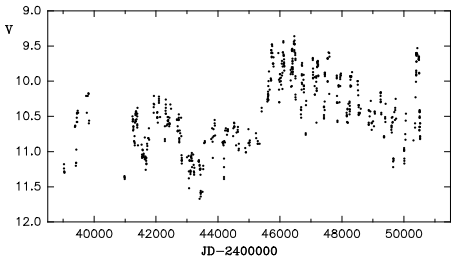

Fig. 1. The V light curve of RY Tau from 1965 to 1997

Spectroscopy: The high–resolution échelle spectrograph SOFIN at the 2.56 m Nordic Optical Telescope (La Palma, Spain) was used. The spectral range covered was 4500–9000 Å, the resolving power 25 000. For a typical spectrum, the S/N ratio was 100–200 longward of 5000 Å. One spectrum of RY Tau was taken at low brightness of the star on 4/5 Dec 1995, and several spectra were taken at high brightness during 20 Nov–01 Dec 1996. At low brightness in Dec 95, the star varied smoothly from V= $10\overset{\mathrm{m}}{.}8$ to $10\overset{\mathrm{m}}{.}5$; the nearest photometric measurement was obtained 4 days after the spectrum; we interpolate the brightness to V= $10\overset{\mathrm{m}}{.}65 \pm 0\overset{\mathrm{m}}{.}1$ at Dec 04, 1995. At high brightness, the first échelle spectrum was taken on Nov 20/21, 1996, at V= $9\overset{\mathrm{m}}{.}72$, simultaneously with photometry (see Fig. 2). The spectra of 84 Her (G1 III), 27 Ari (G5 III–IV), 70 Peg (G7 III) and δ Eri (K0 IV) were taken for comparison purposes.

Several spectra of RY Tau in the regions of Hα and Na D were also taken at the coudé spectrograph of the 2.6 m Shajn reflector at the Crimean Astrophysical Observatory, with a resolving power of 40 000.

The journal of our spectroscopic observations is presented in Table 1.

3. Results

3.1. Photometry

The photometric data are given in Table 2, and the light curve in the V–band for the period 1965–1997 is displayed in Fig. 1. A major part of these data (before JD 2 448 000) were included in the catalogue by Herbst et al. (1994). The last brightening started in October 1996 (JD 2 450 360). Within about 40 days, the star raised up to V= $9\overset{\mathrm{m}}{.}6$ and stayed at this level during three months, with small fluctuations of $0\overset{\mathrm{m}}{.}1 - 0\overset{\mathrm{m}}{.}2$ (Fig. 2). The subsequent fading of brightness down to V= $10\overset{\mathrm{m}}{.}8$ lasted for about one month, to the end of the observational season in March 1997. At the maximum brightness the average B–V colour was redder by about $0\overset{\mathrm{m}}{.}15$ as compared to that at the

Table 1. Spectroscopic observations of RY Tau 1989–1996.

Obs: CrAO – Crimean Astrophysical Observatory, Ukraine
NOT – Nordic Optical Telescope, La Palma, Spain
λ =spectral region: 1 – Hα
2 – Hα, Na D
3 – Hα, Na D, 6400 Å
4 – 4500–9000 Å
EW – equivalent width of the Hα emission in Å
F – flux in the Hα emission in 10^{-12} erg cm^{-2} s^{-1} Å^{-1}
When only one digit after the decimal point is given for the V magnitude, V has been interpolated from the closest points in the measured light curve.

date	JD 24...	Obs	λ	V	EW	F
30/31 Oct 89	47830.4	CrAO	2	$9\overset{m}{.}9$	14.6	15.6
07/08 Nov 89	47838.5	CrAO	2	$10\overset{m}{.}3$	18.7	15.2
10/11 Nov 89	47841.4	CrAO	2	$10\overset{m}{.}25$	22.0	14.9
18/19 Nov 89	47849.5	CrAO	1	$10\overset{m}{.}45$	24.9	20.2
30/31 Jan 90	47922.4	CrAO	1	$10\overset{m}{.}30$	17.4	12.9
08/09 Mar 90	47959.3	CrAO	1	$9\overset{m}{.}9$	12.0	12.9
17/18 Mar 90	47968.2	CrAO	2	$9\overset{m}{.}9$	12.3	13.2
19/20 Mar 90	47970.3	CrAO	1	$9\overset{m}{.}9$	11.4	12.0
22/23 Mar 90	47973.2	CrAO	2	$9\overset{m}{.}9$	7.6	8.1
04/05 Dec 95	50056.5	NOT	4	$10\overset{m}{.}65$	17.6	9.4
15/16 Nov 96	50403.5	CrAO	3	$9\overset{m}{.}62$	8.6	11.9
20/21 Nov 96	50408.5	NOT	4	$9\overset{m}{.}72$	6.0	7.6
20/21 Nov 96	50408.6	CrAO	3	$9\overset{m}{.}72$	6.0	7.6
25/26 Nov 96	50413.5	NOT	4	$9\overset{m}{.}7$	6.4	8.2
28/29 Nov 96	50415.7	NOT	4	$9\overset{m}{.}7$	8.5	10.9
29/30 Nov 96	50417.6	NOT	4	$9\overset{m}{.}7$	5.9	7.6
30/01 Dec 96	50418.6	NOT	4	$9\overset{m}{.}7$	10.3	13.3
01/02 Dec 96	50419.6	NOT	4	$9\overset{m}{.}7$	7.3	9.4
12/13 Dec 96	50430.5	CrAO	3	$9\overset{m}{.}6$	10.8	15.2

minimum brightness. The same change can be noticed in the U–B colour, but with larger scatter. The V *versus* B–V diagram is shown in Fig. 3: like was observed for previous photometric changes, the star becomes slightly redder when fading from V= $9\overset{m}{.}5$ to $10\overset{m}{.}0$, but then turns to become bluer when even fainter, with some intrinsic dispersion in the colours (Fig. 3).

3.2. Polarimetry

RY Tau is located in a region of large and non–uniform interstellar extinction. The value of A_V toward RY Tau was estimated as $1\overset{m}{.}24$ to $1\overset{m}{.}88$ by different observers (Cohen & Kuhi 1979, Kuhi 1974, Cernicharo et al. 1985).

Therefore, one may expect a large degree of interstellar polarization, comparable to the intrinsic polarization of RY Tau. Efimov (1980) found an interstellar polarization of $P_{\max} = 2.69\%$ with a position angle of PA= 27° for the wavelength of maximum polarization 0.55 μm, using observations of different stars in the vicinity of RY Tau and applying the normal law of interstellar extinction with $A_V = 1\overset{m}{.}88$. After that publication, a large set of polarimetric UBVRI observations of RY Tau was carried out at the Crimean Astrophysical Observatory in the period of 1981–1987. Using the new method for determination of interstellar polarization proposed by Shakhovskaya et al. (1987), we made a new estimation of the interstellar polarization toward RY Tau, based on more than 140 observations of the star: $P_{\max} = 2.84 \pm 0.14\%$, PA= $26° \pm 1\overset{\circ}{.}4$. The Serkowski law of polarization was adopted with the maximum polarization wavelength of 0.55 μm (Whittet 1977).

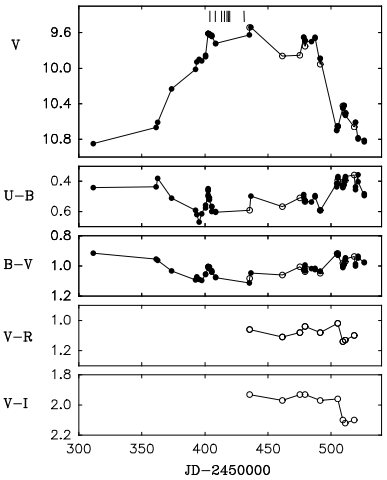

Fig. 2. The event of brightening in 1996/97. *Filled circles:* UBV photometry, *open circles* UBVRI photometry. The bars above the lightcurve indicate the dates of spectroscopic observations.

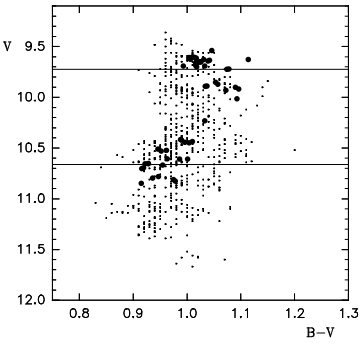

Fig. 3. Variability of brightness and colour of RY Tau. *Dots:* data of 1965–1997. *Filled circles:* the last event of brightening in 1996/97. The two dashed lines indicate the two levels of brightness, when spectroscopic observations were obtained.

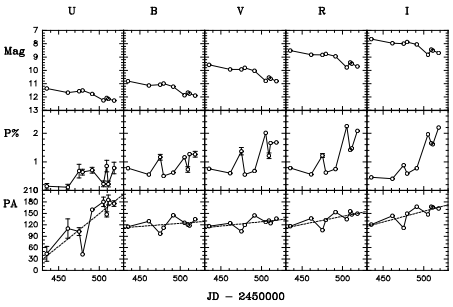

Fig. 4. Polarimetric observations in Dec 96–Mar 97; *upper panel:* the light curve in different bands; *central panel:* intrinsic polarizations P (%); *lower panel:* position angles PA (degrees).

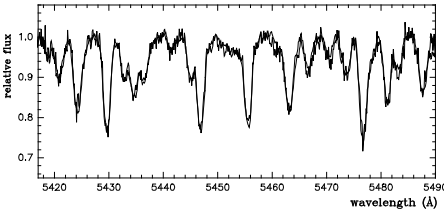

Fig. 5. Two overplotted spectra of RY Tau: one was taken at low brightness of the star, the other is the average spectrum at high brightness. The spectral lines belong to V I and Fe I of low excitation potentials, which are sensitive to the photospheric temperature. No difference in the line profiles exceeding 0.7 % of the continuum level was detected.

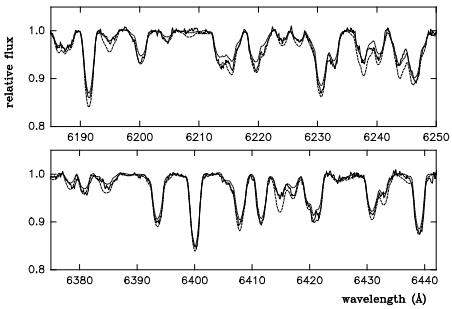

Fig. 6. Two fragments of the photospheric spectrum of RY Tau (*solid line*) compared to the reference spectra of G2 V (Sun, *dotted line*) and G1 III (84 Her, dashed line). All wavelengths are in the stellar restframe.

During the latest event of brightening of RY Tau in 1996, we started polarimetric observations in December 1996, when the star was already at high brightness, and followed the decline of brightness to the end of the observational season. The results of the observations are given in Table 3 and shown in Fig. 4. After correction for the interstellar polarization, the intrinsic polarization of RY Tau and its position angle were found to be variable with the brightness of the star. In the V, R and I bands the intrinsic polarization was increasing from 0.5–1.0% at high brightness to about 2% at low brightness. In the U and B bands this tendency is not well expressed. The position angle was progressively rotating as the star fades.

3.3. Spectroscopy

3.3.1. Photospheric spectrum

The depths of the photospheric lines in the 6 échelle spectra taken at high brightness in 1996 are the same; thus here we use the average photospheric spectrum.

The spectra of RY Tau at high and low brightness levels (Fig. 5) show remarkable constancy of the photospheric absorption lines within the accuracy of our measurements, which indicates the constancy of the photospheric temperature within about 40 K, in spite of the one magnitude difference in stellar brightness. From the region of 5000–7000 Å we determined the radial velocity RV$= 18 \pm 1\,\mathrm{km\,s^{-1}}$ and the projected rotational velocity $v \sin i = 52 \pm 2\,\mathrm{km\,s^{-1}}$. Both values are consistent with previous estimates (see e.g. Hartmann & Stauffer 1989 and Bouvier 1990).

The photospheric line spectrum of RY Tau is very similar to the solar spectrum, taken with the same spectrograph (day sky spectrum) and spun up to $v \sin i = 52\,\mathrm{km\,s^{-1}}$. Another suitable standard star is 84 Her: G1 III, $T_{\rm eff} = 5760$ K, $\log g = 3.2$ (Berdyugina 1994). The photospheric line depths and ratios in the spectrum of RY Tau are in the range given by spectra of the Sun and 84 Her (Fig. 6), in the spectral interval of 4500–8800 Å. An upper limit for the veiling factor can be set to ≤ 0.1. Therefore, we estimate the spectral type of RY Tau as G1–G2 IV with the intrinsic B–V colour $0\overset{\rm m}{.}65 - 0\overset{\rm m}{.}68$. At the bright state, RY Tau had V$= 9\overset{\rm m}{.}5 - 9\overset{\rm m}{.}7$ and B–V$= 0\overset{\rm m}{.}99 - 1\overset{\rm m}{.}05$, that is $E(\mathrm{B-V}) = 0\overset{\rm m}{.}3 - 0\overset{\rm m}{.}4$ and $A_{\rm V} = 3.2 \cdot E(\mathrm{B-V}) = 1\overset{\rm m}{.}0 - 1\overset{\rm m}{.}3$. With the distance to RY Tau of 140 pc (Elias 1978), we get $M_{\rm V} = 2\overset{\rm m}{.}5 - 3\overset{\rm m}{.}0$, which is in accordance with the spectral classification of G1–G2 IV.

3.3.2. Emission line spectrum

The most prominent emission lines in our spectra of RY Tau are those of Hα and the IR–triplet of Ca II. Weaker emission components are also present in Hβ, He I 5876 Å and Na I D. Of the forbidden emission lines only [O I] 6300 Å is clearly seen.

Fig. 7 shows several fragments of the average spectrum of RY Tau at high brightness. The range of variability in the emission line profiles is shown in Fig. 8.

It is interesting that the relative intensities of the emission components of Hα and the IR Ca II lines drop by a factor of 2–3 between Dec 95 and Nov 96, when the star has brightened by

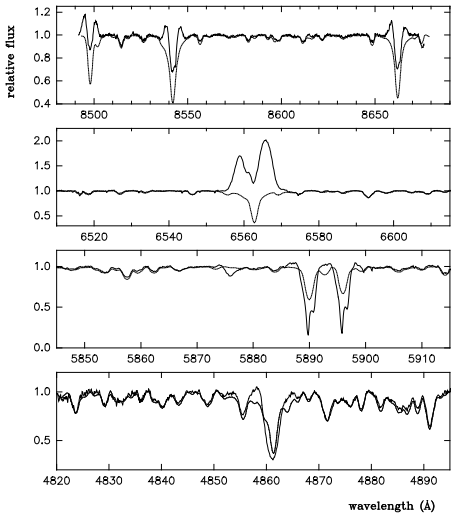

Fig. 7. Fragments of the average spectrum of RY Tau at high brightness in 1996 (*solid line*). The spectrum of 84 Her spun up to $v \sin i = 52\,\mathrm{km\,s^{-1}}$ is shown for comparison (*dotted line*). The wavelengths are in the stellar restframe.

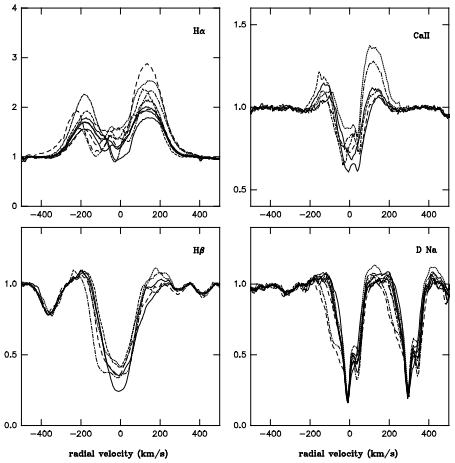

Fig. 8. Variability of line profiles in the spectrum of RY Tau at high brightness in 1996.

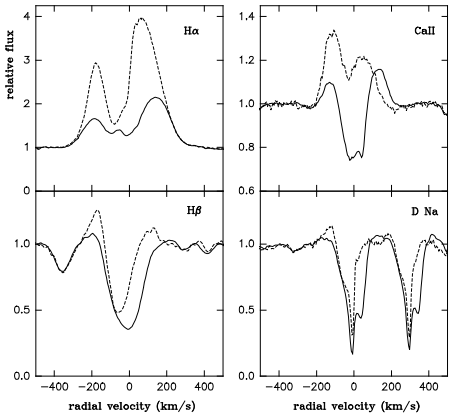

Fig. 9. The different line profiles in the spectrum of RY Tau at different brightness levels of the star; *solid line:* average spectrum at high brightness in 1996 (V= $9\overset{\mathrm{m}}{.}7$); *dashed line:* spectrum at low brightness in 1995 (V= $10\overset{\mathrm{m}}{.}7$).

one magnitude (see Fig. 9). This means that the *flux* radiated in these emission lines has remained about the same.

In the region around 5180 Å, the depths of the absorption lines of Mg I and Fe II at high brightness are consistent with the spectral type of the star (G1–2), but at low brightness these lines were shallower, as if the star were of late F–type. Since the photospheric temperature was the same at the two brightness levels, we conclude that at low brightness the Mg I and Fe II lines were partially filled in with emission. These emissions are shown in the differential spectrum: normalized spectrum at low brightness minus normalized spectrum at high brightness (Fig. 10).

In the high brightness state, the emission components of the sodium doublet are not prominent, while there are variable absorptions in the blue and red wings of the lines. The average equivalent width of the sodium lines is noticeably larger than in the comparison G stars (Fig. 7). The He I 5876 Å line is only slightly variable, with an average profile of inverse P Cyg–type, with the deepest absorption at +15 km s^{-1} and the red absorption wing extending to +100 km s^{-1} (the radial velocities are referred to the stellar restframe).

Since the Hα region was most frequently observed and the photometric history of RY Tau is well documented, we can check if the flux radiated in Hα relates to the stellar brightness. The equivalent widths of the Hα emissions and the fluxes radiated in Hα are given in Table 1. In addition to the spectra listed in Table 1, we also used several older spectra in the Hα region obtained at Crimea in 1988–89 (Petrov & Vilhu 1991).

Fig. 11 shows that the flux in Hα is variable by a factor of three but does not reveal any dependence on the stellar brightness. On average, when the star is fainter, the Hα emission appears stronger, because the range of the continuum variability is

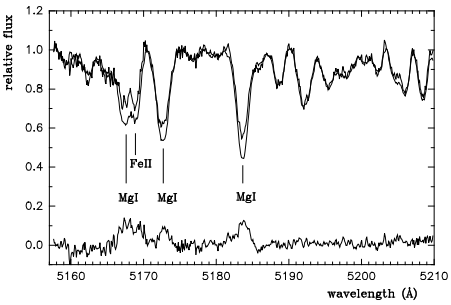

Fig. 10. The spectrum of RY Tau in the region of Mg I(2) 5167, 5172 and 5183 Å and Fe II(42) 5169 Å. The spectrum with the shallower lines is at low brightness (V= $10^{\rm m}.7$), the other one is the average spectrum at high brightness (V= $9^{\rm m}.6$). The curve at the bottom is the difference of the two spectra.

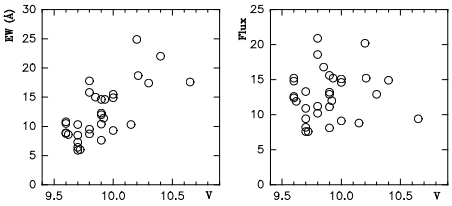

Fig. 11. Equivalent width and flux (in units of 10^{-12} erg cm^{-2} s^{-1} Å^{-1}) in the Hα emission as a function of stellar brightness.

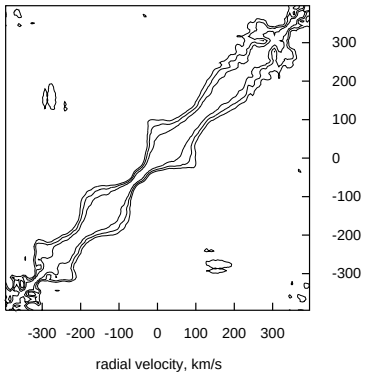

Fig. 12. Contour map of the correlation matrix for variations in the Hα *absolute flux* profile. The lowest contour represents a positive correlation at the 99.9% confidence level.

comparable to the range of intrinsic variability of the emission line flux.

The Hα line profile consists of a broad emission with symmetric wings extending to $\pm$ 400 km s^{-1}, and absorption components which appear and disappear on a time scale of days. There are two preferential velocities of these absorptions: one is around zero velocity and the other is at –100$\pm$50 km s^{-1}; both are clearly visible in the average Hα profile in Fig. 9. This kind of Hα profile variability was observed also in SU Aur (Giampapa et al. 1993, Johns & Basri 1995, Petrov et al. 1996).

The method of the correlation matrix is now commonly used to reveal a correlation in variability between different parts of a line profile or between two different lines. The correlation matrix Hα *versus* Hα plotted in Fig. 12 includes the 19 spectra listed in Table 1. The *absolute flux* profiles of Hα were used to compute the matrix, i.e. the variations of the continuum brightness do not affect the correlation matrix.

The two absorption components of Hα (at 0 and –100 km s^{-1}) vary independently from each other and independently from the rest of the emission profile. There is also no correlation between the blue (< -200 km s^{-1}) and red ($> +200$ km s^{-1}) wings of the line. The appearance of the correlation matrix is not very different from that published by Johns & Basri (1995).

4. Discussion and conclusions

There are at least three physical mechanisms which could account for the light variability of the TTS (see e.g. Herbst et al. 1994).

The first mechanism is an intrinsic one – the magnetic activity manifested in starspots resulting in (periodical) rotational modulation of the stellar brightness (the typical example is V410 Tau).

The second is related to interaction of the star with its circumstellar environment – irregular accretion of matter onto the star. This mechanism is probably dominant in the classical TTS, where accretion components are occasionally observed in the line profiles.

The third is an extrinsic one – obscuration of the star by circumstellar dust clouds. This phenomenon is most clearly observed in the UX Ori–type stars (Grinin et al. 1994), which are earlier spectral type counterparts of the TTS. It was also observed in the TTS RY Lup (Gahm et al. 1989). In a classical TTS, all three mechanisms may be in operation, which makes the observed variability very complicated.

The event of brightening of RY Tau, discussed in this paper, constitutes probably the rare case (for a classical TTS), when only one mechanism is dominant, while the others were not as efficient. Although the inflow of gas is evident through the red–shifted components of the sodium doublet lines and the He I line, the absence of measurable veiling indicates that accretion processes do not affect the brightness of the star. Neither is the presence of dark spots evident: no significant periodicity was found in the light variations. The case of a large polar spot of

variable effective area can also be excluded: such a spot would be visible in the photospheric line profiles.

The constancy of the photospheric parameters indicates that the source of the light variability is extrinsic – the dusty circumstellar environment has changed its opacity along the line of sight, which was observed as an apparent brightening of the star. The increase of the linear polarization accompanying the decrease in brightness supports this conclusion. The circumstellar dust is most probably confined to a disk, i.e. we observe RY Tau almost equator–on. The large value of $v \sin i$ also supports this assumption.

The fact, that the flux radiated in the Hα emission does not correlate with the stellar brightness, may indicate that the emission line source is located mostly *outside* of the star. When the star is obscured by dust, the contribution from the emission line source becomes larger and the emission spectrum appears more prominent, while the flux radiated in emission lines remains about the same or varies independently.

The strengthening of emission lines at minimum brightness was reported earlier by other observers. From simultaneous photometric and spectroscopic observations, Holtzman et al. (1986) found that Hβ changes from absorption, when the star is bright (V$= 9\overset{\mathrm{m}}{.}4$), to emission, when the star is faint (V$= 11\overset{\mathrm{m}}{.}0$), and the forbidden line [O I] 6300 Å became visible when the star was faint. Analysis of IUE spectra showed that the line Mg II 2800 Å changes from absorption to emission when RY Tau is fading from V$= 9\overset{\mathrm{m}}{.}9$ to V$= 10\overset{\mathrm{m}}{.}8$ (Eaton & Herbst 1995). It was noticed also already by Herbig (1961) that the forbidden line of [S II] was more prominent in emission when the star was faint.

From all this, we may conclude that the emitting region is not screened by the circumstellar dusty disk, although we look at the star almost equator–on. The result is quite expected for the forbidden lines, which form in a region extending far out of the star. It could also be expected for Hα, which comes from a large volume of stellar wind, but was not expected for the Ca II emission, which is often treated as an indicator of chromospheric activity. The appearance of emissions in the Mg I and Fe II lines at lower brightness is also surprising. We may conclude that at least Hα and the Ca II emission lines in RY Tau are formed neither in a chromosphere nor in an atmosphere of a boundary layer, otherwise they would be subject to obscuration by dust as well as the central star.

Acknowledgements. We would like to thank V.P. Grinin for helpful discussion. We are also grateful to the referee, Gösta Gahm, for many suggestions to improve the paper. This research was partly supported by the EC Human Capital and Mobility (Networks) grant "Late type stars: activity, magnetism, turbulence" No. ER–BCHRXCT940483.

References

Basri G., Martin E.L., Bertout C., 1991, A&A 252, 625
Bastien P., Landstreet J.D., 1979, ApJ 229, L137
Beckwith S.V.W., Sargent A.L., Chini R.S., Gusten R., 1990, AJ 99, 924
Berdyugina S.V., 1994, Astron. Lett. 20, 631
Bertout C., Basri G., Bouvier J., 1988, ApJ 330, 350
Bouvier J., 1990, AJ 99, 946
Bouvier J., Cabrit S., Fernandez M., Martin E.L., Matthews J.M., 1993, A&A 272, 176
Bouvier J., Covino E., Kovo O., et al., 1995, A&A 299, 89
Cabrit S., Edwards S., Strom S.E., Strom K.M., 1990, ApJ 354, 687
Calvet N., Canto J., Rodriguez L.F., 1983, ApJ 268, 739
Cernicharo J., Bachiller R., Duvert G., 1985, A&A 149, 273
Cohen M., Kuhi L.V., 1979, ApJS 41, 743
Damiani F., Micela G., Sciortino S., Harnden F.R., 1995, ApJ 446, 331
Eaton N.L., Herbst W., 1995, AJ 110, 2369
Edwards S., Snell R.L., 1982, ApJ 261, 151
Efimov Yu.S., 1980, Peremennye Zvezdy 21, 273
Elias J.H., 1978, ApJ 224, 857
Gahm G.F., Fischerström C., Liseau R., Lindroos K.P., 1989, A&A 211, 115
Gahm G.F., Gullbring E., Fischerström C., Lindroos K.P., Lodén K., 1993, A&AS 100, 371
Giampapa M., Basri G.S.,Johns C.M., Imhoff C.L., 1993, ApJS 89, 321
Grinin V.P., Thé P.S., de Winter D., et al., 1994, A&A 292, 165
Hamann F., Persson S.E., 1992, ApJS 82, 247
Hartigan P., Edwards S., Ghandour L., 1995, ApJ 452, 736
Hartmann L.W., Stauffer J.R., 1989, AJ 97, 873
Herbig G.H., 1961, ApJ 133, 337
Herbig G.H., 1977, ApJ 214, 747
Herbig G.H., Goodrich R.W., 1986, ApJ 309, 294
Herbst W., Booth J.F., Koret D.L., et al., 1987, AJ 94, 137
Herbst W., Herbst D.K., Grossman E.J., Weinstein D., 1994, AJ 108, 1906
Herbst W., Koret D.L., 1988, AJ 96, 1949
Herbst W., Lavreault R.M., 1990, AJ 100, 1951
Herbst W., Stine P.C., 1984, AJ 89, 1716
Holtzman J.A., Herbst W., Booth J., 1986, AJ 92, 1387
Johns C.M., Basri G., 1995, AJ 109, 2800
Kardopolov V.I., Rspaev F.K., 1995, Astron. Astrophys. Trans. 9, 189
Kuhi L.V., 1974, A&AS 15, 47
Neckel T., Chini R., 1980, A&AS 39, 411
Petrov P.P., 1990, Ap&SS 169, 61
Petrov P.P., Gullbring E., Ilyin I., et al., 1996, A&A 314, 821
Petrov P., Vilhu O., 1991, RY Tauri. In: Tuominen I., Moss D., Rüdiger G. (eds.) Proc. IAU Coll. 130, The Sun and Cool Stars: activity, magnetism, dynamos. Lecture Notes in Physics 380, Springer, Berlin, p. 471
Serkowski K., 1969, ApJ 156, L55
Shakhovskaya N.I., Shakhovskoj N.M., Beskrovnaja N.G., 1987, Bull. Crim. Astrophys. Obs., 75, 110
Valenti J.A., Basri G., Johns C.M., 1993, AJ 106, 2024
Vardanyan R.A., 1964, Soobshch. Byurak. Obs. 35, 3
Vrba F.J., Chugainov P.F., Weaver W.B., Stauffer J.S., 1993, AJ 106, 1608
Whittet D.C.,1977, MNRAS 180, 29
Zajtseva G.V., 1986, Afz 25, 471
Zajtseva G.V., Kolotilov E.A., Petrov P.P., et al., 1985, SvA Lett. 11, 109
Zajtseva G., Lyutyi V.M., Cherepashchuk A.M., 1974, Afz 10, 357
Zajtseva G., Petrov P., Ilyin I., Duemmler R., Tuominen I., 1996, Inform. Bull. Variable Stars, No. 4408

Paper V

Petrov, P., Duemmler, R., Ilyin, I, Tuominen, I. 1998, "Increase of emission and shell features in the spectrum of the FUor V1057 Cyg", A&A 331, L53

Astron. Astrophys. 331, L53–L56 (1998)

ASTRONOMY AND ASTROPHYSICS

LETTER

Letter to the Editor

Increase of emission and shell features in the spectrum of the FUor V1057 Cyg⋆

P. Petrov[1,2], **R. Duemmler**[2], **I. Ilyin**[2], **and I. Tuominen**[2]

[1] Crimean Astrophysical Observatory, 334413 Nauchny, Crimea, Ukraine
[2] Astronomy Division, University of Oulu, P.O. Box 333, FIN-90571 Oulu, Finland

Received 14 November 1997 / Accepted 6 January 1998

Abstract. High–resolution échelle spectra of the FUor V1057 Cyg were taken during its minimum brightness in 1996–97. The spectra show the appearance of strong shell–components in the lines of low excitation, an increase of the splitting of the photospheric absorption lines, and the appearance of weak emission lines. It is argued that the mysterious line splitting of the absorption lines in the spectrum of V1057 Cyg, which has been interpreted as originating from an accretion disk, can be explained simply by the presence of central emission cores in the broad absorption lines. This emission spectrum of V1057 Cyg has increased in strength relative to the continuum as the star has faded.

Key words: (stars:) circumstellar matter – stars: individual: V1057 Cyg – stars: pre–main sequence – accretion disks – FUors

1. Introduction

The star V1057 Cyg belongs to the small group of the FU Orionis type stars (FUors), pre–main sequence objects which are undergoing an event of eruptive activity (Herbig 1977). Before its flare–up in 1970, V1057 Cyg was a T Tauri star with the characteristic emission line spectrum. After the rise in brightness, its spectrum changed drastically to an A–F supergiant and later to a G supergiant (G2–5 Ib–II, Herbig 1977). Among the known FUors, V1057 Cyg has the fastest rate of brightness decline during the first two decades after the flare–up.

A characteristic feature of all the FUors is the double profile of the absorption lines. This was one of the reasons to interpret the FUors as objects with accretion disks, where the spectrum is formed not in the atmosphere of a supergiant, but in the atmosphere of an optically thick luminous accretion disk rotating at Keplerian velocities (Hartmann & Kenyon 1985). This interpretation was criticized by Petrov & Herbig (1992), who pointed out that the line doubling phenomenon is observed also in some of the shell–supergiants. It was proposed that the absorption line profiles are split due to the presence of emission components at the center of the absorption lines.

In 1995, V1057 Cyg went into a minimum of its brightness (Ibrahimova & Ibrahimov 1997, Kolotilov & Kenyon 1997) and eventually, in 1997, reached almost its pre–outburst level of brightness in the B band. In this letter we show the most conspicuous changes in the spectrum of V1057 Cyg during the minimum brightness, in 1996 and 1997. At the dates of our observations, the star had nearly the same brightness and colour, V$\approx 12\overset{\mathrm{m}}{.}5$, B–V$\approx 2\overset{\mathrm{m}}{.}05$ (E. Kolotilov, private communication).

This is a preliminary report of new observations, with a minimum of interpretation. A more detailed analysis will follow in a later paper.

2. Observations

The high–resolution échelle–spectra of V1057 Cyg were taken on October 30, 1996 and August 15–22, 1997 at the Nordic Optical Telescope (La Palma, Spain) with the SOFIN échelle spectrograph. In October 1996, the spectrum has a S/N ratio of about 100 in the red. In August 1997, a series of exposures with a total exposure time of 24 hours provided a mean spectrum with a S/N ratio of more than 300 in the red. Weak lines of equivalent widths down to 10 mÅ can be identified in the spectrum. The resolution in the average spectrum of August 1997 is about 13 km s^{-1}. The spectra of V1057 Cyg have useful signal in the wavelength range 4800–9000 Å. Spectra of 41 Cyg (F5 II), β Aqr (G0 Ib), 9 Peg (G5 Ib), 40 Peg (G8 II), 84 Her (G2 IIIb) and β And (M0 IIIa) were taken for comparison.

3. Emission lines

A number of emission lines, in addition to H α and the Ca II lines, appeared in the spectrum of V1057 Cyg in August 1997 (cf. Figs. 1 and 2), as compared to the spectrum of 1996 and those previously published. The most conspicuous is the line Fe I (12) λ8047Å. The peak of the emission is at the stellar velocity (–16 km s^{-1}), its width is slightly less than the

Send offprint requests to: P. Petrov (e-mail: Peter.Petrov@Oulu.Fi)

⋆ Based on observations obtained at the 2.56m Nordic Optical Telescope, Roque de Los Muchachos Observatory, La Palma/Spain.

LETTER

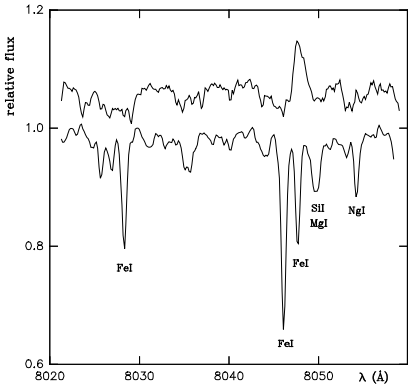

Fig. 1. The emission of Fe I (12) λ8047Å in the spectrum of V1057 Cyg in August 1997 (upper bold curve). The spectrum of β Aqr is shown for comparison, with the identification of a few lines. The spectra are shifted in relative fluxes for clarity.

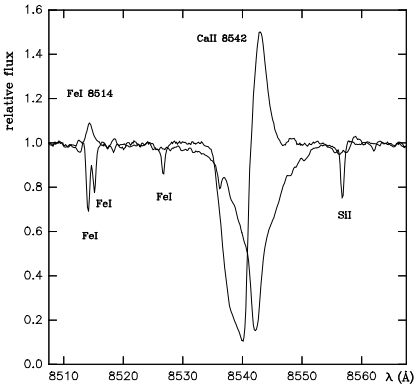

Fig. 2. The emissions of Ca II (2) λ8542Å and Fe I (60) λ8514Å in the spectrum of V1057 Cyg in August 1997 (bold curve). The spectrum of β Aqr is shown for comparison.

width of the photospheric absorption lines. The other emissions are Fe I (60) λ8514Å, Fe II (40) λ6516Å, Ca I (1) λ6572Å and Fe I (12) λ7912Å. It is interesting to note that all of these lines are strong in emission in the spectrum of the pre–main sequence star VY Tau (Herbig 1990). The H α and IR Ca II lines show P Cyg–profiles with the blue–shifted absorption extending up to –380 and –250 km s^{-1}, respectively.

4. Emission components in the photospheric absorption lines

The photospheric absorption lines in the high–quality spectrum of V1057 Cyg obtained in August 1997 are much shallower than in the spectra published so far, which makes a comparison with the spectra of standard stars rather difficult. The ratio of the photospheric line intensities can set limits for the spectral type of F7–G5 Ib–II. The lines of higher excitation potentials, which are supposed to be less affected by emission and shell-components (see below) were used for the spectral classification.

Most of the photospheric absorption lines appear double with an emission–like component at the bottom of the absorption. The wings of the absorption lines near the continuum level (5–7% below the continuum) can be fitted by a rotational profile with $v \sin i$ of about 50 km s^{-1}, with a scatter of $\pm$10 km s^{-1} for the individual lines. No systematic trend of this parameter with wavelength was found in the spectral range 5000–8800 Å.

The most interesting finding is that the line doubling, i.e. the velocity separation between the two absorption dips, has increased in October 1996, and even more so in August 1997, as compared to the spectra published so far.

Comparison with the spectra of V1057 Cyg, published by Kenyon et al. (1988)[1] and by Hartmann & Calvet (1995), shows that the line width of the absorption near the continuum level remains the same, but the central emission-like reversal has increased, and the depth of the absorption has been reduced. Due to this effect, some of the weaker lines have almost vanished. At lower S/N ratio, the spectrum would have a "washed out" appearance.

As noted above, several low–excitation lines of Fe I and Ca I have clearly gone over into emission. It is reasonable that the same phenomenon should appear to a lesser degree in other, higher–excitation lines, as a central emission core. This would cause those absorption lines to appear double, precisely as is observed (a typical example is shown in Fig. 3). The strength of the emission spectrum has increased with respect to the continuum as the star has become fainter, so the "line doubling" is now quite striking.

The effect of the line splitting by emission components is most clearly demonstrated by the changes in the profile of Fe I λ6191 Å. The spectra of V1057 Cyg in this region published before were taken in 1988 (Welty et al. 1992) and in 1992 (Hartmann & Calvet 1995). In both spectra the line is not split, with a central depth of about 13% of the continuum level. In October 1996, the line had the same depth, but the weak emission core was already present. In August 1997, the line depth was reduced to 5% and the emission core rose up almost to the continuum level (see Fig. 4). Obviously, this line splitting is entirely due to the rise of the emission core.

[1] The high–resolution spectra published by Kenyon et al. (1988) as well as those by Welty et al. (1992) and Hartmann & Calvet (1995), referred to below, were taken when the star was about $1^{\rm m}$ brighter, V= $11\overset{\rm m}{.}5 - 11\overset{\rm m}{.}6$, B–V= $1\overset{\rm m}{.}7 - 1\overset{\rm m}{.}8$ (Ibrahimova & Ibrahimov 1997).

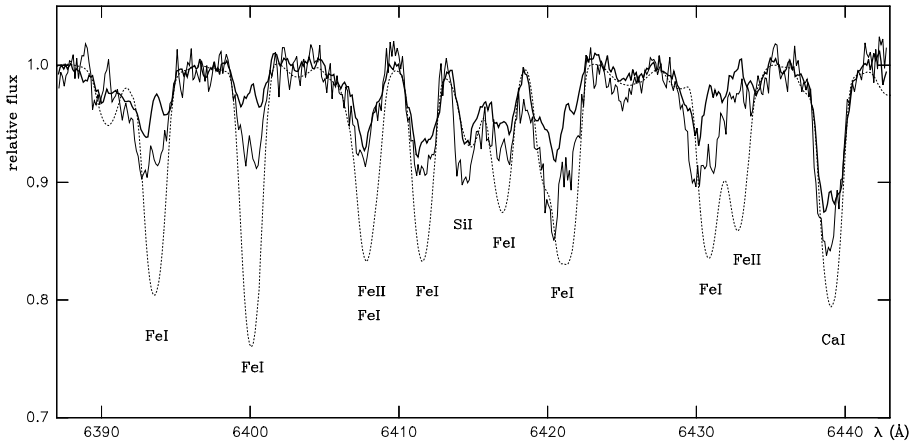

Fig. 3. The bold curve is the spectrum of V1057 Cyg in August 1997, the thin solid curve that in October 1996; the dotted line is the spectrum of β Aqr, spun up to $v \sin i = 50$ km s^{-1}. Note the rise of the emission cores which makes some of the absorption lines appear split.

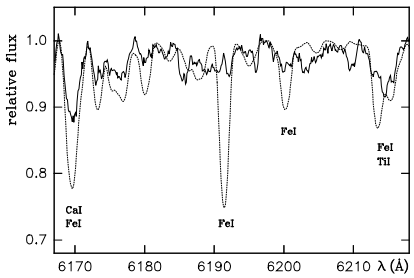

Fig. 4. The bold line is the spectrum of V1057 Cyg in August 1997. The dotted line is the spectrum of β Aqr, spun up to $v \sin i = 50$ km s^{-1}. Note the emission core in Fe I λ6191Å.

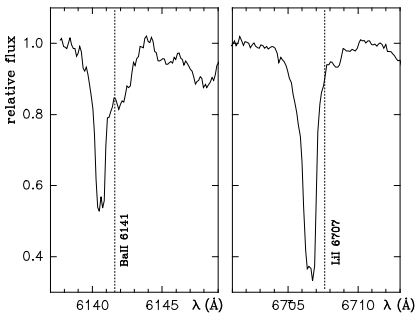

Fig. 5. The blue–shifted shell components in Ba II (2) λ6141Å and in Li I (1) λ6707Å in the spectrum of V1057 Cyg in August 1997. The line positions in the stellar restframe are indicated.

Another argument in favour of this interpretation of the line splitting is that the splitting is *differential*, i.e. the intensities of the emission components at the bottom of the absorption lines are not the same in different lines. The weaker lines of the highest excitation potentials ($>$ 5 eV) are not split, while most of the stronger lines of lower potentials (2–4 eV) are split by an emission component. The velocity separation between the double absorption dips is, on average, 44 km s^{-1} in the red part of the spectrum (as compared to 30 km s^{-1} reported by Hartmann & Kenyon 1985). This value is, however, very different in individual lines: the lines most strongly filled in by emission are split up to 60 km s^{-1} (e.g. Fe I λ6393Å, Fe I λ6400Å).

5. Shell components of the low excitation lines

Another obvious difference in the new spectra of V1057 Cyg as compared to those published before is the appearance of numerous sharp, blue–shifted shell–components of absorption lines of low excitation ($<$ 1 eV) (Figs. 5 and 6). The shell components were stronger in the spectrum of October 1996 than in the spectrum of August 1997. In October 1996, besides the atomic shell–lines, a few weak TiO bands were present in the spectrum, for example the R_1 band of the TiO γ–system near 6781 Å. The sharp head of the TiO band was also blue–shifted,

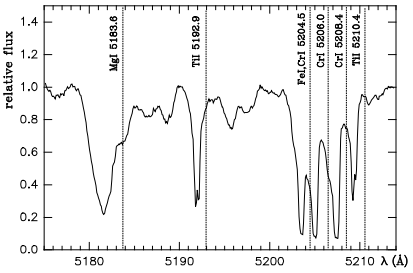

Fig. 6. The shell components in Mg I, Ti I and Cr I lines in the spectrum of V1057 Cyg in August 1997. The line positions in the stellar restframe are indicated.

showing that the bands originate in the expanding shell. In August 1997, the TiO bands have disappeared together with the weaker shell–components of atomic lines.

Some of the blue–shifted shell–lines have no photospheric counterparts at the stellar velocity, because they are too weak in a G–type spectrum, but rather strong in the spectrum of a cool expanding shell.

The radial velocities of the shell components range from –40 to –55 km s^{-1}. The stronger the shell–absorption, the larger its blue–shift. In August 1997, most of the shell–components had two just resolved peaks of absorption separated by 16 km s^{-1} (e.g. Ba II λ6141Å, see Fig. 5). The weak emission line of Ca I (1) λ6572Å is also accompanied by a distinct shell–absorption at –45 km s^{-1}.

6. Discussion and conclusions

The remarkable changes in the spectrum of V1057 Cyg indicate that the fading in brightness, the formation of a cool, expanding shell, and the increase of emission lines may be physically related phenomena.

The dimming of the star, accompanied by the appearance of weak emission lines might be considered as the beginning of the return of the star to its pre–outburst T Tau state. In this case, however, one would expect a change of the spectral type to late K of lower luminosity, which is not observed.

The brightness fading was interpreted by Kolotilov & Kenyon (1997) as due to a dust condensation event in the outflowing wind. The development of the dense cool shell and the absence of appreciable change in spectral type, reported in this letter, seem to support this hypothesis. This implies that the current photometric minimum is temporary, and the star will eventually recover to its previous brightness level.

The presence of emission cores in the broad photospheric absorption lines can quite simply account for the mysterious line splitting in the spectrum of V1057 Cyg (and probably in other FUors as well), as was proposed by Petrov & Herbig (1992) for FU Ori itself. It is the fading of V1057 Cyg, and the consequent enhancement of this emission spectrum, that has made this interpretation so much more persuasive. This is not to deny that FUors may have accretion disks, but only to assert that their absorption line doubling has another explanation. It remains to be investigated whether the emissions are formed somewhere in the wind, which is responsible for the P Cyg–profiles in Ca II and H α.

In any case, these new data put more restrictions on the models of FUors, whose nature is still far from being understood.

Acknowledgements. We are very grateful to George Herbig, Gösta Gahm and Svetlana Berdyugina for useful discussions and critical comments. Evgenij Kolotilov kindly provided us with the new photometric data of V1057 Cyg. We thank the referees for many suggestions. This work was partly supported by the EC Human Capital and Mobility Network project "Late–type start: activity, magnetism, turbulence" (No. ER–BCHRXCT940483). The observations were partly supported by the European Commission through the Activity "Access to Large–Scale Facilities" within the Programme "Training and Mobility of Researchers".

References

Hartmann L., Calvet N., 1995, AJ 109, 1846
Hartmann L., Kenyon S.J., 1985, ApJ 299, 462
Herbig G.H., 1977, ApJ 217, 693
Herbig G.H., 1990, ApJ 360, 639
Ibrahimova V.M., Ibrahimov M.A., 1997, IBVS 4479
Kenyon S.J., Hartmann L., Hewett R., 1988, ApJ 325, 231
Kolotilov E.A., Kenyon S.J., 1997, IBVS 4494
Petrov P.P., Herbig G.H., 1992, ApJ 392, 209
Welty A.D., Strom S.E., Scott S.E., Hartmann L.W., 1992, ApJ 397, 260

This article was processed by the author using Springer-Verlag LaTeX A&A style file *L-AA* version 3.

Paper VI

Berdyugina, S.V., Jankov, S., Ilyin, I, Tuominen, I., Fekel, F.C. 1998, "The active RS Canum Venaticorum binary II Pegasi. I. Stellar and orbital parameters", A&A 334, 863

Astron. Astrophys. 334, 863–872 (1998)

ASTRONOMY AND ASTROPHYSICS

The active RS Canum Venaticorum binary II Pegasi⋆

I. Stellar and orbital parameters

S.V. Berdyugina[1,2], S. Jankov[3], I. Ilyin[1], I. Tuominen[1], and F.C. Fekel[4]

[1] Astronomy Division, University of Oulu, P.O. Box 333, FIN-90571 Oulu, Finland (e-mail: sveta@ukko.oulu.fi)
[2] Crimean Astrophysical Observatory, P.O. Nauchny, Crimea, 334413 Ukraine
[3] Universidade de São Paulo, Depto. de Astronomia, C.P. 30627, São Paulo 01051, Brazil
[4] Center for Automated Space Science and Center of Excellence in Information Systems, Tennessee State University, Nashville, TN 37203, USA

Received 11 December 1997 / Accepted 5 March 1998

Abstract. A detailed model atmosphere analysis of high-resolution and high S/N CCD spectra of II Peg has yielded for the first time a self-consistent set of fundamental parameters of the primary component: $T_{\rm eff}$=4600 K, log g=3.2, [M/H]=–0.4, $\xi_{\rm t}$=2.0 km s^{-1}. In addition, 121 new high quality radial velocity measurements[1] allowed us to determine improved orbital parameters, resulting in a new orbital ephemeris of $T_{\rm conj}$=2449582.9268+6.724333E. The position of the primary of II Peg in the HR diagram with the new parameters corresponds to a K2 IV star with mass ≈0.8 $M_\odot$. The evolved character of the star is confirmed by the C/N ratio, which is reduced significantly relative to the solar value. The unspotted V magnitude of the star of $6\overset{\rm m}{.}9$ is estimated from the observed variations of the TiO bands and quasi-simultaneous photometry. The blend of Li I 6707 Å is suspected to vary in equivalent width due to spot modulation. The lithium abundance for the unspotted star, Li/H=1.0±0.1, is found to be consistent with other post-main sequence chromospherically active stars. Combining all parameters, the radius R ≈ 3.4 $R_\odot$ and the inclination $i \approx 60^\circ$ of the primary are estimated with the assumption that its rotational axis is perpendicular to the orbital plane. The secondary is probably a M0-M3 V star with a mass of about 0.4 $M_\odot$.

Key words: stars: binaries: spectroscopic – stars: fundamental parameters – stars: abundances – stars: activity – stars: individual: II Peg

Send offprint requests to: S.V. Berdyugina

⋆ based on observations collected at the Nordic Optical Telescope (NOT), La Palma, Spain; the 2.6 m telescope of the Crimean Astrophysical Observatory, Ukraine; the 2.7 m and 2.1 m telescopes of the McDonald Observatory, USA; the coudé feed telescope of the Kitt Peak National Observatory, USA

[1] Table 2 is also available in electronic form at the CDS via anonymous ftp to cdsarc.u-strasbg.fr (130.79.128.5) or via http://cdsweb.u-strasbg.fr/Abstract.html.

1. Introduction

II Peg (HD 224085) was discovered to show periodic photometric variability by Chugainov (1976a). Now it is known as one of the most active RS CVn type stars, which are usually G-K subgiants or giants in close binaries. The periodic photometric variability of such stars is interpreted in terms of cool surface spots analogous to sunspots but much enhanced in scale. The existence of cool spots on the surface of II Peg is confirmed by the presence of TiO bands in the observed spectrum of the star (Vogt 1981).

Sanford (1921) obtained the earliest radial velocity measurements of the primary of II Peg and found that the orbit is nearly circular. Although the orbit was subsequently refined by several authors, the best previous ephemeris still predicts the radial velocities with an accuracy ±2.5 km s^{-1}, which is unsatisfactory for our purposes.

Several spectral types of the primary of II Peg have been determined, ranging between K0 and K3 in temperature, and between III and V in luminosity. Rucinski (1977) deduced a spectral type of K2-3 IV-V and noted some inconsistencies in the line ratios. The secondary of II Peg is unseen and probably a low-mass main sequence star.

For some time the presence of Li I 6707 Å line in the spectrum of II Peg was suggested to be an indication that the star must be rather young. Thus, because of its location slightly above the main sequence, the star was suggested to be in a late stage of pre-main sequence evolution (Rucinski 1977). However, Fekel & Balachandran (1993) and Randich et al. (1994) found the presence of substantial amounts of Li to be typical in many chromospherically active stars. The question is whether these relatively high Li abundances are due to enhanced chromospheric activity or rather are a consequence of the evolutionary history of the stars.

This first part of our study of II Peg is based primarily on new high-resolution spectroscopy of II Peg during 1994-1996. The main purpose of these observations was to produce new surface images of the primary, but we found it extremely useful to exploit them for (i) improving the orbital parameters, (ii)

determining new atmospheric parameters of the primary in a self-consistent way, and (iii) determining the evolutionary status of both components of the binary. The results of this study should be considered as input for the subsequent surface imaging of the primary of II Peg (Berdyugina et al. 1998a) and an analysis of its chromospheric activity (Berdyugina et al. 1998b). The structure of this paper is as follows. The observation and data reduction procedures are described in Section 2. Orbital parameters are determined in Section 3. Atmospheric parameters of the primary together with the lithium abundance and C/N ratio are presented in Section 4. The fundamental parameters of the components of II Peg are discussed in Section 5, and finally, Section 6 presents a summary of our work.

2. Observations and data reduction

Observations were carried out in 1994-1996 with the SOFIN échelle spectrograph (Tuominen 1992) fed by the 2.56 m Nordic Optical Telescope (NOT) at the Roque de los Muchachos Observatory, La Palma, Canarias. The data were acquired with the 2nd camera equipped with a CCD detector of 1152×298 pixels, yielding a wide spectral range (in 14 orders) of approximately 5500-8500 Å. For all observing runs the projected width of the slit was set to be $0\farcs5$ on the sky, providing a spectral resolving power $\lambda/\Delta\lambda \approx 83\,000$. With this setup, the dispersion at 6170 Å was 37 mÅ per pixel. A typical exposure time of $\approx 1^{\rm h}$ achieved a signal-to-noise ratio of more than 200 for most spectra. Additionally, one exposure of β Gem was obtained with the same setup to determine the velocity zero-point of the spectrograph and to use as a standard in spectrum synthesis calculations. It is a known standard star in both cases.

During the 1996 season II Peg was also observed with the coudé spectrograph installed on the 2.6 m telescope of the Crimean Astrophysical Observatory. The detector was CCD SDS 9000, Photometrics GmbH with 1024×400 pixels. With the slit of $0\farcs4$ and dispersion of 65 mÅ per pixel a resolving power as large as 41 000 was obtained. The covered spectral range was about 60 Å centered at 6170 Å or 7065 Å. The signal-to-noise ratio of an individual exposure was in most cases greater than 150.

From 1978 to 1980, 5 spectroscopic observations were obtained with the 2.7 m or 2.1 m telescopes, coudé spectrographs, and Reticon detectors at the McDonald Observatory. The spectra were centered at 6430 Å or 6700 Å, with $\lambda/\Delta\lambda$ = 20 000 and S/N $>$ 150. Observations were continued from 1990 to 1997 with the coudé feed telescope, coudé spectrograph, and a TI CCD at Kitt Peak National Observatory. Twenty spectra were centered at 6430 Å except for one at 6700 Å and one at 6565 Å, having $\lambda/\Delta\lambda$ = 30 000 and S/N $>$ 200. These observations were used only for the radial velocity measurements.

The reduction of the SOFIN data, described by Ilyin (1997), included bias, scattered light, and flat field corrections, extraction of spectral orders, and wavelength calibration. The latter is obtained with a thorium-argon comparison spectrum. Finally, the wavelengths were corrected for the Earth's motion. The Crimean spectra were reduced similarly except for the steps specifically relating to the echelle spectra.

Great care was taken in the continuum normalization, since the numerous photospheric lines are affected by the large rotational broadening, so the true continuum is not observed in almost all spectral regions. In the first iteration the continuum level was defined by a smoothing cubic spline drawn through estimated continuum points. In the next iteration the spectrograms were normalized to a common continuum level by comparing the observed spectra with a synthetic one, broadened to the same rotational velocity. In principle, it should suffice, if the synthetic spectrum describes perfectly the spectrum of the star. In any case, it could be improved after subsequent estimates of stellar parameters.

Table 1. Radial velocities of β Gem.

HJD	Order	λ_c,Å	RV,km s^{-1}
2450383.7681	34	6725	3.52
”	35	6534	3.74
”	36	6353	3.74
”	37	6181	3.57
”	39	5864	3.60
		Mean =	3.63±0.04

3. Parameters of the orbit

3.1. Zero-point velocity of the SOFIN spectrograph

To estimate the zero-point velocity of the SOFIN spectrograph, we measured the radial velocity of β Gem (HD 62509), which is recommended as a standard radial velocity star with RV=+3.3±0.1 km s^{-1}(Astronomical Almanac 1997). The RV of β Gem was measured by cross-correlating observed spectra with synthetic ones for five orders containing strong absorption lines. The source of line lists was the Vienna Atomic Line Database (hereafter VALD, Piskunov 1995), and stellar parameters were taken from the detailed model atmosphere analysis of the star by Drake and Smith (1991). The results of the measurements are presented in Table 1. There are no significant differences among radial velocities measured from different orders nor is there a systematic trend with wavelength. Thus, comparing the mean value with the assumed one, we deduce the *instant* zero-point velocity correction of the SOFIN spectrograph of 0.3±0.1 km s^{-1}. We call it *instant* because this is only a measurement of that value at a certain moment. In reality the correction might be a more complicated function. It should be stressed that we did not take into account the determined velocity correction in the subsequent reduction, but we wanted only to estimate how large it is.

3.2. A log of RV measurements of II Peg

We have obtained a total of 121 new observations (59 from SOFIN, 37 from Crimea, 5 from McDonald, and 20 from KPNO), and the data sets have rather good phase coverage.

The SOFIN observations have velocities measured from several orders, increasing the accuracy of those radial velocity measurements. Unfortunately, many of the 14 orders could not be used because numerous atmospheric lines in some wavelength regions strongly disturb the cross-correlation function.

The radial velocities of II Peg from the SOFIN and Crimean data were measured by cross-correlating the observed spectra with the synthetic spectra calculated with appropriate atmospheric parameters. Probably, such a procedure is more accurate than using a standard-star spectrum due to the possible inconsistency of relative strengths of lines and, therefore, shapes of rotationally broadened blends. Furthermore, the RV measurements could be improved after the new stellar parameters were determined. Also, note that the line list for the spectra calculations was improved using the spectrum of β Gem (this procedure is discussed in Section 3 as well). From the SOFIN data we used spectra of seven orders: the orders given in Table 1 as well as the 27th (λ_c=8440 Å) and the 41st (λ_c=5560 Å). Again, we found no significant systematic velocity trend among orders spanning wavelengths from 5560 to 8440 Å.

The McDonald and KPNO spectra were measured with the cross-correlation procedure of Fitzpatrick (1993). However, only the least blended 3 or 4 lines were used. In some cases the correlation profile was obviously asymmetric. In such cases the fits emphasized the shoulders rather than the center of the profile. Velocities were determined relative to the IAU standard stars ι Psc, α Ari, or HR 8551, whose velocities were taken from Scarfe et al. (1990). Also used as standards were μ Her (Stockton & Fekel 1992) and β Aql, the latter tied to the IAU system and having an assumed velocity of –40.2 km s^{-1}.

Earlier radial velocity measurements of II Peg, 25 RVs from Sanford (1921), 6 RVs from Halliday (1952), 1 RV from Heard (1956), 2 RVs from Rucinski (1977), and 2 RVs from Vogt (1981), were used in the period determination. So, the available data presently consists of 157 values, spanning from 1917 to 1997. Thus, we have a fortunate opportunity to derive new, much more accurate, orbital parameters of II Peg. We suspect that the presentation of the whole log of the measurements in Table 2 is relevant for both the present discussion and the future.

3.3. The orbit

For our purpose we used the program FOTEL3 developed by Hadrava (1995), which is able to deduce the orbital period value together with other parameters for both circular and eccentric orbits. The first step was to determine new values of the period P and eccentricity e. A first solution was found for all radial velocity measurements listed in Table 2 with appropriate weights which were determined from the variances to the fit. It is given in Table 3. Note that the fit allowed different γ-velocities for different data sets. In comparison to the previous published values of P and e by Vogt (1981) the new values are much more accurate. Moreover, if only new RVs are used to determine the eccentricity, then it drops to 0.0025±0.0026. Such a small value of the eccentricity could be probably ignored for the present, and the orbit can be considered as circular.

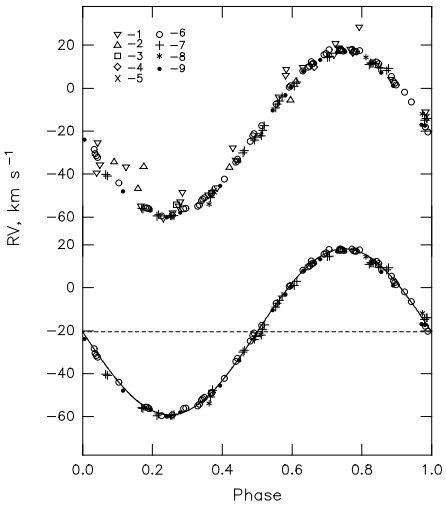

Fig. 1. Radial velocity measurements phased with the new ephemeris T_{conj} = 2449582.9268 + 6.724333 E. The top displays all measurements with the same reference numbers as in Table 2, while the bottom shows the new data only with the Solution 2 as a solid line (see Table 3).

The accuracy of the data sets is obviously rather different, and the new measurements are significantly more accurate, especially the SOFIN data. For this reason we assumed the period from the all-data solution and the eccentricity to be zero and found the best solution from the new data appropriately weighted. Two solutions are given in Table 3, and the measurements phased with the ephemeris T_{conj} = 2449582.9268 + 6.724333 E are shown in Fig. 1.

4. Atmospheric parameters of the primary

4.1. Inputs for spectra calculations

A list of atomic line parameters for a given wavelength region was obtained from VALD for lines having a central depth of 1% or more.

A number of molecular lines were added to the list, since the presence of many molecular lines in spectra of stars with effective temperature T_{eff}<5000 K is quite noticeable. Although weaker than most atomic lines, they are so numerous that they can effectively reduce the continuum level in spectra of rapidly rotating stars. In those regions that we used for our study the most significant contribution to the photospheric spectrum from molecular lines is due to rotational transitions of a number of vibrational bands of the CN ($A^2\Pi - X^2\Sigma$) red system. The main sources of the CN line parameters are the following: wavelengths are from laboratory measurements by Davis & Phillips

Table 2. Radial velocities (RV, km s^{-1}) data. References (ref): 1 - Sanford (1921); 2 - Halliday (1952); 3 - Heard (1956); 4 - Rucinski (1977); 5 - Vogt (1981); 6 - SOFIN; 7 - Crimea; 8 - McDonald; 9 - KPNO.

HJD 2400000+	RV	ref	HJD 2400000+	RV	ref	HJD 2400000+	RV	ref	HJD 2400000+	RV	ref	HJD 2400000+	RV	ref
21441.480	–11.1	1	43031.914	16.6	4	50295.592	–18.0	6	50289.463	–40.9	7	50403.191	–14.0	7
21556.196	–25.5	1	43037.888	9.9	4	50295.640	–20.3	6	50290.419	–59.5	7	50403.209	–13.9	7
21592.126	–46.5	1	43362.823	–13.1	5	50297.658	–56.2	6	50290.451	–58.8	7	50409.158	8.3	7
21823.489	28.5	1	43452.864	–47.4	5	50297.697	–56.0	6	50291.449	–51.0	7	50409.194	9.3	7
21833.454	–55.0	1	49578.684	–49.0	6	50298.657	–34.3	6	50291.488	–47.7	7	43744.942	14.4	8
21860.387	–53.0	1	49579.654	–17.5	6	50298.696	–33.0	6	50292.423	–22.1	7	44474.870	–53.9	8
22216.449	–60.5	1	49580.608	12.5	6	50299.686	0.6	6	50292.455	–19.5	7	44475.870	–21.6	8
22533.360	–49.7	1	49581.543	17.6	6	50299.714	1.1	6	50292.487	–17.4	7	44478.983	–11.9	8
22541.442	–4.2	1	49582.541	–6.4	6	50381.354	17.5	6	50297.427	–59.5	7	44480.855	–59.9	8
22565.392	–36.7	1	49583.627	–44.1	6	50381.386	17.6	6	50297.466	–59.2	7	48060.983	11.6	9
22566.480	–48.6	1	49584.655	–59.1	6	50381.421	17.4	6	50299.428	–9.1	7	48427.968	–60.0	9
22567.513	–33.5	1	49585.661	–42.3	6	50382.390	03.2	6	50299.462	–7.3	7	49620.799	7.9	9
22568.470	5.9	1	49586.659	–7.3	6	50382.414	02.4	6	50300.422	14.5	7	49901.986	–33.9	9
22569.398	15.4	1	49587.679	17.9	6	50382.438	01.5	6	50300.464	14.7	7	49902.991	0.7	9
22593.191	–58.1	1	49910.656	18.1	6	50383.361	–30.5	6	50301.417	9.6	7	49903.879	16.7	9
22594.353	–27.9	1	49910.677	18.0	6	50383.389	–31.5	6	50301.458	9.4	7	49968.868	–45.5	9
22595.380	8.6	1	49911.645	5.5	6	50383.409	–32.3	6	50312.468	–24.0	7	49969.881	–10.3	9
22596.327	20.6	1	49912.645	–28.4	6	50384.366	–55.6	6	50312.496	–22.7	7	49970.790	13.2	9
22624.297	4.2	1	49913.631	–55.6	6	50384.407	–56.1	6	50348.301	10.9	7	49971.801	12.0	9
22625.348	–39.4	1	49914.636	–55.0	6	50385.414	–52.3	6	50348.332	11.7	7	49972.814	–17.3	9
22626.203	–55.0	1	49914.675	–54.3	6	50385.443	–51.6	6	50348.351	11.6	7	49973.721	–48.0	9
22629.318	9.7	1	49915.655	–24.7	6	50385.472	–51.0	6	50353.299	–5.9	7	50263.973	–57.9	9
22630.235	18.2	1	49916.664	8.1	6	50386.402	–22.2	6	50353.347	–3.9	7	50265.994	–3.2	9
22650.187	18.8	1	49917.614	18.0	6	50386.430	–21.1	6	50357.368	–55.9	7	50362.762	–17.0	9
22652.308	–35.8	1	49918.626	–1.9	6	50387.468	9.7	6	50357.389	–56.2	7	50401.635	16.9	9
32100.731	–46.7	2	49920.668	–59.5	6	50387.499	10.2	6	50359.314	–30.0	7	50404.609	–56.9	9
32873.567	–34.2	2	49921.627	–49.3	6	50387.536	11.2	6	50359.341	–29.1	7	50630.951	7.3	9
33149.836	–36.4	2	49921.645	–48.7	6	50387.569	11.5	6	50360.309	1.0	7	50631.961	–23.9	9
33199.733	–5.4	2	50293.634	15.6	6	50388.348	17.2	6	50360.352	3.0	7	50637.908	1.1	9
33507.881	–36.8	2	50293.676	16.2	6	50388.376	17.0	6	50402.171	11.5	7			
33542.779	3.3	2	50294.647	12.2	6	50388.401	16.9	6	50402.210	11.7	7			
34266.707	–54.2	3	50294.690	11.3	6	50289.431	–40.2	7	50403.164	–14.8	7			

Table 3. The results of two orbit solutions. The best one is from the new data only. The reference code for different γ-velocities listed in Solution 1 is the same as for Table 2.

Element	Solution1, all RVs		Solution2, New RVs	
P, days	6.724333	±0.000010	6.724333	
e,	0.0065	±0.0055	0.0	
K_1, km s^{-1}	38.36	±0.22	38.66	±0.13
$a_1 \sin i$, $R_\odot$	5.1		5.2	
f_1(m), $M_\odot$	0.03939		0.04028	
$T_{\rm maxRV}$, HJD	2449581.2500	±0.0048	2449581.2457	±0.0039
$T_{\rm conj}$, HJD	2449582.9220	±0.0048	2449582.9268	±0.0039
γ, km s^{-1}	–17.8	±1.0 (1)	–20.5	±0.1
	–16.2	±2.7 (2,3)		
	–22.1	±0.6 (4)		
	–18.5	±1.3 (5)		
	–20.5	±0.1 (6)		
	–21.5	±0.3 (7)		
	–21.9	±1.0 (8)		
	–21.8	±0.2 (9)		

(1963); band oscillator strengths and molecular constants are from the RADEN database (Kuznetzova et al. 1993); lower level excitation energies and rotational intensity factors are calculated with formulas from the book by Kovacs (1969).

Stellar model atmospheres used are from Kurucz (1993). When necessary, a model with specific parameters was obtained from the grid by simple parabolic interpolation using three appropriate points in both effective temperature and surface gravity for a given metallicity. A code used for the synthetic spectrum calculations is described in detail by Berdyugina (1991). It includes calculations of opacities, intensities and fluxes in the continuum and atomic and molecular lines. Also, number densities of atoms and molecules are calculated under the assumption of dissociative equilibrium.

4.2. The standard star fit

As mentioned previously, β Gem (K0 IIIb) was chosen as a standard star for both radial velocity measurements and synthetic spectrum calculations. Although it is somewhat more luminous than the primary of II Peg, we obviously can use its spectrum to check most of our inputs for the synthetic spectrum calculations. Using the parameters of the star determined by Drake & Smith (1991) from a very detailed analysis, we have interpolated a model with $T_{\rm eff}$=4865 K and $\log g$=2.75 from the model grid. Other known parameters are the iron abundance [Fe/H]=–0.04 (assuming the solar value Fe/H=7.50 in scale of H=12), the calcium abundance Ca/H=6.25, microturbulence $\xi_{\rm t}$=1.4 km s^{-1}, and broadening due to the combined effects of rotation and macroturbulence, represented by a Gaussian function with width of 3.5 km s^{-1}. Note that the iron abundance was determined using 'solar' oscillator strengths. Additionally, the carbon, nitrogen and oxygen abundances were adopted at first as C/H=8.30, N/H=8.14, O/H=8.78 in accordance with Kjaergaard et al. (1982).

First calculations of the β Gem spectrum revealed a number of 'missing' and 'wrong' atomic lines in the input line list. For the CN lines, increasing the nitrogen abundance N/H by 0.1 dex resulted in a very good fit. Since accurate and reliable oscillator strengths are not available for the complete set of atomic lines used in the calculations, we tried to model the standard star's spectrum to derive 'stellar oscillator strengths' and used them in the subsequent analysis of the II Peg spectrum. Such a differential analysis also was used to avoid (or reduce) non-LTE effects in lines of the neutral atoms. Obviously, the set of the 'stellar oscillator strengths' cannot be considered a unique one because it contains uncertainties due to both the stellar parameters of the standard star and the stellar model used. Moreover, the latter is impossible to avoid in any case but can be reduced in the differential analysis. Unfortunately, some missing lines in the line list have not been identified even in the solar spectrum, where they are observed as well but are very weak. We stress that the final input line list is very important for our subsequent study, when we apply the surface imaging technique to the spectrum of II Peg.

Table 4. Measured projected rotational velocity

Season	Profile Fe I	$v \sin i$
	λ,Å	km s^{-1}
1994	6173.341	22.4
1994	6180.203	22.6
1995	6173.341	22.7
1995	6180.203	22.8
	Mean =	22.6

4.3. The rotational velocity and macroturbulence.

To determine the projected rotational velocity, $v \sin i$, of the primary, we used the profiles of the Fe I 6173.341 Å and 6180.203 Å photospheric absorption lines extracted from the average SOFIN spectra for two seasons: 1994 and 1995. Though the first line is magnetically sensitive, the expected strength of the magnetic field will not disturb its profile so that it may affect our results. The profiles and their Fourier transforms are shown in Fig. 2. The measured projected velocities, corresponding to a linear limb darkening coefficient of ε=0.7 (Al-Naimiy 1978), are given in Table 4. The first zero of the Fourier transform of the rotational profile was chosen for the projected rotational velocity measurements, since it is less affected by noise and small-scale intrinsic variability. To determine the macroturbulence, $\zeta_{\rm t}$, the synthesized profile has previously been convolved with the instrumental profile. Being less affected by noise, the first and second lobes of the Fourier transform of the observed mean profiles have been better fitted with the same value of an isotropic Gaussian macroturbulence of 4 km s^{-1}. The small residuals of the measured radial velocities along with the linear form of the bisector show that all deformations in individual profiles have been well averaged in the mean profiles. However, note that the positions of the second and third zeros of the rotational profile indicate that the observed linear limb darkening coefficient is less than its theoretical value. This would imply a lower projected rotational velocity together with a higher macroturbulence (of about 1-2 km s^{-1}). The projected rotational velocity of 23.1 $\pm$1.0 found by Fekel (1997) from 4 of the KPNO spectra is in excellent agreement with our SOFIN value of 22.6 km s^{-1}.

4.4. The parameters of the atmosphere

About 20 lines of different elements were chosen from those regions where the spot contribution to the spectrum appears to be insignificant. Since the equivalent widths of most lines do not display noticeable variation with phase, the average SOFIN spectrum of II Peg has been used in the analysis. At first, spectra of II Peg were averaged separately for the three seasons: 1994, 1995, and 1996. But no significant differences were found among them, and so the total averaged SOFIN spectrum of II Peg was used.

To obtain a self-consistent set of parameters we used the following procedure.

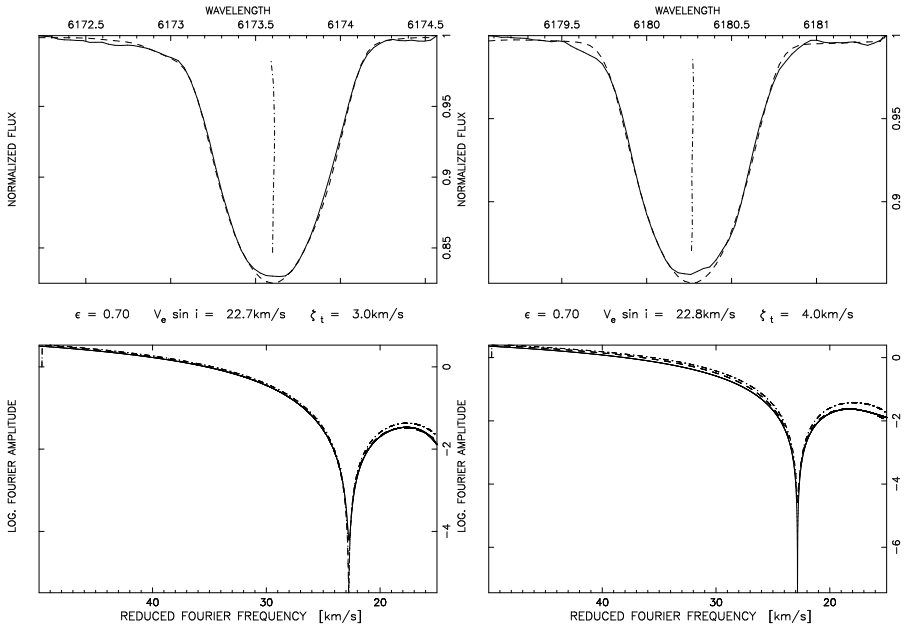

Fig. 2. Observed profiles (upper panels) of Fe I lines at 6173.341 Å (left) and 6180.203 Å (right) and their Fourier transforms (bottom panels). The dash-dotted line presents the Fourier transform of the rotationally broadened synthetic spectrum without macroturbulence, while the dashed line presents the profile with macroturbulence of 3 and 4 km s^{-1}.

1. Assuming first an appropriate pair of $T_{\rm eff}$ and $\log g$, we analyzed neutral metal lines to produce a set of curves (loci of constant equivalent width) on a diagram of metal abundance, [M/H], as a function of microturbulence, $\xi_{\rm t}$. The curves intersect in a narrow region which provides the initial estimate for [M/H] and $\xi_{\rm t}$ (Fig. 3a). Note that 'loci of constant equivalent width' in the sense of the synthetic spectrum calculations means the best fit to the observed spectrum.

2. Using the initial estimates of [M/H] and $\xi_{\rm t}$, we analyzed both neutral and ionized metal lines to produce a set of curves on a diagram of $T_{\rm eff}$ versus $\log g$. Since lines of ionized metals are sensitive to both parameters, and lines of neutral metals are sensitive mostly to temperature, the intersection region gives an initial estimate of a pair of $T_{\rm eff}$ and $\log g$ values (Fig. 3b).

3. The previous two stages were iterated until a self-consistent set of parameters was obtained. The results are given in Table 5.

Table 5. Atmospheric parameters of the primary of II Peg

Parameter	Value
$T_{\rm eff}$, K	4600±100
$\log g$	3.2±0.2
[M/H]	–0.4±0.1
$\xi_{\rm t}$, km s^{-1}	2.0±0.5
$\zeta_{\rm t}$, km s^{-1}	3.5±0.5
$v \sin i$, km s^{-1}	22.6±0.5

4.5. The lithium abundance

The lithium equivalent width has been measured by several authors. Chugainov (1976b) estimated a lithium abundance of Li/H=1.5 from a blend of 0.110 Å and claimed that the age of the star should be less than 1 Gyr. Rucinscki (1977) measured the equivalent width of the blend to be 0.055±0.010 Å and suggested that the star might be in a late stage of pre-main sequence evolution. Vogt (1981) has reported the observed feature at 6707.8 Å with an equivalent width of 51±1 mÅ to be clearly a blend of three lines: Fe I 6707.4 Å, Li I 6707.8 Å, and V I 6708.1 Å. Thus, the pure lithium equivalent width must be somewhat less than 51 mÅ.

Our results show the equivalent width of the blend ranging from 53 mÅ to 65 mÅ in 1994-1996 (with the accuracy of ±2

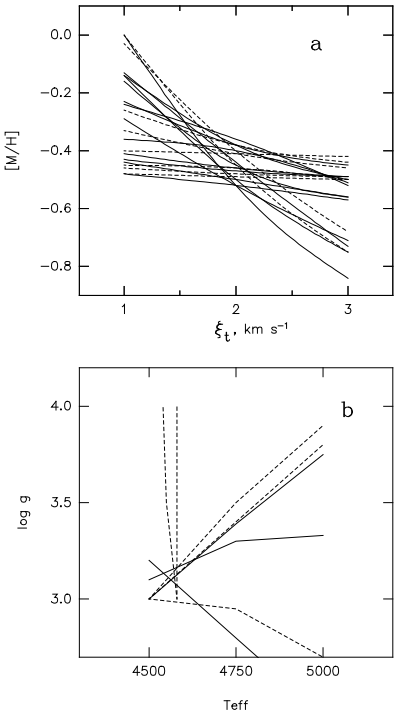

Fig. 3a and b. Diagrams for the self-consistent determination of the atmospheric parameters of the primary of II Peg: **a** metallicity [M/H] and microturbulence ξ_t, **b** effective temperature $T_{\rm eff}$ and surface gravity log *g*. Solid curves are due to iron lines, and dashed ones are due to other metals.

mÅ), which with our new atmospheric parameters corresponds to a Li/H abundance range of 1.0 to 1.1 (Fig. 4). Using quasi-simultaneous photometric observations (Jetsu 1996, Berdyugin 1997) and simultaneous measurements of the central depth of the TiO bands at 7054 Å and 7125 Å we investigated whether the lithium equivalent width correlates with the spot coverage of the stellar disk. Giampapa (1984) predicted that chromospherically active stars would have significant variations in the strength of the lithium line as the size of the spot area on the visible hemisphere changes during a rotation cycle. Several groups, including Patterer et al. (1993) and Martin & Claret (1995), have examined lithium in pre-main sequence stars and claimed to have detected lithium equivalent width variations. Jeffries et al.'s (1994) observations of the young K dwarf BD+22 4409 have provided the most convincing evidence linking lithium equivalent width changes to changes in spot area. Fekel (1996) reviewed the relationship between spots and lithium equivalent width variations. He concluded that significant variations are not likely to be detected except in the most active stars that have significant contrast between the spotted and unspotted hemispheres. II Peg is indeed one of the most active known RS CVn binaries. But even in its case the variations are less than 25%, and a correlation with the brightness of the star is not quite evident (Fig. 4), although it probably exists. In fact, such a correlation seems to be disturbed by other effects. To estimate the unspotted V magnitude of the star, the variations of the central depth of the TiO bands at 7054 Å and 7125 Å are plotted versus photometric measurements in Fig. 4. The presence of TiO bands in the spectrum of II Peg is not compatible with its spectral class, and the bands are usually interpreted as originating in the regions of cool spots. From the linear regressions fitted to the data we estimate that at the historical brightness maximum of V=$7\overset{\rm m}{.}2$ the central depths of the TiO bands would be ≈1–2%. Extrapolating the TiO regressions to the zero value of the central depths provides an estimate of the V magnitude of $6\overset{\rm m}{.}9$ for the star with no spots. Similarly, Neff et al. (1995) concluded that at the historical brightness maximum at least 35% of the surface was covered with spots, and the V magnitude corresponding to the unspotted star should be equal to $6\overset{\rm m}{.}8$. For the lithium blend the extrapolation to the $6\overset{\rm m}{.}9$ magnitude gives an equivalent width of about 55±5 mÅ. Thus, taking into account all uncertainties, we conclude that the true value of the lithium abundance Li/H is about 1.0±0.1, and the spot contribution can be responsible only for 10-20% of the equivalent width of the blend.

The lithium abundance in conjunction with other stellar parameters is known to be a stellar age indicator. K0–K2 zero-age main sequence dwarf field stars have Li/H = 2.8–3.0 (Ambruster et al. 1994), nearly equal to that found in late-type pre-main sequence stars (Basri et al. 1991). Lithium abundances determined for such young field stars and T Tauri stars indicate that the equivalent widths and the corresponding abundances found for II Peg are inconsistent with a pre-main sequence evolutionary state. Fekel & Balachandran (1993) and Randich et al. (1994) have shown that moderate lithium abundances of 1.0–2.0 are found in a number of post-main sequence chromospherically active stars. Thus, the lithium abundance of II Peg appears to be quite consistent with such results. Its post-main sequence evolutionary state, discussed in section 5, is also confirmed by the observed C/N ratio (section 4.6).

4.6. The C/N ratio

A good criterion for the evolutionary state of a star is the C/N ratio (abundance ratio in the linear scale). For young or main sequence stars the C/N ratio should be close to the solar value of 4.8, while more evolved stars after the first dredge-up should display a much lower ratio, which depends slightly on the initial mass. For example, two K1 subgiants studied by Lambert&Ries (1981) show C/N ratios of 2.95 and 2.34. To determine this ratio for the primary of II Peg, the head of the (2,0) band of the CN red system was modelled with different amounts of carbon, while abundances of oxygen and nitrogen were set to the typical values

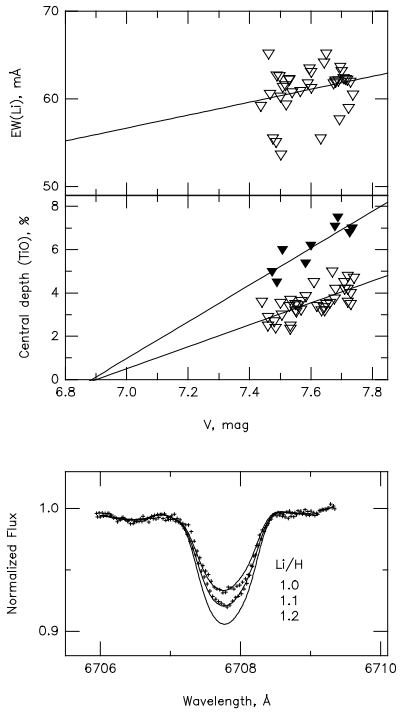

Fig. 4. The variation of the equivalent width of the 6707 Å blend and the central depth of the TiO band at 7125 Å in 1994-1996 (light triangles) and the TiO band at 7054 Å in 1996 (filled triangles) with V magnitude (top). At the bottom the lithium blend at the minimum (55 mÅ) and maximum (65 mÅ) equivalent width observed in 1994-1996 (symbols) and synthetic spectra calculated with three values of Li/H (lines).

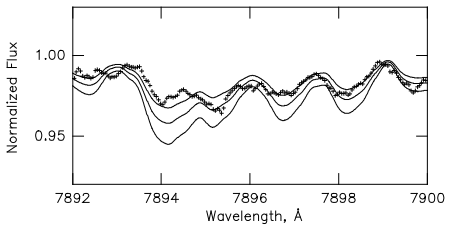

Fig. 5. The spectrum modelled in the region of the head of the (2,0) band of the CN red system. The observed spectrum is shown with symbols, while the lines are the calculated spectra with different values of the C/N ratio: 2.75, (the deepest one), 2.2, and 1.74 (the most shallow one).

for low metallicity subgiants: [O/H]=0.5·[Fe/H] (Clegg et al. 1981) and [N/H]=+0.24 (Lambert&Ries 1981). The reduced C/N ratio of ≤ 2 (Fig. 5) confirms the presence of processed CN-cycle matter in the atmosphere of the primary and, thus, its post-main sequence state.

5. Fundamental parameters of the components

The determined projected rotational velocity and the photometric period of the star (Strassmeier et al. 1993) result in the relation $R_1 \geq 3.0 R_\odot$. This corresponds to the radius of a subgiant star. The evolved character of the star is confirmed by the reduced C/N ratio estimated in Section 4. In addition, the galactic velocity-components indicate that II Peg is an old disk object (Eggen, 1978). With the new parallax value of 0.″02362 from the Hipparcos Catalogue (Perryman et al. 1997) and an unspotted visual magnitude of the star of $6^m.9$, an absolute magnitude $M_V=3^m.8$ is determined. This value is significantly above that for main sequence stars of the same effective temperature ($M_V=7^m.0$), less than that of giants ($M_V=0^m.6$), and very close to the value of $3^m.1$ for cool subgiants (Lang 1992). Thus, there is no doubt that the primary of II Peg has evolved from the main sequence to the base of the red-giant branch. Then, the mass of the primary should be in the range of 0.7–1.1 $M_\odot$, where the lower limit corresponds to a main sequence star with $T_{\rm eff}$=4600K, while the upper limit is for a giant with the same temperature (Lang 1992). The corresponding ranges for the stellar radius and the inclination of the rotational axis are 3.5–4.4 $R_\odot$ and 60°–40°, respectively.

Since with present observing techniques the secondary is invisible at all wavelengths, its luminosity should be at least 100 times less than that of the primary, i.e. $M_V \leq 8^m.8$. This corresponds to a M0 main sequence star with a mass of 0.5 $M_\odot$. From the mass-mass diagram calculated with the mass function for various combinations of mass and orbital inclination (Fig. 6), narrower ranges for the radius and the inclination of the rotational axis of the primary can be found under the assumption that its rotational axis is perpendicular to the orbital plane. From a sample of synchronously rotating RS CVn binaries with similar periods, Glebocki & Stawikowski (1995) found that such an assumption is justified. The upper limit for the radius, then, drops to 3.8 $R_\odot$, while the lower limit for the stellar inclination grows to 53°. One can see that the upper limit for the mass of the secondary and the assumption of the perpendicularity of the rotational axis to the orbital plane significantly reduce the probable domain of the parameters of the binary, though they are still consistent. Then, for $\log g$= 3.2–3.4 the parameters are the following: $M_1/M_\odot$=0.8±0.1, $M_2/M_\odot$=0.4±0.1, $R_1/R_\odot$=3.4±0.2, i=60°±10°. Scaltriti et al. (1990) attempted to estimate the orbital inclination from the linear polarization measurements. Unfortunately, the amplitude of the variability was comparable with the errors of the measurements, which resulted in a biased estimate of the inclination of 75°. The absence of the variability would be interpreted as an orbital inclination of 90° in that model. Additionally, the confidence level of that

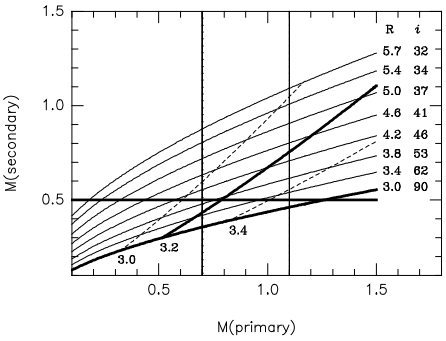

Fig. 6. The mass-mass diagram for II Peg (in solar units). The thin solid curves are calculated for the fixed values of the radius of the primary and the inclination (numbers in the left). The dashed lines are loci of the primary with a fixed value of log g (numbers at the bottom). The heavy solid lines show the boundaries with log g=3.2, R_1=3.0 $R_\odot$, and M_2=0.5 $M_\odot$, while the vertical lines are the boundaries for the mass of the primary (see text).

estimate is from 0° to 80° in accordance with Wolinski & Dolan (1994). Therefore, the estimate of 75° can be considered only as the highest possible inclination of the orbit.

6. Conclusions

From new high-resolution and high S/N spectra of II Peg, the following results have been obtained:

1. New orbital parameters have been determined, the ephemeris being improved: $T_{conj} = 2449582.9268 + 6.724333E$.

2. A detailed model atmosphere analysis of the spectrum of II Peg has yielded for the first time a self-consistent set of fundamental parameters of the primary component: T_{eff}=4600 K, log g=3.2, [M/H]=–0.4, ξ_t=2.0 km s^{-1}.

3. The blend of Li I 6707 Å is suspected to vary in equivalent width due to spot modulation. The lithium abundance for the unspotted star was determined: Li/H=1.0±0.1. It is found to be consistent with the lithium abundances in other post-main sequence chromospherically active stars.

4. An unspotted V magnitude of $6\overset{m}{.}9$ was estimated from the observed variations of the TiO bands and quasi-simultaneous photometry.

5. With our new parameters the position of the primary of II Peg in the HR diagram corresponds to a K2 IV star with mass 0.8±0.1 $M_\odot$. The evolved character of the star is confirmed also by the C/N ratio, which is reduced significantly relative to the solar value.

6. By combining all parameters, the radius R_1 = 3.4±0.2 $R_\odot$ and the inclination i=60°±10° of the primary have been estimated with the assumption that its rotational axis is perpendicular to the orbital plane.

7. The unseen secondary is believed to be a M0-M3 main sequence star with a mass of about 0.4±0.1 $M_\odot$.

Acknowledgements. The research described in this publication was made possible in part by grants R2Q000 and U1C000 from the International Science Foundation and by grant A-05-067 from the ESO C&EE Programme. The work by S.B. was supported by a grant from the Centre for International Mobility (CIMO), Finland. F.C.F has been supported in part by NASA grants NAG8-1014 and NCC5-228 plus NSF grant HRD-9550561. We are grateful to Dr. Sumner Davis for the computer-readable catalogue of laboratory wavelengths of TiO and CN lines and to Dr. Ludmila Kuznetsova who provided the band oscillator strengths and molecular constants from the RADEN database. Dr. Rudolf Duemmler is acknowledged for discussions.

References

Al-Naimiy H.M, 1978, Ap&SS 53, 181
Ambruster C.W., Brown A., Fekel F.C., 1994, The 8 Cambridge Workshop on Cool Stars Stellar Systems, and the Sun, ASP Conf. Ser., Vol. 64, p. 348
Basri G., Martin E.L., Bertout C., 1991, A&A 252, 625
Berdyugin A.V., 1997, private communication
Berdyugina S.V., 1991, Izv. Krymsk. Astrofiz. Obs. 83, 102
Berdyugina S.V., Ilyin I., Tuominen I., 1998a, in preparation
Berdyugina S.V., Ilyin I., Tuominen I., 1998b, in preparation
Byrne P.B., Panagi P.M., Lanzafame A.C., et al., 1995, A&A 299, 115
Chugainov P.F., 1976a, Izv. Krym. Astrofiz. Obs. 54, 89
Chugainov P.F., 1976b, Izv. Krym. Astrofiz. Obs. 55, 85
Clegg R.E.S., Lambert D.L., Tomkin J., 1981, ApJ 250, 262
Davis S.P., Phillips J.G., 1963, The Red System $(A^2\Pi - X^2\Sigma)$ of the CN molecule, University of California Press., Berkely
Dempsey R.C., Linsky J.L., Fleming T.A., Schmitt J.H.M.M., 1993, ApJS 86,599
Drake J.J., Smith G., 1991, MNRAS 250, 89
Drake S., Simon T., Linsky J.L., 1989, ApJS 71, 905
Eggen O.J., 1978, Inf. Bull. Variable Stars, 1426
Fekel F.C., 1996, In: Strassmeier K.G., Linsky J.L. (eds.) Proc. IAU Symp. 176, Stellar Surface Structure. Kluwer Acad. Publ., Dordrecht, p. 345
Fekel F.C., 1997, PASP 109, 514
Fekel F.C., Balachandran S., 1993, ApJ 403, 708
Fitzpatrick M.J. 1993, in: Hanish R., Brissenden R., Barnes J. (eds.) Astronomical Data Analysis Software and Systems II, ASP, San Francisco, p. 472
Giampapa, 1984, ApJ 277, 235
Glebocki R., Stawikowski A., 1995 Acta Astronomica 45, 725
Hadrava P., 1995, FOTEL3 - user's guide, Astronomical Institute, Academy of Science, Ondrejov
Halliday I., 1952, J.R.A.S. Canada 46, 103
Heard J.F., 1956, Publ. David Dunlap Obs. 2, 107
Henry G.W., Eaton J.A., Hamer J., Hall D.S., 1995, ApJ 97,513
Huenemoerder D.P., Ramsey L.W., 1987, ApJ 319, 392
Ilyin I.V., 1997, Licentiate Dissertation, University of Oulu
Jeffries R.D., Byrne P.B., Doyle J.G., et al., 1994, MNRAS 270, 153
Jetsu L., 1996, private communication
Kjaergaard P., Gustafsson B., Walker G.A.H., Hultqist L., 1982, A&A 115, 145
Kovacs I., 1969, The rotational Structure in the Spectra of Diatomic Molecules, Academiai Kiado, Budapest
Kurucz R.L., 1993, Kurucz CD No. 13

Kuznetzova L.A., Pazyuk E.A., Stolyarov A.V., 1993, Russ. J. Phys. Chem. 67, 2046
Lambert D.L., Ries L.M., 1981, ApJ 248, 228
Lang K.R., 1992, Astrophysical Data, Springer-Verlag
Martin E.L., Claret A., 1996, A&A 306, 408
Nations H.L., Ramsey L.W., 1981, AJ 85,1086
Neff J.E., O'Neal D., Saar S.H., 1995, ApJ 452, 879
O'Neal D., Neff J.E., 1997, AJ 113, 1129
Perryman M.A.C., Lindegren L., Kovalevsky J. et al., 1997, A&A 323, L49
Patterer R.J., Ramsey L., Huenemoerder D.P., Welty A.D., 1993, AJ 105, 1519
Piskunov N.E., Kupka F., Ryabchikova T.A., Weiss W.W., Jeffrey C.S., 1995, A&AS 112, 525
Randich S., Giampapa M.S., Pallavicini R.,1994,A&A 283,893
Rucinski S.M., 1977, PASP 89, 280
Sanford R.F., 1921, ApJ 53, 201
Scaltriti F., Piirola V., Coyne G.V., et al., 1993, A&AS 102, 343
Scarfe C.D., Batten A.H., Fletcher J.M. 1990, Publ. Dominion Astrophys. Obs. 18, 21
Schaerer D., Meynet G., Maeder A., Schaller G., 1993, A&AS, 98, 523
Stockton R.A., Fekel F.C., 1992, MNRAS 256, 575
Strassmeier K.G., Hall D.S., Fekel F.C., Scheck M., 1993, A&AS 100, 173
Tuominen I., 1992, Nordic Optical Telescope News 5, 15
Vogt S.S., 1981, ApJ 247, 975
Wolinski K.G., Dolan J.F., 1994, MNRAS 267, 5

Paper VII

Berdyugina, S.V., Berdyugin, A.V., Ilyin, I., Tuominen, I. 1998, "The active RS Canum Venaticorum binary II Pegasi. II. Surface images for 1992-1996", A&A 340, 437

Astron. Astrophys. 340, 437–446 (1998)

ASTRONOMY AND ASTROPHYSICS

The active RS Canum Venaticorum binary II Pegasi

II. Surface images for 1992–1996⋆

S.V. Berdyugina[1,2], **A.V. Berdyugin**[1,2,3], **I. Ilyin**[1], **and I. Tuominen**[1]

[1] Astronomy Division, University of Oulu, P.O. Box 333, FIN-90571 Oulu, Finland (e-mail: sveta@ukko.oulu.fi)
[2] Crimean Astrophysical Observatory, P.O. Nauchny, Crimea, 334413 Ukraine
[3] Tuorla Observatory, University of Turku, Väisäläntie 20, FIN-21500 Piikkiö, Finland

Received 7 July 1998 / Accepted 21 August 1998

Abstract. Using new high-resolution and high signal-to-noise ratio spectroscopic observations carried out in 1992–1996, nine surface images of II Peg are obtained. The inversion technique applied is the recently developed Occamian approach, which does not put any artificial constraints on the solution and provides an error analysis of the solution. The surface imaging is applied to Ca I, Fe I, and Ni I lines simultaneously, a number of blending atomic and molecular lines being included into the line list.

Two high-latitude active regions are found to dominate in all seasons, which determine the spectroscopic and photometric variability. No cool polar cap is seen. The positions of the spots are constantly migrating to earlier orbital phases with approximately the same rate. This motion of the spot configuration means a shorter rotational period, which is just about the mean photometric period. The mean longitude separation between the active regions is about 180°. This is considered as two active longitudes. The largest of the two spots seems to be close to the central meridian, i.e. tends to be faced toward the secondary. In 1994 it changed its position from one active longitude to another, showing the effect of switching the activity between the longitudes.

Key words: stars: activity – stars: imaging – stars: individual: II Peg – stars: late-type – stars: starspots

1. Introduction

II Peg (HD 224085) is known as one of the most active RS CVn stars. Broad-band photometry shows V-band variations up to $0\overset{m}{.}5$ with a mean period of 6.71 days suggesting that the photometric variability is due to rotational modulation. These variations are accompanied with colour variations, the faintest phases being the reddest, which can be interpreted in terms of cool surface spots analogous to sunspots but much enchanced in scale. The long-term studies (Henry et al. 1995, and references therein) based on available photometric data starting from 1974 show radical changes of the photometric wave, from almost sinusoidal, to irregular or flat. The changes in the light curve are consistent with re-arrangement of the spot distribution over the stellar surface. A crude interpretation by the two-spot model reveals the surface fraction of the active component covered by spots to be as large as 40% and indicates that the spotted regions migrate at different rates towards decreasing orbital phase.

Vogt (1981) and Huenemoerder & Ramsey (1987) made a quantitative study of the effect of spots in the TiO bands. They found that a substantial fraction of the photosphere must be spotted (with a spot coverage of 35–40%), while Neff et al. (1995) found that cool starspots (T≈3500 K) are always visible, with a fractional projected coverage of the visible hemisphere varying from 54% to 64% as the star rotates. Recently, O'Neal & Neff (1997) have detected excess of OH absorption due to cool spots on the surface of II Peg and found for one epoch a spot filling factor between 35% and 48%. First surface images of II Peg for the 1992–1994 seasons reported by Hatzes (1995) have shown polar or high-latitude spots and several equatorial and sub-equatorial spots with total coverage of about 15% of the visible surface.

The present study is based on new high-resolution and high signal-to-noise ratio spectroscopic observations carried out in 1992–1996 with different instruments. These observations have been partly used already for improving the orbital parameters and determining new atmospheric parameters of the primary and the evolutionary status of both components of the binary (Berdyugina et al. 1998b, Paper 1). A set of important parameters for surface imaging, e.g. projected rotational velocity, inclination, effective temperature, surface gravity, microturbulence and orbital parameters, are used in the present study from Paper 1.

A new inverse technique is used for surface imaging. It is the recently developed Occamian approach, which has been applied to the surface imaging problem and tested with simulated data

Send offprint requests to: S.V. Berdyugina

⋆ based on observations collected at the Nordic Optical Telescope (NOT), La Palma, Spain; the McMath telescope of the National Solar Observatory, USA; the 2.6 m and 1.25 m telescopes of the Crimean Astrophysical Observatory, Ukraine; the 2m telescope of the National Astronomical Observatory, Rozhen, Bulgaria; the 2m telescope of the Pic du Midi Observatory, France

Table 1. Spectroscopic observations

	Instrument	Season	Sp. region
1	Coudé spectrograph, 2m telescope, Rozhen	1992, Aug.	6160–6200 Å $\lambda/\Delta\lambda\approx30000$ 10 spectra
2	MUSICOS spectrogr., 2m telescope, Pic du Midi	1992, Aug.	6110–6190 Å $\lambda/\Delta\lambda\approx40000$ 8 spectra
3	Stellar spectrograph, McMath telescope, NSO	1993, Dec. 1994, Nov. 1995, Jan. 1995, Oct.	6150–6200 Å $\lambda/\Delta\lambda\approx90000$ 46 spectra
4	Échelle spectrograph SOFIN, 2.6m NOT, La Palma	1994, July 1995, July 1996, July 1996, Oct.	5500–8500 Å $\lambda/\Delta\lambda\approx83000$ 58 spectra
5	Coudé spectrograph, 2.6m telescope, Crimea	1996, Aug.	6140–6200 Å $\lambda/\Delta\lambda\approx41000$ 37 spectra

by Berdyugina (1998). Main advantages of the new approach are that (1) it does not use any a priori artificial constraints, but the resulting solution is nevertheless stable with respect to measurement errors and uncertainties in the adopted stellar parameters, and (2) it allows to estimate the variances of the solution, which were not available with other techniques used in surface imaging before.

2. Observations

II Peg was observed with different instruments in 1992–1996. The most important information on the whole data set is given in Table 1. The spectra obtained with the SOFIN spectrograph on the Nordic Optical Telescope (NOT) and the coudé spectrograph on the 2.6m telescope of the Crimean Astrophysical Observatory have been used already for determining the stellar and orbital parameters of II Peg in Paper I. The quality and reduction of those spectra have been described in Paper I, too. The spectra obtained with other instruments were reduced in the same way. The reduction included bias and flat field corrections, wavelength calibration, and corrections for the motion of the Earth. Finally, the wavelengths were corrected for the orbital motion of the primary. When available two consecutive exposures were added to increase the S/N ratio. All available observations have been divided into nine season sets and phased according to the orbital ephemeris from Paper I, which is used throughout this paper:

$$\mathrm{T_{conj}} = \mathrm{HJD}2449582.9268 + 6.724333E \quad (1)$$

with the primary in the back at phase 0. Heliocentric Julian dates, orbital phases, and S/N ratios of the spectra used for surface imaging are presented in Table 2.

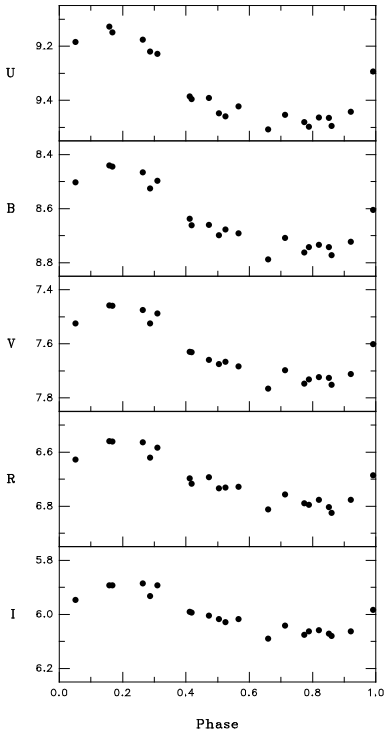

Fig. 1. UBVRI observations of II Peg in August-November 1996 vs. orbital phase.

Supporting photometric observations have been arranged in August–November 1996 with the photometer-polarimeter constructed by V. Piirola and installed on the 1.25m telescope of the Crimean Astrophysical observatory. The observations were obtained in the standard Johnson UBVRI bands with HD 223925 as the comparison star (U=$8^{\rm m}.185$, B=$8^{\rm m}.195$, V=$8^{\rm m}.152$, R=$8^{\rm m}.072$, I=$8^{\rm m}.103$). The observations are given in Table 3 and Fig. 1.

3. Calculations

3.1. Local line profiles

For surface imaging the 6160–6200 Å region has been chosen, because it is the only common region for all nine sets of the observations. It contains the Ca I, Fe I, and Ni I lines, which are often used for surface imaging of late-type stars. These lines are temperature sensitive and strong enough in the specrum of II Peg. Note that Fe I 6173 Å is a magnetically sensitive line

Table 2. Nine sets of spectroscopic observations used for the surface imaging. The column Ins. denotes the instrument from Table 1.

HJD 2400000+	Phase	S/N	Ins.	HJD 2400000+	Phase	S/N	Ins.	HJD 2400000+	Phase	S/N	Ins.
1. *August 1992*				4. *November 1994*				7. *October 1995*			
48846.5888	0.4965	135	1	49631.7810	0.2653	190	3				
48847.5842	0.6445	150	1	49632.8125	0.4187	170	3	50003.7242	0.5783	200	3
48847.6166	0.6493	120	2	49633.7454	0.5574	210	3	50005.6896	0.8706	180	3
48847.6628	0.6562	120	2	49634.7210	0.7025	190	3	50006.6320	0.0107	180	3
48848.5558	0.7890	120	1	49635.7290	0.8524	180	3	50007.6451	0.1614	160	3
48848.6054	0.7964	120	1	49636.7379	0.0024	190	3	50008.7165	0.3207	180	3
48848.6094	0.7970	120	2	49680.6590	0.5341	210	3	50016.6193	0.4960	190	3
48848.6705	0.8061	110	2	49682.6743	0.8338	180	3	50017.6780	0.6534	200	3
48849.5090	0.9308	180	1	49684.6252	0.1239	190	3	50018.6629	0.7999	190	3
48849.5860	0.9422	120	1	49694.6900	0.6207	120	3				
48849.6437	0.9508	180	2	49695.6536	0.7640	150	3	8. *July 1996*			
48850.5424	0.0845	105	1	49696.6033	0.9052	180	3				
48850.6501	0.1005	140	2					50289.4470	0.0692	240	5
48851.5935	0.2408	110	1	5. *January 1995*				50290.4350	0.2161	280	5
48851.6593	0.2506	120	2					50291.4666	0.3695	200	5
48852.5821	0.3878	100	1	49740.5749	0.4444	140	3	50292.4549	0.5165	205	5
48852.6521	0.3982	100	2	49751.6231	0.0874	150	3	50293.6553	0.6951	280	4
48853.5770	0.5357	100	1	49752.6133	0.2347	220	3	50294.6685	0.8457	200	4
2. *December 1993*				49753.5895	0.3799	150	3	50295.6159	0.9866	230	4
49315.6797	0.2567	220	3	49754.6075	0.5313	220	3	50297.4508	0.2595	300	5
49315.7472	0.2668	210	3	49755.5994	0.6788	190	3	50297.6774	0.2932	255	4
49316.6158	0.3959	200	3					50298.6765	0.4418	305	4
49317.6461	0.5491	220	3	6. *July 1995*				50299.4496	0.5567	130	5
49318.6328	0.6959	280	3					50299.6998	0.5939	255	4
49369.5993	0.2753	230	3	49910.6555	0.7377	210	4	50300.4427	0.7044	220	5
49370.5919	0.4229	200	3	49910.6768	0.7409	240	4	50301.4417	0.8530	270	5
49371.6744	0.5839	190	3	49911.6449	0.8849	290	4	50312.4821	0.4948	220	5
49372.5747	0.7178	190	3	49912.6448	0.0336	250	4				
3. *July 1994*				49913.6311	0.1802	240	4	9. *October 1996*			
49578.6835	0.3690	190	4	49914.6363	0.3297	190	4				
49579.6544	0.5133	190	4	49914.6746	0.3354	200	4	50381.3870	0.7419	290	4
49580.6080	0.6552	190	4	49915.6549	0.4812	240	4	50382.4138	0.8946	300	4
49581.5425	0.7941	220	4	49916.6640	0.6313	230	4	50383.3866	0.0393	260	4
49582.5406	0.9426	170	4	49917.6137	0.7725	200	4	50384.3866	0.1880	290	4
49583.6266	0.1041	240	4	49918.6255	0.9230	230	4	50385.4429	0.3451	310	4
49584.6549	0.2570	250	4	49920.6676	0.2267	260	4	50386.4163	0.4898	290	4
49586.6594	0.5551	290	4	49921.6269	0.3693	150	4	50387.5010	0.6512	280	4
49587.6787	0.7067	200	4	49921.6447	0.3720	150	4	50388.3750	0.7811	200	4

as well, but the expected strength of the magnetic field does not disturb its profile so that it might affect our results, given the spectral resolution, S/N, and stellar rotation. Also, simultaneous inversion of several lines can significantly reduce the effect of systematic deviations in a certain line. So, the effect of the magnetic field is ignored in the present calculations. A list of atomic line parameters has been obtained from VALD (Piskunov et al. 1995) for lines having a central depth of 1% or more. A number of molecular lines were included into the list, since the presence of many molecular lines in spectra of stars with effective temperature $T_{\rm eff}$<5000 K is quite noticeable. In the region we used for our study the most significant contribution to the photospheric spectrum from molecular lines is due to rotational transitions of a number of vibrational bands of the CN red system. The main sources of the CN line parameters are the following: wavelengths are from laboratory measurements by Davis & Phillips (1963); band oscillator strengths and molecular constants are from the RADEN database (Kuznetsova et al. 1993); lower level excitation energies and rotational intensity factors are calculated with formulas given by Kovacs (1969). For testing the line parameters, the spectrum of β Gem (K0 IIIb) was used as was described in Paper 1.

Another important molecule for our calculation is TiO, whose bands are known to dominate in the spot spectrum of II Peg in the visible region. There are a few strong TiO bands in the region chosen for surface imaging, which arise in the triplet electronic transition $X^3\Delta - B^3\Pi$ between ground vibrational states and belong to the $\gamma\prime$-system. Since TiO bands are

Table 3. Photometric observations

HJD 2400000+	Phase	U	B	V	R	I
50294.4905	0.8192	9.463	8.734	7.723	6.776	6.058
50297.4762	0.2632	9.176	8.466	7.475	6.563	5.886
50298.4777	0.4122	9.385	8.638	7.630	6.697	5.990
50301.4875	0.8598	9.495	8.772	7.752	6.825	6.079
50303.4888	0.1574	9.127	8.441	7.458	6.560	5.892
50312.3322	0.4725	9.392	8.660	7.659	6.693	6.005
50314.4508	0.7876	9.498	8.742	7.731	6.795	6.063
50319.4031	0.5241	9.459	8.677	7.667	6.731	6.028
50325.4140	0.4180	9.395	8.661	7.631	6.716	5.993
50326.4114	0.5663	9.423	8.692	7.683	6.728	6.017
50327.3980	0.7130	9.453	8.709	7.698	6.757	6.042
50330.4553	0.1677	9.149	8.445	7.460	6.561	5.893
50331.4123	0.3100	9.228	8.498	7.488	6.583	5.893
50339.4434	0.5043	9.448	8.698	7.675	6.734	6.017
50361.4234	0.7731	9.480	8.762	7.747	6.789	6.076
50362.4195	0.9212	9.442	8.722	7.712	6.777	6.063
50363.2957	0.0515	9.185	8.503	7.525	6.627	5.947
50376.3361	0.9908	9.290	8.605	7.602	6.685	5.983
50394.2845	0.6600	9.507	8.787	7.765	6.812	6.090
50402.2972	0.8516	9.465	8.742	7.726	6.803	6.072
50405.2233	0.2867	9.220	8.525	7.525	6.621	5.932

Table 4. Parameters of II Peg

Parameter	Value
$T_{\rm eff}$	4600 K
log g	3.2
[M/H]	–0.4
$\xi_{\rm t}$	2.0 km s^{-1}
$\zeta_{\rm t}$	3.5 km s^{-1}
$v \sin i$	22.6 km s^{-1}
i	60°

well seen in the spectrum of II Peg, and their strengths correlate with the spot visibility (see Paper 1 and references therein), their presence must be taken into account in the surface imaging calculations. For testing the positions and relative intensities of the TiO bands the spectrum of the cool giant δ Oph (M0.5 III) was used. The catalogue of the measured wavelengths of the TiO lines has been kindly provided by Phillips & Davis (1996). Band oscillator strengths and molecular constants are from Davis et al. (1986). Lower level excitation energies and rotational intensity factors are calculated.

After the line list was compiled, a set of local line profiles for a temperature range of 3500–6000 K and ten angular points on the stellar disk has been calculated using the stellar atmosphere models by Kurucz (1993) and the parameters of the atmosphere determined in Paper 1 (see here Table 4). A proper instrumental profile for a given set of observations was included in the calculations as well. A code used for synthetic spectrum calculations is described in detail by Berdyugina (1991). It includes calculation of opacities, intensities and fluxes in the continuum and atomic and molecular lines. Also, number densities of atoms and molecules are calculated under the assumption of their dissociative equilibrium.

3.2. Inversion

For the inversion of the line profiles to the stellar images a new surface imaging technique has been used. It is the Occamian approach which has been developed by Terebizh (1995) as a common approach to inverse problems. Recently, it was applied to the surface imaging problem by Berdyugina (1998). The Occamian approach significantly differs from both the maximum entropy method and Tikhonov regularization, which are widely used in surface imaging. The common approach of these methods is to use a priori constraints for finding a unique and smooth solution. The Occamian approach does not use any artificial constraints for finding such a solution. With simulated data and test calculations it was shown that the Occamian approach can restore stellar images under various conditions. It allows also for a convenient estimation of the variances of the resulting solution, seemingly for the first time in surface imaging.

A 6°×6° grid on the stellar surface was used for integrating local line profiles to normalized flux profiles. With a set of stellar atmosphere models, the stellar image is considered as the distribution of effective temperature across the stellar surface, as usual for surface imaging. Obviously, the resulting temperature scale of the images is model dependent. Therefore, we used photometric observations as additional constraints for the temperature scale of the images, where they were available (Sect. 4.3). Error distributions over the stellar surface have been calculated along with the temperature maps for all seasons (Sect. 4.2).

4. Results of surface imaging

4.1. Images

The surface imaging technique was applied simultaneously to the following lines: Fe I 6165 Å, 6173 Å, 6180 Å; Ca I 6166 Å; Ni I 6175 Å, 6177 Å, 6178 Å. Fig. 2 displays nine images of II Peg from 1992 to 1996, error distributions over the stellar surface for each season, and fits to the line profiles. Images are shown with the coordinate grid of 30° in both latitude and longitude and the inclination of the rotation axis of 60° as was adopted in the calculations. For most data sets phase coverage was quite satisfactory, except the two seasons, December 1993 and January 1995, when phase gaps were as large as 0.54 and 0.41, respectively.

To calibrate the temperature scale of the the images we used our photometric observations for 1996 (Table 3) and those by Henry et al. (1995) for 1992 and by Shevchenko (1996) for 1994 and 1995. We calculated B−V and V−R variations, transforming the temperatures to colours with a calibration, based on a list of dwarfs and subgiants with known temperatures (Bell & Gustafsson 1989) and on BVR-measurements taken from the SIMBAD database. We find that the temperature scale of the

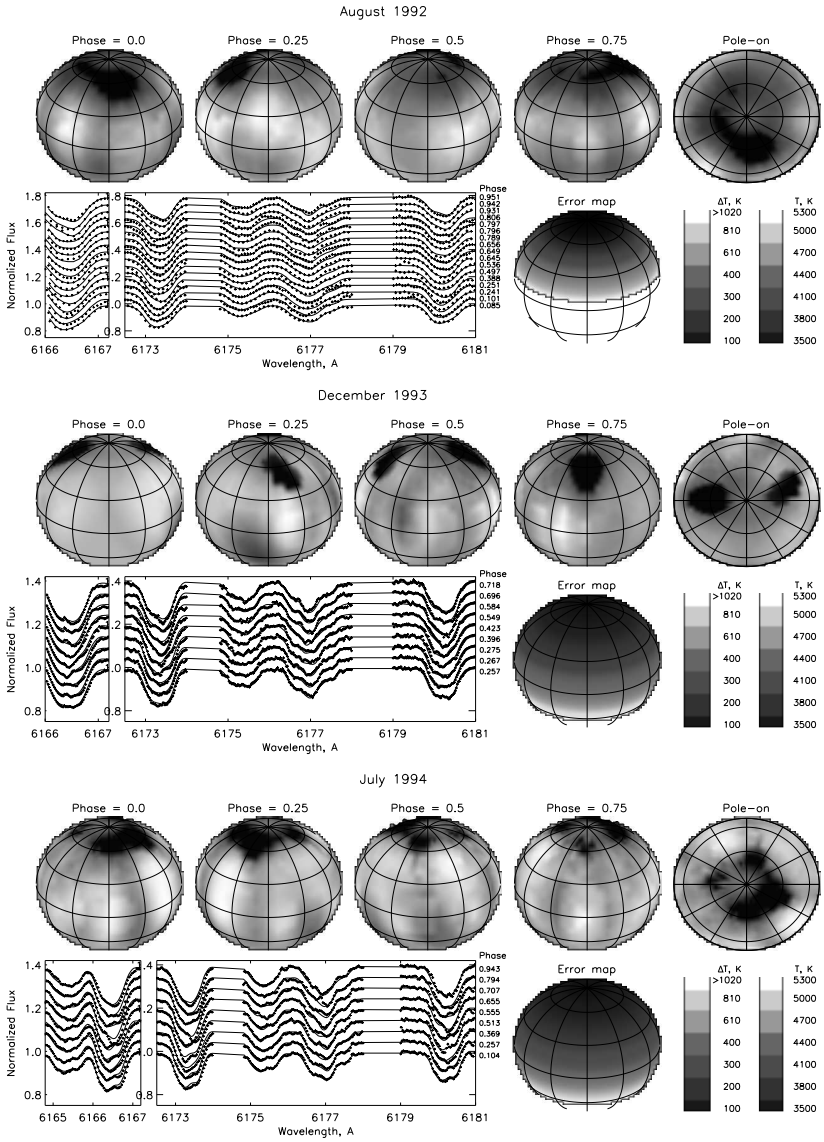

Fig. 2. Images of the primary of II Peg in the scale of effective temperatures of the models in four orbital phases and pole-on projection. The coordinate grid is 30° in both latitude and longitude. The observed and calculated line profiles are shown by symbols and lines, respectively. The error maps show the distributions of the temperature errors, averaged in longitudes.

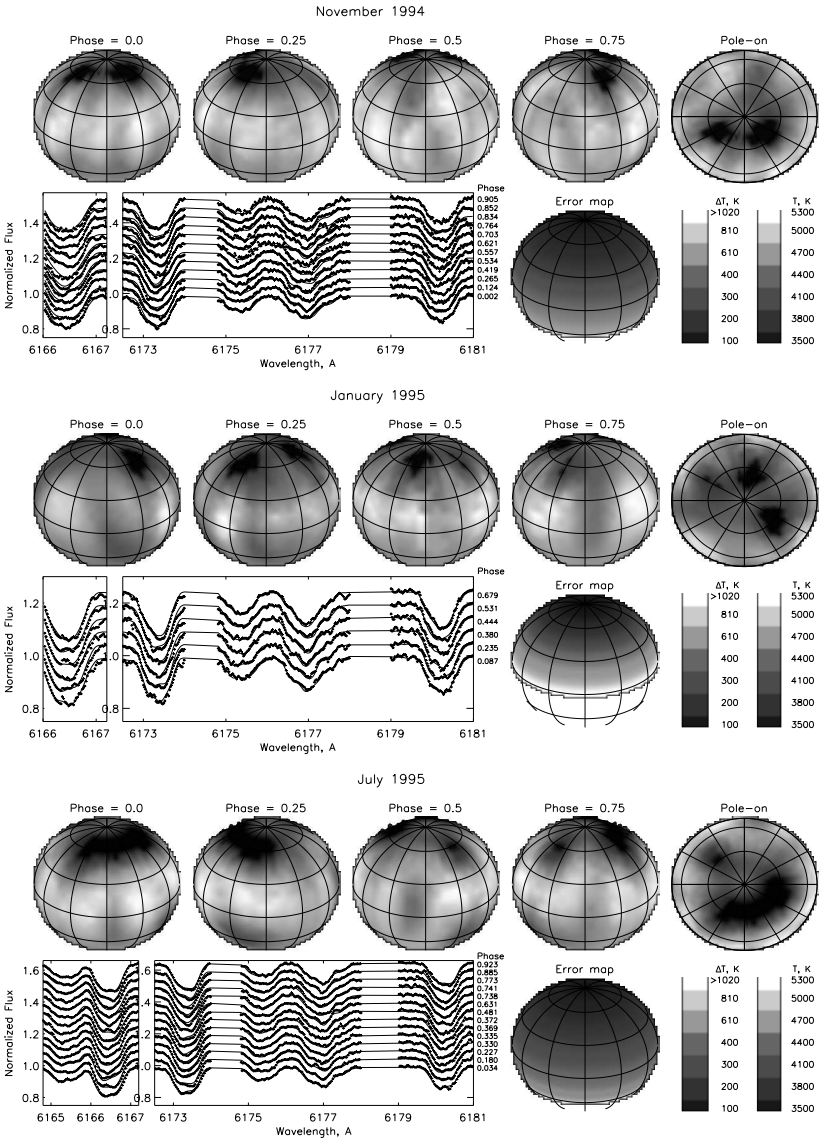

Fig. 2. (continued)

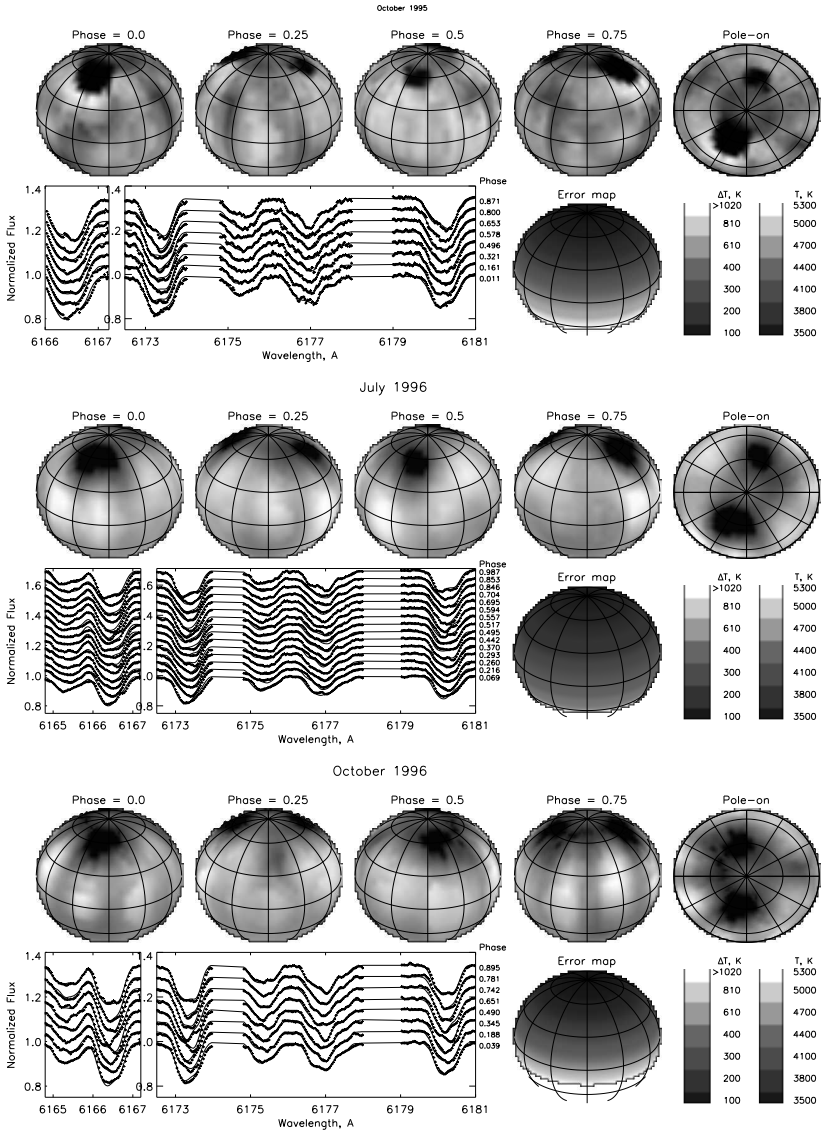

Fig. 2. (continued)

images fit satisfactorily both mean value and amplitude of the colour indices (Fig. 3), and therefore the effective temperature of the star of 4600K$\pm$100K and the spot temperature of 3500 K obtained can be considered as good estimates.

Common properties of the images of II Peg in 1992–1996 are that two high-latitude active regions dominate in all seasons, and no polar cap is seen. The spots appear in the $45°-75°$ latitude belt, which is in accordance with the flux-tube calculations by Schlusser et al. (1996) for rapidly rotating stars with deep convective zones. There are no significant features near the equator, and the stellar activity and variability appear to be determined by the high-latitude spot configuration. Spots can be joined in extended groups or be well separated. Larger spots use to have irregular shapes with unresolved substructure. Hatzes (1995) has obtained three images of II Peg for 1992–1994, and two of them showed a cool polar cap with appendages. Comparison of the present images with his results for two close seasons (August 1992 and July 1994) shows that the positions of the appendages correspond to our dominant spots, or groups of spots. However, the presence of the polar cap and low-latitude spots seem to be arguable (see discussion about the errors in Sect. 4.2).

The most dramatic evolution of the spot structure on a short time scale has happened in 1995. Comparison of the two images for July and October 1995 reveals that the extended group of spots seen in July was disrupted only two months later into two spots separated by half a period. The simultaneous photometric observations confirm the appearance of the spot near the phase 0.5 in October 1995. It is interesting that in July 1995 during the spectroscopic observations for surface imaging a strong flare was observed. A preliminary analysis of the flare was made by Berdyugina et al. (1998a) and will be presented in details in a forthcoming paper. The flare was lasted more than five days and was seen in chromospheric emission lines (Ca II, He I) and in cores of many strong absorption lines. One can suppose that the spot disruption and the strong flare are the connected events. Our future monitoring of the star for surface imaging and flaring could help to study this possible connection.

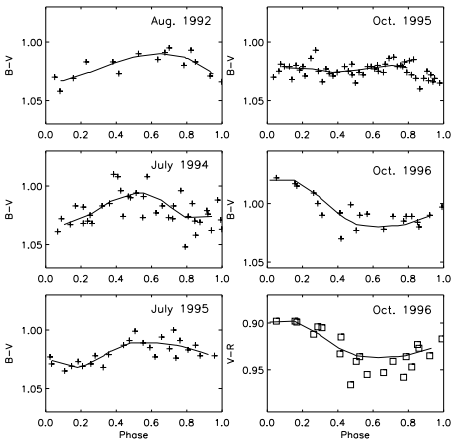

Fig. 3. Colour index variations: observed (crosses: B-V; squares: V-R) and calculated from the images (lines).

4.2. Error maps

The Occamian approach provides error estimates of the solution, which in most cases constitute lower limits of the true errors (see e.g. Berdyugina 1998). As is seen from the error distributions, the accuracy of the temperature values decreases toward lower latitudes. This can be understood from the visibility of the stellar surface for the observer: the pole region is seen in all rotational phases, while others are observable only at certain phases. Thus, high-latitude spots are more reliable, while equatorial and subequatorial features seem to be mainly due to inconsistencies of the calculations and observations. With the adopted inclination i=60° and the grid of $6°\times6°$, the total number of the points on the stellar surface, n, where the temperature has to be estimated, is 1500. As was concluded from the test calculations (Berdyugina 1998), the number of the observations, m, namely wavelength points in the profiles in all available phases, should be a few times the number of parameters to be estimated. Then, for the present calculations m has to be at least 3000. Such a large number can be obtained only with many profiles inverted simultaneously and many rotational phases. However, in some cases this was not achieved due to poor phase coverage and a limited number of line profiles (see Table 5). Therefore, the number of independent parameters p (principal components), which can be estimated with the available data, is less than n, and the quality of the data can be evaluated by the nearness of p and n. Note, however, that p is always smaller than 1400 even for large m, because of small projected areas of the lowest latitudes and limited phase coverage, leading to extremely large errors there. The errors decrease with increasing m, but the speed of this decrease is a strong function of latitude.

The error maps in Fig. 2 are shown in the scale of temperatures averaged in longitudes, since the error gradient in latitudes is much larger than in longitudes. One can see that even in the areas with the best information the errors are quite large, usually about 100–500 K for high latitudes, and more for lower latitudes. However, one should stress, that the images are obtained without constraints due to $T_{\rm eff}$ of the star. In fact, the $T_{\rm eff}$ value is used only to determine the first approximation of the solution, or unspotted stellar surface. Then, underdetermined parts of the stellar surface keep their initial approximation, and the stellar image looks smooth. However, if $T_{\rm eff}$ is not known, and the first approximation is quite far from the real unspotted surface, the final map might be different due to a high sensitivity of the non-linear problem to the first approximation. Then, while the *formal* error estimates will be the same as before, the real errors are much larger. The accuracy of the solution is determined by the *real* amount of information on the temperatures contained in the limited set of observations.

Table 5. Image statistics: m – number of wavelength points in the whole set; n – number of the parameters (number of points on the stellar surface where the temperature is to be estimated); p – number of the principal components which can be estimated with available m.

	Image	m	n	p
1	Aug. 1992	1634	1500	869
2	Dec. 1993	3204	$''$	1360
3	July 1994	2396	$''$	1325
4	Nov. 1994	4272	$''$	1400
5	Jan. 1995	2136	$''$	1222
6	July 1995	3724	$''$	1400
7	Oct. 1995	2848	$''$	1375
8	July 1996	3855	$''$	1400
9	Oct. 1996	2056	$''$	1130

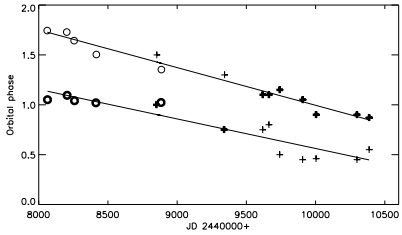

Fig. 4. A plot of the reconstructed spot longitudes on II Peg versus time. Spots from the images are shown by crosses, and spots from the photometric two-spot modelling by Henry et al. (1995) are shown by circles. Larger spots are denoted by heavier symbols. The linear fits to the two active longitudes are shown by lines.

4.3. Spot areas

Our estimates of the projected spot areas obtained from the images are within 10–15%. Hatzes (1995) also reported a spot coverage of only 15% and concluded that the surface imaging underestimates the overall spot areas. Neff et al. (1995) estimated the projected spot areas, as the star rotates, to be varying from 54% to 64% in October 1989. Later, they revised their TiO calibration and reduced those values to 43% and 55%, respectively, for the same observations (O'Neal et al. 1996). They determined similar values for September 1992. Recently, they detected excess OH absorption due to cool spots on the surface of II Peg and found for June 1996 a spot filling factor between 35% and 48% (O'Neal & Neff 1997). Thus, the amplitude of the spot filling factor variation is approximately the same for different seasons and different molecular bands, namely about 10–13%, and this well coinsides with the estimates obtained from the surface images. However, the permanently spotted area contributing to the bands is much larger (30–50%) and not seen in the images.

Our observations of the TiO bands published in Paper 1 confirm this conclusion. We found that calculations of the bands from the images can reproduce the observed amplitudes, while fitting the non-variable depth of the bands needs enormous increase of the spot areas. Note that one of the reason of this inconsistensy, however, could be the absence of appropriate stellar atmosphere models for low $T_{\rm eff}$ and log g. Therefore, at the moment one can conclude that the present surface images show at least the variable part of the activity of II Peg, and the origin of the non-variable part is still not understood.

4.4. Spot migration

Spot positions in the images are the most realiable restored parameters, especially their longitudes. Therefore, we considered phases of crossing the central meridian by spots in the orbital reference frame. Here, the central meridian corresponds to the conjunction when the primary is behind the secondary according to the ephemeris given by Eq. (1). Plotting the phases versus the mean epoch of observation shows clear migration of the spot configuration to earlier orbital phases with approximately the same rate (Fig. 4). Then, this migration means a *shorter* rotational period of the spots in comparison with the orbital period. The mean rate of the spot migration is found to be $(-0.117 \pm 0.009)^\circ$ day^{-1}, which results in a rotational period $P_{\rm rot}$ = 6.7095 $\pm$ 0.0013 days. This is close to the photometric period $P_{\rm phtm}$ = 6.7158 days, averaged over the values found by Henry et al. (1995). The difference in the rotational and orbital periods can be interpreted as either non-synchronous rotation or differential rotation. However, the mean latitude of the spots is approximately the same in the images, and there is no possibility to distinguish these effects.

In Fig. 4 the spot positions are arranged into two permanent narrow bands. The mean longitude separation between the bands is about 0.5 in phase, or 180°. This can be considered as two long-lived active longitudes rotating with their own period in the orbital reference frame and, therefore, having no preferred orientation. One can notice, however, that the *relative size* of the two spots is changing in such a way that at any given time the spot close to the central meridian, i.e. below the secondary, is the largest. It changes its location from one active longitude to the other in 1994, showing the effect of switching the activity between the longitudes. A similar behaviour with two migrating active longitudes was also discovered in other RS CVn stars (Berdyugina & Tuominen 1998).

From two-spot modelling of long-term photometric observations of II Peg for 1974–1992, Henry et al. (1995) found two active longitudes with a separation of 0.43 in phase. Since their latest photometric observations correspond to our earliest spectroscopic observations, we plot their latest spots in Fig. 4, too. One can see that the photometric modelled spots well follow the behaviour of the spots from the images. The periods found in the present paper and by Henry et al. are indeed similar. Moreover, the position of the larger spot corresponds to the same active longitude as was found from the images. Therefore, one can conclude that the images and the independent photometric two-spot modelling are compatible, and active longitudes on II Peg exist for at least 6.5 years and probably will be seen again in future observations.

5. Conclusions

Using new high-resolution spectroscopic observations of II Peg and the Occamian approach as an inversion technique, nine surface images for 1992–1996 have been obtained from the simultaneous inversion of Ca I, Fe I, and Ni I lines. From the analysis of the images the following conclusions are drawn:

1. The temperature scale and spot configuration found are compatible with the available photometric observations.
2. Two high-latitude spots dominated on the surface of II Peg in 1992–1996, and no polar cap was seen.
3. The positions of the spots were constantly migrating to earlier orbital phases with approximately the same rate.
4. The rotational period of the spots is close to the photometric period.
5. Two active longitudes separated by about 180° with no preferred orientation can be deduced from the spot positions. They are compatible with the results of the two-spot photometric modelling by Henry et al. (1995) for 1990–1992.
6. The largest spot tends to be close to the line of centres in the binary and faced toward the secondary. It changed its location from one active longitude to the other in 1994, showing the effect of switching the activity between the longitudes.

Acknowledgements. We are grateful to Dr. Sumner Davis for the computer-readable catalogue of laboratory wavelengths of TiO and CN bands and to Dr. Ludmila Kuznetsova for providing band oscillator strengths and molecular constants from the RADEN database. We thank Dr. Gregory Henry and Dr. V.S. Shevchenko for providing photometric observations and Dr. Rudolf Duemmler for useful discussions. Inversions were carried out on the Cray C94/128 supercomputer in the Center of Scientific Computing (Espoo, Finland). Data from VALD and SIMBAD have been used in the paper. This research was partly supported by grants from the Centre for International Mobility (CIMO), Finland.

References

Bell R.A., Gustafsson B., 1989, MNRAS 236, 653
Berdyugina S.V., 1991, Izv. Krymsk. Astrofiz. Obs. 83, 102
Berdyugina S.V., 1998, A&A 338, 97
Berdyugina S.V., Ilyin I., Tuominen I., 1998a, in ASP Conf Ser. 154, The Tenth Cambridge Workshop on Cool Stars, Stellar Systems, and the Sun, eds. R.A. Donahue & J.A. Bookbinder, San Francisco: ASP, CD-1477
Berdyugina S.V., Jankov S., Ilyin I., Tuominen I., Fekel F.C., 1998b, A&A 334, 863 (Paper I)
Berdyugina S.V., Tuominen I., 1998, A&A 336, L25
Davis S.P., Littleton J.E., Phillips J.G., 1986, ApJ 309, 449
Davis S.P., Phillips J.G., 1963, The Red System ($A^2\Pi - X^2\Sigma$) of the CN molecule, University of California Press, Berkely and Los Angeles
Hatzes A., 1995, in Strassmeier K.G. (ed.), *Poster Proceedings: Stellar Surface Structure*, IAU Symp. 176, Univ. Vienna, p. 87
Henry G.W., Eaton J.A., Hamer J., Hall D.S., 1995, ApJS 97, 513
Huenemoerder D.P., Ramsey L.W., 1987, ApJ 319, 392
Kovacs I., 1969, The rotational Structure in the Spectra of Diatomic Molecules, Academiai Kiado, Budapest
Kurucz R.L., 1993, Kurucz CD No. 13
Kuznetzova L.A., Pazyuk E.A., Stolyarov A.V., 1993, Russ. J. Phys. Chem. 67, 2046
Neff J.E., O'Neal D., Saar S.H., 1995, ApJ 452, 879
O'Neal D., Saar S.H., Neff J.E., 1996, ApJ 463, 766
O'Neal D., Neff J.E., 1997, AJ 113, 1129
Phillips J.G., Davis S.P., 1996, private communication
Piskunov N.E., Kupka F., Ryabchikova T.A., Weiss W.W., Jeffrey C.S., 1995, A&AS 112, 525
Schuessler M., Caligari P., Ferriz-Mas A., Solanki S.K., Stix M., 1996, A&A 314, 503
Shevchenko V.S., 1996, private communication
Terebizh V.Yu., 1995, Uspekhi Fiz. Nauk 165, 143
Vogt S.S., 1981, ApJ 247, 975

Paper VIII

Berdyugina, S. V., Ilyin, I., Tuominen, I. 1999, "The active RS Canum Venaticorum binary II Pegasi. III. Chromospheric emission and flares in 1994-1996", A&A 349, 863

Astron. Astrophys. 349, 863–872 (1999)

ASTRONOMY AND ASTROPHYSICS

The active RS Canum Venaticorum binary II Pegasi

III. Chromospheric emission and flares in 1994–1996⋆

S.V. Berdyugina, I. Ilyin, and I. Tuominen

Astronomy Division, University of Oulu, P.O. Box 3000, FIN-90401 Oulu, Finland

Received 23 April 1999 / Accepted 19 July 1999

Abstract. We analyse observations of the very active RS CVn-type star II Peg carried out simultaneously in chromospheric and photospheric lines in 1994–1996. We describe the correlation of the strength of the He I D_3, Ca II K and Ca II 8498 Å emissions with the spot position on the stellar disk. A two-component structure is suggested in the chromosphere of II Peg, similar to that in the corona: nonvariable component (cool plages) with constant contribution to the line emission and variable, active one (hot plages) showing a growth of its activity during 1994–1996. The active component is related to the spots seen in the photosphere.

Two subsequent flares on July 19–23, 1995 were observed in the He I D_3 and Ca II K and 8498 Å lines showing strong *narrow red-shifted* emissions. The development of the flares took a few hours and decay lasted several days. At the maximum of the flaring, in addition to the narrow components, *broad blue-shifted* emissions appeared in He I and Ca II K and in the cores of many strong absorption lines. The broad components are attributed to the process of the explosive evaporation from the low chromosphere. The amount of energy released in different lines is determined. From the radial velocity curve of the He I emission the location of the radiating matter is deduced. It appears to be related to the largest active region which is seen in the stellar image. The flare occurred concurrently with the break of the extended group on two well separated spots. On October 26, 1996 another flare was observed in three spectra, as narrow emissions in the He I and Ca II 8498 Å lines but without development in other lines. It probably was a late stage of the flare decay.

Key words: stars: activity – stars: chromospheres – stars: flare – stars: individual: II Peg

1. Introduction

II Peg (HD 224085) is one of the most active RS CVn binaries showing remarkable photometric variability, Hα and Ca II H&K emission, UV, radio, and soft X-ray radiation. This activity is attributed to the primary, rather than to the unseen secondary, and indicates its active photosphere, chromosphere, and corona. Our analysis of the optical spectrum of the star has revealed that the primary is an old-disk K2 IV star which has evolved to the base of the Red Giant Branch. The secondary is thought to be a low-mass main-sequence M-dwarf (Berdyugina et al. 1998a, Paper 1). Stellar images of the primary show a long-lived spot structure in its photosphere (Berdyugina et al. 1998b, Paper 2). The spots migrate in the orbital reference frame with a constant rate and comprise two active longitudes which are active by turns and, thus, determine a magnetic cycle of 9.3 years, (Berdyugina & Tuominen 1998).

Early spectroscopic observations of the star have revealed strong emissions in the Ca II H&K and Hα lines (Rucinski 1977). The emission in Hα was noticed to be asymmetric with an enhanced blue wing and strongly correlated with spot visibility. It is more intense when the spot regions are on the visible hemisphere (Bopp & Noah 1980; Vogt 1981). The same spatial correlation has been observed for emission lines from the high-temperature transition region and chromosphere in the UV (Rodonó et al. 1987; Byrne et al. 1987). This has been interpreted as evidence of large magnetic loops overlying spot areas and forming plages in the outer atmosphere. Recently published monitoring observations in chromospheric lines (Byrne et al. 1995, 1998; Montes et al. 1997) have shown that the star in its quiescent (out-of-flare) state is continually variable. The profile of Hα has exhibited broad emission wings which suggest complicated velocity fields in the deep chromosphere with both upward and downward motions. It was suggested also that the broad wings of Hα are the result of microflaring in the chromosphere since they are reminiscent of broad wings of transition region lines in solar and stellar explosive events.

II Peg is a high-rate flaring star, especially in the UV and in X-rays. From the far UV and X-ray spectrum a bimodal temperature structure of the quiescent corona of II Peg was inferred (Tagliaferri et al. 1991, Mewe et al. 1997). During a flare, the cool component of the corona seems to show the same parameters as the quiescent spectrum, while the hot component increases considerably both in emission measure and in temperature. By studying the decay of a flare, Mewe et al. (1997) found that in comparison with flares on other types of stars the flare on II Peg had a very long duration, large associated vol-

Send offprint requests to: S.V. Berdyugina (sveta@ukko.oulu.fi)

⋆ Based on observations collected at the Nordic Optical Telescope (NOT), La Palma, Spain

ume and relatively low density. Evidence for highly extended (probably loop-like) flaring structures also was found by Doyle et al. (1992). Another long-lasting flare in X-rays was reported by Tagliaferri et al. (1991): the development of the flare took a few hours, while the decay lasted about two days. The total radiative loss from the chromosphere and transition region during such flares can be up to $3{\cdot}10^{35}$ erg (Doyle et al. 1989a, 1989b; Tagliaferri et al. 1991).

Flares on II Peg in the optical spectral lines have been reported several times (Bopp & Noah 1980; Huenemoerder & Ramsey 1987; Huenemoerder et al. 1990; Mohin & Raveendran 1993; Byrne et al. 1995, 1998; Montes et al. 1997). Sudden enhancements of the Hα and Ca II lines and development of the emission in the He I lines are always attributed to flare-like events. The ratio of the emission of Hα to that of Hβ is found to be a good indicator of a flare: in quiescent state it is similar to the ratio in solar prominences, while during line enhancements it decreases toward values more typical of solar flares. Analogously, absorption in the He I lines is attributed to plages, while detection of any emission is immediately connected to flares, as in the Sun.

There are a few reports of flares detected in the optical U-band (Doyle et al. 1991; Mathioudakis et al. 1992; Henry & Newsom 1996), while no flares were observed during monitoring by Byrne et al. (1994). This suggests that II Peg can be in states of different flare activity.

In our paper we present additional evidence of the spatial correlations of the quiescent emission in the Ca II K, Ca II 8498 Å and He I D_3 lines with the photospheric spots seen in the stellar images and photometric light curves during 1994–1996 (Paper 2). Also, we report on two optical flares observed spectroscopically on July 19–23, 1995 and October 26, 1996. For the first flare we present unique data acquired from a large spectral region and lots of spectral lines.

2. Observations

Observations were carried out in 1994–1996 with the SOFIN échelle spectrograph fed by the 2.56 m Nordic Optical Telescope (NOT) on La Palma, Canarias. During three seasons, July 1994, July 1995, and August 1996, a total of 58 spectra in the 5500–8500 Å region have been obtained. These spectra have been reduced and used for determining the orbital and stellar parameters of the star in Paper 1 and for surface imaging in Paper 2. Dates, phases and quality of the observations have been given in those papers. Additionally, 20 spectra in the 3850–4500 Å region were obtained in 1995 and 1996. A catalog of the observations is given in Table 1. Three lines, Ca II K, Ca II 8498 Å, and He I D_3, are available for the analysis of the chromospheric emission, though because of the orbital motion of the star and the chosen échelle frame position, the Ca II 8498 Å line was observed at the very edge of the CCD at certain phases. Therefore, only a peak intensity can be measured for this line over the period.

The spectral resolving power achieved in the spectra is from 75000 to 83000 for blue and red regions, respectively. The signal-to-noise ratio of the spectra increases from 20 to 150 for the wavelengths from 3850 Å to 4500 Å and was 200–300 for redder wavelengths. The reduction of the spectra is described in Paper 1. Quasi-simultaneous photometry of the star was presented in Paper 2. All observations are phased according to the orbital ephemeris from Paper 1, which is used throughout this paper:

$$\mathrm{T_{conj}} = \mathrm{HJD}\,2449582.9268 + 6.724333E \quad (1)$$

with the primary in back at phase zero.

Two flare events have been recorded on July 19–23, 1995 and October 26, 1996. Emissions appeared during the flares were obtained from the observed spectra by subtracting the quiescent spectra observed one rotation before. Unfortunately, no simultaneous photometry for the flares is available.

Table 1. Spectroscopic observations in the 3850–4500 Å region.

Date	HJD 2400000+	Phase	Date	HJD 2400000+	Phase
	1995			*1996*	
12/07	49910.7138	0.7467	29/07	50293.7250	0.7058
13/07	49911.7245	0.8966	31/07	50295.7073	0.0003
15/07	49913.7082	0.1917	02/08	50297.7366	0.3024
16/07	49914.7189	0.3421	03/08	50298.7369	0.4511
17/07	49915.7190	0.4909	04/08	50299.7421	0.6004
18/07	49916.7154	0.6390	24/10	50381.4590	0.7531
20/07	49918.6723	0.9300	25/10	50382.4685	0.9029
22/07	49920.7183	0.2344	26/10	50383.4302	0.0458
			27/10	50384.4497	0.1975
			28/10	50385.5085	0.3549
			29/10	50386.4705	0.4978
			31/10	50388.4265	0.7888

3. The out-of-flare chromospheric emission

3.1. The Ca II lines

The Ca II K and IRT Ca II 8498 Å lines are the traditional spectral probes of the low chromosphere. They show distinct variations with the spot visibility, especially in the year 1996 (Fig. 1). The variations are similar to those usually seen in Hα: the emission is more intense when the light curve is near minimum, in other words, when the spotted regions are on the visible hemisphere. As was mentioned, such a correlation suggests the presence of plages in the outer atmosphere overlying the spots. The maximum of the out-of-flare emissions in the lines has increased since 1995, while the minimum emission is at the same level for both years. This can be caused by an increase in the amount of material above the spots, in the lower chromosphere, while the nonactive hemisphere of the star has not changed its emission during the period of 1995–1996.

3.2. The He I D_3 line

This line is formed in the upper chromosphere. Nevertheless, it shows similar behaviour to the Ca II lines. When spots are becoming visible, the helium line is gradually transforming from

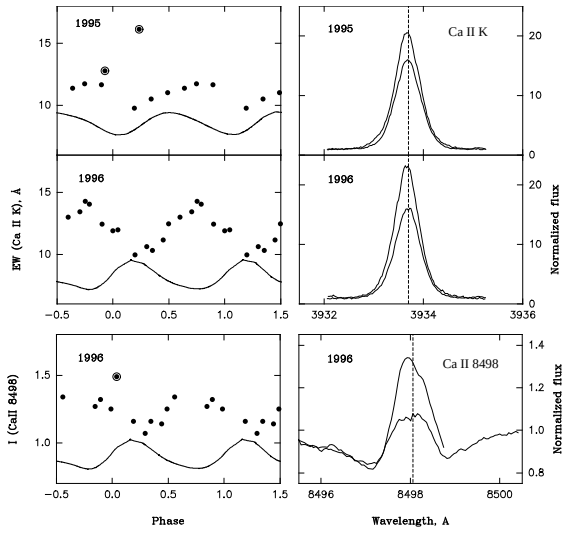

Fig. 1. *Left panels:* Equivalent width variations of the Ca II K line in 1995–1996 and central intensity variations of the Ca II 8498 Å line in 1996. Emphasized dots are the flares on July 19–23, 1995 and October 26, 1996. The curves below the dots are the V-band variations for the seasons. Phases have been calculated with the orbital ephemeris given by Eq. 1. *Right panels:* The profiles of the Ca II lines with the maximum and minimum equivalent widths observed at the seasons. Vertical dashed lines indicate the rest wavelengths in the frame of the primary.

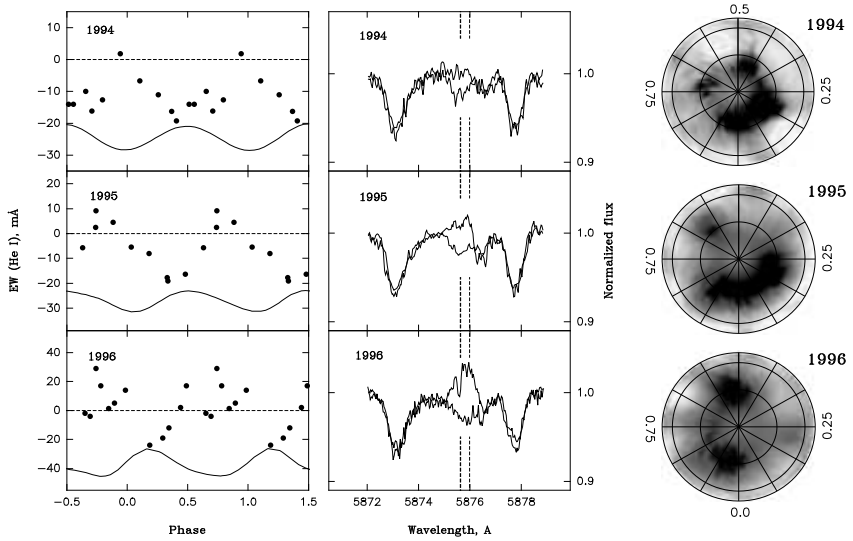

Fig. 2. Same as Fig. 1 for the He I D_3 line in 1994-1996. The flares on July 19–23, 1995 and October 26, 1996 are out of scale. Negative values of equivalent widths mean that the line was observed in absorption, while positive values indicate the line to be in emission. The emission in the line has been increasing during 1994–1996, while the absorption was at the same level. Three images of II Peg in the pole-on projection are shown for the three years from Paper 2.

absorption to emission (Fig. 2). As was mentioned, an absorption in the line is always attributed to plages, while any emission is considered as a primary indication of flares. However, our observations show that even in the quiescent, out-of-flare state the He I D_3 line can appear in emission which fills the absorption up to 30 mÅ above the continuum (about 50 mÅ in total). This emission indicates very hot plasma in the upper chromosphere, above the spots and low-chromosphere plages which are seen in the Ca II lines. The stratification is reminiscent of a large magnetic loop overlying the spots. The quiescent emission in the He I D_3 line increased significantly during 1994–1996, as seen in Fig. 2. This, again, suggests a growth in volume of the hot matter in the upper chromosphere. The amount of the absorption corresponding to the nonactive hemisphere of the star was stable during 1994–1996, about 20 mÅ.

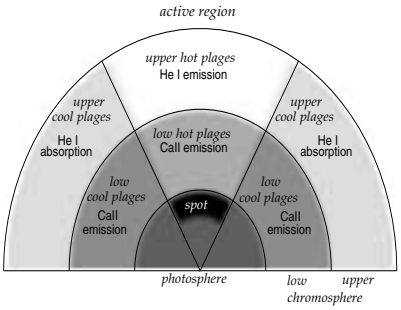

Fig. 3. The structure of the active region in the atmosphere of II Peg as seen from the stellar images and He I D_3 and Ca II K emissions.

3.3. The structure of active regions

As the observations of the chromospheric indicators were carried out simultaneously with the photospheric lines, from which the surface images of the star were obtained (Paper 2), we have the opportunity to study the radial structure of the active regions from the photospheric level to the upper chromosphere. In Fig. 2 three stellar images are shown for July 1994, July 1995, and October 1996 from Paper 2, which are relevant for the present observations. In 1994 and 1995 the largest active region is seen in the phase intervals of 0.9–0.25 and 0.8–0.25, respectively. It has moved in phase during the year because of the difference between the orbital and spot rotation periods, as was discussed in Paper 2. The maximum emission in the chromospheric lines occurs at the phases 0.9 and 0.8 in 1994 and 1995, respectively, corresponding to the edge of the active region. This suggests that a gross amount of the active plasma was concentrated in the part of the active region, near its edge. This part at the phase 0.9 has survived to the end of 1996 at all three levels – photosphere, low chromosphere, and upper chromosphere. The other part of the active region, with no significant matter in the chromosphere, near the phase $\sim$0.2, migrated to the phase $\sim$0.5 during only two months, after the strong flare on July 19–23, 1995 (see Sect. 4.4). The resulting active region near the phase 0.5 survived to the end of 1996 and accumulated a significant amount of the matter in the chromosphere. This has caused the increase of the emission in the Ca II K and He I D_3 lines in 1996. The two active regions of 1996, near the phases 0.9 and 0.5, are seen in the helium emission as two local maxima overlying the broad photometric minimum (Fig. 2).

Summarising the above discussion, we suggest that there are two temperature components in the chromosphere of II Peg (Fig. 3). First, an *active* component, which consists of the plages overlying the spots. In the upper chromosphere it is hot and dense enough to give a moderate emission in helium lines. Second, a *nonactive*, cool component, which is the rest of the chromosphere of lower temperature. It results in an absorption in helium lines. The higher temperature of the plages in the active component arises from the additional, magnetic heating in the magnetic loops connected to the spots. The nonactive component seems to be stable for years, while the active component is changeable at various time scales: months, days, and hours. The two-temperature structures are observed at all levels of the atmosphere of II Peg: spots and unspotted surface in the photosphere, hot and cool plages in chromosphere, hot and cool components in the corona (e.g. Mewe et al. 1997). Considering the active and nonactive components in the atmosphere, the former includes spots and hot components of the chromosphere and corona, while the latter consists of the other parts. Therefore, the temperature gradients in the components are rather different – it is much steeper in the active component. This should be taken with caution when modeling the outer atmosphere of II Peg and other active stars by fitting observed line emissions.

4. The flare on July 19–23, 1995

4.1. The upper-chromosphere line He I D_3

The flare started on July 19, 1995 and was noticed first in the He I D_3 line which appeared as a strong, asymmetric, redshifted, narrow emission (Fig. 4). The emission was seen for 5 days until the end of the observing run (July 23, 1995), even in the low S/N spectrum on July 21 (not shown in the figure). The maximum of the emission was reached on July 22, when in addition to the narrow component, a broad blue-shifted component was seen. At that moment, the two-component emission was observed in the Ca II K and Ca II 8498 Å lines as well as in cores of many absorption lines (see Sect. 4.2). On July 23, all lines had returned to their quiescent shapes, except He I which still showed both emission components, although reduced in strength. The energy released in the flare in the helium line is presented in Table 2.

The asymmetric narrow component of the helium emission is well fitted by two Gaussians of different intensities and FWHM=25–30 km s^{-1} (Fig. 4). These Gaussians are interpreted as the components of the resolved ("doublet") components of the line. They are both red-shifted in respect to the rest wavelengths of 5875.62 Å and 5875.99 Å. The broad, blue-shifted component of FWHM=80 km s^{-1} is attributed to the

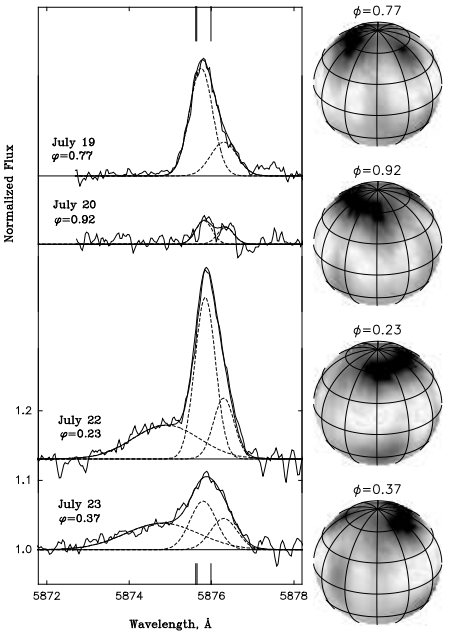

Fig. 4. Profiles of the He I D_3 line during the flare on July 19-23, 1995 and the relevant stellar image showing the spot distribution on the visible hemisphere from Paper 2 at the moments of the observations of the flare. In the profiles: a thin solid line shows the observations, dashed lines are the Gaussian components fitted to the profiles, and a thick solid line is the sum of the Gaussians. Vertical lines show the rest wavelengths of the helium triplet. The profiles are shown in the rest frame of the primary.

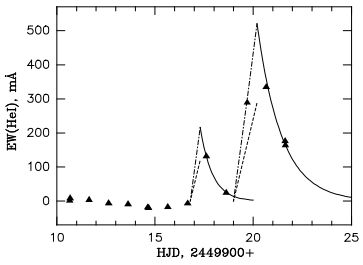

Fig. 5. The equivalent widths of the He I D_3 line versus time. Observations are shown by triangles. The dashed line is the flare development rate of 10 mÅ/h estimated from Huenemoerder et al. (1990), and the dash-dotted line is that of 18 mÅ/h estimated from Montes et al. (1997). Exponential decays of the flares are shown by the solid line: $e^{-1.6t}$ for the first flare and $e^{-0.8t}$ for the second one (t is in days).

Table 2. The energy released in the flare on July 19–23, 1995 in the He I D_3 and Ca II lines caculated with d=42.3 pc (π=0.″02362). ΔT is the exposure time.

Date	ΔT (s)	EW (Å)	F (erg s^{-1}cm^{-2})	E (erg s^{-1})
		He I D_3		
19/07/1995	2715	0.132	$4.47{\cdot}10^{-13}$	$0.96{\cdot}10^{29}$
20/07/1995	3600	0.025	$8.46{\cdot}10^{-14}$	$0.18{\cdot}10^{29}$
21/07/1995	840	0.290	$9.82{\cdot}10^{-13}$	$2.11{\cdot}10^{29}$
22/07/1995	3600	0.335	$1.13{\cdot}10^{-12}$	$2.42{\cdot}10^{29}$
23/07/1995	1500	0.177	$5.99{\cdot}10^{-13}$	$1.28{\cdot}10^{29}$
23/07/1995	1500	0.165	$5.58{\cdot}10^{-13}$	$1.20{\cdot}10^{29}$
		Ca II K		
20/07/1995	3610	1.10	$1.49{\cdot}10^{-12}$	$3.19{\cdot}10^{29}$
22/07/1995	4200	6.43	$8.70{\cdot}10^{-12}$	$1.86{\cdot}10^{30}$
		Ca II 8498 Å		
22/07/1995	3600	0.477	$1.67{\cdot}10^{-12}$	$3.58{\cdot}10^{29}$
23/07/1995	3000	0.255	$0.89{\cdot}10^{-12}$	$1.91{\cdot}10^{29}$

first, stronger, narrow component. The relative intensity of the narrow Gaussians changes during the flare. This can be caused by evolving excitation conditions in the emitting matter.

It was noticed that flares on II Peg have a very long duration in comparison with flares on other types of stars (e.g. Mewe et al. 1997). The long time scale is determined by a low density and a large volume of a flare. To see the development of the flare, we plot the equivalent widths of the He I line versus time in Fig. 5. Actually, two subsequent flares were possibly observed: on July 19–20 and July 21–23. Both flares developed during a few hours, while their decays have taken about 1.5 days for the first flare and even more, probably about 3 days, for the second flare. Such a strong emission in the He I line has never been observed in II Peg or other active stars. Previously reported equivalent widths of the emission in the He I D_3 line observed in II Peg are more than a factor of two smaller. All the emissions have been interpreted as indications of flares, although only two of them have been seen as developing, in November 1988 (Huenemoerder et al. 1990) and September 1995 (Montes et al. 1997). From the two papers we estimated the rates of increase of the helium emission of 10 mÅ/h and 18 mÅ/h, respectively. The second rate suits our data better, within uncertainties. Assuming an exponential decay of the flare, we found that the first flare faded out as fast as $e^{-1.6t}$, while the second, stronger one decreased slower, as $e^{-0.8t}$ (t is in days). The latter is probably caused by the slower decay of the broad component, as seen from the profiles. A total radiative loss in the helium line during the flare is about $8{\cdot}10^{34}$ erg.

4.2. The low-chromosphere and upper-photosphere lines

Emission in the Ca II lines significantly increased during the flare. We have observed only two phases in Ca II K and two phases in Ca II 8498 Å. The behaviour of the emissions correlates well with that of the helium line. Two components – broad

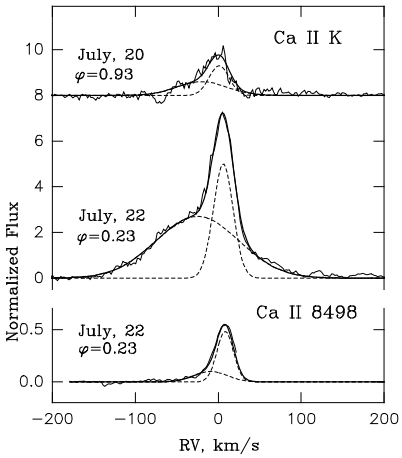

Fig. 6. Profiles of the Ca II K and 8498 Å lines during the flare on July 19–23, 1995. The notation is the same as in Fig. 4. The profiles are shown in the rest frame of the primary.

blue and narrow red – are distinctly seen in the Ca II emissions at the maximum of the flare (Fig. 6). The energy released during the flare in the calcium lines is presented in Table 2.

At the maximum of the flare, emission components appear in the line cores of very strong absorption lines and also in high-excitation lines, which are formed in the low chromosphere and upper photosphere. A list of the lines along with the parameters of the Gaussian components fitted to the profiles is presented in Table 3. With a semi-empirical chromosphere model of II Peg recently developed by Short et al. (1998) we have calculated the LTE depths of formation of the line cores which showed the emissions (Fig. 8). Those lines whose cores are formed in the low chromosphere show distinct two-component emissions. Their profiles are displayed in Fig. 7. The average FWHM and RV of the blue components are of 32 km s^{-1} and –6 km s^{-1}, respectively; those of the red components are of 12 km s^{-1} and +8 km s^{-1}, respectively. The weaker absorption lines whose cores are formed in the upper photosphere show weaker, single-component emissions with FWHM=12 km s^{-1} and RV=7 km s^{-1}, on average. Only a limited number of them is given in Table 3.

As seen from Fig. 8, there is a probable decrease in the released energy when going into deeper layers of the atmosphere. The appearance of the strong red-shifted emission component in He I on July 19 signals that particle beams have rushed into the chromosphere. They heated the atmosphere as deep as $\log \tau_{5000} < -1$ and caused the collisionally excited, red-shifted emissions in the line cores. This downflow was seen during at least 5 days in the helium line, 2–3 days in the Ca II lines, and at least one day in other lines. A similar downflow was observed in Mg II h&k during a flare on II Peg in 1983 (Doyle et al. 1989b) and also in flares on other RS CVn stars. When the beams are rushed into the dense chromosphere, they heat its matter, and the heated plasma fills the flare volume through the process of chromospheric evaporation (e.g. Haisch et al. 1991). Such upward turbulent motion is observed as broad, blue-shifted emission components in many lines, and it was seen at least two days in He I and once in other lines. The evaporation comes from the low chromosphere, $\log \tau_{5000} < -3$.

One must note that broad blue-shifted components in the spectrum of II Peg were previously observed only in the profiles of the Mg II h&k lines at the maximum of the flare in 1983 (Doyle et al. 1989b). In other active stars they have been occasionally observed in Hα (HK Lac, RS CVn-type binary, Bopp & Talcott 1980), Ca II H&K and blue Balmer lines (AT Mic, M-dwarf, Gunn et al. 1994), He I D_3, Na I D, Fe II and Si II (S CrA and T Tau, TTS, Hamann & Persson 1992; Hartmann 1982). In all the cases the emissions were observed as rare transient phenomena with lifetimes from 15 min to 2 days.

Our observations relate solely the appearance of broad blue-shifted components in permitted emission lines with the process of chromospheric evaporation during the strongest flares. Also, we show that in active stars the explosive evaporation can arise from the low chromosphere level, while in solar flares it comes from the upper chromosphere and is seen only in ultraviolet and X-ray radiation (e.g. Fisher 1987).

4.3. The location of the flare

Since the He I emission was observed at four orbital phases during the flare and six phases in the quiescent state, its orbital motion can be used to estimate probable location of the flare. Varying the γ-velocity of the orbit obtained from the photospheric lines (Paper 1), the best fit to the He I velocities was found (Fig. 9). One can see that the amplitude of the orbital motion of the He I emission is well fitted by that of the photospheric lines, only γ-velocities are different. Since the amplitude value is determined by the distance to the mass centre of the system, the flare origin has to be on the primary of II Peg. In other words, it should either overtake the whole chromosphere or be in the plane crossing the mass centre and visible pole of the primary and preserving its distance to the mass centre of the system due to (quasi)synchronous rotation. The latter case is the most probable since a flare is presumed to be a local event. Also, we stress that the narrow components in He I observed in the flare are red-shifted *at all orbital phases*, for more than half a period. This suggests that the emitting matter was located somewhere above the pole. Taking into account that (i) there was a large active region near the pole, (ii) the flare has been observed at the phases when the region was crossing the visible hemisphere (Fig. 4), and (iii) the quiescent helium emission was connected to the spots, we suggest that the flare likely arose close to the pole and next to the active region observed in 1995. The flare appears to be related to the active component of the chromosphere which is seen from the quiescent helium and calcium emissions.

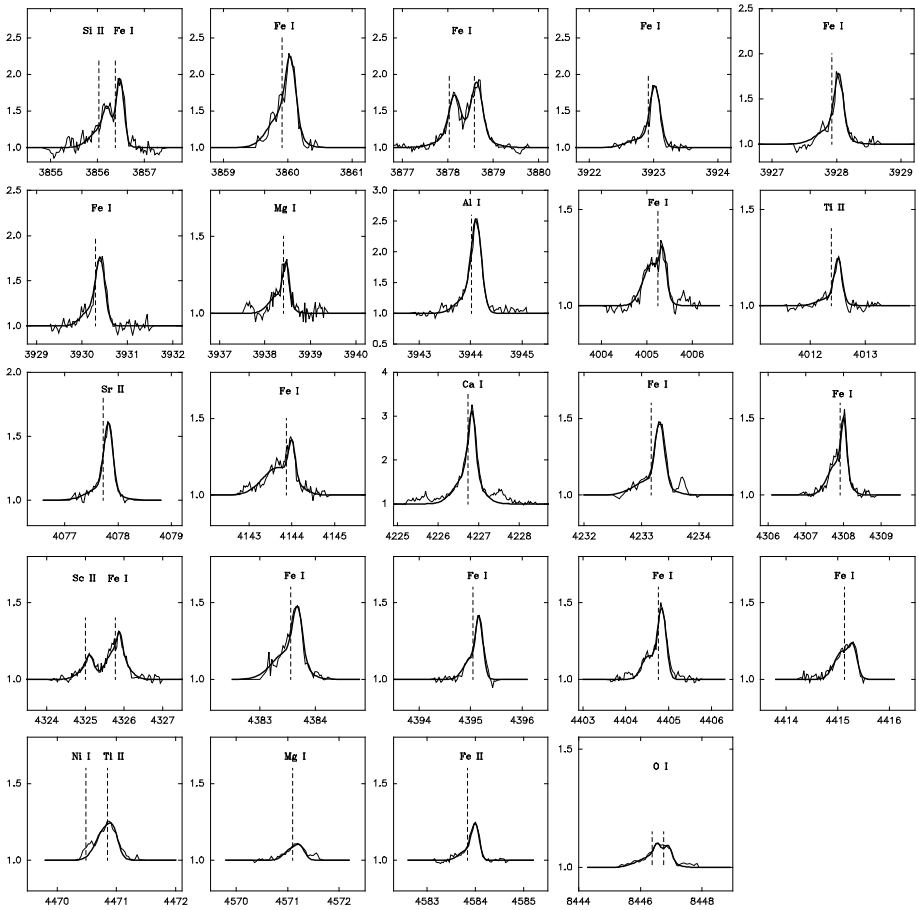

Fig. 7. Profiles of the emissions that appeared at the cores of strong and high-excitation lines at the maximum of the flare, on July 22, 1995.

4.4. The post-flare spot distribution

The connection of the flare to the largest active region is also favoured by the subsequent observations of the star. It appears that on July 19, 1995 II Peg experienced a heavily active flaring stage. One rotation before (during 7 days) the star was in its normal, quiescent state. Then, we observed 5 days of flaring which, obviously, has not finished on July 23. Two weeks later, on August 5–9, 1995, additional flare activity was recorded by EUVE (Osten et al. 1998 and private communication). Then, one month later, on September 13–14, 1995, a new flare was observed in the helium line and Hα (Montes et al. 1997).

We suggest that this strong flare activity, started on July 19, 1995 and observed during two months, occurred concurrently with the radical change of the spot structure on the stellar surface. In Fig. 10 we display two surface images and two light curves from Paper 2 corresponding to July 1995 (before the flare) and October 1995 (after the flare). The break of the large active region into two smaller ones after the heavy flaring is well seen in the images. A clear development of the secondary

Table 3. Parameters of the emissions observed at the maximum of the flare on July 22, 1995: equivalent widths EW (Å), maximum intensity I, full width at half maximum FW (km s^{-1}) and radial velocity RV (km s^{-1}).

Two-component emissions									*Some of the single-component emissions*					
λ,Å	Elem.	EW	*Broad component*			*Narrow component*			λ,Å	Elem.	EW	*Narrow component*		
			RV	FW	I	RV	FW	I				RV	FW	I
3856.018	Si II	:	:	:	:	13.3	12.5	0.30	3858.303	Ni I	0.125	7.9	18.6	0.42
3856.377	Fe I	0.344	–20.2	39	0.28	8.1	12.4	0.85	3865.527	Fe I	0.067	6.4	15.6	0.27
3859.916	Fe I	0.403	–1.2	31	0.45	10.2	12.5	0.90	4071.530	V I	0.056	7.0	13.2	0.25
3878.028	Fe I	0.149	:	:	:	8.5	18.6	0.50	4071.745	Fe I	0.056	8.1	11.8	0.28
3878.584	Fe I	0.458	–18.1	62	0.25	4.3	18.6	0.70	4092.394	Co I	0.036	4.9	11.8	0.18
3922.919	Fe I	0.215	–9.1	30	0.12	7.9	12.2	0.78	4167.277	Mg I	0.036	9.8	13.0	0.16
3927.929	Fe I	0.198	–2.2	31	0.17	8.2	10.6	0.65	4224.172	Fe I	0.025	10.5	12.8	0.11
3930.303	Fe I	0.256	–7.9	30	0.19	7.9	15.2	0.65	4225.460	Fe I	0.030	14.0	11.4	0.15
3933.664	Ca II	6.430	–25.0	100	2.70	6.0	24.4	5.00	4227.434	Fe I	0.054	5.9	12.8	0.24
3938.406	Mg I	0.103	–8.1	30	0.12	4.8	10.6	0.25	4246.835	Sc II	0.029	9.5	12.8	0.13
3944.016	Al I	0.473	–8.8	30	0.25	7.3	15.2	1.40	4300.049	Ti II	0.065	9.0	12.6	0.29
4005.250	Fe I	0.144	–9.7	30	0.22	8.2	10.4	0.20	4301.927	Ti II	0.038	9.4	11.2	0.19
4012.385	Ti II	0.058	–2.6	30	0.04	9.3	10.4	0.22	4303.229	Co I	0.040	6.2	11.2	0.20
4077.722	Sr II	0.168	–2.4	38	0.10	7.2	11.8	0.52	4305.714	Sc II	0.025	12.2	12.6	0.11
4143.875	Fe I	0.209	–14.1	52	0.18	9.1	11.6	0.24	4312.869	Ti II	0.021	8.0	9.8	0.12
4226.734	Ca I	0.848	–0.3	42	0.70	6.8	12.8	1.45	4314.087	Sc II	0.025	7.0	8.4	0.17
4233.168	Fe II	0.147	–1.3	38	0.10	10.6	11.4	0.40	4314.304	Fe II	0.019	9.9	9.8	0.11
4307.911	Fe I	0.195	–5.6	33	0.21	6.9	11.2	0.35	4314.800	Ti I	0.044	4.9	11.0	0.22
4324.999	Sc II	0.055	–3.4	28	0.05	8.3	13.8	0.12	4314.980	Ti II	0.052	8.9	12.4	0.23
4325.772	Fe I	0.145	–0.1	34	0.20	8.2	9.8	0.12	4399.772	Ti II	0.019	8.4	9.6	0.11
4383.555	Fe I	0.195	–5.1	36	0.18	8.6	12.4	0.35	4470.144	Mn I	0.022	2.2	10.8	0.11
4395.038	Ti II	0.106	–2.6	19	0.13	9.0	9.6	0.35	4481.134	Mg II	0.017	5.4	9.4	0.10
4404.760	Fe I	0.168	–16.3	20	0.15	5.4	13.6	0.45	4481.327	Mg II	0.032	14.3	10.8	0.16
4415.130	Fe I	0.064	–3.4	20	0.08	11.6	10.8	0.17	5857.458	Ca I	0.012	4.9	10.2	0.05
4470.854	Ti II	0.095	–3.6	20	0.20	6.4	10.6	0.10	6162.180	Ca I	0.033	6.1	12.8	0.08
4571.100	Mg I	0.040	0.0	20	0.08	9.8	10.4	0.05	6169.043	Ca I	0.012	6.6	12.6	0.04
4583.835	Fe II	0.066	–2.3	20	0.06	10.8	10.4	0.22	6169.565	Ca I	0.011	6.1	9.8	0.04
5875.620	He I	0.335	–36.8	82	0.05	11.7	25.6	0.24	6191.189	Ni I	0.020	7.9	13.6	0.06
5875.989	He I	:	:	:	:	15.9	25.6	0.07	6191.568	Fe I	0.020	6.2	15.6	0.06
8446.384	O I	0.048	–6.5	28	0.03	5.9	8.6	0.06	6347.098	Si II	0.011	10.0	18.0	0.02
8446.755	O I	0.051	–5.5	28	0.03	5.1	8.6	0.07	6371.357	Si II	0.006	6.7	9.4	0.03
8498.052	Ca II	0.477	–8.7	40	0.10	8.3	19.8	0.48	6545.900	Mg II	0.008	6.5	9.0	0.03
									6717.688	Ca I	0.014	5.5	14.2	0.04
									7148.157	Ca I	0.015	5.8	9.2	0.05

minimum in the light curve confirms this event. Considering the solar case, large flares erupt near emerging magnetic flux regions, when old and new magnetic structures interact with one another, and the level of flare activity can remain high during many days. Similarly, on two RS CVn type stars, HK Lac (Catalano & Frasca, 1994) and HR1099 (Zhai et al. 1994), new spotted regions were noticed in light curves after strong optical flares. Our results give another clear evidence for the connection between a flare eruption and changes in the surface spot structure on other stars but the Sun.

5. The flare on October 26, 1996

The flare was seen as a narrow emission in He I D_3 and an increased emission in Ca II 8498 Å. As in the flare in July 1995, the helium emission was red-shifted and asymmetric, with two narrow components in the profile (Fig. 11). No broad components have been observed. A decrease of the emission in both lines during two hours is seen well in three subsequent exposures. The energy released in the flare is presented in Table 4. Other lines retained their quiescent shapes. The most probable explanation of the observed emission is a late stage of the flare decay.

6. Conclusions

From the analysis of the simultaneous observations of the very active RS CVn-type star II Peg, carried out in chromospheric and photospheric lines in 1994–1996, the following results have been obtained:

1. A strong correlation of the strength of the He I D_3, Ca II K and Ca II 8498 Å emissions with the spot position on the stellar disk has been revealed. An analysis of this correlation has suggested a two-component structure in the chromosphere of II Peg, similar

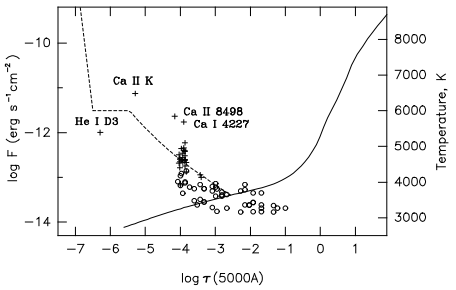

Fig. 8. Fluxes of the emissions that appeared in the line cores at the maximum of the flare on July 22, 1995 versus optical depths of formation of the line cores, τ_{5000}, calculated from the LTE model with $T_{\rm eff}$=4600 K, log g=3.2, [M/H]=-0.4 (solid line) updated by the semi-empirical chromosphere model (dashed line, Short et al. 1998). Crosses are the emissions with broad and narrow components, circles show the emissions with narrow components only.

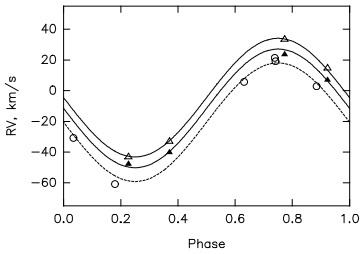

Fig. 9. Radial velocities of the emission in He I in 1995: circles are the quiescent emission, triangles are the two Gaussians fitted to the narrow components of the emission observed during the flare on July 19–23, 1995. The orbit deduced from the photospheric lines is shown with dashed lines. The best fits to the He I velocities are shown with solid lines.

to that in the corona. An *active* component which consists of the plages overlying the spots is hot and dense enough to give a moderate quiescent emission in helium lines from the upper chromosphere. A *nonactive*, cool component, which is the rest of the chromosphere of lower temperature, results in a quiescent absorption in helium lines. The nonactive component is found to be stable for years, while the active component is changeable on various time scales. It increased in emission during 1994–1996 indicating the growth of the general activity level of II Peg.

2. Two subsequent flares in July 1995 were observed. The first flare, on July 19–20, 1995 was identified in the He I D_3 line which appeared as an asymmetric, red-shifted, narrow emission. Some excess of the emission in the Ca II K line was seen as well. The development of the flare took a few hours and decay lasted two days. The subsequent flare, on July 21–23, 1995 was the strongest flare ever observed in the optical lines. At the the

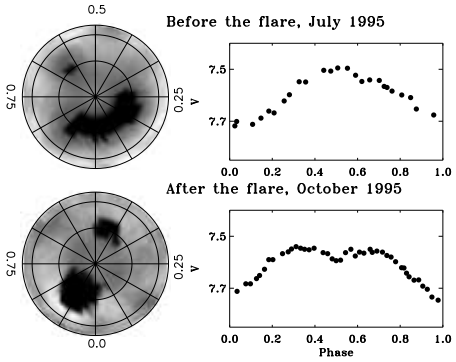

Fig. 10. The surface images and light curves for the times before and after the strong flare on July 19–23, 1995. As is suggested, the flare occured concurrently with the radical change of the spot structure on the stellar surface.

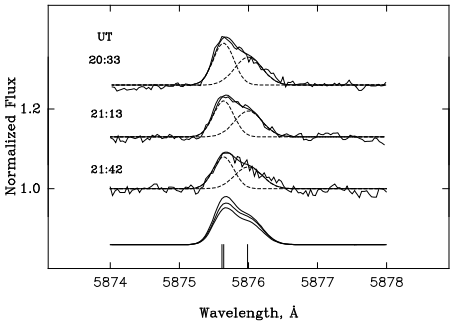

Fig. 11. Profiles of He I D_3 on October 26, 1996 (see the notation in Fig. 4.

Table 4. The energy released in the flare on October 26, 1996 in the He I D_3 and Ca II 8498 Å lines caculated with d=42.3 pc (π=0.″02362). ΔT is the exposure time.

HJD 2450000+	ΔT (s)	EW (Å)	F (erg s^{-1}cm^{-2})	E (erg s^{-1})
		He I D_3		
383.3612	2400	0.077	$2.72\cdot10^{-13}$	$5.83\cdot10^{28}$
383.3846	2400	0.068	$2.40\cdot10^{-13}$	$5.15\cdot10^{28}$
383.4092	960	0.058	$2.05\cdot10^{-13}$	$4.31\cdot10^{28}$
		Ca II 8498 Å		
383.3612	2400	0.170	$5.87\cdot10^{-13}$	$1.26\cdot10^{29}$
383.3846	2400	0.164	$5.67\cdot10^{-13}$	$1.22\cdot10^{29}$
383.4092	960	0.156	$5.40\cdot10^{-13}$	$1.16\cdot10^{29}$

maximum of the flare, in addition to the narrow emission components, broad blue-shifted emissions appeared in He I and Ca II K and in the cores of many strong absorption lines. The narrow, red-shifted emissions have been attributed to downflows in the active region, and the broad, blue-shifted emissions have been regarded as indications of upward motions of heated plasma within the flare volume through the process of the explosive chromospheric evaporation.

3. From the radial velocity curve of the He I emission the location of the radiating matter has been deduced. It appeared to be related to the largest active region which was seen in the stellar image. The flare occurred concurrently with the break of the extended group into two well separated spots.

4. On October 26, 1996 another flare was observed in three spectra, as narrow emissions in the He I and Ca II 8498 Å lines but without development in other lines. It was concluded to be a late stage of a flare decay.

Acknowledgements. We thank our referee, Dr. T. Ayres, for very useful comments and numerous corrections which improved the paper. Nordic Optical Telescope is operated on the island of La Palma jointly by Denmark, Finland, Iceland, Norway, and Sweden, in the Spanish Observatorio del Roque de los Muchachos of the Instituto de Astrofisica de Canarias.

References

Berdyugina S.V., Berdyugin A.V., Ilyin I., Tuominen I., 1998b, A&A 340, 437 (Paper 2)
Berdyugina S.V., Jankov S., Ilyin I., Tuominen I., Fekel F.C., 1998a, A&A 334, 863 (Paper 1)
Berdyugina S.V., Tuominen I., 1998, A&A 336, L25
Bopp B.W., Noah P.V., 1980, PASP 92, 333
Bopp B.W., Talcott J.C., 1980, AJ 85, 55
Byrne P.B., Doyle J.G., Brown A., Linsky J.L., Rodonó M., 1987, A&A 180, 172
Byrne P.B., Lanzafame A.C., Sarro L.M., Ryans R., 1994, MNRAS 270, 427
Byrne P.B., Panagi P.M., Lanzafame A.C., et al., 1995, A&A 299, 115
Byrne P.B., Abdul Aziz H., Amado P.J., et al., 1998, A&AS 127, 505
Catalano S., Frasca A., 1994, A&A 287, 575
Doyle J.G., Butler C.J., Byrne P.B., Rodonó M., Fowles W., 1989a, A&A 223, 219
Doyle J.G., Byrne P.B., van den Oord G.H.J., 1989b, A&A 224, 153
Doyle J.G., Kellett B.J., Byrne P.B., et al., 1991, MNRAS 248, 503
Doyle J.G., van den Oord G.H.J., Kellett B.J., 1992, A&A 262, 533
Fisher G.H., 1987, ApJ 317, 502
Gunn A.G., Doyle J.G., Mathioudakis M., Houdebine E.R., Avgoloupis S., 1994, A&A 285, 489
Haisch B., Strong K.T., Rodonó M., 1991, ARA&A 29, 275
Hamann F., Persson S.E., 1992, ApJS 82, 247
Hartmann L., 1982, ApJS 48, 109
Henry G.W., Newsom M.S., 1996, PASP 108, 242
Huenemoerder D.P., Ramsey L.W., 1987, ApJ 319, 392
Huenemoerder D.P., Ramsey L.W., Buzasi D.L., 1990, CSSS 6, 236
Mathioudakis M., Doyle J.G., Avgoloupus S., et al., 1992, MNRAS 255, 48
Mewe R., Kaastra J.S., van den Oord G.H.J., Vink J., Tawara Y., 1997, A&A 320, 147
Mohin S., Raveendran A.V., 1993, A&A 277, 155
Montes D., Fernández-Figueroa M.J., De Castro E., Sanz-Forcada J., 1997, A&AS 125, 263
Osten R.A., Brown A., Ayres T.R., 1998, In: Donahue R.A., Bookbinder J.A. (eds.) APS Conf. Ser. 154, The Tenth Cambridge Workshop on Cool Stars, Stellar Systems, and the Sun. ASP, San Francisco, CD-1540
Rodonó M., Byrne P.B., Neff J.E., et al., 1987, A&A 176, 267
Rucinski S.M., 1977, PASP 89, 280
Short C.I., Byrne P.B., Panagi P.M., 1998, A&A 338, 191
Tagliaferri G., White N.E., Doyle J.G., et al., 1991, A&A 251, 161
Vogt S.S., 1981, ApJ 247, 975
Zhai D.S., Foing B.H., Cutispoto G., et al., 1994, A&A 282, 168

Paper IX

Berdyugina, S. V., Berdyugin, A. V., Ilyin, I., Tuominen, I. 1999, "The active RS Canum Venaticorum binary II Pegasi. IV. The spot activity cycle", A&A 350, 626

Astron. Astrophys. 350, 626–634 (1999)

ASTRONOMY AND ASTROPHYSICS

The active RS Canum Venaticorum binary II Pegasi

IV. The spot activity cycle⋆

S.V. Berdyugina[1], **A.V. Berdyugin**[1,2], **I. Ilyin**[1], **and I. Tuominen**[1]

[1] Astronomy Division, University of Oulu, P.O. Box 3000, 90401 Oulu, Finland
[2] Tuorla Observatory, University of Turku, Väisäläntie 20, 21500 Piikkiö, Finland

Received 21 May 1999 / Accepted 26 August 1999

Abstract. A total of 6 new surface images of II Peg obtained for the years 1997 and 1998 confirms the recently revealed permanent active longitude structure. The lower limit of the active longitudes' lifetime is now extended up to 25 years. A new "flip-flop" phenomenon, redefined as a switch of the activity between the active longitudes, has started in summer of 1998. It coincides reasonably well with the moment predicted from the activity cycle of the star. This confirms definitely the cyclic behaviour of the activity of II Peg we recently discovered. Therefore, we assign numbers to the cycles of 4.65 yr since the earliest photoelectric observations of II Peg and define the active longitudes as "odd" and "even" corresponding to odd and even numbers of cycles. With such a definition, in late 1998 the 7th cycle began and the "odd" active longitude became more active. From the analysis of the spot area evolution within the active longitudes we conclude that the activity cycle is developed as a rearrangement of the nearly constant amount of the spot area between the active longitudes. We discuss the "flip-flop" phenomenon as a tracer of stellar activity and the role of the unseen secondary in establishing the cycle.

Key words: stars: activity – stars: imaging – stars: individual: II Peg – stars: late-type – stars: starspots

1. Introduction

II Peg (HD 224085) is one of the most active RS CVn stars, which shows significant photometric variability due to rotational modulation of cool spots (Henry et al. 1995, and references therein). The presence of cool spots on its surface is proved by the observations of TiO bands in its spectrum, which is not compatible with the spectral classification of the star as K2 IV (Vogt 1981; Huenemoerder & Ramsey 1987; Neff et al. 1995, Berdyugina et al. 1998a, hereafter Paper 1).

Recently, we started an extensive study of II Peg with the surface imaging technique. We determined a set of important parameters for surface imaging: projected rotational velocity, inclination, effective temperature, surface gravity, microturbulence and orbital parameters (Paper 1). We obtained 9 surface images of the star for 1992–1996 and found two active longitudes migrating in the orbital reference frame and showing effect of switching of the activity (Berdyugina et al. 1998b, Paper 2). The active longitudes have been confirmed by a new analysis of the published photometric data on a time scale of 23 years (Berdyugina & Tuominen 1998, hereafer BT). Also, it was found that the switching of the activity is periodically repeated with an activity cycle of about 4.65 years. A new cycle was expected to start in the beginning of 1999. Actually, as we show in the present paper, it started about half a year earlier. We noticed also that dramatic spot redistributions during the cycle can follow by strong flares observed in optical chromospheric lines (Berdyugina et al. 1999, Paper 3).

The main aim of the present paper is to confirm the predicted cyclic spot evolution on II Peg with new surface maps and give a review of the collected images and results. We present and analyse new observations obtained in 1997 and 1998 and obtaine 6 new stellar images (Sects. 2 and 3). Also, we test the stability of the images to the choice of the spectral lines and demonstrate that the obtained maps are free from systematic errors (Sect. 3). We discuss a total of 15 images of the star covering 7 years and show that the systematic pattern in the spot evolution of II Peg is a real phenomenon (Sect. 4).

2. Observations

II Peg was observed with the SOFIN échelle spectrograph on the Nordic Optical Telescope (NOT) in June, August, December of 1997 and in July, October and November of 1998. The data were acquired with the 2nd camera equipped with a CCD detector of 1152×298 pixels, yielding a wide spectral range (in 14 orders) of approximately 5500–8500 Å. For all observing runs the projected slit width was set to be $0\farcs5$ on the sky, providing a spectral resolving power $\lambda/\Delta\lambda \approx 83\,000$. With this setup, the dispersion at 6170 Å was 37 mÅ per pixel. A typical exposure time of $\approx 1^{\rm h}$ achieved a signal-to-noise ratio of more than 150

Send offprint requests to: S.V. Berdyugina (sveta@ukko.oulu.fi)

⋆ Based on observations collected at the Nordic Optical Telescope (NOT), La Palma, Spain; the 1.25 m telescope of the Crimean Astrophysical Observatory, Ukraine; the Phoenix 10 robotic telescope, APT Observatory, Arizona, USA.

Table 1. Spectroscopic observations used for surface imaging.

HJD 2450000+	Orbital phase	S/N	HJD 2450000+	Orbital phase	S/N
June 1997			*August 1997*		
617.6806	0.8814	290	676.7282	0.6626	260
618.7228	0.0364	160	677.7530	0.8150	140
619.6771	0.1784	225	678.7238	0.9594	200
620.6808	0.3276	315	679.7437	0.1111	230
621.6632	0.4737	305	680.7487	0.2605	180
622.7006	0.6280	265	681.7498	0.4094	160
623.7048	0.7773	250	682.7518	0.5584	230
624.6663	0.9203	350	683.7525	0.7072	170
625.6828	0.0715	290			
626.6972	0.2223	310			
627.6799	0.3685	310			
December 1997			*July 1998*		
794.3299	0.1516	240	997.7040	0.3987	240
795.3688	0.3060	220	998.7229	0.5502	200
796.3837	0.4570	180	999.7124	0.6974	250
802.4199	0.3547	210	1000.6908	0.8429	210
804.3949	0.6484	70	1001.7000	0.9929	260
804.4928	0.6630	160	1002.6995	0.1416	230
805.3296	0.7874	170	1003.6988	0.2902	250
805.4564	0.8063	160	1004.7008	0.4392	250
806.3580	0.9403	170	1005.6942	0.5870	250
806.4635	0.9560	100	1006.6938	0.7356	80
807.3710	0.0910	150	1008.7060	0.0349	190
807.4000	0.0953	130	1009.7031	0.1831	200
			1010.6938	0.3305	145
October 1998			*November 1998*		
1088.4290	0.8887	300	1121.4835	0.8043	180
1089.4189	0.0359	350	1122.3434	0.9322	330
1090.4713	0.1924	350	1123.4634	0.0988	400
1091.4087	0.3318	420	1124.4759	0.2494	220
1092.4339	0.4843	180	1125.4884	0.3999	180
1093.4435	0.6344	200	1126.4836	0.5479	150
1094.4552	0.7849	320	1127.4852	0.6969	240

for most spectra. The spectra were reduced with the 3A software designed by Ilyin (1996). The reductions included bias and flat field corrections, wavelength calibration, and corrections for the motion of the Earth. Finally, the wavelengths were corrected for the orbital motion of the primary, using the parameters from Paper 1. All observations have been divided into 6 season sets and phased according to the orbital ephemeris from Paper 1, which is used throughout this paper:

$$\mathrm{T_{conj}} = \mathrm{HJD}2449582.9268 + 6.724333E \quad (1)$$

with the primary in the back at phase zero. Heliocentric Julian dates, orbital phases, and S/N ratios of the spectra used for surface imaging are presented in Table 1.

Supporting photometric observations were arranged for both years. In August–September 1997, observations were carried out with the photometer-polarimeter constructed by V. Piirola and installed on the 1.25 m telescope of the Crimean Astrophysical Observatory, Ukraine. The observations were made in the standard Johnson UBVRI system with HD 223925 as a comparison star. In other seasons of 1997/98, photometry was acquired with the Phoenix 10 robotic telescope, APT Observatory, Arizona, in the UBV bands with HD 224930 as a comparison star. The errors of the observations are typically about $0\overset{\mathrm{m}}{.}010$ or less. The observations are shown in Fig. 1 and given in Tables 2 and 3[1].

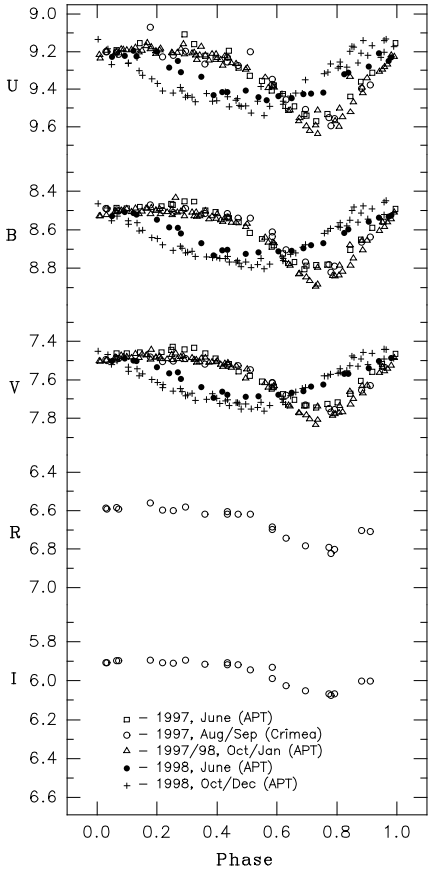

Fig. 1. New photometric observations of II Peg acquired in 1997/98. Phases were calculated with the orbital ephemeris given by Eq. (1).

[1] Tables 2 and 3 are available in electronic form at the CDS via anonymous ftp to cdsarc.u-strasbg.fr (130.79.128.5) or via http://cdsweb.u-strasbg.fr/Abstract.html

3. Surface imaging

3.1. The stability test

For compatibility with the previous 9 images of II Peg obtained in Paper 2, the 6160–6200 Å region was chosen for surface imaging. As inversion technique the Occamian approach was used (Berdyugina 1998). It was applied to the following lines: Fe I 6173 Å, 6180 Å, 6200 Å; Ni I 6175 Å, 6177 Å, 6178 Å; V I 6199 Å. The local line profiles were calculated in the same way as in Paper 2, with many blends from atomic and molecular lines. The stellar parameters used are from Paper 1.

Taking into account the experience of other authors in surface imaging (e.g. Rice & Strassmeier 1998), we made a test of stability of an image to the choice of spectral lines. For one season, June 1997, we calculated a set of images from individual lines of different spectral regions. To the lines mentioned above, 5 new lines were added: Ni I+Fe I+Y I 6191 Å, Ca I 6717 Å, Ti I 6743 Å, Ca I+Ni I 5857 Å, and Ti I 5866 Å. A total of 9 individual images is shown in Fig. 2. Although the used lines exhibit different amplitudes of variations because of their different temperature sensitivity, strength and blending, all the images show clear repeatability of the main spot features. The largest active region is well seen in all images at the same longitudes and latitudes, only its area varies from line to line: the stronger profile variations, the larger area of the region. The smaller spots in the opposite hemisphere are generally recovered with lower contrast because of their smaller effects in the profiles and, therefore, display more variations from line to line. Nevertheless, they are clearly seen in all the images on the same location.

Finally, we averaged the 9 images with equal weights and calculated the standard deviation map (Fig. 3). In some cases, this procedure can formally indicate real errors of the solution, especially when a large number of images is averaged. For a limited set of images obtained from limited sets of observations, it can give only low estimates of the errors. Talking about the errors of the individual maps, one must note that if only one line profile taken for a number rotational phases is used for surface imaging, a number of data points is generally several times fewer than a number of the image points. Then, most part of the image points is linearly dependent and, therefore, contains systematic errors which cannot be estimated. For more details, the reader is addressed to the discussion of the error analysis in surface imaging by Berdyugina (1998).

Naturally, the average map in Fig. 3 show the same spot features as the individual maps. However, comparing the averaged image with the individual images, one can notice that a certain part of the information on the shapes of the active regions and their contrast is lost after averaging. This happens because of averaging in the domain of results rather than in the domain of data. If all the lines (or even several of them) were inversed simultaneously, the information would not averaged but summed up. This is well seen when the averaged map in Fig. 3 is compared with the image for June 1997 in Fig. 4, which was obtained from the simultaneous inversion of 6 line profiles, as in Paper 2. The spot structure is generally the same, but the smaller spots are recovered with more certainty. Also, the standard deviation map in Fig. 3 and the error map in Fig. 4 for June 1997, which both includes low estimates of real errors, show generally the same values, about $\leq$100–200 K. Therefore, we conclude that the method and the lines used in Paper 2 result in the images which are accurate enough and stable to the choice of the spectral lines.

3.2. The new images

Fig. 4 displays 6 new images of II Peg for 1997 and 1998, error distributions over the stellar surface for each season, and fits to the line profiles. The images are shown with a coordinate grid of 30° in both latitudes and longitudes, and the inclination of the rotation axis of 60° as was adopted in the calculations. For all data sets, phase coverage was satisfactory. In all seasons the line profiles showed remarkable variability due to large spots which were recovered in the images. The quality of the fits to the line profiles corresponds on average to the S/N values of the spectra. Small systematic deviations which are seen sometimes in the profiles are generally caused by errors either in an average temperature of the visible hemisphere at a given phase or in the continuum normalization. These result mostly in differences of line strengths rather than line shapes.

To test independently the images, the photometric observations were not used as a constraint of the solution in the inversion but were compared with the photometric curves calculated from the images. For this purpose, as in Paper 2, we transformed the calculated flux variations to B–V variations using the semi-empirical calibration based on the temperature scale for G and K dwarfs and subgiants by Bell & Gustafsson (1989). We found that the restored spot distributions are in good agreement with the seasonal B–V colour variations (Fig. 5), although the above mentioned errors in the average temperatures at certain phases are also seen in the colour fits. The discrepancies of $0\overset{\mathrm{m}}{.}01$ in B–V give the estimates of the average temperature errors of about 20 K.

As in Paper 2, we determined the longitudes of the active regions, which were measured from the meridians crossing the centres of the active regions. The errors of such measurements depend on shapes and extents of the regions and temperature distributions within them. In most cases, the errors are less than 20°. This is accurate enough to see the spot migration over years. The longitudes are plotted versus time in Fig. 6 together with the data from Paper 2. One can see that the positions of the two active regions observed in 1997 and 1998 correspond well to the active longitude structure.

Also, for all 15 images presented in Paper 2 and in the present paper, we calculated the projected spot areas within the active regions, as fractions of the visible hemisphere. The spot area was considered as that of the temperature lower than 3800 K. This limit allows to account low contrast spot features which are certainly seen in the profiles. Variations of the limit of $\pm$100 K change the spot area by about $\pm$ 2%. The spot areas are also plotted versus time in Fig. 6. The evolution of the active regions from 1992 to 1998 is discussed in Sect. 4.

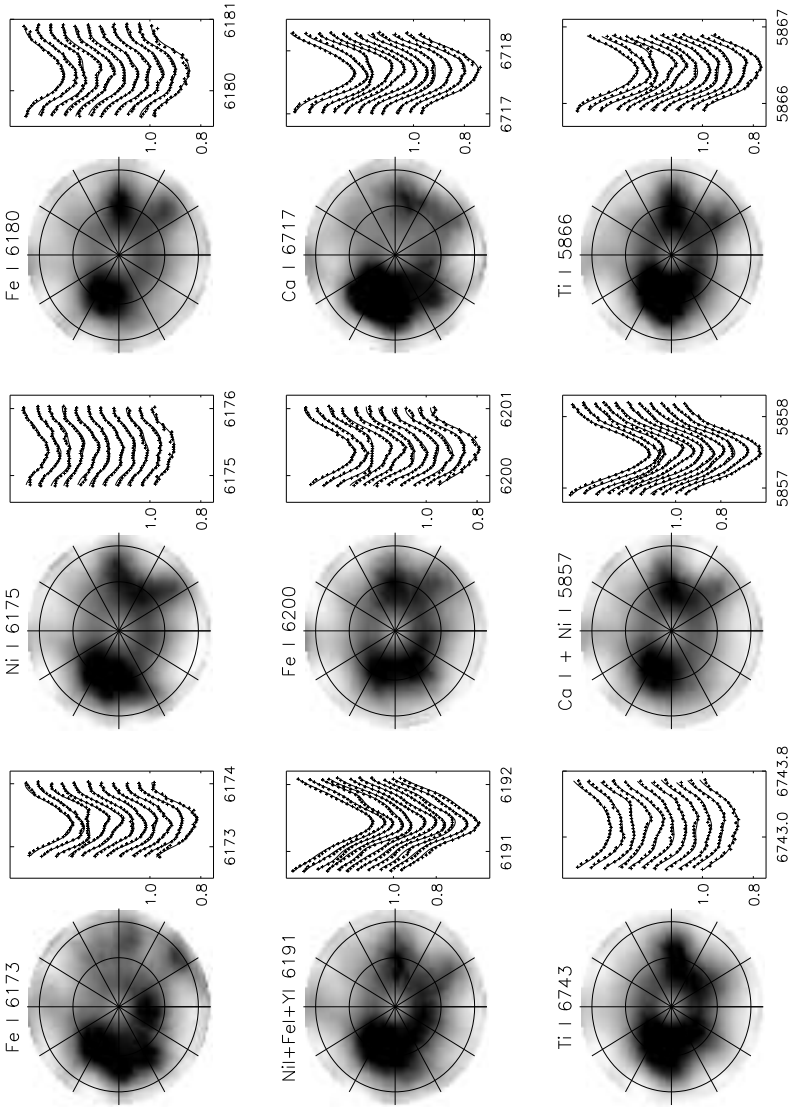

Fig. 2. Surface images of II Peg obtained from individual spectral lines for June 1997. The images are shown in the pole-on projection for better visibility of the high-latitude spots. Each map is supplied with the fit of the line profiles: observations are shown by crosses, while solid lines represent the solution. Phases of the profiles are given in Fig 4.

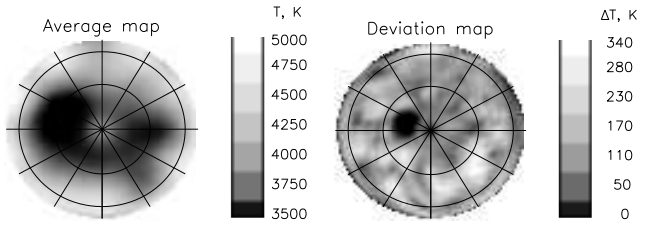

Fig. 3. The map averaged from the individual images shown in Fig. 2 and the standard deviation map. The smallest deviations are seen in the spot features.

4. Discussion

4.1. The active longitudes and the activity cycle

In 1992–1996 two high-latitude active regions dominated on the surface of II Peg and migrated in the orbital reference frame with a period of $6\overset{d}{.}7066$. This period is $0\overset{d}{.}0177$ shorter than the orbital one and was suggested to be the rotational period of the spots at a given latitude. In Paper 2 we interpreted the two active regions as a long-lived active longitude structure and confirmed it by a new analysis of the published photometric data (BT). The new images for 1997 and 1998 still show two high-latitude active regions which moved now close to the phases 0.25 and 0.75 in the orbital reference frame (Figs. 4 and 6). The positions of the regions correspond well to the active longitude structure and the rate of its migration. For now, this structure has been seen for 25 years.

In all 15 images for 1992–1998, one of the active regions is generally larger than the other one, and at some moments they change suddenly their size, as is seen from Fig. 6. For instance, in 1994, the formerly larger active region decreased in size, while the other increased and remained the larger one until the end of 1997. During these 4 years, the larger region moved from phase 0.1 to phase 0.75 (negative phase migration). The smaller region, on the opposite hemisphere, moved from phase 0.75 to phase 0.3 during the same time. In July 1998, the relative spot areas had again changed dramatically. The formerly large active region at phase 0.75 had decreased significantly and moved to lower latitudes, from 60° to 30°. Such low latitude spots have never been seen in the images before. At the same time, the formerly smaller region near phase 0.25 had increased in area at high latitudes (60°). The dramatic spot area redistribution caused a significant transformation of the light curve shape: the minimum moved from phase 0.75 to 0.5 and became much broader (Fig. 1).

The described spot evolution indicates clearly a *spot activity cycle* which is seen for the first time in stellar surface images. Its length of about 4 years coincides well with the value of 4.65 yr which was previously determined from the long-term photometric data by BT. The cycle is seen as the spot area evolution within the active longitudes, or as a switch of the activity from one longitude to the other. A total (double) cycle was defined as the time needed for the activity to return to the same active longitude (BT). In order to label the active longitudes, in Table 4 we give the starting times and subsequent numbers of the half-cycles since the first photoelectric observations of the star, in accordance with the results by BT. Then, we call the active longitudes "odd" and "even" as corresponding to odd and even numbers of half-cycles. In the half-cycle with an odd number, the "odd" active longitude shows the stronger activity, and vice versa. Such a nomination appears to be reasonable recalling that active regions are associated with magnetic field structures, generated by a dynamo operating in the convective envelopes. Large-scale, stable non-axisymmetric magnetic fields (two active longitudes) separated by half a period and symmetrically located in high-latitudes of both hemispheres relative to the equator can be antisymmetric in the polarity, as showed new model calculations made by Tuominen et al. (1999). For now, however, until we know the polarity of the active longitudes, the proposed designation is the only possibility to distinguish them.

The latest half-cycle, number 7, was expected to start in the beginning of 1999. However, the earliest spot redistribution was already noticed in June 1998 in the light curve and in July 1998 in the stellar image. Rapid changes in the structure of the active regions are seen when the three images for 1998 are compared. The now strongest high-latitude region at phase 0.3 (July 1998) then spreads out and seems to assemble smaller, lower latitude features, resulting in an extended group covering about 150° in longitudes (October 1998). Finally, the group consists of three moderate size spots which are spread over one hemisphere (November 1998). The images show that during about half a year the star is prepared to start a new half-cycle. This process takes several months, as was concluded by BT, and is accompanied by rapid and dramatic spot redistribution, as seen from the images. With the designation proposed above, the "odd" active longitude has become more active in the 7th cycle. As seen from Fig. 6, during the previous half-cycle, this active longitude was occupated by the smaller active region which displayed significant internal motions near the average location, in the phase interval of ± 0.15. This is factor of 3 larger the error of determination of spot positions. On the other hand, the positions of the larger active region on the "even" active longitude are scattered only within the phase interval of 0.05, which is comparable with the error. It would be interesting to see in the future is this difference stable and what determines such a difference.

Undoubtedly, the alteration of the relative spot areas in July 1998 corresponds to a new switch of the active longitudes, simi-

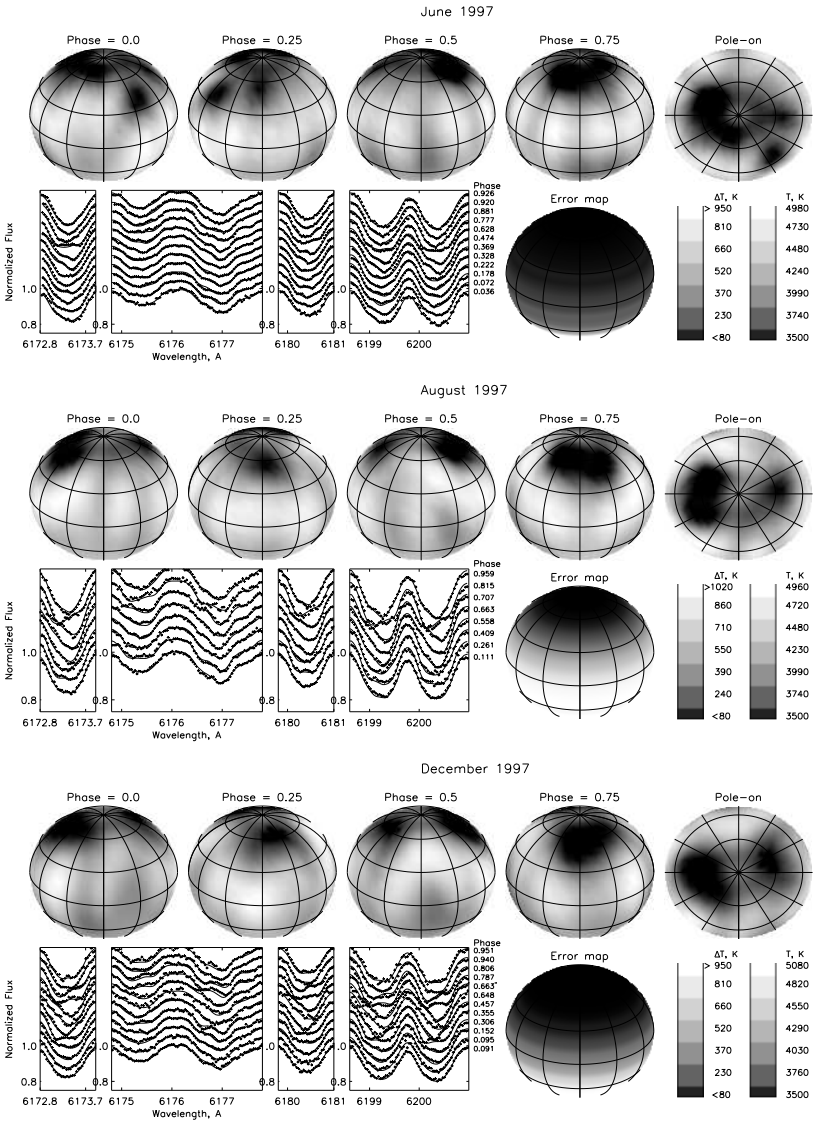

Fig. 4. Images of the primary of II Peg in the scale of the effective temperatures of the models, shown for four orbital phases and in the pole-on projection. The observed and calculated line profiles are shown by symbols and lines, respectively. The error maps show the distributions of the temperature errors, averaged in longitudes.

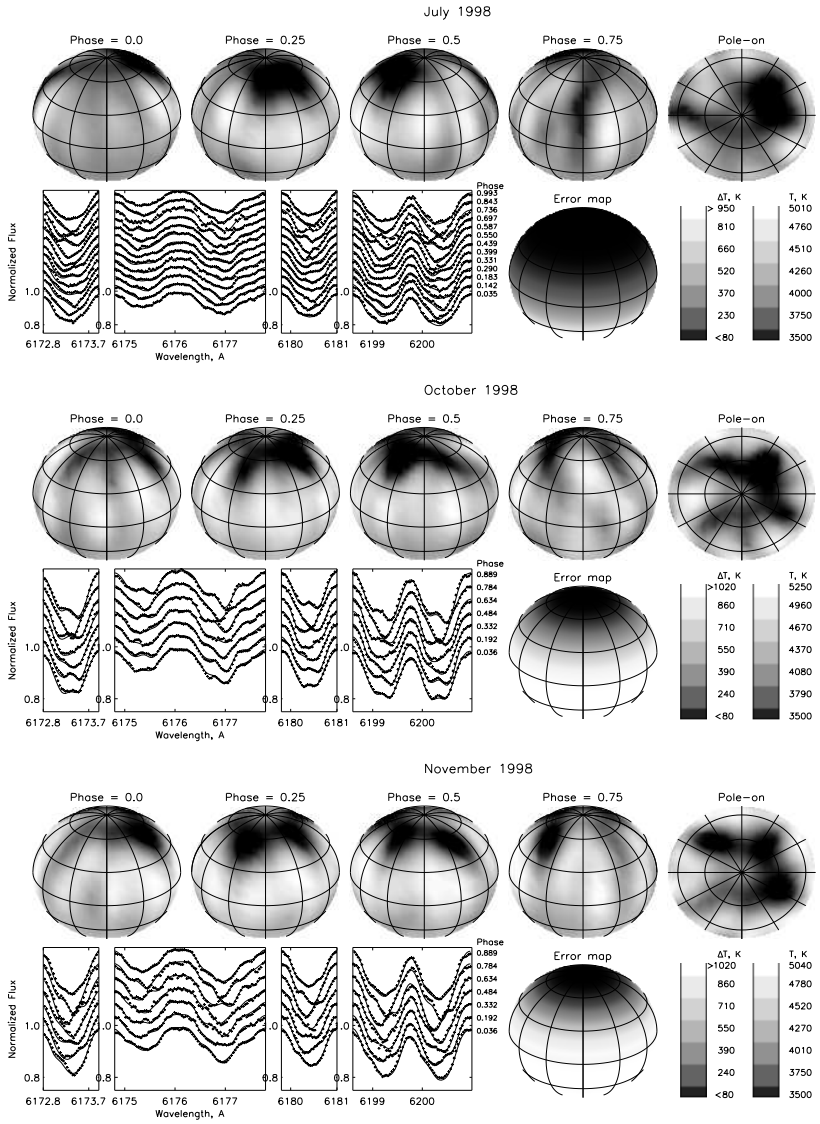

Fig. 4. (continued)

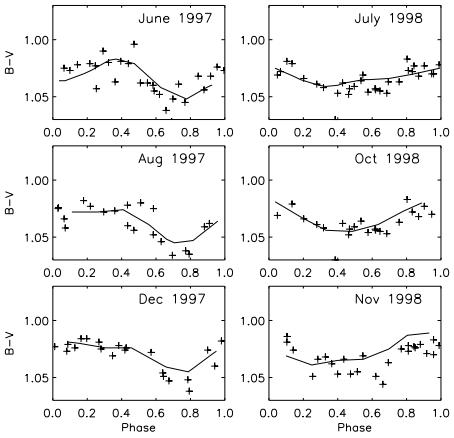

Fig. 5. B–V colour index variations: observed (crosses) and calculated from the images (lines).

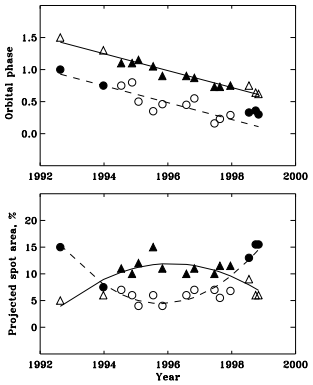

Fig. 6. The reconstructed spot longitudes and projected spot areas on II Peg versus time. Triangles and the solid line show the "even" active longitude, while circles and the dashed line present the "odd" active longitudes (see description in Sect. 4.1). Larger active regions are denoted by filled symbols.

lar to the event of 1994 (Fig. 6). It started only half a year earlier than was predicted from the previous observations. Such a coincidence confirms definitely the cyclic behaviour of the activity of II Peg we discovered (BT). Therefore, the switching events can be confidently regarded as tracers of the stellar activity cycles.

One must stress again that the spot activity cycle on II Peg is seen as the spot area evolution within the active longitudes. If total spot area is considered, it is approximately constant during the cycle (see Fig. 6). Then, the cycle is developed as a rearrangement of the nearly constant amount of the spot area. Such spot redistribution was earlier suspected by e.g. Henry et al. (1995) from their analysis of photometric data of RS CVn stars. They noticed that the mean brightness of most stars remains roughly constant, while maximum brightness increases and minimum brightness drops and the amplitude of variations increases. Such a behaviour is possible only if the constant amount of the spot area is symmetrically redistributed between two stellar hemispheres, or, as we show, between two active longitudes. So, the presence of two active longitudes on the stellar surface seems to be of the utmost importance for the establishment of the activity cycle on II Peg and other similar stars.

4.2. The "flip-flop" phenomenon

A *shift* of the concentrated part of spot-activity exactly to the other side of stellar surface was called a "flip-flop" phenomenon. It was found from photometric observations for the extremely rapidly rotating single late-type giant FK Com (Jetsu et al. 1991). A *switch* of the activity between the active longitudes which we discovered on II Peg (Paper 2) results actually in the same photometric behaviour as for FK Com. As seen from the images (Fig. 4) and the light curves (Fig. 1), while the spots keep their positions at approximately the same longitudes during 1997/98, the light minimum has shifted by about –0.25 in phase within only half a year or less. It cannot be explained by the spot drift in the orbital reference frame, since this is several times slower. The only reason of the shift is the *evolution of the relative spot areas* within the active longitudes, as seen from the images. Later on, the light curve minimum is expected to move closer to phase 0.25 and, then, drift in the orbital reference frame to phase 0.75 during the next 4 years as it did in the previous half-cycle. Therefore, no actual significant spot shift for a short time is needed to explain the 0.5 phase shift of the light minimum in the "flip-flop" phenomenon. Thus, the switch of the activity between the active longitudes due to relative spot area evolution (as in Fig. 6) is a more suitable definition of the "flip-flop" phenomenon at the present time.

It is very important that the "flip-flop" phenomenon is no longer a rare and unpredictable event observed for only one star. Recently, a new analysis of published long-term photometric

Table 4. The cycles of the activity of II Peg

Cycle Number	JD2400000+	Year
1	41050	1971.25
2	42750	1975.92
3	44450	1980.58
4	46150	1985.25
5	47850	1989.88
6	49550	1994.54
7	51250	1999.20

observations revealed such a behaviour to be typical for other RS CVn-type stars as well (BT). Moreover, the "flip-flop" is a cyclic phenomenon. This is distinctly confirmed by the present new images of II Peg. We consider it to be a new tracer of activity cycles on spotted stars as was suggested by BT, and we intend to study how it correlates with other, traditional tracers.

4.3. An effect of the secondary

We noted already in the previous papers that the active longitudes have no preferable orientation with respect to the line connecting the stellar centres in the binary. In other words, rotation of spots is generally not synchronized with the orbital motion, at least at the high latitudes where the spots appear. Nevertheless, the largest active region is always seen in the hemisphere which faces the secondary. The region migrates during a cycle from orbital phase 0.25 to phase 0.75 crossing the central meridian at phase 0.0. The switching between the active longitudes results in a shrinkage of the region near phase 0.75 and expansion of the region near 0.25 which then migrates again in the same direction. One can suppose that such a behaviour is caused by the secondary component in the binary. It affects the magnetic activity of the primary and probably plays a significant role in the "magnetic" synchronization of the stars and perhaps in establishing the activity cycle of the primary.

5. Conclusions

Using new high-resolution and high signal-to-noise ratio spectroscopic observations carried out in 1997–1998, we obtained 6 new surface images of II Peg. The surface imaging was applied to several neutral metal lines simultaneously, with the Occamian approach as the inversion technique. We tested the stability of the images to the choice of spectral lines and showed that *the images are free from the systematic errors*.

We found that two high-latitude active regions continued to dominate the images in 1997 and 1998. The positions of the active regions correspond well to the previously found two active longitudes separated by about 180°. Their lifetime is now extended up to 25 years, taking into account earlier photometric data.

Switching of the dominating activity between the active longitudes ("flip-flop" event) has started in summer of 1998, which is in good agreement with the moment predicted from the activity cycle. This confirms the cyclic behaviour of the activity of II Peg we have discovered (BT). The new stellar images have shown for the first time how the star was preparing to start a new cycle. This process took several months and was accompanied by rapid and dramatic spot redistribution.

We numbered the activity half-cycles of 4.65 yr since the earliest photoelectric observations of the star. Also, we labeled the active longitudes as "odd" and "even" which correspond to odd and even numbers of half-cycles. In the half-cycle with an odd number, the "odd" active longitude shows the stronger activity, and vice versa. Such a designation is helpful for distinguishing the active longitudes before we know their other properties. The 7th half-cycle has begun in late 1998.

From the analysis of the spot area evolution within the active longitudes we concluded that the activity cycle is developed as a rearrangement of *the nearly constant amount of the spot area* between the active longitudes.

We confirmed that the largest active region on the surface of II Peg shows the tendency to be closer to the secondary component of the binary. The secondary seems to affect the magnetic activity of the primary and play a significant role in the "magnetic" synchronization of the stars and, perhaps, in establishing the activity cycle.

Acknowledgements. We thank our referee, Dr. K.G. Strassmeier, for his valuable comments and suggestions and Dr. R. Duemmler for useful discussion and proposed corrections. Inversions were carried out on the Cray C94/128 supercomputer in the Center of Scientific Computing (Espoo, Finland). Data from VALD and SIMBAD have been used in the paper. This research was partly supported by grants from the Centre for International Mobility (CIMO), Finland.

References

Bell R.A., Gustafsson B., 1989, MNRAS 236, 653
Berdyugina S.V., 1998, A&A 338, 97
Berdyugina S.V., Tuominen I., 1998, A&A 336, L25 (BT)
Berdyugina S.V., Jankov S., Ilyin I., Tuominen I., Fekel F.C., 1998a, A&A 334, 863 (Paper 1)
Berdyugina S.V., Berdyugin A.V., Ilyin I., Tuominen I., 1998b, A&A 340, 437 (Paper 2)
Berdyugina S.V., Ilyin I., Tuominen I., 1999, A&A, in press (Paper 3)
Byrne P.B., Lanzafame A.C., Sarro L.M., Ryans R., 1994, MNRAS 270, 427
Henry G.W., Eaton J.A., Hamer J., Hall D.S., 1995, ApJS 97, 513
Huenemoerder D.P., Ramsey L.W., 1987, ApJ 319, 392
Ilyin I.V., 1996, Licentiate Dissertation, University of Oulu
Jetsu L., Pelt J., Tuominen I., Nations H., 1991, In: Tuominen I., Moss D., Rüdiger G. (eds.) The Sun and Cool Stars: activity, magnetism, dynamos. IAU Coll. 130, Lect. Not. Phys. vol. 380, Springer, Berlin, p. 381
Neff J.E., O'Neal D., Saar S.H., 1995, ApJ 452, 879
Rice J.B., Strassmeier K.G., 1998, A&A 338, 972
Tuominen I., Berdyugina S.V., Korpi M., Rönty T., 1999, In: Ferriz Mas A. (ed.) Stellar Dynamos: Non-Linearity and Chaotic Flows. ASP Conf. Ser., v. 178, p. 195
Vogt S.S., 1981, ApJ 247, 975

Paper X

Berdyugina, S. V., Ilyin, I., Tuominen, I. 1999, "The long-period RS Canum Venaticorum binary IM Pegasi. I. Orbital and stellar parameters", A&A 347, 932

Astron. Astrophys. 347, 932–936 (1999)

ASTRONOMY AND ASTROPHYSICS

The long-period RS Canum Venaticorum binary IM Pegasi

I. Orbital and stellar parameters⋆

S.V. Berdyugina, I. Ilyin, and I. Tuominen

Astronomy Division, University of Oulu, P.O. Box 3000, FIN-90401 Oulu, Finland

Received 30 April 1999 / Accepted 21 May 1999

Abstract. New high-resolution and high signal-to-noise ratio spectroscopic observations carried out in 1996–1997 are analysed. A total of 85 new high quality radial velocity measurements are used for determining the new orbital parameters: T_{conj}=HJD2450342.883+24.64880E, e=0.0, γ=–14.09 km s^{-1}, K_1=34.39 km s^{-1}. A model atmosphere analysis of the averaged spectrum of the star has yielded a self-consistent set of fundamental parameters of the primary component: $T_{\rm eff}$=4450 K, log g=2.4, [M/H]=0.0, ξ_t=1.6 km s^{-1}, v sin$i$=26.5 km s^{-1}. The primary is found to be a typical K2 III giant with the mass of about 1.5 $M_\odot$ which has undergone the first convective mixing on the Red Giant Branch ([C/H]=–0.32, [N/H]=0.30, C/N=1.15). The unspotted V magnitude of the star of $5\overset{\rm m}{.}55$ is estimated from the observed variations of the TiO band and quasi-simultaneous photometry. Combining all parameters, the radius and inclination of the primary as well as a probable spectral class of the secondary are estimated.

Key words: stars: abundances – stars: activity – stars: binaries: spectroscopic – stars: fundamental parameters – stars: individual: IM Peg – stars: late-type

1. Introduction

IM Pegasi (HD 216489) is a long-period ($24\overset{\rm d}{.}6$) single-line spectroscopic binary classified as an RS CVn type star by Hall (1976). It appears to have a circular orbit and almost synchronized rotation. The spotted K2 II-III primary shows significant light curve variations with the maximum amplitude in the V band of $0\overset{\rm m}{.}3$ (Strassmeier et al. 1997). IM Peg also shows rotational modulation of the Ca II infrared triplet, Hα, and Mg II h&k emission (Huenemoerder et al. 1990, Dempsey et al. 1993, 1996). From a single spectropolarimetric measurement, the magnetic field was clearly detected on the star by Donati et al. (1997).

The present paper is the first part of our study of the star. Here, we present our observations from 1996 and 1997 and determine new orbital elements and stellar parameters with better accuracy than those previously obtained. These new parameters are used in our subsequent papers where we study the spot distribution on the stellar surface with the surface imaging technique and chromospheric activity of the star.

Send offprint requests to: S.V. Berdyugina (sveta@ukko.oulu.fi)

⋆ based on observations collected at the 2.6 m telescope of the Crimean Astrophysical Observatory, Ukraine and the Nordic Optical Telescope (NOT), La Palma, Spain

2. Observations and data reduction

In 1996 spectroscopic observations were carried out with the coudé spectrograph on the 2.6 m telescope of the Crimean Astrophysical Observatory. The spectra were obtained with the 1st camera equipped with a CCD detector SDS 9000, Photometrics GmbH of 1024×400 pixels. With the slit of $0\overset{''}{.}4$ and dispersion of 65 mÅ/pix a resolving power of about 40 000 was achieved. The covered spectral range was about 60 Å centered at 6170 Å. Two exposures of ≈20 min were typically obtained, that provided the signal-to-noise ratio of an individual exposure of about 250.

In 1997 the star was observed with the SOFIN échelle spectrograph fed by the 2.56 m Nordic Optical Telescope (NOT), La Palma, Canarias. The data were acquired with the 2nd camera equipped with a CCD detector of 1152×298 pixels. Two échelle frames centered at 6180 Å and 7055 Å almost completely covered the spectral range of approximately 5500–8500 Å. For all observing runs the projected width of the slit was set to be $0\overset{''}{.}5$ on the sky, providing a spectral resolving power $\lambda/\Delta\lambda \approx 83\,000$. With this setup, the dispersion at 6170 Å was 37 mÅ/pix. A typical exposure time of 15 min achieved a signal-to-noise ratio of about 200 for most spectra.

The reduction of the SOFIN data, described by Ilyin (1997), included bias, scattered light, and flat-field corrections, extraction of spectral orders, and wavelength calibration. The latter is obtained with a thorium-argon comparison spectrum. Finally, the wavelengths were corrected for the Earth's motion. The Crimean spectra were reduced similarly except for the steps specifically relating to the échelle spectra. The Julian dates of all spectroscopic observations are given in Table 1.

3. Parameters of the orbit

A total of 85 new observations were used to determine new orbital parameters. The radial velocities were measured by cross-

Table 1. Radial velocities data

HJD 2450000+	RV, km s^{-1}	ref	HJD 2450000+	RV, km s^{-1}	ref	HJD 2450000+	RV, km s^{-1}	ref	HJD 2450000+	RV, km s^{-1}	ref
320.3855	–29.820	1	409.1188	16.604	1	624.6155	–28.805	2	683.7237	16.456	2
324.4004	–49.804	1	410.2835	19.110	1	624.6230	–28.651	2	683.7322	16.635	2
325.4121	–50.194	1	412.1521	16.648	1	625.6353	–20.295	2	735.5340	1.061	2
326.3850	–46.690	1	413.1524	15.327	1	625.6435	–20.273	2	735.5446	0.963	2
327.4263	–42.358	1	414.1480	6.116	1	626.6567	–11.539	2	736.5674	–8.222	2
331.3644	–8.045	1	415.1713	2.093	1	626.6624	–11.330	2	737.3925	–15.473	2
348.2273	–49.210	1	417.1289	–16.450	1	627.6452	–2.943	2	794.2832	–45.070	2
353.2663	–33.140	1	418.1573	–21.981	1	627.6518	–2.845	2	795.3332	–40.677	2
357.3160	0.928	1	420.1373	–39.040	1	676.6828	–5.390	2	795.3449	–40.762	2
359.2699	14.473	1	421.1315	–44.218	1	676.6902	–5.308	2	796.3377	–34.745	2
360.2654	17.094	1				677.7337	3.437	2	797.3047	–27.500	2
364.3888	10.661	1	617.7301	–42.261	2	677.7404	3.533	2	797.3911	–26.930	2
365.4010	1.563	1	618.6913	–45.753	2	678.7014	10.141	2	797.4123	–26.954	2
376.2793	–43.734	1	618.7026	–45.926	2	678.7074	10.209	2	802.3858	12.943	2
401.1248	–41.540	1	619.7147	–48.013	2	679.7178	15.642	2	804.3108	19.978	2
402.1285	–37.521	1	620.6375	–48.207	2	679.7239	15.556	2	804.3199	19.818	2
403.1255	–27.474	1	620.6452	–48.145	2	680.7042	19.285	2	805.3023	20.061	2
404.1280	–18.953	1	621.7066	–46.026	2	680.7103	19.239	2	805.3078	20.083	2
405.1257	–9.814	1	621.7164	–45.820	2	681.6908	20.580	2	806.3119	18.387	2
406.1570	–4.296	1	622.6684	–41.673	2	681.6968	20.506	2	806.3244	18.527	2
407.1349	7.009	1	623.6625	–35.783	2	682.6949	19.589	2			
408.2645	11.931	1	623.6702	–35.710	2	682.7010	19.666	2			

References (ref): 1 – Crimean observations, 2 – SOFIN observations.

correlating the observed spectra with the synthetic spectra calculated with appropriate atmospheric parameters. Such a procedure was successfully applied to e.g. II Peg observations by Berdyugina et al. (1998), where the zero-point velocity of the SOFIN spectrograph of about 0.3 km s^{-1} for the end of 1996 was estimated. From the SOFIN data we used spectra of seven orders which were free from the Earth atmosphere absorption. No systematic velocity trend among orders was found. The accuracy of the RV measurements averaged from the orders was about 0.15 km s^{-1}, while for the Crimean observations it was about 0.8 km s^{-1}. The measurements are presented in Table 1. Earlier radial velocity measurements of IM Peg, 20 RVs from Harper (1920, 1935) and 19 RVs from Oláh et al. (1998), were used in the period determination. So, the available data presently consist of 125 values spanning from 1919 to 1997.

For our purpose we used the program FOTEL3 developed by Hadrava (1995), which is able to deduce the orbital period value together with other parameters for both circular and eccentric orbits. The first step was to determine new values of the period P and eccentricity e. A first solution was found for all radial velocity measurements with equal weights. The fit allowed different γ-velocities for different data sets: γ(Harper)=–13.14±0.38 km s^{-1}, γ(Oláh et al.)= –13.31±0.37 km s^{-1}, γ(Crimea)=–14.88±0.20 km s^{-1}, γ(SOFIN)=–14.09±0.04 km s^{-1}. The period and eccentricity values were found to be $24^{\rm d}.64880\pm0^{\rm d}.00005$ and 0.006±0.007, respectively. In comparison to the recently published values of P and e by Oláh et al. (1998), the new value of the period is more accurate, and that of the eccentricity is one order less. Such a small value of the eccentricity can be ignored for the present, and the orbit can be considered as circular.

Table 2. Orbital elements

Element	Value
P, days	24.64880±0.00005
e	0.006±0.007
K$_1$, km s^{-1}	34.42±0.06
$a_1 \sin i$, R$_\odot$	16.76±0.04
f_1(m), M$_\odot$	0.1042±0.0006
T$_{\rm conj}$, HJD	2450342.883±0.007
γ, km s^{-1}	–14.09±0.04

The accuracy of the data sets is rather different and the new SOFIN measurements are significantly more accurate. For this reason, we assumed the period from the all-data solution and the eccentricity to be zero and found the best solution from the SOFIN data only. The solution is given in Table 2, and the measurements phased with the ephemeris

$$\mathrm{T_{conj}} = 2450342.883 + 24.64880E \quad (1)$$

are shown in Fig. 1. The epoch corresponds to the conjunction with the primary in the back. This ephemeris is used throughout this paper for all observations.

4. Stellar parameters

4.1. $T_{\rm eff}$, log g, and metallicity

For determining atmospheric parameters of the primary, the 53 SOFIN spectra were averaged, and the resulting spectrum with

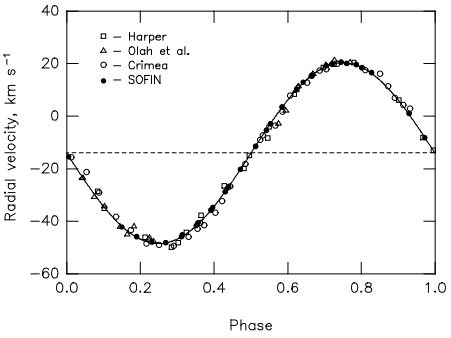

Fig. 1. Radial velocity measurements phased with the new ephemeris $T_{conj} = 2450342.883 + 24.64880\,E$. The solution from Table 2 is shown as a solid line. The γ-velocities of the sets are reduced to the SOFIN value.

S/N≈1000 covering almost all the region from 5500 Å to 8500 Å was used in the analysis. The spot contribution to the averaged spectrum was found to be insignificant. The effective temperature $T_{\rm eff}$, surface gravity $\log g$, metallicity [M/H], and microturbulence $\xi_{\rm t}$ are determined as a self-consistent set of parameters using the synthetic spectra calculations.

A list of atomic line parameters for a given wavelength region was obtained from VALD (Piskunov et al. 1995). It was checked by comparison of the calculated spectrum with the observed one of a slow rotating normal giant β Gem (K0 IIIb), as was done in our recent analysis of the other active star II Peg (Berdyugina et al. 1998). A great number of molecular lines have been added to the list, since their presence in spectra of cool giants is quite noticeable. Stellar model atmospheres used are from Kurucz (1993). A code used for the synthetic spectrum calculations is described in detail by Berdyugina (1991).

Estimates of the projected rotational velocity obtained by different authors are somewhat scattered: 24 km s^{-1}(Ottmann et al. 1998), 25±1 km s^{-1}(Donati et al. 1997), 25.6±1 km s^{-1}(De Medeiros & Mayor 1995), 28.2±1 km s^{-1}(Fekel 1997). Possessing the excellent quality observed spectrum, we have obtained our own estimates of the rotational velocity, $v \sin i$, and macroturbulence, $\zeta_{\rm t}$. A number of strong and well isolated lines were studied with the Fourier transform. The following values were determined: $v \sin i$=26.5±0.5 km s^{-1} and $\zeta_{\rm t}$=4.0±0.5 km s^{-1}.

To determine the atmospheric parameters, a total of about 20 lines of Fe I, Fe II, Si I, Si II, and Ca I were chosen. Assuming first an appropriate pair of $T_{\rm eff}$ and $\log g$, we produced a set of curves (loci of the best fitted lines) on a diagram of metal abundance, [M/H], as a function of microturbulence $\xi_{\rm t}$ (Fig. 2). The curves intersected in a narrow region which provided an initial estimate for a pair of [M/H] and $\xi_{\rm t}$. With these values, a set of loci on a diagram of $T_{\rm eff}$ versus $\log g$ was calculated. Their intersection gave an initial estimate of a pair of $T_{\rm eff}$ and

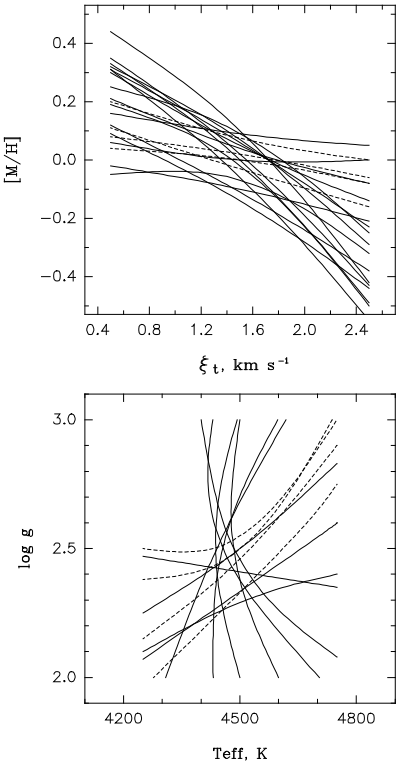

Fig. 2. Diagrams for the self-consistent determination of the atmospheric parameters of the primary of IM Peg: metallicity [M/H], microturbulence $\xi_{\rm t}$ (*upper panel*) and effective temperature $T_{\rm eff}$, surface gravity $\log g$ (*low panel*). Curves present loci of the best fitted spectral lines with the synthetic spectrum: Fe I, Si I and Ca I (solid curves) and Fe II and Si II (dashed curves). The curves intersect in narrow regions which provide estimates of the parameters. These are presented in Table 3.

$\log g$ values. After a few iterations a self-consistent set of the parameters was found. These are presented in Table 3.

With the atmospheric parameters obtained, the primary of IM Peg is classified as K2 III, in reasonable agreement with the previous classification. It has solar metallicity with an uncertainty of ±0.1 (assuming for the Sun Fe/H=7.55, Si/H=7.50, Ca/H=6.32). The spectrum of the star was recently analysed by Ottmann et al. (1998). As a temperature indicator they used the Hα line which is significantly disturbed by the variable emission, as seen in our spectra. This resulted in remarkable over-

Table 3. Atmospheric parameters of the primary of IM Peg

Parameter	Value
$T_{\rm eff}$, K	4450±50
$\log g$	2.4±0.1
[M/H]	0.0±0.1
$\xi_{\rm t}$, km s^{-1}	1.6±0.2
$\zeta_{\rm t}$, km s^{-1}	4.0±0.5
$v \sin i$, km s^{-1}	26.5±0.5

estimation of the effective temperature and, as a consequence, the surface gravity.

4.2. The CNO abundances

The abundances of the CNO-elements are good indicators of the stellar evolution. In the spectrum of IM Peg many appropriate features can be found for determining the carbon and nitrogen abundances: rotational transitions in vibrational bands of the CN ($A^2\Pi - X^2\Sigma$) red system and C_2 ($A^3\Pi_g - X^3\Pi_u$) Swan system. For the oxygen abundance, no good features can be found: high-excitation lines of O I are obviously disturbed by the active chromosphere, and the line of [O I] at 6363 Å is blended too much. Therefore, it is reasonable to assume that the oxygen abundance in IM Peg is of the solar value (O/H=8.92, Lambert 1978) and we can then determine the abundances of C and N.

For the synthetic spectra calculations we used the line lists provided by Davis & Phillips (1963) and Phillips & Davis (1968). The band oscillator strengths and molecular constants were obtained from the RADEN database (Kuznetsova et al. 1993). Lower level excitation energies and rotational intensity factors were calculated with formulae from the book by Kovacs (1969). The number densities of CN and C_2 were calculated under the assumption of their dissociative equilibrium with a great number of atoms and molecules. The procedure used for determining the CNO abundances is similar to that described by Berdyugina (1993).

The carbon abundance, [C/H]=–0.32, was determined from the head of the C_2 (0,1) band at 5633 Å. The feature is blended partly by atomic lines, but the accuracy of about 0.1 for the abundance can be easily achieved. The nitrogen abundance, [N/H]=0.30, was determined from the heads of the CN (2,0) and (3,1) bands and numerous features from those bands in the regions 7895–7900 Å and 8039–8065 Å. The internal accuracy of the nitrogen abundance is about 0.05. The resulting C/N ratio of 1.15 corresponds well to an evolved giant which has undergone the first convective mixing in its atmosphere on the Red Giant Branch.

4.3. Fundamental parameters of the components

The value of the unspotted V magnitude of the star is important for estimating the fundamental parameters of the binary components. It can be determined from the variability of the TiO bands. The effective temperature of the primary is too high to show evidence of the TiO bands in the spectrum from the unspotted photosphere. Nevertheless, a noticeable depression due to TiO lines is seen at λ7054 Å, at the head of the strong band $\gamma(0,0)R_3$, that is typical for spotted G-K stars. The depth of the band correlates well with the V magnitude, in other words, with the spot visibility (Fig. 3). The quasi-simultaneous photometric observations used will be presented in our forthcoming paper. We suggest that the zero value of the central depth corresponds to the unspotted magnitude of the star, V_0. Then, from the linear regression fitted to the data we estimate V_0=5$^{\rm m}$.55±0$^{\rm m}$.05. It is close to the brightest maximum of V=5$^{\rm m}$.6 ever observed (Strassmeier et al. 1997). The value of V_0 should be corrected for the interstellar extinction, but the latter is expected to be of the same order as the uncertainty of V_0. Thus, with the parallax value of 0″.01033 from the Hipparcos Catalogue, an absolute magnitude M_V=0$^{\rm m}$.62 can be found. It is very close to the statistical value of 0$^{\rm m}$.5 for K2 III stars (Lang 1992). This is in good agreement with the newly determined atmospheric parameters of the primary.

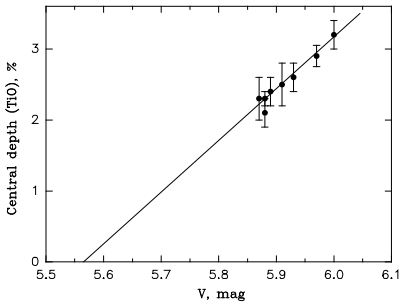

Fig. 3. The variation of the central depth of the TiO $\gamma(0,0)R_3$ band at 7054 Å with the V magnitude (dots with error bars). The line represents a linear regression fitted to the data and indicates the unspotted V magnitude of IM Peg when the depth of the TiO band is equal to zero.

The projected rotational velocity of 26.5 km s^{-1} and the photometric period of the star of 24$^{\rm d}$.39 (Strassmeier et al. 1993) result in the relation $R_1 \geq 12.7\,R_\odot$. This corresponds to the radius of a giant with a spectral class of K0–K2 III. From the mass function f_1(m) a mass-mass diagram for various combinations of masses and orbital inclination can be calculated (Fig. 4). Under the assumption that the stellar rotational axis is perpendicular to the orbital plane, one can estimate the masses of the binary components, the primary's radius and the inclination. Such an assumption is justified for synchronously rotating RS CVn binaries (Glebocki & Stawikowski 1995). The low limit of R_1 and the value of $\log g$=2.4±0.1 determine the probable range for the masses of the binary components. This range can be restricted from above by the upper limit of the secondary's mass. Since with present observing techniques the secondary is invisible at all wavelengths, its luminosity should be at least 100 times less than that of the primary, i.e. $M_V \leq 5^{\rm m}.6$. This corresponds to a G8 main sequence

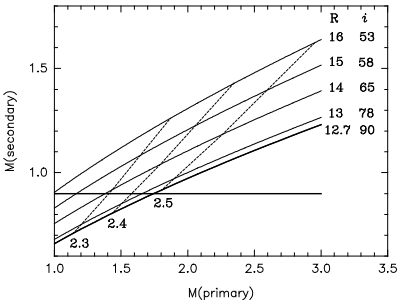

Fig. 4. The mass-mass diagram for IM Peg (in solar units). The thin solid curves are calculated for the fixed values of the radius of the primary and the inclination (numbers in the left). The dashed lines are loci of the primary with a fixed value of $\log g$ (numbers at the bottom). The probable parameters of the binary components are in the area restricted by the heavy solid lines with $R_1 > 12.7\ R_\odot$ and $M_2 < 0.9\ M_\odot$ and next to $\log g$=2.4

star with a mass of 0.9 $M_\odot$ (Lang 1992). Then, in the mass-mass diagram the probable range for all parameters is significantly reduced. With $\log g$=2.4±0.1 one can find the following values: $M_1/M_\odot$=1.5±0.2, $R_1/R_\odot$=13.3±0.6, $65^\circ \leq i \leq 80^\circ$, $M_2/M_\odot$=0.8±0.1. Note that the secondary's mass cannot be less than 0.7 $M_\odot$ because of the low limit of $\log g$. Therefore, it could be e.g. a K0 dwarf.

5. Summary

From new high-resolution and high S/N spectra of IM Peg, the following results have been obtained:

1. New orbital parameters have been determined, the ephemeris being improved: T_{conj} = 2450342.883 + 24.64880*E*, e=0.0, γ= –14.09 km s^{-1}, K_1=34.39 km s^{-1}.

2. A model atmosphere analysis of the spectrum of IM Peg has yielded a self-consistent set of fundamental parameters of the primary component: T_{eff}=4450 K, $\log g$=2.4, [M/H]=0.0, ξ_t=1.6 km s^{-1}. This corresponds to a K2 III star. The observed abundances of the carbon and nitrogen suggest that the primary has undergone the first convective mixing in its atmosphere on the Red Giant Branch.

3. An unspotted V magnitude of $5\overset{m}{.}55$ was estimated from the observed variation of the TiO band and quasi-simultaneous photometry. The absolute magnitude of the star of $0\overset{m}{.}62$ is found.

4. By combining all parameters, the radius R_1 = 13.3±0.6 $R_\odot$ and the inclination $65^\circ \leq i \leq 80^\circ$ of the primary have been estimated with the assumption that its rotational axis is perpendicular to the orbital plane.

5. The unseen secondary is believed to be a K0 main sequence star with a mass of about 0.8±0.1 $M_\odot$.

Acknowledgements. We thank the referee Dr. De Medeiros for valuable remarks. The Nordic Optical Telescope is operated on the island of La Palma jointly by Denmark, Finland, Iceland, Norway, and Sweden, in the Spanish Observatorio del Roque de los Muchachos of the Instituto de Astrofisica de Canarias. Data from RADEN, SIMBAD, and VALD have been used in the paper. This research was partly supported by grants from the Centre for International Mobility (CIMO), Finland, and by grants R2Q000 and U1C000 from the International Science Foundation, and by grant A-05-067 from the ESO and C&EE Programme.

References

Berdyugina S.V., 1991, Izv. Krymsk. Astrofiz. Obs. 83, 102
Berdyugina S.V., 1993, Astron. Lett. 19, 378
Berdyugina S.V., Jankov S., Ilyin I., Tuominen I., Fekel F.C., 1998, A&A 334, 863
Davis S.P., Phillips J.G., 1963, The Red System ($A^2\Pi - X^2\Sigma$) of the CN molecule. University of California Press, Berkely
Dempsey R.C., Bopp B.W., Henry G.W., Hall D.S., 1993, ApJS 86, 293
Dempsey R.C., Neff J.E., O'Neal D., Oláh K., 1996, AJ 111, 1356
Donati J.-F., Semel M., Carter B.D., Rees D.E., Cameron A.C., 1997, MNRAS 291, 658
Fekel F.C., 1997, PASP 109, 514
Glebocki R., Stawikowski A., 1995 Acta Astron. 45, 725
Hadrava P., 1995, FOTEL3 - user's guide. Astronomical Institute, Academy of Science, Ondrejov
Hall D.S, 1976, In: Fitch W.S. (ed.) Multiple Periodic Variable Stars. IAU Coll. 29, Reidel, Dordrecht, p. 287
Harper W.E., 1920, Publ. DAO 1, 203
Harper W.E., 1935, Publ. DAO 6, 251
Huenemoerder D.P., Ramsey L.W., Buzasi D., 1990, ApJ 350, 763
Ilyin I.V., 1997, Licentiate Dissertation, University of Oulu
Kovacs I., 1969, The rotational Structure in the Spectra of Diatomic Molecules. Academiai Kiado, Budapest
Kurucz R.L., 1993, Kurucz CD No. 13
Kuznetzova L.A., Pazyuk E.A., Stolyarov A.V., 1993, Russ. J. Phys. Chem. 67, 2046
Lambert D.L., 1978, MNRAS 182, 249
Lang K.R., 1992, Astrophysical Data. Springer-Verlag
De Medeiros J.R., Mayor M., 1995, A&A 302, 745
Oláh K., Marik D., Houdebine E.R., Dempsey R.C., Budding E., 1998, A&A 330, 559
Ottmann R., Pfeiffer M.J., Gehren T., 1998, A&A 338, 661
Phillips J.G., Davis S.P., 1968, The Swan System of the C_2 Molecule. University of California Press, Berkeley
Piskunov N.E., Kupka F., Ryabchikova T.A., Weiss W.W., Jeffrey C.S., 1995, A&AS 112, 525
Strassmeier K.G., Bartus J., Cutispoto G., Rodonò M., 1997, A&AS 125, 11
Strassmeier K.G., Hall D.S., Fekel F.C., Scheck M., 1993, A&AS 100, 173

Paper XI

Berdyugina, S. V., Berdyugin, A. V., Ilyin, I., Tuominen, I. 2000, "The long-period RS Canum Venaticorum binary IM Pegasi. II. First surface images", accepted by A&A

A&A manuscript no.
(will be inserted by hand later)

Your thesaurus codes are:
06(08.09.1; 08.19.6; 08.01.2; 08.12.1; 08.09.2 IM Peg)

ASTRONOMY AND ASTROPHYSICS
June 13, 2000

The long-period RS CVn binary IM Pegasi

II. First surface images ⋆

S.V. Berdyugina[1], A.V. Berdyugin[1,2], I. Ilyin[1], and I. Tuominen[1]

[1] Astronomy Division, P.O. Box 3000, FIN-90014 University of Oulu, Finland
[2] Tuorla Observatory, University of Turku, Väisäläntie 20, FIN-21500 Piikkiö, Finland

Received 10 April 2000 / Accepted 25 May 2000

Abstract. New high-resolution, high signal-to-noise ratio spectroscopic observations and UBV photometry carried out in 1996-1999 were analysed with the surface imaging technique. A total of 8 images of IM Peg was obtained for the first time. A huge high-latitude active region was found to dominate the stellar surface and decreased in area during the period of the observations. At the same time, on the opposite hemisphere (in longitudes), smaller spots were developing. The spots were migrating in the orbital reference frame, the period of spot rotation being of $24\overset{\mathrm{d}}{.}73\pm0\overset{\mathrm{d}}{.}02$. The spots constitute two active longitudes on opposite stellar hemispheres, similar to other RS CVn stars. The evolution of the spot areas within the active longitudes indicates a stellar activity cycle, during which one active longitude dominates the stellar activity, to be about 6.5 years. Then, a total cycle, comprising two consecutive periods of activity of both active longitudes, is about 13 years. In 1999, the activity switched to the other active longitude. This declared the beginning of a new (half-) cycle.

Key words: binaries: spectroscopic – stars: imaging – starspots – activity – late-type – individual: IM Peg

1. Introduction

We continue our study of the single-lined RS CVn-type binary IM Pegasi (HD 216489). In Paper 1 (Berdyugina et al. 1998) we presented a detailed analysis of the photospheric spectrum of the star and determined, with high accuracy, stellar and orbital parameters. Many of those parameters are of great importance for the present study – the surface imaging of the star.

For the last decade, the technique of stellar surface imaging was extensively used for studying cool active stars with temperature inhomogeneities, i.e. spots. The most recent and vast account of images has been given by Strassmeier (2000). According to this, 208 images for 53 cool stars of different types have been obtained to date. Despite this, the processes maintaining and governing the stellar activity are still far from being understood. There are various reasons for this, the most important is the short time span covered by images and large, seasonal, gaps between them. The number of images for a given star is often too small to draw conclusions about the stellar activity as a phenomenon. In our opinion, the most fruitful way is to maintain monitoring of the most prominent targets for reasonably long times with good seasonal coverage. This will result in a series of images which can be searched for spot evolution, long-lived structures, surface differential rotation, etc. Such a tactic has already resulted in fairly interesting results for a few stars (V711 Tau, Vogt et al. 1999; II Peg, Berdyugina et al. 1998, 1999; EI Eri, LQ Hya, see references in Strassmeier 2000). To date, these four stars are the best studied with the surface imaging technique, with the number of images more than 10 per star.

In spite of its long period ($24\overset{\mathrm{d}}{.}65$), we have chosen IM Peg as one of our targets for surface imaging monitoring because of its brightness ($\mathrm{V}=5\overset{\mathrm{m}}{.}6$) and rather prominent activity. The active component in this binary is a "normal" K2 III star with typical parameters for giants except the rapid rotation and chromospheric activity (see Paper 1). From time to time, generally since 1970, but more regularly since 1991, IM Peg was observed photometrically (see compilation by Strassmeier et al. 1997). In 1991, the star significantly reduced its mean brightness (by $0\overset{\mathrm{m}}{.}15$ in V) and, being at this level, demonstrated the largest ever observed amplitude of the variability in the fall of 1995 ($\Delta V=0\overset{\mathrm{m}}{.}36$). We started our spectroscopic observations 8 months later, in summer 1996, when the amplitude was still large ($0\overset{\mathrm{m}}{.}32$). Here, we present the first images of IM Peg for 4 years, 1996-1999, two images per year. We trace the spot evolution during the decrease of

Send offprint requests to: S.V.Berdyugina(sveta@ukko.oulu.fi)
⋆ based on observations collected at the Nordic Optical Telescope (NOT), La Palma, Spain; the 2.6 m and 1.25 m telescopes of the Crimean Astrophysical Observatory, Ukraine; the 2m telescope of the National Astronomical Observatory, Rozhen, Bulgaria.

Table 1. Spectroscopic observations used for surface imaging.

HJD 2450000+	Phase	S/N	HJD 2450000+	Phase	S/N	HJD 2450000+	Phase	S/N	HJD 2450000+	Phase	S/N
1996			*1997*			*1998*			*1999*		
320.3855	0.087	315	617.7301	0.151	310	997.6590	0.564	180	1325.7350	0.874	220
324.4004	0.250	210	618.6970	0.190	215	998.6667	0.605	275	1327.7438	0.956	155
325.4121	0.291	290	619.7147	0.231	240	999.6650	0.646	280	1328.7463	0.996	135
326.3850	0.331	360	620.6416	0.269	305	1000.6429	0.685	215	1329.7395	0.037	120
327.4263	0.373	265	621.7115	0.312	250	1001.6495	0.726	255	1330.7393	0.077	220
331.3644	0.533	400	622.6684	0.351	240	1002.6552	0.767	215	1331.7412	0.118	180
348.2273	0.217	295	623.6664	0.391	210	1003.6596	0.808	250	1332.7375	0.158	205
353.2663	0.421	310	624.6193	0.430	295	1004.6544	0.848	295	1333.7358	0.199	215
357.3160	0.586	370	625.6403	0.471	340	1005.6522	0.888	295	1383.7155	0.226	205
359.2699	0.665	350	626.6596	0.513	305	1006.6487	0.929	205	1384.7146	0.267	270
360.2654	0.705	430	627.6485	0.553	320	1008.6667	0.011	250	1385.7056	0.307	210
364.3888	0.872	360	676.6865	0.542	330	1009.6586	0.051	240	1386.7218	0.348	180
365.4010	0.914	305	677.7371	0.585	290	1088.5102	0.250	310	1387.7151	0.389	225
376.2793	0.355	395	678.7044	0.624	325	1089.3766	0.285	255	1388.7033	0.429	230
401.1248	0.363	410	679.7209	0.665	310	1090.4230	0.328	260	1389.7211	0.470	180
402.1285	0.404	390	680.7073	0.706	280	1091.3660	0.366	260	1390.7042	0.510	200
403.1255	0.444	380	681.6938	0.746	290	1092.3800	0.407	230	1391.6966	0.550	250
404.1280	0.485	400	682.6980	0.786	300	1093.3910	0.448	270	1392.6997	0.591	255
405.1257	0.525	300	683.7280	0.828	255	1094.4126	0.489	220	1393.6838	0.631	225
406.1570	0.567	420	735.5393	0.930	250	1095.5023	0.533	195	1394.7098	0.672	230
407.1349	0.607	405	736.5674	0.972	280	1096.5326	0.575	80	1443.5138	0.652	240
408.2645	0.653	360	737.3925	0.005	400	1097.5870	0.618	160	1444.5111	0.692	210
409.1188	0.687	420	794.2832	0.313	290	1121.4344	0.586	220	1445.5514	0.735	215
410.2835	0.734	270	795.3391	0.356	450	1122.4017	0.625	240	1447.5424	0.816	200
412.1521	0.810	410	796.3377	0.397	220	1123.3838	0.665	250	1449.5606	0.898	155
413.1524	0.851	190	797.3694	0.438	160	1124.3835	0.705	220	1471.6012	0.792	200
414.1480	0.891	425	802.3858	0.642	240	1125.3957	0.746	240	1472.6078	0.833	230
415.1713	0.933	295	804.3154	0.720	245	1126.4442	0.789	180	1473.6223	0.874	170
417.1289	0.012	350	805.3051	0.760	310	1127.4384	0.829	210	1475.5391	0.952	200
418.1573	0.054	300	806.3182	0.802	220				1481.2978	0.185	245
420.1373	0.134	240							1482.4048	0.230	250
421.1315	0.175	270							1483.2762	0.266	235
423.3231	0.263	110							1484.3012	0.307	205
									1485.2855	0.347	215
									1505.2851	0.158	200
									1509.3069	0.322	240

the amplitude of the photometric wave and find evidence for long-lived spot structure.

2. Observations

Spectroscopic observations were carried out in 1996 with the 2.6 m telescope of the Crimean Astrophysical Observatory and in 1997–1999 with the 2.56 m Nordic Optical Telescope (NOT), La Palma. The spectral resolving power $\lambda/\Delta\lambda$ in the region of the lines used for surface imaging (6180Å) was about 40 000 and 80 000, respectively. Other details of the quality of the observations with the two telescopes have been given in Paper 1. Additionally, in 1999, 5 spectra were obtained with the 2 m telescope of the National Astronomical Observatory, Rozhen, Bulgaria, with the resolving power of about 30 000.

In 1996, the observations were carried out in August-October (JD2450320–376) and November-December (JD245401–423). These provided two sets with a good phase coverage, 14 and 19 phases, respectively.

In 1997, the observations were carried out in June, August, October and December. We divided these observations into two slightly overlapping sets: June–October (JD2450617–737) and October–December (JD2450735–806). The first set has an excellent phase coverage (22 phases), while the second has a phase gap from 0.0 to 0.3.

In 1998, a total of 31 phases has been obtained in July, October and November. These constituted two overlapping sets: JD2450997–1094 and JD2451005–1127. This provided an acceptable phase coverage for both sets, with gaps of only about 0.2.

Table 2. Photometric observations

HJD 2450000+	Phase	U	B	V
663.4800	0.0047	8.232	7.262	6.055
667.5468	0.1696	8.152	7.195	5.997
668.4558	0.2065	8.119	7.169	5.969
669.4619	0.2473	8.093	7.141	5.952
672.4750	0.3696	8.022	7.058	5.876
675.4232	0.4892	8.000	7.051	5.872
676.4906	0.5325	8.021	7.068	5.880
677.4491	0.5714	7.990	7.050	5.860
679.4676	0.6533	8.000	7.050	5.860
680.4500	0.6931	8.010	7.060	5.870
681.4024	0.7318	8.050	7.090	5.900
684.3131	0.8499	8.100	7.130	5.950
695.3505	0.2976	8.050	7.120	5.930
696.3652	0.3388	8.050	7.110	5.910
698.3590	0.4197	8.030	7.080	5.890
699.3517	0.4600	8.000	7.050	5.870
700.3553	0.5007	8.020	7.060	5.880
704.4002	0.6648	8.030	7.070	5.880
705.2732	0.7002	8.020	7.070	5.880
706.3231	0.7428	8.040	7.080	5.900
709.3124	0.8641	8.120	7.170	5.970
714.3163	0.0671	8.210	7.260	6.060

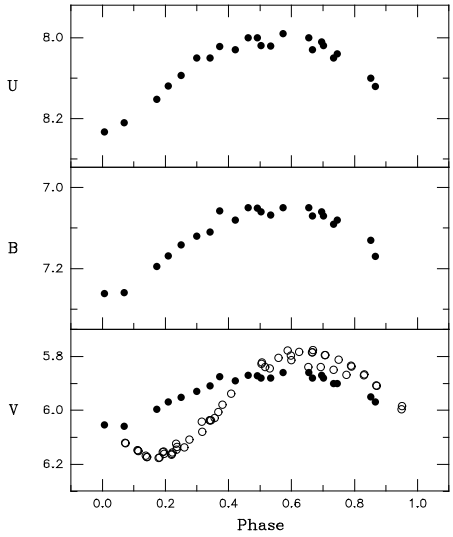

Fig. 1. UBV observations of IM Peg in August-September 1997 (dots; present paper) and in Nov-Dec 1996 (open circles; Strassmeier et al. 1999). The data are phased with the ephemeris given by Eq. (1).

In 1999, 36 phases had been obtained in the period from the end of May to the end of November. Again, we were not able to avoid overlapping because of missing important phases in some months. Two sets were created as follows: May–September (JD2451325–1449) and August–November (JD2451388–1509). In the second set, the observations from the NOT and Rozhen Observatory were combined, accounting for the different instrumental profiles.

All observations were phased according to the orbital ephemeris from Paper 1, which is used throughout this paper:

$$T_{conj} = 2\,450\,342.883 + 24.64880\,E \qquad (1)$$

with the primary in the back at phase zero. Heliocentric Julian dates, orbital phases, and S/N ratios of the spectra used for surface imaging are presented in Table 1.

Supporting photometric observations were arranged in August–September 1997 with the photometer-polarimeter installed on the 1.25 m telescope of the Crimean Astrophysical observatory (Piirola 1973). The observations were carried out in the standard UBV system with HD 216635 as a comparison star (U=$8^m.34$, B=$7^m.60$, V=$6^m.56$). The observations are presented in Table 2 and Fig. 1. For the fall of 1997 we used observations published by Strassmeier et al. (1999), while for other seasons no photometric observations have yet been published.

3. Surface imaging

3.1. Local line profiles

We have chosen the 6160–6200 Å region as the region for surface imaging of K giants and subgiants. It contains Fe I, Ni I and V I lines which are strong enough but not yet saturated and have different temperature sensitivities. We found that for proper temperature imaging, the combination of Ni I and V I lines is very useful, since their intensities change in opposite directions with changing temperature, and this strongly constrains the solution. These lines were previously used for surface imaging of the RS CVn-type star II Peg (Berdyugina et al. 1998, 1999).

A list of atomic line parameters was obtained from VALD (Piskunov et al. 1995, Kupka et al. 1999) for lines having a central depth of 1% or more. A number of molecular lines were included in the list. The line list was previously tested using the β Gem (K0 IIIb) spectrum as was reported by Berdyugina et al. (1998). A set of local line profiles for the temperature range of 3500–6000 K and ten limb angles on the stellar disk was calculated using the stellar atmosphere models by Kurucz (1993) and the parameters of the atmosphere obtained in Paper 1 and presented in Table 3. The instrumental profiles were approximated by the Gaussian functions with a width cor-

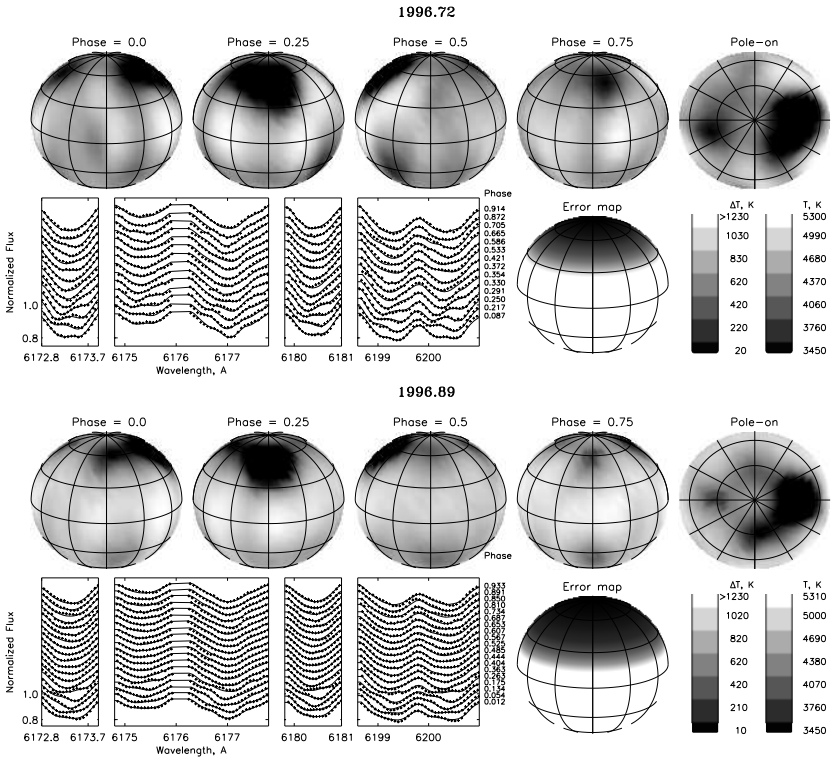

Fig. 2. Images of IM Peg for 1996–1999 shown for four orbital phases and also in the pole-on projection and fits to the line profiles (symbols are observations, and lines are calculations). The error maps show the distributions of the temperature errors, averaged in longitudes. Images are shown with a coordinate grid of 30° in both latitude and longitude and with the inclination of the rotation axis of 70° as was adopted in the calculations.

responding to the resolution of the given spectrograph. The code used for synthetic spectrum calculations was described in detail by Berdyugina (1991).

3.2. Images

For the inversion of the line profiles to the stellar images the Occamian approach was used (Berdyugina 1998). The approach does not use any artificial constraints for finding a unique and smooth solution. It allows also for a convenient estimation of the variances of the resulting solution. Recently, it was successfully used for surface imaging of II Peg (Berdyugina et al. 1998, 1999) and FK Com (Korhonen et al. 1999). In a recent paper (Berdyugina et al. 1999) we also tested the stability of the images to the choice of spectral lines. We showed that significant spot

Table 3. Atmospheric parameters of the primary of IM Peg used for surface imaging (from Paper 1).

Parameter	Value
$T_{\rm eff}$, K	4450
$\log g$	2.4
[M/H]	0.0
$\xi_{\rm t}$, km s^{-1}	1.6
$\zeta_{\rm t}$, km s^{-1}	4.0
$v \sin i$, km s^{-1}	26.5
i	70°

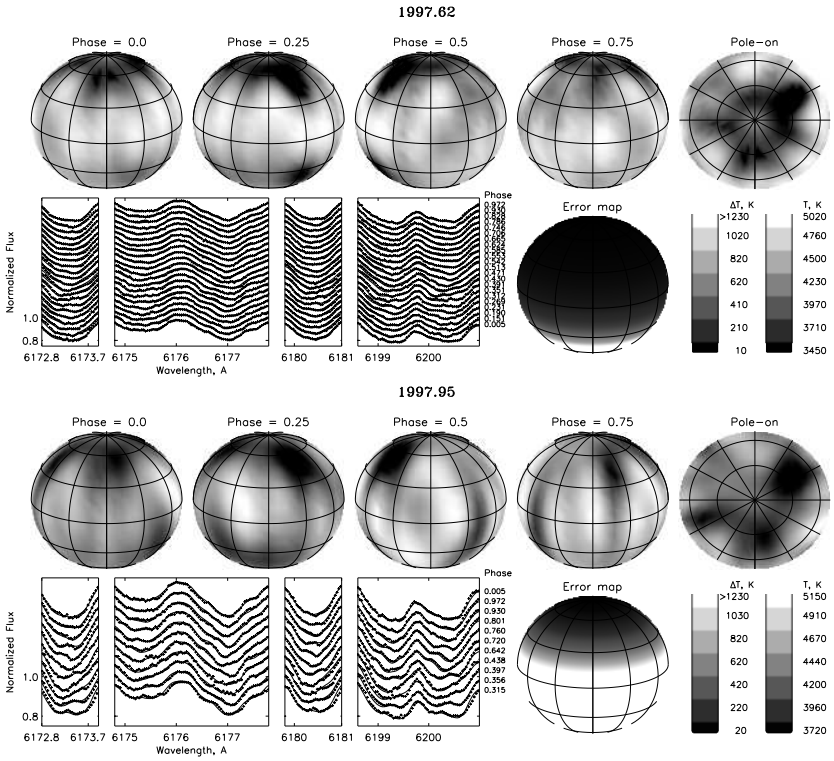

Fig. 2. (continued)

features are seen in all strong and temperature sensitive lines, and the best map is obtained when all lines are used in inversions simultaneously. Thus, we showed that our maps are free from systematic errors, and spots seen in the maps result from real spectral features observed in the line profiles rather than from misfits between models and observations.

A grid of $6^\circ \times 6^\circ$ on the stellar surface was used for integrating the local line profiles to normalized flux profiles. With a given set of stellar atmosphere models, the stellar image is considered as the distribution of effective temperature across the stellar surface. Obviously, the resulting temperature scale of the images is model dependent. To test the temperature scale of the images, we used our photometric observations for 1997 (Table 2) and those by Strassmeier et al. (1999) for 1996. Unfortunately, no photometry is published for the years 1998 and 1999. We calculated the B–V and V–R colour indices, transforming the temperatures to the colours with the calibration for evolved giants by McWilliam (1990). The calculated mean values and amplitudes of the colour indices were compared with the photometric observations.

Figure 2 displays images of IM Peg, error distributions over the stellar surface for each season, and fits to the line profiles. As was indicated, the images for the years 1997, 1998 and 1999 are partly overlapping in phases within a given season. This allowed us to obtain full-surface maps spanning a few months and, thus, to study the spot evolution on this time scale. We found that the temperature scales of the images and the spot distributions fit satisfactorily both mean values and amplitudes of the colour indices: V–R for 1996 and B–V for 1997 (Fig. 3). This provides an independent test of the images. A small difference between the observed and calculated colour indices for the

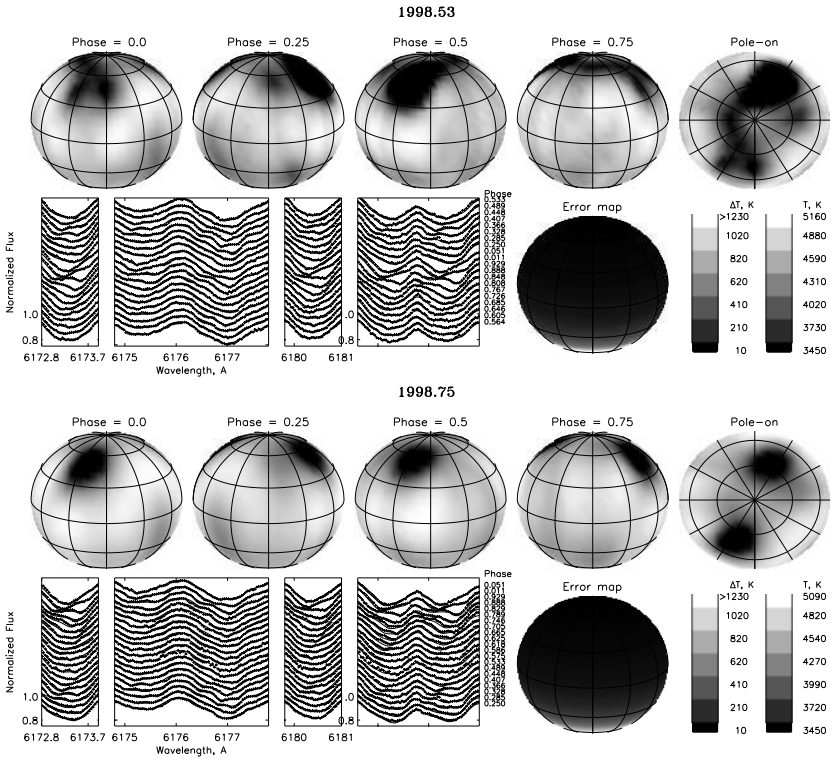

Fig. 2. (continued)

1996.89 image at the maximum brightness is caused probably by underestimating the contrast of the spot at phase 0.75. This spot is more prominent in the previous image, 1996.72.

As was mentioned, the Occamian approach supplies error estimates of the solution, which constitute lower limits of the true errors (see e.g. Berdyugina 1998). For high-quality observations (high signal-to-noise and large amount of observations), this estimates are comparable with the standard deviations, which can be determined if several maps obtained from different spectral lines are averaged (Berdyugina et al. 1999). This indicates the stability of the solution to external errors. The accuracy of the temperature values decreases toward lower latitudes (see Fig. 2). Thus, high-latitude spots are restored with better accuracy. Note, however, that for five images, the quantity of the observations used is quite sufficient for restoring even the equatorial regions where no spots were recovered. In those images the errors at the equator are of ∼200K and smaller in the upper latitudes.

4. Spot evolution

4.1. Spot parameters

We started our spectroscopic observations a few months after the largest amplitude in V-band was observed in the end of 1995. A huge active region at phase 0.25, seen in the first stellar image, 1996.72, seems to be the one which was responsible for the large amplitude. Since the photometric amplitude was slightly reduced during these months, the size of the region can be expected to have been even larger at its maximum. During the period of observations the size of the region has significantly diminished, while in the opposite hemisphere (in longitudes) smaller spots

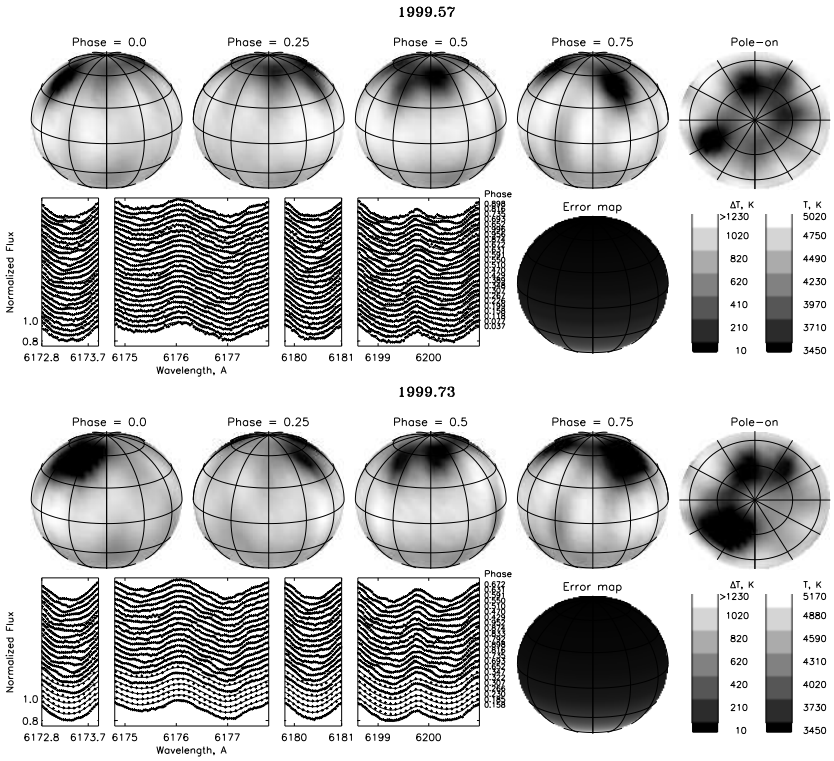

Fig. 2. (continued)

were constantly developing. Photometric observations for the seasons show a decrease of the amplitude in the V-band from $0^m.3$ in 1996 (Strassmeier et al. 1997, 1999) to $0^m.22$ in 1997 (our observations). Also, the brightness maximum decreased by $0^m.05$ (see Fig. 1). This clearly confirms the observed spot evolution. The light curve amplitude in 1998 should have been lower, however no photometric observations are available to us.

In Table 4 we present the spot parameters measured from the maps: phase, the moment of passing the central meridian and the projected spot area in percentage of the stellar disk area. Phases of spots were measured from the parabolic fits to minima of the temperature distribution averaged over the spot latitudes. The moments in Julian days were calculated from the phases with the ephemeris given by Eq. (1) as the closest times to the observations. Here, the central meridian corresponds to the conjunction when the primary is behind the secondary. Spot areas were measured as those with the temperature below 4000K. One must note also that spots appear in the latitude interval of 30°–75°, with spot centres from 45° to 63°.

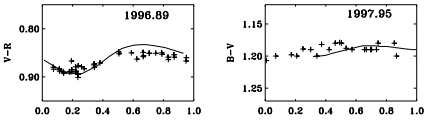

Fig. 3. Colour index variations: observed (crosses) and calculated from the images (lines).

Table 4. Spot parameters: φ - orbital phase, T - heliocentric Julian day at the moment of the spot passage through the central meridian minus 2450000, A - projected spot area in percentage of the stellar disk area.

Season		Spot 1	Spot 2	Spot 3
1996.72	φ	0.258	0.775	
	T	324.594	361.986	
	A	15.9	2.6	
1996.89	φ	0.258	0.742	
	T	423.189	410.470	
	A	15.1	1.6	
1997.62	φ	0.342	0.958	0.758
	T	622.450	736.229	682.001
	A	10.9	3.2	2.4
1997.95	φ	0.342	0.042	0.808
	T	794.991	738.299	806.478
	A	8.4	2.6	1.6
1998.53	φ	0.425	0.942	0.292
	T	994.228	1006.971	1089.544
	A	11.4	6.5	1.9
1998.75	φ	0.425	0.925	
	T	1092.823	1129.796	
	A	6.8	6.0	
1999.57	φ	0.508	0.825	0.425*
	T	1390.654	1324.521	1388.608
	A	2.6	6.2	1.3
1999.73	φ	0.525	0.858	0.408
	T	1391.073	1448.579	1388.189
	A	3.6	11.0	1.6

(*) In the 1999.57 image, even four spots can be distinguished, the 4th spot having the following parameters: φ=0.275, T=1384.911, A=1.3.

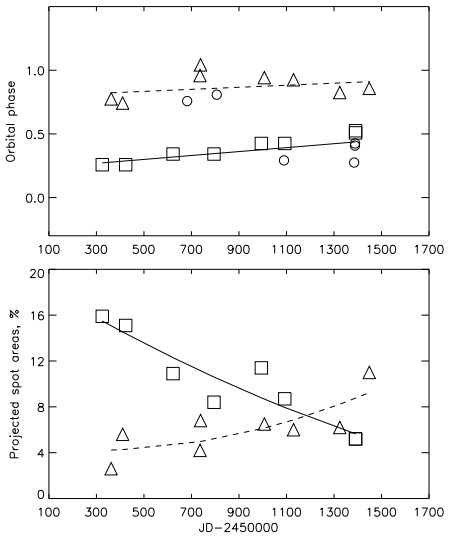

Fig. 4. Positions and projected areas of spots recovered in the images. Spot1, Spot2 and Spot3 from Table 4 are shown by squares, triangles and small circles, respectively. Active longitudes are shown by solid and dashed lines. In the low plot, the area of Spot3 was added to that of Spot1 or Spot2.

Note that the largest spot (Spot1, A=15.9%) has a surprisingly huge linear size, about $6.5\,R_\odot \times 10.5\,R_\odot$ with the radius of IM Peg being about $13\,R_\odot$ (Paper 1). This is only two times smaller than the absolute record (HD12545, K0III, Strassmeier 1999). It is clear that such large "solid" spots should gradually dissipate, as is seen in the images of IM Peg.

4.2. Active longitudes

In Fig. 4 we plot the phases and areas of the spots versus date (from Table 4) to see the spot migration and evolution. It is clearly seen that Spot1 and Spot2 are well separated by about half a period while Spot3 joins either Spot1 or Spot2. The spot positions clearly indicate two active longitudes on the stellar surface separated by about 180°, similar to other RS CVn stars (Berdyugina & Tuominen 1998; Berdyugina et al. 1999). During the period of our observations (1996-1999) the active longitudes slightly migrated to later phases in the orbital reference frame with an average rate of about $0\overset{\circ}{.}5\,\mathrm{day}^{-1}$. The average spot period is then $24\overset{\mathrm{d}}{.}73 \pm 0\overset{\mathrm{d}}{.}02$. This differs significantly from the photometric period of $24\overset{\mathrm{d}}{.}39$ given by Strassmeier et al. (1993) and a more recent long-term average of $24\overset{\mathrm{d}}{.}49$ presented by Strassmeier et al. (1997). However, one must note that seasonal values of the photometric period found in the literature vary within the interval from $24\overset{\mathrm{d}}{.}1$ to $25\overset{\mathrm{d}}{.}2$. This suggests strong variations of the spot distribution from season to season.

4.3. Activity cycle

If one looks at the spot area evolution within the active longitudes (lower panel in Fig. 4), more similarities to other RS CVn stars can be found. While in one active longitude the spot areas were decreasing during the observation period (Spot1), in the other they were gradually increasing (Spot2). The area of Spot3 was added to that of Spot1 or Spot2. In late 1998, the two active regions became almost the same in area and, shortly afterwards, in 1999, they altered in such a way that the dominating activity switched to the other active longitude (Spot2).

This effect has been first observed in the images of II Peg (Berdyugina et al. 1999) and discovered in photometric light curves of four other RS CVn stars (Berdyugina & Tuominen 1998). We suggested that the moment

of switching corresponds to the beginning of a new activity cycle and the time between two switches determines the length of the cycle. This was confirmed for II Peg. As for IM Peg, we probably traced about half of the cycle. Since the maximum spot area in the dominating longitude (Spot1) was expected to be near the end of 1995 (maximum observed light curve amplitude), the cycle length can be estimated to be as long as 6.5 years. Thus, this cycle probably started in the middle of 1992.

The years 1991 and 1992 were a remarkable time for IM Peg. It showed the smallest amplitude of variability and the faintest mean magnitude when compared with previous observations (see the light curves in Fig. 25 in Strassmeier et al. 1997). Two almost equal minima were observed at that time, one becoming significantly deeper afterwards. Such a light curve evolution suggests the estimate of the cycle of 6.5 yr to be rather reliable. One must note, however, that during the 6.5 yr cycle only one active longitude was dominating the activity. As was previously suggested, a *total cycle* of the stellar activity comprises two consecutive periods of activity of both active longitudes (Berdyugina & Tuominen 1998). This results in the total cycle length of IM Peg of about 13 years.

A close look at the light curves for the period from 1991 reveals another interesting fact. While the mean magnitude remains roughly constant, the maximum and minimum brightness increases and drops, respectively, almost symmetrically, and the amplitude of the variability increases. Such behaviour is possible only if a nearly constant amount of the spot area is symmetrically redistributed between two stellar hemispheres, namely between two active longitudes. Such a spot evolution is observed for many RS CVn stars. For II Peg, we showed that symmetric spot redistribution is a key process in establishing an activity cycle (Berdyugina et al. 1999). The same conclusion can be made now for IM Peg as well.

5. Conclusions

New high-resolution spectroscopic observations have been used for the first surface imaging of the visible component of the RS CVn binary IM Pegasi. With the Occamian approach as an inversion technique, several line profiles were simultaneously inverted, and a total of 8 stellar images for 1996-1999 were obtained. From the analysis of the images the following conclusions can be drawn:

1. Spots appear in high and mid latitudes, in the interval of 30°–75°, with centres between 45° and 63°.

2. A huge active region at phase 0.25 is seen in the first stellar image in 1996 with a linear size of about $6.5\,R_\odot \times 10.5\,R_\odot$. It significantly diminished during the period of the observations, while in the opposite stellar hemisphere (in longitudes) smaller spots were constantly developing. This active region has presumably existed since at least 1992, reaching its maximum area in the end of 1995.

3. The spots indicate two active longitudes separated by about 180°, which were constantly migrating to later orbital phases during the years of observations. The period of the spot rotation is estimated to be $24^{\rm d}.73 \pm 0^{\rm d}.02$.

4. In one active longitude, the spot areas decreased during the observation period, while in the other they gradually increased. In late 1998, the two active regions became almost the same in area and in 1999 the dominating activity has switched to the other active longitude. This indicated the beginning of a new activity cycle.

5. The length of the cycle, during which one active longitude dominates the activity of IM Peg, is estimated to be 6.5 years.

Acknowledgements. We are thankful to Dr. Klaus G. Strassmeier for the complete set of photometric observations of IM Peg, which he kindly made available for us, and for his valuable comments to the paper. We thank Drs. R. Duemmler, I. Iliev and L. Iliev for obtaining observations with the 2m telescope of the National Astronomical Observatory, Rozhen, Bulgaria. Also, we are thankful to Dr. R. Duemmler for his useful remarks to the manuscript. Inversions were carried out on the Cray C94/128 supercomputer in the Center of Scientific Computing (Espoo, Finland). The Nordic Optical Telescope is operated on the island of La Palma jointly by Denmark, Finland, Iceland, Norway, and Sweden, in the Spanish Observatorio del Roque de los Muchachos of the Instituto de Astrofisica de Canarias.

References

Berdyugina S.V., 1991, Izv. Krymsk. Astrofiz. Obs. 83, 102
Berdyugina S.V., 1998, A&A 338, 97
Berdyugina S.V., Berdyugin A.V., Ilyin I., Tuominen I., 1998, A&A 340, 437
Berdyugina S.V., Berdyugin A.V., Ilyin I., Tuominen I., 1999, A&A 350, 626
Berdyugina S.V., Ilyin I., Tuominen I., 1999, A&A 347, 932 (Paper 1)
Berdyugina S.V., Jankov S., Ilyin I., Tuominen I., Fekel F.C., 1998, A&A 334, 863
Berdyugina S.V., Tuominen I., 1998, A&A 336, L25
Dempsey R.C., Bopp B.W., Henry G.W., Hall D.S., 1993, ApJS 86, 293
Dempsey R.C., Bopp B.W., Henry G.W., Hall D.S., 1994, in Caillault J.P. (ed.) Cool Stars, Stellar Systems, and the Sun, ASP Conf. Ser. 64, p. 393
Dempsey R.C., Neff J.E., O'Neal D., Olah K., 1996, AJ 111, 1356
Donati J.-F., Semel M., Carter B.D., Rees D.E., Cameron A.C., 1997, MNRAS 291, 658
Huenemoerder D.P., Ramsey L.W., Buzasi D., 1990, ApJ 350, 763
Korhonen H., Berdyugina S.V., Hackman T., Duemmler R., Ilyin I., Tuominen I., 1999, A&A 346, 101
Kupka F., Piskunov N.E., Ryabchikova T.A., Stempels H.C., Weiss W.W., 1999, A&AS 138, 119
Kurucz R.L., 1993, Kurucz CD No. 13
McWilliam A., 1990, ApJS 74, 1075

Oláh K., Marik D., Houdebine E.R., Dempsey R.C., Budding E., 1998, A&A 330, 559
Piirola V., 1973, A&A 27, 383
Piskunov N.E., Kupka F., Ryabchikova T.A., Weiss W.W., Jeffrey C.S., 1995, A&AS 112, 525
Strassmeier K.G., 1999, A&A 347, 225
Strassmeier K.G., 2000, in The Eleventh Cambridge Workshop on Cool Stars, Stellar Systems, and the Sun, eds. R.J. García López, R. Rebolo, and M.R. Zapatero Osorio (San Francisco: ASP), PASPC in press
Strassmeier K.G., Bartus J., Cutispoto G., Rodono M., 1997, A&AS 125, 11
Strassmeier K.G., Hall D.S., Fekel F.C., Scheck M., 1993, A&AS 100, 173
Strassmeier K.G., Serkowitsch E.,Granzer Th., 1999, A&AS 140, 29
Vogt S.S., Hatzes A.P., Misch A.A., Kürster M., 1999, ApJS 121, 546